Cranfield UNIVERSITY

Deborah Saban

Wake Vortex Modelling and Simulation for Air Vehicles in Close Formation Flight

School of Engineering

Submitted for the degree of Ph.D.

Cranfield UNIVERSITY

Dynamics, Simulation and Control Group
Department of Aerospace Sciences
School of Engineering

Submitted for the degree of Ph.D.
Academic Year 2009–2010

Deborah SABAN

Wake Vortex Modelling and Simulation for Air Vehicles in Close Formation Flight

Supervisor: **Dr James F Whidborne**

January 2010

Abstract

The aim of this research is to develop realistic models of aerodynamic cross-coupling effects that can be incorporated in real-time or near real-time simulations of Unmanned Aerial Vehicles (UAVs) in close formation flight. These would permit the assessment of the risks and issues associated with wake vortex evolution and encounter and the analysis of their consequences on the design of automatic control systems and the development of safe and reliable operating procedures. A number of wake vortex modelling techniques that can be used in formation flight simulations are reviewed. A novel Wake Vortex Model (WVM) is developed, implemented, verified, validated and successfully integrated within a Matlab/Simulink simulation environment. The code, named ELL because it is based on Weissinger's extended lifting line theory, meets the following requirements: (i) it is generic and can easily be adapted to accomodate any wing planform and air vehicle configuration; (ii) it is computationally rapid enough to be used in real-time or near real-time simulations; (iii) and it is sufficiently representative to support studies of aerodynamic interaction between multiple air vehicles during formation reconfiguration and air-to-air refuelling simulations. Simulink test scenarios of two Aerosonde UAVs are developed to test and validate the use of ELL within simulation models, and the simulation environment is interfaced with visualisation tools in order to facilitate the evaluation of multiple air vehicle dynamic interaction.

Acknowledgements

Firstly, I would like to express my sincere gratitude to my supervisor, Dr James Whidborne, for his constant help, advice, guidance and good mood during the past three years. Thanks must also go to the former Head of the Dynamics, Simulation and Control group Mike Cook for his encouragements, insightful anecdotes and advice, and to Dr Alastair Cook for his help and expertise on many aspects of flight dynamics. I also wish to thank the other members of the group, especially Dr Annalisa Buonanno, Rick Drury, Pierre-Daniel Jameson, Sunan Chumalee and Stuart Andrew for the many helpful and interesting discussions we have had together.

I would like to acknowledge Cobham for their financial support. In particular, I am grateful to my industrial partners, Richard Bourne, Dr Adrian Craven and Harvey Wilson for their support and their professionalism.

I am indebted to Clement Toussaint, from the Onera-DCSD, Toulouse, for allowing me to use a Matlab code that he had written using Weissinger's extended lifting line theory. His code proved to be a starting point for the development of ELL.

I also wish to thank the Worshipful Livery of Coachmakers and Coach Harness Makers of London, who awarded me the 2007 Eric Beverley Bursary, and the International Aviation Womens Association, who awarded me the 2008 International IAWA Scholarship. A special mention goes to the Worshipful Livery of Coachmakers and Coach Harness Makers Past Master Group Captain Marcus Wills CVO OBE, for his friendship and generous support.

These scholarships provided me with the financial support to visit the world leading research groups in the area of autonomous formation flight (Technion, Israel; Texas A&M University, USA, and the University of Texas at Arlington, USA), and to attend and present my research at the AIAA Modeling and Simulation Technologies Conference in Chicago, in August 2009. These trips proved to be very beneficial for my work, as

they enabled me to extend and deepen my knowledge, to disseminate my work through the presentations I had the opportunity to give, and by sharing views and experiences with the experts I met, to obtain valuable feedback on how my research aims could best be achieved. In this respect, I am particularly indebted to Dr John Valasek – from Texas A&M University – and to Dr Tal Shima – from the Technion – for their helpful comments and suggestions, and to Dr Atilla Dogan – from the University of Texas at Arlington – whose valuable advice has helped to steer my work in the right direction.

Finally, I would like to express my deepest gratitude to my family and my friends, without whom I would never have reached this point: my parents Claudine and Philippe, my brothers Gabriel and Ouri, my friends Audrey, Marie-Line and Morgane, my partner Jack and his family, especially Wendy and Mike, for their patience, their tireless encouragements, and their continual love and support. I am very fortunate to have these people in my life.

Contents

List of Figures

List of Tables

Nomenclature

a	Unit direction vector of the airfoil
A	AIC matrix; state matrix
a_0	Lift slope
b	Wing span
B	Magnetic field; input matrix
C	Output matrix
C_D	Drag coefficient
C_{D_0}	Zero lift drag coefficient
C_L	Lift coefficient
C_{L_q}	Lift coefficient due to pitch rate
C_{L_0}	Zero angle of attack lift coefficient
C_{L_α}	Slope of the $C_L - \alpha$ plot
C_{LL}	Rolling moment coefficient
C_{LL_p}	Rolling moment coefficient due to roll rate
C_{LL_r}	Rolling moment coefficient due to yaw rate
$C_{LL_{r_0}}$	Zero lift rolling moment coefficient due to yaw rate
C_{LL_0}	Rolling moment coefficient about the aerodynamic centre of the wing
C_{LL_β}	Rolling moment coefficient due to sideslip
$C_{LL_{\beta_0}}$	Zero lift rolling moment coefficient due to sideslip
C_M	Pitching moment coefficient
C_{M_q}	Pitching coefficient due to pitch rate
C_{M_0}	Pitching moment coefficient about the aerodynamic centre of the wing
C_{M_α}	Slope of the $C_M - \alpha$ plot
d	Unit direction vector of the lifting line
D	Drag
D	Transmission matrix
d_x	Longitudinal distance
d_y	Lateral distance

$\mathbf{dl}$	Elementary vector
f	Fuel state
$\mathbf{G}$	Vorticity vector
h	Perpendicular distance from the field point P to the vortex branch line; altitude
I	Current intensity
K	Feedback gain
l	Chord length
L	Lift
$\mathbf{L}$	Lift vector
L'	Spanwise lift distribution
$\mathbf{n}$	Unit vector in the normal direction
N	Number of aircraft
n_{seg}	Number of discretisation segments
n_{wing}	Number of wings
p	Body roll rate; pressure
P	Field point
q	Body pitch rate
r	Body yaw rate; radial distance from the vortex core centre
$\mathbf{r}$	Radius vector
$\mathcal{R}$	Reference frame
r_c	Vortex core radius
r_d	Dispersion radius
r_i	Internal core radius
r_o	External core radius
r_{roll}	Rolling moment radius
s	Spanwise load factor
S	Wing area
t	Time parameter
u	Axial velocity component
$\mathbf{u}$	Input vector
U	Axial velocity deficit
v	Lateral velocity component
V	Air vehicle velocity; airflow velocity
$\mathbf{V}$	Air vehicle velocity vector;
ve	Twist angle (washout)
$\mathbf{V_i}$	Induced translational wind velocity vector
$\widetilde{\mathbf{Vi}}$	Effective induced translational wind velocity vector

V_θ	Tangential velocity
w	Normal velocity component
x, X	x coordinate
$\mathbf{x}$	State vector
y, Y	y coordinate
$\mathbf{y}$	Output vector
z, Z	z coordinate

Greek symbols

α	Angle of attack
$\alpha_{L=0}$	Angle of zero lift
α_0	Angle of incidence
β	Angle of sideslip
γ	Angular parameter
Γ	Vortex strength, circulation
δ	Dihedral angle; angular parameter
Δ	Incremental quantity
ϵ	Boundary parameter
ε	Taper ratio; eddy viscosity
ζ	Rudder deflection angle; damping
η	Elevator deflection angle
θ	Pitch attitude; angular parameter
Θ	Pitch attitude
λ	Aspect ratio
Λ	Notation used to designate an air vehicle
μ_0	Magnetic constant
ν	Kinematic viscosity of the air
ξ	Aileron deflection angle
ρ	Fluid density
τ	Age of the vortex branch; throttle setting
ϕ	Bank angle
Φ	Bank angle; velocity potential
φ	Sweepback angle at 1/4-chord
χ	Track angle
ψ	Heading angle
Ψ	Heading angle; gravitational potential
ω	Axial velocity
$\boldsymbol{\omega_i}$	Induced rotational wind velocity vector

$\widetilde{\boldsymbol{\omega}}_{\mathbf{i}}$	Effective induced rotational wind velocity vector
Ω	Engine speed

Subscripts

0	Initial; origin
c	Vortex centre; calculation point
d	Demanded
e, E	Earth-referenced variable
eff	Effective
i	Induced
j, k	Indices
lat	Lateral variable
$longi$	Longitudinal variable
m	Middle
rel	Relative
$trim$	Trimmed variable
x, y, z	Components of a vector in the x, y, z axes
∞	Upstream

Other notations

$\dot{}$	Time derivative
$\tilde{}$	Effective

Abbreviations

AAR	Automated Aerial Refueling
AARD	Autonomous Airborne Refueling Demonstration
AFF	Autonomous Formation Flight
AIAA	American Institute of Aeronautics and Astronautics
AIC	Aerodynamic Influence Coefficient
ASTRAEA	Autonomous Systems Technology Related Airborne Evaluation & Assessment
ATC	Air Traffic Control
ATD	Along-Track Distance
AVDS	Aviator Visual Design Simulator
AVOSS	Aircraft VOrtex Spacing System
AV-SAVE	Air Vehicle Simulation and Visualisation Environment
CERFACS	Centre Européen de Recherche et de Formation Avancée en Calcul Scientifique
CFD	Computational Fluid Dynamics
CG	Centre of Gravity
CPU	Central Processing Unit
DCM	Direction Cosine Matrix
DCSD	Département Commande des Systèmes et Dynamique du vol
DLR	Deutsches Zentrum für Luft- und Raumfahrt
EC	European Commission
ELL	Extended Lifting Line
ETWIRL	European Turbulent Wake Incident Reporting Log
FCS	Flight Control System
FGC	Formation Geometry Centre
GPS	Global Positioning System
HVM	Horseshoe Vortex Model
IAWA	International Aviation Womens Association

IP	Internet Protocol
LAN	Local Area Network
LES	Large Eddy Simulation
LQR	Linear-Quadratic Regulator
NASA	National Aeronautics and Space Administration
NED	North East Down
NLR	Nationaal Lucht- en Ruimtevaartlaboratorium
ONERA	Office National d'Etudes et Recherches Aérospatiales
OTD	Off-Track Distance
P	Proportional
PC	Personal Computer
P+I	Proportional Integral
PID	Proportional Integral Derivative
PIV	Particle Image Velocimetry
RAM	Random-Access Memory
SAS	Stability Augmentation System
SCS	Simulation Control Station
SE	Synthetic Environment
SEU	South East Up
SPPO	Short Period Pitching Oscillation
TAP	Terminal Area Productivity
TASS	Terminal Area Simulation System
UAV	Unmanned Aerial Vehicle
UDP	User Datagram Protocol
USAF	United States Air Force
VL	Virtual Leader
VLM	Vortex Lattice Method
WAVENC	WAke Vortex Evolution and ENCounter
WVM	Wake Vortex Model

Chapter 1

Introduction

1.1 Background

UAVs (Unmanned Aerial Vehicles) constitute a valuable observation platform – between ground-based sensors and high-flying satellites – and a cheaper, safer alternative to large, piloted aircraft. During the last decade, UAVs have mostly been employed by the military to perform dull, dirty or dangerous duties (commonly referred to as the three "D" missions), including ground attacks, battlefield command, reconnaissance and surveillance. Today, the "bird's eye view" they provide has potential applications in many other areas, such as homeland security (police surveillance, border patrol, etc.), public services (fire fighting, search and rescue, power-line and pipeline inspections, chemical and pollution sensing, climate monitoring, etc.), and the commercial sector (geographic surveys, aerial communications networks, crop spraying, etc.). Japan has been using remote controlled helicopters to perform crop inspection and spraying for almost 20 years [Dalamagkidis, Valavanis and Piegl, 2008; Shim, Han and Yeo, 2009]. In 2002, Japan counted more than 2000 motorbike-sized Yamaha RMAX models in service, and in 2008 the fleet of Japanese industrial UAVs had outnumbered the fleet of manned vehicles used for agriculture purposes. Since 2000, Japanese UAVs have also been used to monitor active volcanoes.

However, expanding the use of UAVs to routine commercial and civilian applications requires their integration into non-segregated airspace, and, therefore, the establishment of an appropriate regulatory framework [Dalamagkidis, Valavanis and Piegl, 2008; Loh, Bian and Roe, 2009]. The British national programme ASTRAEA (Autonomous Systems Technology Related Airborne Evaluation & Assessment), funded by the government's Department of Trade and Industry, focuses on the development of new and existing technologies, systems, facilities, regulations and protocols which are needed to

allow uninhabited air vehicles to operate safely and routinely in the British controlled airspace, thereby bringing economic, environmental and security benefits to the UK. Further information about the ASTRAEA programme may be found on the project website [*ASTRAEA Website: http://www.projectastraea.co.uk/*, N.d.].

Finally, as some UAV missions require close proximity formation flying, a detailed understanding of the interactive coupling between air vehicles is needed to maintain a safe formation and to avoid excessive structural and control loads. Therefore, in order to investigate safe and reliable operating procedures for close formation flight, analyse structural loading, and design and test automatic control systems, realistic models of the wake vortex effects induced by one vehicle upon another need to be developed and incorporated into real-time or near real-time simulation environments.

1.2 Objectives & Requirements of the Research

This research has been undertaken in cooperation with Cobham plc and in support of the British national programme ASTRAEA (see Section 1.1). The aim of the work presented in this thesis has been to develop realistic models of aerodynamic coupling between air vehicles flying in close proximity in order to permit the assessment of the risks and issues associated with wake vortex evolution and encounter. This was achieved by pursuing the following objectives:

1. Identify the different wake vortex modelling techniques and review the work carried out on autonomous formation flight, including autonomous aerial refuelling.
2. Develop, verify and validate a Wake Vortex Model (WVM) that meets the following requirements:
    - be generic and easily adapted to fit any wing planform and air vehicle configuration,
    - be computationally rapid enough to be used in real-time or near real-time simulations, and
    - be sufficiently representative to support studies of aerodynamic interaction between multiple air vehicles during formation reconfiguration and air-to-air refuelling simulations.
3. Design a Flight Control System (FCS) and autopilot functions for the Aerosonde UAV (using an available Aerosonde dynamics model) in order to validate and test the WVM in UAV close formation flight simulations.

4. Interface visualisation tools with the simulation environment in order to facilitate the evaluation of multiple air vehicle dynamic interaction.

1.3 Thesis Outline

The layout of this thesis reflects the objectives stated in Section 1.2. Chapter 2 summarises the work published on wake vortex effects characterisation (Section 2.1), and reviews the approaches to the modelling of these effects in the case of close formation flight and aerial refuelling (Section 2.2). The research carried out in the field of autonomous formation flight is also presented (Section 2.3), along with the different simulation environments and visualisation techniques (Section 2.4).

The theoretical background necessary to the WVM development is introduced in Chapter 3. This material is drawn from Schlichting [1979], Anderson [2007], Bertin and Smith [1998], Katz and Plotkin [2001] and Houghton and Carpenter [1993], and includes some elements of potential flow theory (Section 3.1), as well as an overview of Prandtl's classical lifting line theory (Section 3.2) and of Weissinger's extended lifting line theory (Section 3.3). These are followed by a discussion about the consideration of viscosity effects – vortex cores and vortex velocity distribution profiles – leading to the choice of a wake vortex modelling technique, a vortex profile and a viscous core (Section 3.4).

Chapter 4 discusses the development (Section 4.2) and the implementation (Section 4.3) of a novel WVM. The code (ELL) computes the steady-state velocities induced on one air vehicle by the wake(s) of the others using the Kurylowich vortex model in combination with Weissinger's extended lifting line theory. Furthermore, in order to facilitate reconfiguration scenarios where the relative positions of the vehicles within the formation vary, thereby modifying the influence of one aircraft upon another, each vehicle must be capable of behaving as both a wake-generating and a wake-encountering entity depending on its position relative to the others. This is achieved by modelling all aircraft using the same technique.

Chapter 5 describes how ELL was verified (Section 5.3) and validated (Section 5.4). The verification process includes the analysis of the influence on the induced velocity field of: (i) the choice of a reference frame (Subsection 5.3.2); (ii) the distance between two vehicles of a formation (Subsection 5.3.3); (iii) the airspeed, angle of attack and angle of sideslip of the incoming airflow (Subsection 5.3.4). The validation process

consists of comparing the effective induced wind velocities (Subsection 5.4.2) and the incremental aerodynamic forces and moments coefficients (Subsection 5.4.3) obtained with ELL with experimental and computational results published by Blake and Gingras [2004] and Dogan, Venkataramanan and Blake [2005].

Chapter 6 aims at testing and validating the use of ELL within close formation flight simulations. A Simulink Aerosonde UAV model is used (Section 6.2) and a preliminary analysis is performed in order to determine whether the tailplane should be taken into account in the computation of the wake-induced effects (Section 6.3). The Aerosonde FCS capabilities are then demonstrated through the analysis of the Aerosonde response to a transient wind gust (Section 6.4). Finally, two test scenarios – including formation keeping and a formation reconfiguration manoeuvre – are simulated and their results are presented and analysed (Sections 6.5 and 6.6 respectively).

The conclusions of the research, contributions to knowledge and recommendations for future work are outlined in Chapter 7.

In addition, a brief presentation of the Aerosonde's FCS is given in Appendix A, and details regarding the interfacing of visualisation tools with the simulation environment can be found in Appendix B. Finally, the list of publications is presented in Appendix C.

1.4 Achievements

The main achievements of this research are covered in Chapters 4 to 6. They may be summarised as follows:

(i) **Theoretical developments:** the extended lifting line method was used in combination with a viscous core, and the method was applied to model the wake vortex effects between air vehicles in close formation flight (Chapter 4).

(ii) **Wake Vortex Model:** a novel WVM – called ELL – based on the theoretical developments mentioned above was developed, implemented, verified, and validated (Chapters 4 and 5).

(iii) **Applications:** the use of ELL within near real-time simulations to assess and analyse mutual aerodynamic coupling effects and support the design of suitable automatic control systems was demonstrated. In particular, it was shown that unlike previous work carried out in this field, ELL can be used for reconfiguration

scenarios where leading and following air vehicles exchange positions (Chapter 6).

The main elements of Chapter 4 were presented at the 24^{th} International UAV Systems Conference [Saban and Whidborne, 2009*a*]. These, along with the validation process in Chapter 5, were published in the Aeronautical Journal [Saban, Whidborne and Cooke, 2009]. The results of Chapter 6 were included in a presentation at the 2009 AIAA Modeling and Simulation Technologies Conference [Saban and Whidborne, 2009*b*]. In addition, the relevant review and theoretical materials are covered in Chapters 2 and 3 respectively.

1.5 Software Tools

The following software tools have been used during this research:

- MATLAB [*The Mathworks Official Website: http://www.mathworks.com/*, N.d.]: MATLAB is a technical computing environment developed by The MathWorks.
- Simulink [*The Mathworks Official Website: http://www.mathworks.com/*, N.d.]: Simulink, also developed by The MathWorks, is a simulation and model-based design package which can be coupled with MATLAB.
- FlightGear [*FlightGear Official Website: http://www.flightgear.org/*, N.d.]: FlightGear, developed by the FlightGear project, is a free, open-source, multi-platform, cooperative flight simulator development project, which can be interfaced with Simulink.
- AVDS [*AVDS Official Website: http://www.rassimtech.com/*, N.d.]: AVDS (Aviator Visual Design Simulator), developed by Rasmussen Simulation Technologies Ltd., is a realtime interactive visual tool for control system engineering. It can be used in a MATLAB/Simulink environment via the "AVDS Toolbox for MATLAB" designed for this purpose.

Chapter 2

Literature Review

2.1 Characterisation of Wake Vortex Effects

2.1.1 A Blessing or a Curse?

Wake vortex effects are both a blessing and a curse. On the one hand, wake vortices represent severe atmospheric disturbance to other air vehicles: this constrains the operational capacity of airports, as a large safety distance between aircraft must be maintained during two consecutive take-offs or landings; this also complicates the air-to-air refuelling task as the presence of interactions makes it more difficult for the receiver to maintain its position behind the tanker; finally, the critical role that wake vortices play in the detection of military aircraft has led to the research and development of techniques to provoke their premature decay or breakdown.

On the other hand, optimally spaced vehicles benefit from favourable wake vortex induced interactions similar to that used by geese when flying in formation [Beukenberg and Hummel, 1990]. These benefits include reduced induced drag for the trailing aircraft, which translates into significant fuel savings and/or increased range with a given payload.

Consequently, with the current and growing need for new technologies to lower fuel costs, and for new Air Traffic Control (ATC) procedures to increase the capacity of airports without compromising safety [Proctor and Switzer, 2000], the benefits, as well as the risks and issues associated with wake vortex evolution and encounter need to be assessed. For that, a better understanding of vortex formation, evolution, control, decay and breakdown is needed.

2.1.2 Motion, Decay, Breakdown and Associated Hazards

Kurylowich [1979], from the Wright-Patterson Flight Research Laboratory, analysed the motion, decay and breakdown of vortex wakes generated by both airplanes and helicopters, and developed an encounter model to assess their impact on USAF operations. The wake behind an airplane was modelled using a pair of vortices with viscous cores and time decay effect.

He was followed by Greene [1986], from the NASA Langley Research Center, who developed an approximate model of wake vortex motion and decay in the atmosphere. The effects of density stratification, turbulence and Reynolds number were analysed. The wake was characterised by a descending oval-shaped region of fluid created by the pair of counter-rotating wing-tip vortices.

Ten years later, an AGARD (Advisory Group for Aerospace Research & Development) conference brought together experts from various organisations such as FAA, NASA, DLR and ONERA to review the advances in prediction, methodology and experimental techniques related to aircraft wake research [*Proceedings of the AGARD Fluid Dynamics Panel Symposium on "The Characterisation & Modification of Wakes from Lifting Vehicles in Fluid"*, 1996].

Amongst them, Hoeijmakers [1996] presented the fundamental fluid dynamics aspects of the vortex wake, along with a survey of mathematical models which could be used for numerical simulations of this phenomenon. He pointed out that different methods should be used depending on the region of the wake which is to be modelled, namely:

(i) the roll-up region (approximately 20 wing spans),

(ii) the vortex region (approximately 500 wing spans), and

(iii) the decay region (greater than 500 wing spans).

In particular, for near wake regions, potential flow methods (panel methods) employing a rigid wake approximation seem adequate.

Between December 1997 and February 2000, the EC-funded research project WAVENC (WAke Vortex Evolution and ENCounter) permitted to gain a better insight into the wake vortex phenomenon [De Bruin, 2000*a*,*b*]. This project, which involved partners such as NLR, Aerospatiale, CERFACS, DLR, and ONERA, included the exploitation of ETWIRL (European Turbulent Wake Incident Reporting Log) data, the experimental study (using PIV) and numerical simulation of wake vortex evolution up to the far wake

region, the development of aerodynamic interaction models for wake vortex encounter, as well as the implementation of a simple WVM (VORTEX, developed by CERFACS) and a strip theory model from ONERA into a Synthetic Environment (SE) for real-time simulations of wake vortex encounters. The results from the WAVENC project were used in the subsequent projects C-Wake (wake vortex characterization and control) and S-Wake (assessment of wake vortex safety).

Finally, Rossow and James [2000], from the NASA Ames Research Center, estimated that a hazardous level persists for wake crossings at cruise altitudes for times up to about 20 minutes (up to 200 nautical miles) behind the wake generating aircraft. He based his estimates on the observation of cross-sectional sizes of wakes as they age and on the calculation of vertical loads due to the wake-induced downwash. He also described a technique for avoiding vortex wakes at cruise altitudes based on the utilisation of a GPS to keep track of the location and the estimated size of the wake of each aircraft.

2.1.3 Experimental Work

A great amount of experimental work was also carried out for these purposes. A few relevant examples are discussed here. Vlachos and Telionis [2003] conducted experiments in a water tunnel to characterise the aerodynamic interaction between finite wings flying in very close proximity, and used PIV to visualise the velocity field downstream of the wings. They showed that the strength of the vortices generated by one wing is modified by the presence of another wing. In other words, in the case of formation flying, the leader is also affected by the presence of the follower.

More recently, Karakus, Akilli and Sahin [2008] also used PIV to investigate the details of the formation, structure, and development of near-field wing tip vortices generated by an airfoil NACA0012.

Finally, Allen and Breitsamter [2009] used hot-wire anemometry in a wind tunnel to visualise the flow-field of the vortex wake of a system composed of a wing and a tailplane as part of the EC Project FAR-Wake (“Fundamental Research on Aircraft Wake Phenomena”). The four counter-rotating neighboured vortices development (due to the positive lift generated on the wing and negative lift generated on the tail plane) were shown up to 48 spans downstream of the model, i.e. in a region including the near field, the extended near field and the far field. Their respective circulation and span ratio were chosen so that that the strong interaction between the neighbouring counter-rotating vortices would accelerate the wake vortex decay and alleviate the wake vortex

hazard.

2.2 Modelling of Wake Vortex Effects

2.2.1 Approaches to the Modelling of Wake Vortices

There are essentially two approaches to the real-time modelling of wake vortices:

(i) Look-up databases containing *a priori* values of the vortex effects obtained from either theoretical and/or experimental methods: CFD models [Spence et al., 2005; Le Moigne and Qin, 2006; Spence et al., 2007], wind/water tunnel [Vlachos and Telionis, 2003; Myatt and Blake, 1999; Blake, 2000] and/or flight test measurements [Hansen and Cobleigh, 2002; Hansen et al., 2002; Vachon et al., 2002];

(ii) Online computational methods. These methods can be classified in four categories, from the simplest to the most involved:

- methods using Prandtl's lifting line theory, i.e. a superposition of horseshoe vortices along the lifting line (with or without viscous core), e.g. Bloy et al. [1986], Bloy, Ali and Trochalidis [1987], Bloy and Trochalidis [1989], Bloy and Trochalidis [1990], Bloy, Trochalidis and West [1991] and Pachter, D'Azzo and Proud [2001];
- Vortex Lattice Methods (VLM), e.g. Bloy et al. [1993] and Melin [2000]);
- improved methods taking account of the roll-up of the wake, e.g. Bloy and West [1994], Bloy and Joumaa [1995*a*], Bloy and Lea [1995], Wang and Mook [2003], Denis [2004] and Karkehabadi [2004];
- online CFD computations, e.g. Kenny, Takeda and Thomas [2008].

The last, obviously, requires enormous computational power.

In addition to being costly to generate, look-up database approaches are extremely computationally demanding to handle and are only relevant for a specified air vehicle and a range of flight conditions. Simple computational methods are rapid, but their results are not always realistic or accurate enough. Hence choosing a computational method to model the vortex wake involves finding a compromise between accuracy on the one hand and cost and rapidity of execution on the other hand [Margason et al., 1985].

2.2.2 Wake Vortex Effects During Close Formation Flight and Aerial Refuelling

In the 1980's and 90's, Bloy and colleagues [Bloy et al., 1986; Bloy, Ali and Trochalidis, 1987; Bloy and Trochalidis, 1989, 1990; Bloy, Trochalidis and West, 1991; Bloy et al., 1993; Bloy and West, 1994; Bloy and Joumaa, 1995*b*,*a*; Bloy and Lea, 1995], from the University of Manchester, pioneered the field of wake vortex effect modelling during air-to-air refuelling. These effects were investigated both theoretically and experimentally, and various computational methods, from relatively simple wake models based on a horseshoe vortex representation of the tanker's wing [Bloy et al., 1986; Bloy, Ali and Trochalidis, 1987] to more realistic roll-up models of the wake [Bloy and Joumaa, 1995*a*] were used.

In 1986 and 1987, the lateral [Bloy et al., 1986] and longitudinal [Bloy, Ali and Trochalidis, 1987] dynamic stability and control of a large receiver aircraft during air-to-air refuelling were investigated using a simple horseshoe vortex to represent the tanker's wing. In Bloy and Trochalidis [1989], the performance and longitudinal stability and control of a large receiver aircraft during aerial refuelling was re-assessed using a horseshoe vortex to model the tanker's wing, and a VLM to represent the receiver's. In Bloy and Trochalidis [1990], aerodynamic interactions between two aircraft in air-to-air refuelling with varying vertical separation were calculated using a horseshoe vortex for the tanker and either a VLM or the lifting line theory for the receiver. Apart from the pitching moment estimates, fairly good agreement was obtained between the model predictions and wind-tunnel experiments. The method was adapted in Bloy, Trochalidis and West [1991] for the case of a flapped tanker aircraft, by using horseshoe vortices from both the wing and the flap tips to represent the tanker wing. Comparison with wind-tunnel results showed significant differences, which were ascribed to the fact that the theoretical model was taking account of neither the roll-up of the tanker wake, nor the viscous decay of the vortices. In Bloy et al. [1993], further improvements to the model were obtained by representing the tanker wing wake by a flat vortex sheet model while still calculating the aerodynamic loads on the receiver using a VLM. Overall, the predictions of the model compared favourably with data obtained in a low-speed wind-tunnel.

In Bloy and West [1994], a rolled-up vortex sheet model of the tanker's wake was used to estimate the downwash and sidewash over the receiver. Again, the theoretical results obtained using this model compared favourably with experimental data [Bloy and Lea, 1995]. Bloy and Joumaa [1995*a*] coupled the wake roll-up method developed in Bloy

and West [1994] with a VLM and approximate expressions for the receiver fuselage effect, to study the stability and control of a Hercules receiver aircraft behind a KC-10 tanker during air-to-air refuelling. In Bloy and Khan [2001], an approximate single-point receiver model was used for real-time aerial refuelling flight simulations. This used the tanker wake conditions at the receiver centre of gravity (CG) and calculated the translational and rotational components of the velocity induced by the tanker wake on the receiver. Overall, the model compared satisfactorily with that developed previously in Bloy and West [1994]. However, because the wake velocity field induced by the tanker, which is highly non uniform, was only estimated at the CG of the receiver aircraft, the accuracy of the results was quite limited and the model was unsuitable for cases involving large receiver aircraft. Finally, in Bloy and Khan [2002], a static model of the hose and drogue was added to the previous flight simulation model in order to predict the hose shape and the loads induced on the receiver probe during contact.

A large amount of work was also carried out by Blake and colleagues from the Wright-Patterson Air Force Research Laboratory to model wake vortex effects. Blake and Multhopp [1998] used a horseshoe vortex with viscous core and a VLM to analyse the optimum configuration for formation flight (relative position, distribution of lift across a formation, optimum cruise altitude), as well as the effect of accuracy in maintaining lateral position and the effect of rotation of the lead aircraft. Myatt and Blake [1999] presented wind-tunnel data for the trail aircraft in a two-ship formation and developed possible simplifications to the form of the aerodynamic mathematical model needed for adequate simulation of close formation flight. Blake [2000] developed a simplified mathematical representation of the aerodynamics for simulation of an arbitrary large number of tailless vehicles in close formation flight. A combination of wind tunnel results and vortex lattice analysis were used to reduce the number of state variables included in the aerodynamic coupling terms.

Wagner et al. [2001] used HASC95 – a VLM developed by NASA – to study the drag reduction in tight formation flight for two and for three T-38 Talon aircraft. The analysis showed that a 2D model of the aircraft gives almost identical results as a 3D-model. Therefore, the 2D model was selected to perform the analysis, which showed fuel benefits in the range of 11.5% for a tight three ship formation flight of T-38s operating at Mach 0.54 at 10,000 feet. Flight tests were performed in Wagner et al. [2002] in order to confirm the drag benefits shown by the previous theoretical study. The flight test data showed $8.8\% \pm 5.0\%$ savings for the follower in a two ship formation; however the flight test data for a three ship formation were inconclusive. The reason was supposed to be because no station-keeping controller was used making it extremely difficult for

the pilot to hold a near perfect position in the vortex.

Finally, Blake et al. presented wind-tunnel measurements of aerodynamic interference effects between two delta-wing aircraft in close proximity [Blake and Gingras, 2004], and between one delta-wing (UAV) and a larger KC-135R tanker [Blake, Dickes and Gingras, 2004]. The experimental data were compared with predictions from the HASC95 planar VLM. In both cases, the effects were well predicted, except for the induced drag. It was found in Blake and Gingras [2004] that although the wake-induced lift was slightly over-predicted when the aircraft overlapped in the spanwise direction, the predicted and experimentally derived boundaries between stable and unstable regions of three positional stability derivatives (change in lift and pitching moment with vertical position and change in rolling moment with lateral position) were in good agreement. Finally, it was shown in Blake, Dickes and Gingras [2004] that the aerodynamic interference effects vary significantly with relative lateral and vertical spacing, but only weakly with relative longitudinal spacing.

2.2.3 Should the Roll-up of the Wake be Taken Into Account?

Descriptions of wake vortex numerical models which take account of the roll-up of the vortex sheet were provided in Beukenberg and Hummel [1990], who computed the interaction between the wakes of two aircraft in formation by representing the wakes as rolled-up sheets and the wings as lifting lines, and in Wang and Mook [2003], who developed an unsteady VLM which integrates the roll-up of the wake as part of the solution.

Denis [2004] studied the importance of taking account of the roll-up of the wing in simulations of vehicles in close formation flight. She developed a simplified vortex sheet roll-up method for formation flight. Two elliptically loaded wings were studied. The roll-up of the leader's vortex sheet was computed in the Trefftz plan using a linear vorticity panel method. A smoothing parameter and a truncation of the vortex sheet in highly rolled-up areas were introduced to stabilise the computations. The trailing vehicle was modelled as a lifting line and its induced drag and rolling moment were computed through a near-field analysis. Results showed that, if the induced drag of the trailing vehicle is very well predicted by a simple horseshoe vortex model with viscous core, the roll-up of the wake needs to be taken into account for the rolling moment estimates to be accurate.

Finally, the negligible effects that the wake roll-up of the leader has on the induced-drag

predictions of the follower were confirmed by Bramesfeld and Maughmer [2008] for high aspect ratio wings. Two wake representations – with and without roll-up – were used and led to similar results, with the exception of the range of lateral separations for which the minimum induced drag was obtained: the fixed-wake model, which predicted a wider range, overestimated the benefits of formation flying. Furthermore, no vortex core was used to prevent the singularities due a discrete distribution of horseshoe vortices where the vortex strength is concentrated on an infinitely thin filament; instead, both models used a continuous distribution of the vorticity.

2.2.4 Other Models

Other wake evolution and encounter models include:

- **LinAir** [Durston, 1993]: LinAir is a nonplanar, multiple lifting surface aerodynamics program. It was first developed by NASA in 1983, and is now used by several universities and companies such as Boeing, AeroVironment, Northrop and Lockheed, as well as by NASA's researchers for the preliminary analysis of unconventional or new design concepts. The wing is partitioned both spanwise and chordwise, and the wake detaches from the wing at its trailing edge. No vortex core is used, and singularities are avoided by setting the position of the wake so that it does not interfere with downstream control points.

- **Tornado** [*Tornado Website: http://www.redhammer.se/tornado/index.html*, N.d.]: Tornado is an open source vortex lattice MATLAB implementation for linear aerodynamic wing applications. It was originally developed by Melin [2000], as part of his MSc Thesis at the KTH (Royal institute of Technology), Sweden, and has been subsequently further developed as a collaboration between the KTH, the University of Bristol and Redhammer Consulting Ltd. Tornado gives very good results and visuals for any type of wing planform, but is too slow to be used in real-time applications.

- **WakeCAD** [Capetta, Giulietti and Innocenti, 2001]: WakeCAD is a MATLAB toolbox which has been developed at the University of Pisa in 2001 to calculate the aerodynamics forces and moments induced by a lifting surface system on another when flying in close proximity. The leader's wake is modelled with horseshoe vortices and induced forces and moments are introduced in the wingman equations of moments through additional coefficients. However, the details given and the results presented in Capetta, Giulietti and Innocenti [2001] are too scant to enable a proper evaluation of the method.

- **WakeScene** [Holzäpfel et al., 2009]: WakeScene (Wake Vortex Scenarios Simulation) is a software package developed by DLR for airports to determine the wake vortex encounter probability during approach and landing, depending on the traffic mix, the aircraft trajectories and the meteorological conditions. A stochastic approach is used to predict the wake vortex evolution and the potential hazard areas.

- **TASS** [Switzer, 1996; Shen et al., 1999; Proctor and Switzer, 2000]: TASS (Terminal Area Simulation System), developed at the NASA Langley Research Centre, is a 3D time-dependent, nonlinear, compressible, non hydrostatic Large Eddy Simulation (LES) model which uses a meteorological framework to simulate and quantify the vortex wake motion and decay in relation to atmospheric variables.

- **AVOSS** [Hinton, 1996]: AVOSS (Aircraft VOrtex Spacing System) is a system developed as part of the NASA programme TAP (Terminal Area Productivity), which aims at providing ATC facilities "with dynamical weather dependent separation criteria with adequate stability and lead time for use in establishing arrival scheduling". It uses weather sensors and short-term predictions of the atmospheric state, analytical wake predictions algorithms to assess the wake vortices positions and strengths under the specified atmospheric conditions, and wake vortex safety sensors. AVOSS was successfully demonstrated at Dallas Fort Worth International Airport in July 2000 [Rutishauser and O'Connor, 2001].

2.3 Autonomous Formation Flight

2.3.1 Benefits of Autonomous Formation Flight

A preliminary study of the use of aircraft wakes to achieve power reductions in formation flight was performed by Beukenberg and Hummel [1990] and Hummel [1996]. However, close formation flight requires an enormous amount of effort and concentration for the pilots to maintain their positions in the formation. Therefore, in order to reduce the pilot workload and make it an interesting and viable concept, close formation flying should be partially or fully automated. Jenkinson, Caves and Rhodes [1995] carried a preliminary investigation into the application of automatic formation flight to civil operations and found that it could help the air transport industry to reduce costs and meet the increasing demand.

The benefits of autonomous formation flight were confirmed in 2002, during the Autonomous Formation Flight programme (AFF) at the NASA Dryden Flight Research Center: flight tests with two F/A-18 Hornets demonstrated up to 18% reduction in fuel consumption for the following air vehicle in cruise condition [Lavretsky and Misovec, 2002; Hanson et al., 2002; Hansen et al., 2002; Cobleigh, 2002; Vachon et al., 2002]. The follower's "sweet spot" – i.e. the area of maximum drag reduction, hence maximum benefits – was found to be at a lateral position of 13% wing overlap and vertical positions of level and 13% below the leading airplane. However, the tests also demonstrated that the first peak in vortex induced incremental side force and moments coincide with the sweet spot, thereby making the design of a suitable flight control system more challenging. Also, the flight data suggested that the vortex effects are getting weaker in pitch and roll, but stronger in yaw and side force as the longitudinal distance from the leader increases [Hansen and Cobleigh, 2002].

2.3.2 Autonomous Formation Flight Architecture and Control

A large amount of work about autonomous close formation flight from a control point of view was carried out by Giulietti et al. [Giulietti, Pollini and Innocenti, 2000; Giulietti and Mengali, 2004; Giulietti et al., 2005]. Giulietti, Pollini and Innocenti [2000] investigated the management of several formation structures capable of dealing with a variety of generic transmission and communication failures – including the complete loss of one aircraft – as effectively and autonomously as possible. A FCS was synthesised using LQR control techniques in order to maintain the formation geometry, and a simple horseshoe vortex model was used for the aircraft wake.

Giulietti and Mengali [2004] investigated the flight dynamics and control of three different formation structures. Their analysis concluded in the superiority of the behavioural approach over the leader-wingman and the Virtual Leader (VL) structures to maintain the close formation:

- In the leader-wingman approach, the leader follows a prescribed trajectory while the wingmen maintain their positions in the formation in relation to one another. This approach is intuitive and easy to implement, however the rear aircraft often show poor responses due to string instabilities.
- In the VL structure, each aircraft in the formation maintains its position in relation to a virtual leader (which can be either one aircraft in the formation or a virtual point). The advantage of this structure is that each aircraft shows the same transient, thereby eliminating the propagation errors. However, the aircraft have no awareness of the positions of the others so collisions are difficult to prevent.

- In the behavioural structure, instead of reporting to a “leader”, each aircraft maintains its position in relation to the Formation Geometry Centre (FGC) point, whose position and dynamics depend on the positions and dynamics of all aircraft in the formation. Therefore, not only does this approach guarantee both trajectory tracking and formation keeping with no propagation errors, but collisions are also avoided. However, this strategy is more complex to implement as each aircraft needs the knowledge of all the other state vectors.

In Giulietti et al. [2005], the behavioural approach was implemented for a two-aircraft formation. Two control systems were designed: a trajectory controller for the FGC to follow a prescribed path, and a position controller for the formation geometry to be maintained. As in Giulietti, Pollini and Innocenti [2000], the wake-induced effects were modelled using a simple horseshoe vortex representation of each wing.

Pachter, D’Azzo and Proud [2001] described the development of a formation-hold controller using PI control for the wingman in a leader-wingman tight formation structure. Here too, the wake vortex effects were modelled using a single horseshoe vortex. They demonstrated that the most significant aerodynamic interference effect entails the coupling of the lateral/directional channel into the altitude hold controller. However, they also showed that a FCS designed without due consideration of the aerodynamic coupling effects can still handle them in an acceptable way.

Seanor et al. [2004], from West Virginia University, performed a flight test demonstration using two YF-22 UAV research aircraft models in order to validate a VL formation control scheme for multiple UAVs. The VL scenario was chosen as a low risk way of initially testing the performances of the trajectory-tracking controller.

Finally, Cheng et al. [2008] developed a nonlinear controller for autonomous formation flying using a combination of model predictive control and dynamic inversion control. The controller was validated by simulating a UAV navigating through an obstacle field and satisfactory results were obtained. However, simulations involving multiple UAVs showed a lack of performance.

2.3.3 Autonomous Air-to-Air Refuelling

One specific application of autonomous formation flight is autonomous air-to-air refuelling. Nalepka and Hinchman [2005] showed how UAV missions would benefit from air-to-air refuelling.

In 2006, the NASA Dryden Flight Research Center, in collaboration with DARPA (Defense Advanced Research Projects Agency), conducted a series of test flights directed at demonstrating the feasibility of autonomous air-to-air refuelling using the Navy hose and drogue method, under the AAR (Automated Aerial Refueling) [Hansen, Murray and Campos, 2004; Nalepka and Hinchman, 2005] and AARD (Autonomous Airborne Refueling Demonstration) projects [Dibley, Allen and Nabaa, 2007]. The demonstration was successful.

A vision based sensor [Valasek et al., 2005] and trajectory tracking controller [Tandale, Bowers and Valasek, 2006] were developed at the A&M University, Texas, for probe and drogue autonomous aerial refuelling of UAVs. The drogue was equipped with a system of light-emitting diode beacons, while the tip of the probe was fitted with position-sensing diode receptors. The system, named VisNav, proved to be accurate and reliable. Subsequently, an optical sensor and automatic boom controller for vision based autonomous boom and receptacle aerial refuelling were designed [Doebbler et al., 2007].

McFarlane, Richardson and Jones [2007] developed a cooperative controller for autonomous boom air-to-air refuelling. The controller calculates a target location which the refuelling boom, the receiver UAV and the refuelling envelope centre are to track. They modelled the tanker as a single point which is unaffected by the presence of the receiving vehicle or by atmospheric disturbances, and approximated the wake-induced effects on the receiver as a continuous turbulent wind field based on the Dryden Wind Turbulence Model. However, such a model regards gusts as stochastic disturbances whose velocities are frozen in the mean airflow, and is not suitable to represent the aerodynamic interactions between air vehicles flying in close proximity, as the velocity induced by one vehicle on another depends on variables such as their relative position and orientation, and should be re-estimated as these variables evolve.

Between 2004 and 2009, Dogan and colleagues, from the University of Texas at Arlington, designed various position tracking and station keeping controllers for formation reconfiguration [Venkataramanan and Dogan, 2004*c*; Dogan and Venkataramanan, 2005] and aerial refuelling scenarios [Dogan, Sato and Blake, 2005; Dogan, Kim and Blake, 2007; Waishek, Dogan and Blake, 2009].

Finally, Lewis [2008], Dogan, Lewis and Blake [2008*a*], Dogan, Lewis and Blake [2008*b*], and Dogan, Lewis and Blake [2008*c*] analysed the data from an automated

aerial refuelling test flight conducted with a KC-135 as the tanker and a Learjet 25 as the surrogate receiver UAV. They carried out a power spectrum analysis to identify the components of wind effects on the receiver during air-to-air refuelling, and developed a simulation model which takes account of the prevailing wind, the wake vortex induced wind and the atmospheric turbulence as the three sources of wind that the receiver is exposed to. Power spectral densities and mean variations of both simulation results and flight data were satisfactorily compared. A simple horseshoe vortex with viscous core was used to model the wake vortex effects.

2.4 Simulation Environments & Visualisation Methods

Venkataramanan, Dogan and Blake [2003], Venkataramanan and Dogan [2004*b*], and Dogan, Venkataramanan and Blake [2005] developed a method to compute the aerodynamic coupling between aircraft flying in close proximity within dynamic simulations without explicitly computing the additional force and moment coefficients induced by the leader on the follower: they approximated the nonuniform induced velocity field as uniform wind components and gradients, and used them directly in the equations of motion of the follower(s) with wind terms. They modelled the leading aircraft as a single horseshoe vortex and the follower as a stick diagram composed of four sticks to represent its body: one along the x body axis representing the fuselage length, one along the z body axis representing the fuselage height, and finally two sticks representing each wing (with dihedral and sweep angles). This method was then applied to an air-to-air refuelling simulation scenario, where the receiver's dynamic model was modified in order to take account of the time-varying mass and inertia properties associated with fuel transfer [Venkataramanan and Dogan, 2004*a*]. The same method was also used in Lewis [2008], Dogan, Lewis and Blake [2008*a*], Dogan, Lewis and Blake [2008*b*], and Dogan, Lewis and Blake [2008*c*].

Modi, Long and Plassmann [2002], from the Pennsylvania State University, designed and implemented a computational steering system named POSSE for the real-time visualisation of multiple aircraft wake vortex simulations running on a parallel Beowulf cluster. The wake vortex effects were modelled using a time-decaying horseshoe vortex.

Gimenes et al. [2008] presented a non exhaustive survey of the flight simulation environments which can be used for visualisation purposes, including Microsoft Flight Simulator, X-Plane, FlightGear and Piccolo. However, FlightGear [*FlightGear Official Website: http://www.flightgear.org/*, N.d.; Sorton and Hammaker, 2005], which

is capable of displaying multiple air vehicles when used as an online flight simulator, can only display one aircraft when used with MATLAB/Simulink as a visualisation tool. For this purpose, however, the software AVDS [*AVDS Official Website: http://www.rassimtech.com/*, N.d.], developed by Rasmussen [Rasmussen and Breslin, 1997; Rasmussen and Chandler, 2002] is suitable.

2.5 Chapter Summary

This chapter reviews the work which has been published in the field of characterisation, modelling and simulation of wake vortex effects, as well as autonomous formation flight, including autonomous air-to-air refuelling. It was found that every time a WVM is included in a real-time or near real-time simulation of air vehicles flying in formation, the wake-generating and the wake-encountering vehicles are modelled in different ways. As a consequence, the WVM implicitly requires the preliminary knowledge of the aircraft positions in relation to one another, and leading and following air vehicles cannot exchange role – i.e. position – during a simulation without modifying the WVM.

Chapter 3

Theoretical Background

3.1 Elements of Potential Flow Theory

3.1.1 Definition of Potential Flow

The airflow is assumed to be potential, hence irrotational. It is also assumed to be subsonic, incompressible and inviscid. Consequently:

1. The flow is potential: $\mathbf{V} = \nabla\Phi$, where $\mathbf{V}$ is the flow velocity and Φ is the velocity potential.
2. The flow is incompressible: $\nabla \cdot \mathbf{V} = 0$.

Combining the two equations above leads to $\nabla(\nabla\Phi) = 0$, i.e.:

$$\nabla^2\Phi = 0 \tag{3.1}$$

which is known as the Laplace equation.

This equation's elementary solutions are the uniform flow, the source flow, the doublet flow and the vortex flow. However, as the Laplace equation is linear, any superposition of the elementary solutions is also a solution. Thus, sources lines composed of an arbitrary number of sources, or sheets composed of an arbitrary number of vortices can be formed.

3.1.2 Vortex Flow in 2D

Amongst the elementary solutions of the Laplace equation (Equation 3.1), only the vortex flow can be used to model airflows involving finite lift. In 2D, the vortex flow, sketched in Figure 3.1, is irrotational everywhere except at the origin of the vortex where the vorticity is infinite.

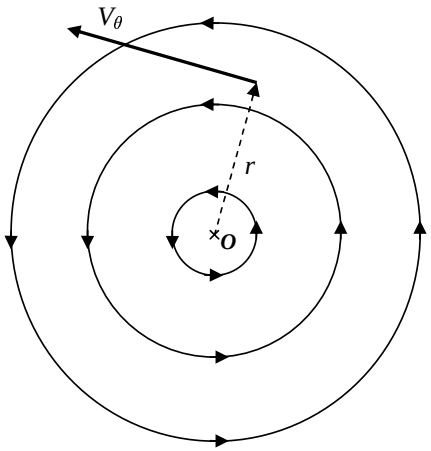

Figure 3.1: 2D vortex flow

The velocity potential Φ for a vortex flow of strength (circulation) Γ is given by:

$$\Phi = -\frac{\Gamma}{2\pi}\theta \tag{3.2}$$

and the corresponding velocity field, in cylindrical coordinates, is:

$$\begin{cases} V_\theta &= -\dfrac{\Gamma}{2\pi r} \\ V_r &= 0 \end{cases} \tag{3.3}$$

3.1.3 Helmholtz Vortex Theorems

The Helmholtz Vortex Theorems describe the three-dimensional motion behaviour of a vortex filament:

1. the strength Γ of a vortex filament is constant along its length,
2. a vortex filament cannot end in a fluid. It must either extend to $\pm\infty$, or end at a solid boundary, or form a closed path.

3.1.4 Biot-Savart Law

The Biot-Savart law is one of the most fundamental equation in potential theory. It was originally derived in electromagnetism, where it describes the magnetic field **B** generated by a steady electric current of intensity I. The vector field **dB** induced at a point P by an elementary segment of the wire **dl** with the current moving in the direction of **dl** is given by:

$$\mathbf{dB} = \frac{\mu_0 I}{4\pi}\frac{\mathbf{dl} \wedge \mathbf{r}}{\|\mathbf{r}\|^3} \tag{3.4}$$

where **r** is the radius vector from the wire element **dl** to the point P, and μ_0 is the magnetic constant.

Similarly, in potential flow theory, the velocity field **dV** induced at a point P by an elementary segment **dl** of a 3D vortex filament of strength Γ is given by:

$$\mathbf{dV} = \frac{\Gamma}{4\pi}\frac{\mathbf{dl} \wedge \mathbf{r}}{\|\mathbf{r}\|^3} \tag{3.5}$$

where **r** is the radius vector from the vortex filament element **dl** to the point P, as illustrated in Figure 3.2.

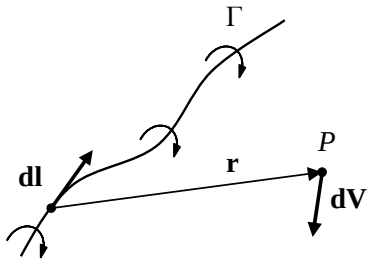

Figure 3.2: Illustration of the Biot-Savart law for a vortex filament

In the case of an infinite straight vortex, Equation 3.5 recovers the 2D vortex flowfield given in Equation 3.3.

3.1.5 Lift Production on an Airfoil of Infinite Span

The lift **L** on an airfoil of infinite span can be modelled with a vortex which is located in the airfoil. Indeed, as illustrated in Figure 3.3, the lift generated by the airfoil is the result of a difference of pressures on its upper and lower surfaces – lower pressure on the upper surface and higher pressure on the lower surface – relative to the pressure at a large distance from the airfoil. According to the Bernoulli equation in the case of an inviscid, incompressible, irrotational and steady flow:

$$\frac{1}{2}V^2 + \Psi + \frac{p}{\rho} = \text{constant} \tag{3.6}$$

throughout the flow, where:

- V is the flow velocity at a point P in the fluid,
- Ψ is the gravitational potential – often neglected,
- p is the pressure at P, and

- ρ is the density of the fluid.

Therefore, the difference of pressures on the contour of the airfoil is equivalent to a higher velocity on the upper surface and a lower velocity on the lower surface, compared to the velocity of the incoming flow $\mathbf{V}_\infty$.

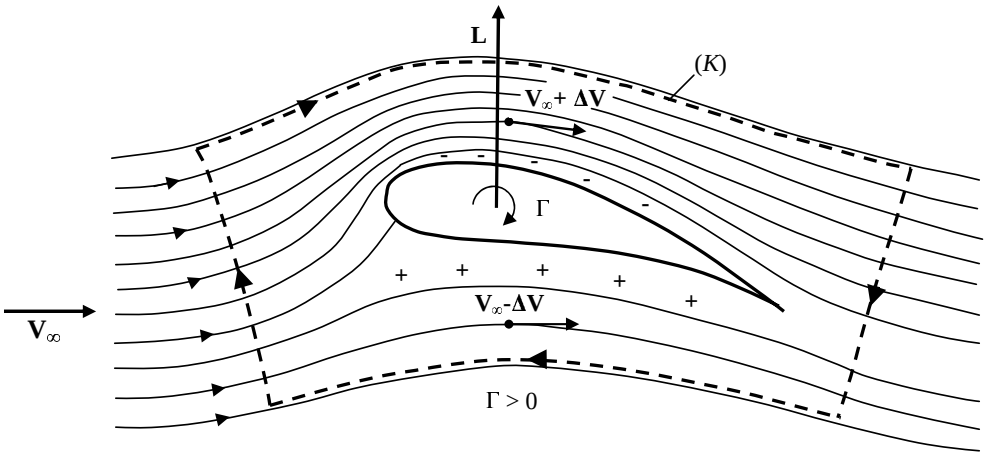

Figure 3.3: Flow around an airfoil and production of lift (reproduced from Schlichting [1979])

Consequently, the circulation, defined as the line integral:

$$\Gamma = \oint_{(K)} \mathbf{V} \cdot \mathbf{dl} \tag{3.7}$$

where:

- (K) is any path enclosing the airfoil, and far enough from it to be located in the region of potential flow and not in its the boundary layer,
- $\mathbf{V}$ is the local fluid velocity, and
- $\mathbf{dl}$ is an infinitesimal length vector along (K),

is non zero. Hence, the differential velocity around the airfoil can be seen as resulting from a clockwise-turning vortex Γ that would be located in the airfoil. This vortex, which is closely linked to the generation of lift, is called the “bound vortex”.

Further calculations in the case of an inclined flat plate at small angles of attack show that the aerodynamic centre of pressure (location where the lift resultant is applied) is

located at the intersection of the profile chord with the quarter-chord line of the airfoil. This result has been expediently extended to all wings at small angles of attack in subsonic conditions, and the bound vortex is subsequently positioned along the quarter-chord line of the airfoil.

The exact relation between the lift L' generated by one unit of span and the circulation Γ in two dimensions is given by the Kutta-Joukowski Lift Theorem:

$$L' = \rho_\infty V_\infty \Gamma \tag{3.8}$$

where ρ_∞ and V_∞ are respectively the fluid density and the fluid velocity far upstream of the airfoil. Furthermore, it can be shown that the lift acts normal to the direction of the incident flow $\mathbf{V}_\infty$.

3.1.6 Lift Production on a Wing of Finite Span

As in the case of an airfoil of infinite span, the lift generated by a wing of finite span can be modelled by a bound vortex, attached to the quarter-chord line of the aforementioned wing. However, in the case of a wing of finite span, an additional phenomenon needs to be taken into account: around the wing-tips of the wing, the air naturally moves from the higher-pressure lower surface to the lower-pressure upper surface. This phenomenon is at the origin of the generation of wing-tip vortices, also known as wake vortices or free vortices, in contrast with the "bound" vortex. Due to its resemblance to a horseshoe, such a vortex system, composed of a bound vortex and two semi-infinite free vortices, is commonly referred to as a "horseshoe vortex". The evolution of these free vortices behind a wing of finite span is illustrated in Figure 3.4.

It is to be noted that in both cases (airfoil of infinite span and wing of finite span), the vortex configuration satisfies the Helmholtz Vortex Theorems (see Subsection 3.1.3).

3.2 Prandtl's Classical Lifting Line Theory

3.2.1 Principle

Prandtl's classical lifting line theory consists in replacing the wing with a finite or infinite number of horseshoe vortices of different widths, all centered around the wing centre-line, and bound to the quarter-chord line of the wing, also referred to as the "lifting line"(see Figure 3.5). The circulation may vary from one horseshoe vortex to

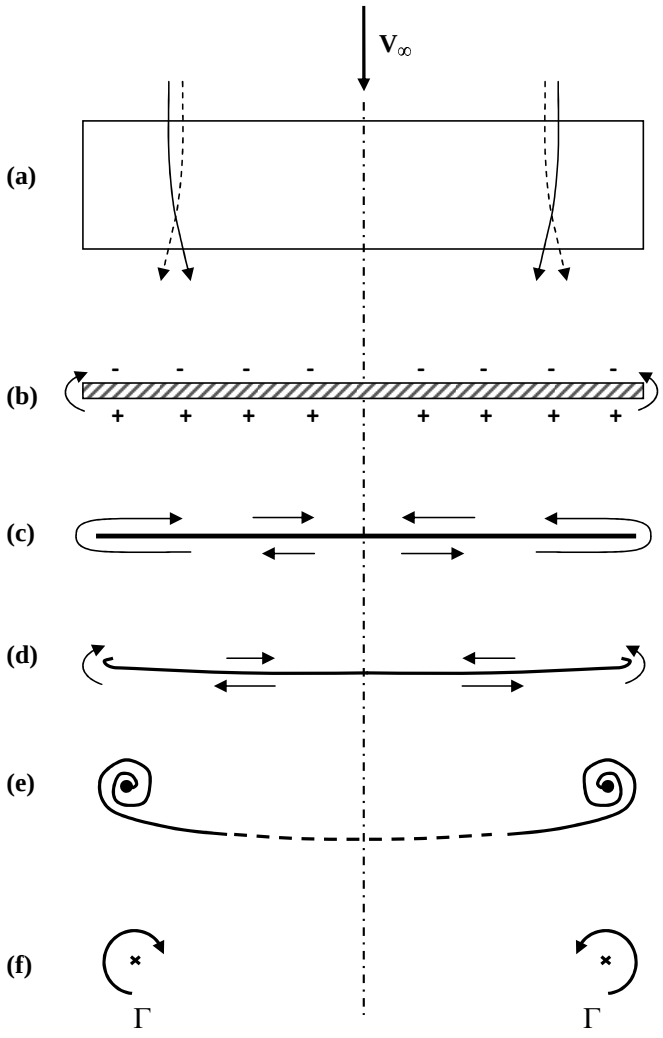

Figure 3.4: Evolution of the free vortices behind a wing of finite span (reproduced from Schlichting [1979])

another but it remains constant along the different branches of a given horseshoe vortex. The vortex sheet, made of the trailing branches of the horseshoe vortices, extends downstream to infinity in parallel with the incident velocity $\mathbf{V}_\infty$.

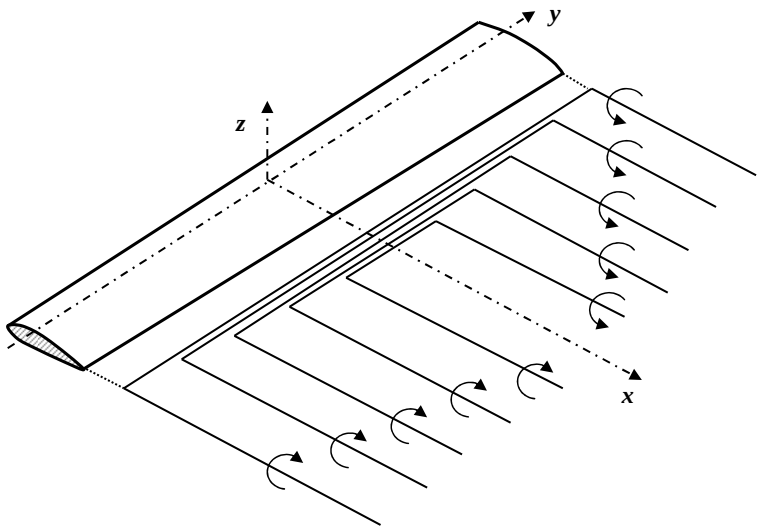

Figure 3.5: Superposition of horseshoe vortices along the lifting line in Prandtl's classical lifting line theory

3.2.2 Fundamental Equation of Prandtl's Lifting Line Theory

The total velocity induced at a point y_0 on the lifting line (which coincides with the axis y) by the trailing vortex sheet is obtained by applying the Biot-Savart law (see Equation 3.5) on each vortex filament and summing the results over the entire sheet. In the case where an infinite number of horseshoe vortices are used along the lifting line, this leads to:

$$V_i(y_0) = -\frac{1}{4\pi}\int_{-b/2}^{b/2}\frac{(\mathrm{d}\Gamma/\mathrm{d}y)\,\mathrm{d}y}{y_0 - y} \tag{3.9}$$

where:

- b is the wing span,
- dy is an infinitesimally small segment of the lifting line located at the coordinate y, and
- $\Gamma(y)$ is the circulation at y.

The corresponding induced angle of attack α_i is given by:

$$\alpha_i(y_0) = \tan^{-1}\left(\frac{-V_i(y_0)}{V_\infty}\right) \simeq -\frac{V_i(y_0)}{V_\infty} = \frac{1}{4\pi V_\infty}\int_{-b/2}^{b/2}\frac{(\mathrm{d}\Gamma/\mathrm{d}y)\,\mathrm{d}y}{y_0 - y} \tag{3.10}$$

Besides, it can be shown that the effective angle of attack α_{eff} obeys:

$$\alpha_{eff}(y_0) = \frac{2\Gamma(y_0)}{a_0(y_0)V_\infty c(y_0)} + \alpha_{L=0}(y_0) \tag{3.11}$$

where:

- $a_0(y)$ is the lift slope at y – usually replaced by the thin airfoil theoretical value of 2π (rad^{-1}),
- $c(y)$ is the wing chord at y, and
- $\alpha_{L=0}(y)$ is the angle of zero lift, which only varies across the span if the wing is twisted.

Finally, an expression of the geometric angle of attack $\alpha = \alpha_{eff} + \alpha_i$ is obtained, with Γ for only unknown:

$$\alpha(y_0) = \frac{2\Gamma(y_0)}{a_0(y_0)V_\infty c(y_0)} + \alpha_{L=0}(y_0) + \frac{1}{4\pi V_\infty}\int_{-b/2}^{b/2} \frac{(\mathrm{d}\Gamma/\mathrm{d}y)\,\mathrm{d}y}{y_0 - y} \tag{3.12}$$

This equation is called the Prandtl's integro-differential equation and its resolution leads to the determination of the circulation Γ at any point along the lifting line.

3.2.3 Derivation of Forces and Moments

Once Γ has been obtained from Equation 3.12, the total lift and induced drag can be derived from the Kutta-Joukowski Lift theorem (Equation 3.8):

$$\text{Lift: } L = \rho_\infty V_\infty \int_{-b/2}^{b/2} \Gamma(y)\,\mathrm{d}y$$

$$\text{Induced Drag: } D_i = -\rho_\infty \int_{-b/2}^{b/2} \Gamma(y) V_i(y)\,\mathrm{d}y$$

Likewise, the wing rolling and yawing moments can be directly computed from the spanwise lift distribution.

3.2.4 Limitations of the Theory

This theory is valid for inviscid, incompressible and steady flows, but is limited to wings with straight quarter-chord lines, i.e. unswept wings. Furthermore, as results

from the exact theory of airfoils in two-dimensional conditions are used for each wing section, accurate results are only obtained for wings with high aspect ratios. Finally, the pitching moment cannot be computed from the spanwise lift distribution as the latter is collapsed to a single line along its 1/4-chord line.

3.3 Weissinger's Extended Lifting Line Theory

The extended lifting line theory – also known as the three-quarter-point method [Schlichting, 1979] or as the simplified lifting-surface theory [DeYoung and Harper, 1948] – was first introduced by Weissinger [1947] for the case of swept-back wings. Compared with the Prandtl's classical lifting line theory discussed in Section 3.2, it applies to wings of any planform and aspect ratio. Also, contrary to the former, the latter allows an approximate value for the pitching moment to be obtained from the spanwise lift distribution. It was adapted for the calculation of nonlinear aerodynamics by Owens [1998].

3.3.1 Principle

The main difference between both methods stems from the distribution of horseshoe vortices along the lifting line: in Prandtl's classical lifting line theory, horseshoe vortices are all centered around the wing centre-line, therefore positioned one into the other, whereas in the extended lifting line theory, horseshoe vortices – although also bound to the quarter-chord lifting line – are positioned one next to the other, as shown in Figure 3.6. This feature allows swept wings to be modelled.

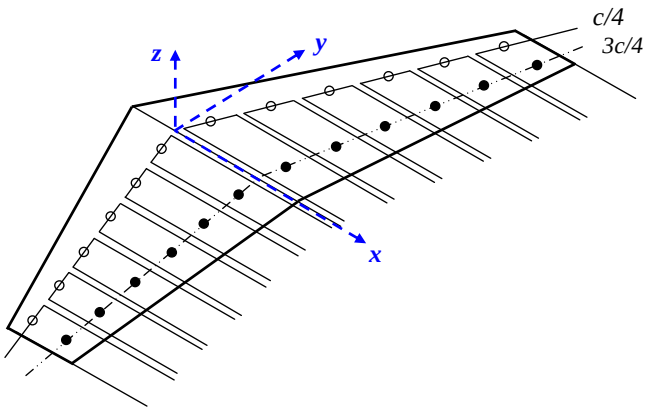

Figure 3.6: Superposition of horseshoe vortices along the lifting line in Weissinger's extended lifting line theory

Furthermore, a different boundary condition is used to determine the value of the circulation Γ along each horseshoe vortex. This condition – also called the kinematic flow condition, or the "Weissinger condition" in reference to the main developer of this method – stipulates that the airflow is tangential to the surface of the wing at its three-quarter chord line. For each horseshoe vortex, one "control point" – or "collocation point" – is defined at the intersection of the horseshoe vortex centre-line and the wing three-quarter chord line. The control points are represented by filled circles in Figure 3.6. The Weissinger condition, applied at each collocation point, can be formulated as:

$$(\mathbf{V_i} + \mathbf{V}_\infty) \cdot \mathbf{n} = 0 \tag{3.13}$$

where:

- $\mathbf{V_i}$ is the velocity induced by all the horseshoe vortices at the collocation point,
- $\mathbf{V}_\infty$ is velocity vector of the upstream airflow, and
- $\mathbf{n}$ is the unit vector normal to the wing surface at the collocation point.

The choice of locating the control points on the three-quarter chord line comes from the two-dimensional thin airfoil theory, where the airfoil lift slope a_0 is equal to 2π. Indeed, the control points should obey:

$$x_p(y) = x_c(y) + \frac{a_0}{2\pi}\frac{c(y)}{2} \tag{3.14}$$

where:

- $x_p(y)$ is the x-coordinate of the control point at y,
- $x_c(y)$ is the x-coordinate of the lifting line at y, and
- $c(y)$ is the wing chord at y.

Therefore:

$$x_p(y) = x_c(y) + \frac{1}{2}c(y) \tag{3.15}$$

As seen in Subsection 3.1.5, for small angles of attack and subsonic conditions, the lifting line is positioned along the quarter-chord line of the wing. Therefore, the collocation points should be located on the three-quarter-chord line.

3.3.2 Fundamental Equation of the Extended Lifting Line Theory

In the extended lifting line theory, the expression of the geometric angle of attack takes the following form:

$$\alpha(y_0) = \frac{1}{4\pi V_\infty} \lim_{\varepsilon \to 0} \left[\frac{4\Gamma(y_0)}{\varepsilon} - \oint_{-b/2}^{b/2} \frac{\Gamma(y)}{(y_0 - y)^2} \left(1 + \frac{x_p(y_0) - x_c(y)}{\sqrt{(x_p(y_0) - x_c(y))^2 + (y_0 - y)^2}} \right) \mathrm{d}y \right] \tag{3.16}$$

where $\oint$, which represents an integration over the intended domain excluding singularities, is defined as:

$$\oint_{-b/2}^{b/2} \ldots \, \mathrm{d}y = \int_{-b/2}^{y_0 - \varepsilon} \ldots \, \mathrm{d}y + \int_{y_0 + \varepsilon}^{b/2} \ldots \, \mathrm{d}y \tag{3.17}$$

Equation 3.16 is the integral equation for the circulation distribution in the extended lifting line theory. As for Equation 3.12, its only unknown is the circulation Γ; therefore, solving Equation 3.16 leads to the determination of the spanwise circulation distribution $\Gamma(y)$, and, using the Kutta-Joukowski Lift Theorem (Equation 3.8), to the derivation of the spanwise lift distribution $L'(y)$. Subsequently, after integration of the spanwise lift distribution over the entire span and projection on the different axes, the total lift, the induced drag, the rolling moment, the yawing moment and, approximately, the pitching moment can be computed, as described in Subsection 3.2.3.

3.3.3 Application to the Modelling of Wake Vortex Effects Between Air Vehicles in Close Formation Flight

One objective of the work has been to model the wake vortex induced effects between air vehicles and implement these effects into near real-time simulations of close formation flying. However, as stated in the survey of wake vortex modelling methods (see Section 2.2), there is a trade-off between the rapidity of execution of a model and the accuracy of the results it provides.

Weissinger's extended lifting line method, as an intermediate between the basic Prandtl's lifting line theory and the more involved VLMs, provides a compromise between accuracy and rapidity, and therefore appeared to be the most suitable technique. In addition, it is simple to compute, generic, flexible (a variable number of horseshoe vortices can be chosen depending on the level of accuracy needed) and, unlike Prandtl's lifting line theory, it is valid for wings of any planform – including swept wings – and aspect ratio.

Weissinger's extended lifting line technique is equivalent to a VLM with no chordwise discretisation of the wing. Adding a chordwise discretisation would increase the computational complexity, and slow down the simulations. Furthermore, the resulting gain in accuracy would be insignificant (except for the estimation of the pitching moment) as the generation of wing-tip vortices is essentially a spanwise phenomenon, due to the wing spanwise load distribution.

3.4 Consideration of Viscosity Effects

3.4.1 Vortex Cores

Viscous effects can be included in the WVM through the addition of vortex "viscous" cores. In particular, using viscous cores gives a better representation of the trailing vortices of a fully rolled-up wake. From a computational point of view, adding a core to the vortex model also removes the singularities associated with infinitely thin vortex filaments crossing downstream control points. However, due to the difficulties in characterising wake vortices, there are still many uncertainties regarding the size of their core radii. Jacquin et al. [2001] lists no less than 5 definitions of vortex core radius:

- **Internal / Viscous core radius r_i:**
  The internal core – or viscous core – encloses the vorticity and viscosity effects due to very large transverse velocity gradients. From the vortex centre, the tangential velocity V_θ increases and reaches a maximum at r_i.

- **External / Inviscid core radius r_o:**
  This core is the result of the inviscid roll-up process of the vortex sheet. It contains less vorticity than the viscous core. The external core radius r_o is where the total circulation Γ of the vortex is attained. No vorticity is contained in the fluid for $r \geq r_o$, i.e. the hypothesis of potential flow is valid outside the external core of the vortex. The values of r_i and r_o can differ a lot.

- **Dispersion radius r_d:**
  The dispersion radius is defined as:

$$r_d^2 = \frac{1}{\Gamma} \int_{-\infty}^{\infty} \int_{-\infty}^{\pm\infty} \left((y - y_c)^2 + (z - z_c)^2 \right) \omega \, \mathrm{d}x \, \mathrm{d}y \tag{3.18}$$

  where y_c and z_c are the coordinates of the vortex centre, and ω the axial vorticity. This radius, which measures the dispersion of axial vorticity in the yz-plane, is widely used.

- **Effective core radius:**
  The effective core radius is defined as:

$$r_{eff} = r_o \exp\left(\frac{1}{4} - \left(\frac{2\pi}{\Gamma}\right)^2 \int_0^{r_o} V_\theta^2(r)\, r\, \mathrm{d}r + \left(\frac{2\pi}{\Gamma}\right)^2 \int_0^{r_o} U^2(r)\, r\, \mathrm{d}r\right) \tag{3.19}$$

  where V_θ is the tangential velocity and U is the axial velocity deficit.

  For a wing of elliptical loading, $r_{eff} \approx 0.11 \cdot \frac{\pi}{4} \cdot b$. Many authors refer to this value as the "vortex core radius".

- **Rolling moment radius:**
  The rolling moment radius is defined as:

$$r_{roll} = \frac{1}{\Gamma} \int_{-\infty}^{\infty} \int_{-\infty}^{\pm\infty} \sqrt{(y - y_c)^2 + (z - z_c)^2}\, \omega\, \mathrm{d}x\, \mathrm{d}y \tag{3.20}$$

  This radius is of particular interest for the evaluation of the hazards associated with wake encounter: the induced rolling moment is all the smaller as r_{roll} is large. Consequently, to reduce the hazards induced by the vortex wake of an aircraft on a following air vehicle, either the vortex circulation should be reduced, or its dispersion should be increased.

The radii $r_o, r_d, r_{eff}, r_{roll} \in O(0.1b)$; however, there are many discrepancies regarding the value of r_i. Finally, as in most cases, the vortex core radius is defined as the axial distance between the vortex centre and the location where the tangential velocity reaches its maximum, $r_c = r_i$.

3.4.2 Vortex Velocity Profiles

Some of the better known vortex velocity profiles are presented in this subsection. They are mostly used to model the fully rolled-up wake, i.e. approximately 4 wing spans behind the wing according to Kurylowich [1979], and 20 wing spans behind the wing according to Hoeijmakers [1996]. The trailing pair is represented by superposing two counter-rotating straight vortices with axisymmetric velocity distributions. The separation distance between the vortices after roll-up is given by $b' = sb$, where s is the spanwise load factor and is defined as:

$$s = \frac{2}{b} \int_0^{b/2} \frac{\Gamma(y)}{\Gamma(y = 0)}\, \mathrm{d}y \tag{3.21}$$

For a wing of elliptical loading, the spanwise load factor is equal to $s = \pi/4$. In practice, this result is used for most types of wings.

In all the models listed below, Γ represents the entire circulation contained in the vortex, r_c the core radius, r the radial distance from the vortex core centre, and b the wing span of the wake-generating vehicle. Furthermore, as the vortices are considered to be straight and of infinite length, the 2D vortex velocity distributions are given.

Helmholtz vortex model

The Helmholtz point vortex [Anderson, 2007; Blake and Multhopp, 1998] is the most basic vortex profile. The vortex is modelled as a concentrated singularity of infinite velocity, i.e. $r_c = 0$. Consequently, the flow is potential at every point except on the vortex itself. The tangential velocity induced by an isolated Helmholtz vortex filament is given by:

$$V_\theta(r) = \frac{\Gamma}{2\pi r} \tag{3.22}$$

Unfortunately, this representation leads to computational problems when the wake crosses the control points of a following air vehicle.

Rankine vortex model

The Rankine vortex model [Sarpkaya, 1989; Hinton and Tatnall, 1997; Gerz, Holzäpfel and Darracq, 2002] assumes that all the vorticity is confined in a viscous core which rotates as a solid body around its centre. Consequently, the potential flow hypothesis is still valid outside the core. The tangential velocity induced by an isolated Rankine vortex filament of radius r_c is given by:

$$V_\theta(r) = \begin{cases} \dfrac{\Gamma}{2\pi r} & \text{when } r > r_c \\ \dfrac{\Gamma}{2\pi}\dfrac{r}{r_c^2} & \text{when } r < r_c \end{cases} \tag{3.23}$$

with an artificial discontinuity at $r = r_c$. Figure 3.7 shows the Rankine vortex model tangential velocity distribution for different values of core radii. In their comparative study of wake vortex models, Gerz, Holzäpfel and Darracq [2002] adopted $r_c = 0.0412b$, and Hinton and Tatnall [1997] used $r_c = 0.05b$.

Finally, the Rankine vortex, having a compact support, is only an approximate solution of the Navier-Stokes equations.

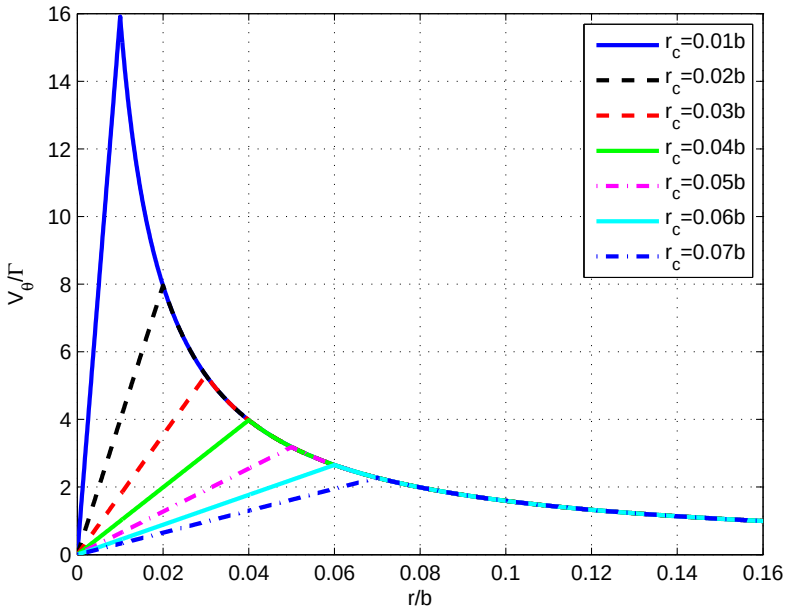

Figure 3.7: Rankine vortex model tangential velocity distribution for different core radii

Hallock-Burnham vortex model

The tangential velocity induced by an isolated Hallock-Burnham vortex filament of radius r_c is given by:

$$V_\theta(r) = \frac{\Gamma}{2\pi}\left(\frac{r}{r^2 + r_c^2}\right) \tag{3.24}$$

and is illustrated in Figure 3.8 for different values of r_c.

The Hallock-Burnham vortex model has been used by many authors with various core radii r_c:

- in Hinton and Tatnall [1997], the core size was chosen to be 5% of the wing span of the wake-generating vehicle;
- in Blake and Multhopp [1998], it was chosen to be 3% of the wing span of the wake-generating vehicle;
- in Gerz, Holzäpfel and Darracq [2002], it was assumed to be 4.12% of the wing span of the wake-generating vehicle;
- Zhang, Wang and Hardin [2003] calculated the core radius using:

$$r_c = 0.2\sqrt{\frac{\Gamma b}{V}} \tag{3.25}$$

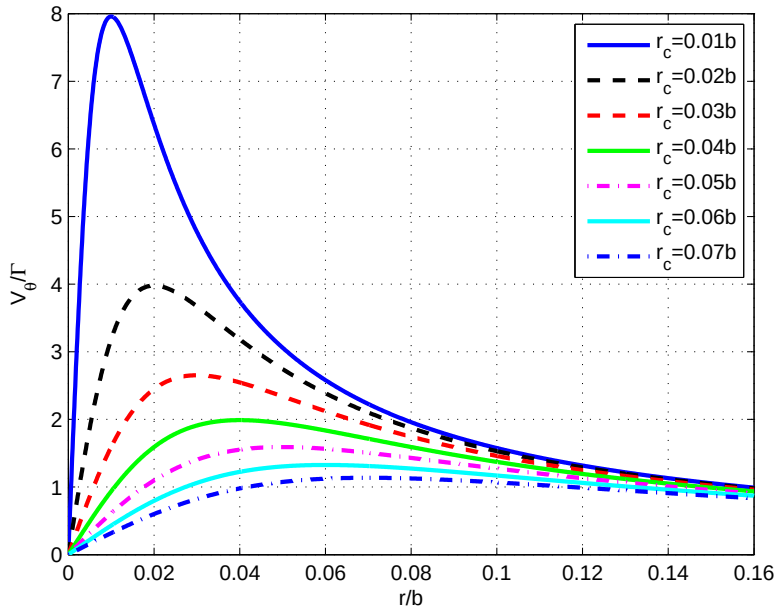

Figure 3.8: Hallock-Burnham vortex model tangential velocity distribution for different core radii

where V is the velocity of the wake-generating aircraft. This led to $r_c = 0.078b$ for a B-747 and $r_c = 0.076b$ for a B-757 during landing.

- finally, Denis [2004] tested different core radii, ranging from 0.5% to 10% of the wing span of the wake-generating vehicle.

Lamb-Oseen vortex model

The Lamb-Oseen vortex model [Sarpkaya, 1989] considers that the vorticity follows a Gaussian distribution of standard deviation $\sqrt{2\nu\tau}$, where ν is the kinematic viscosity of the air and τ is the age of the vortex. The swirl velocity induced by a single Lamb-Oseen vortex filament is given by:

$$V_\theta(r) = \frac{\Gamma}{2\pi r}\left(1 - \exp\left(\frac{-r^2}{4\nu\tau}\right)\right) \tag{3.26}$$

Figure 3.9 shows the evolution of the Lamb-Oseen vortex model tangential velocity distribution with time. As the vortex core size $r_c = 2.24\sqrt{\nu\tau}$ increases with time, the overall vortex shape is conical rather than cylindrical.

When applied to a single vortex in an unbounded incompressible domain, the Lamb-Oseen model is an exact solution of the Navier-Stokes equations. However, as the

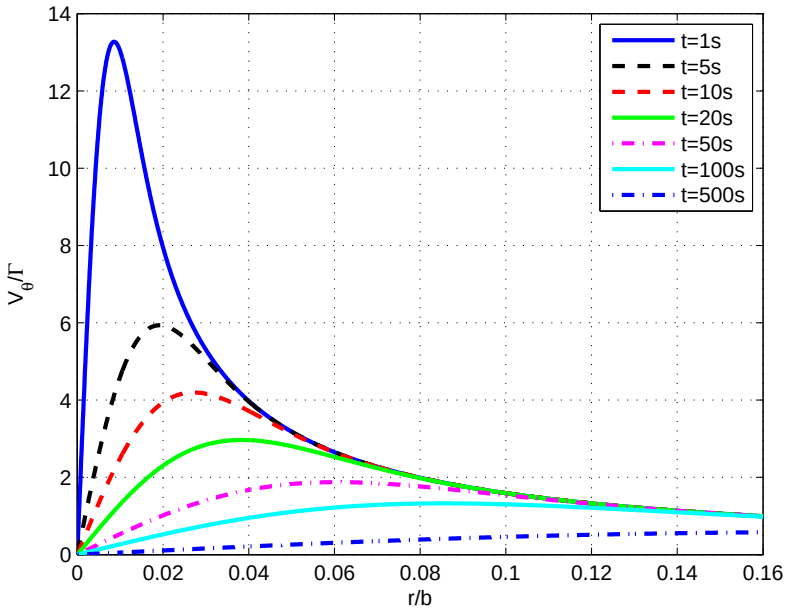

Figure 3.9: Evolution of the Lamb-Oseen vortex model tangential velocity distribution with time

nonlinearity of the Navier-Stokes equations does not permit the superposition of solutions, the velocity field of a multi-Lamb-vortex system is not strictly an exact solution.

A modified form of the Lamb-Oseen vortex has also been used by many authors [Nelson, 1974]:

$$V_\theta(r) = \frac{\Gamma}{2\pi r}\left(1 - \exp\left(\frac{-r^2}{4(\nu + \varepsilon)\tau}\right)\right) \tag{3.27}$$

where ε is the eddy viscosity and is proportional to the circulation Γ. The constant of proportionality is very difficult to measure but it is estimated to be between 10^{-3} and 10^{-4}.

Dogan's modified Helmholtz vortex model

Venkataramanan and Dogan [2004*b*] and Dogan, Venkataramanan and Blake [2005] based their vortex model on Equation 3.27, with ν neglected and $\epsilon = 0.06\Gamma$:

$$V_\theta(r) = \frac{\Gamma}{2\pi r}\left(1 - \exp\left(\frac{-r^2}{4\epsilon\tau}\right)\right) \tag{3.28}$$

This model, which is referred to as the "modified Helmholtz vortex model" in Dogan's

work, was tuned in order to match the velocity distribution given by Rossow and James [2000].

Kurylowich vortex model

Kurylowich [1979] developed an alternate form of the Lamb-Oseen vortex model by re-writing the term in the exponential as a function of the core radius $r_c = 2.24\sqrt{\nu\tau}$:

$$V_\theta(r) = \frac{\Gamma}{2\pi r}\left(1 - \exp\left(-1.26\left(\frac{r}{r_c}\right)^2\right)\right) \tag{3.29}$$

He then tuned r_c so that the velocity distribution of the model would agree with experimental data. His empirical definition of r_c is given by:

$$r_c = 36.2\sqrt{\frac{\nu\tau}{\cos(\varphi)^2}} \tag{3.30}$$

where φ is the sweep angle of the wing 1/4 chord.

The Kurylowich vortex model swirl velocity distribution for different core radii is shown in Figure 3.10.

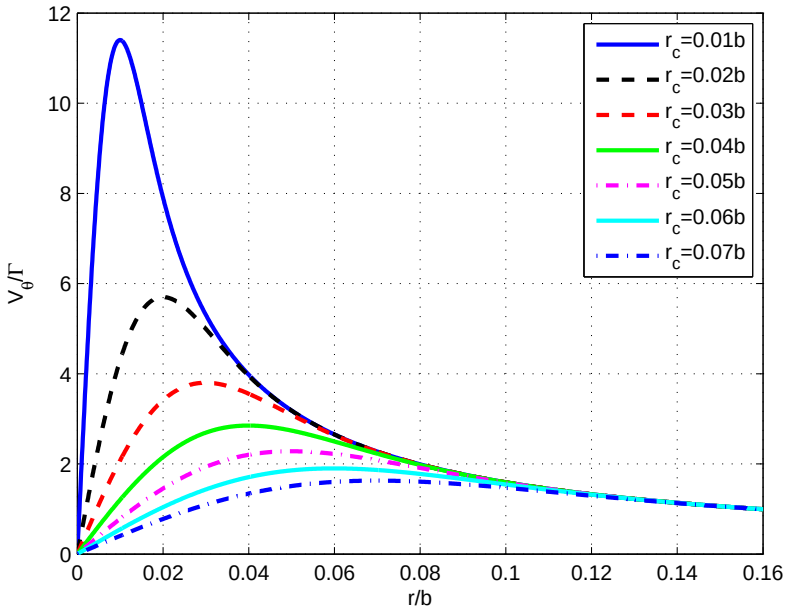

Figure 3.10: Kurylowich vortex model tangential velocity distribution for different core radii

This model was used by Hinton and Tatnall [1997], Gerz, Holzäpfel and Darracq [2002], Zhang, Wang and Hardin [2003], and Denis [2004], using the same core radii as listed for the Hallock-Burnham model.

Proctor vortex model

Proctor [Shen et al., 1999] developed an empirical vortex model based on field measurements of several post roll-up wake vortices:

$$V_\theta(r) = \begin{cases} \dfrac{\Gamma}{2\pi r}\left(1 - \exp\left(-10\left(\dfrac{r}{b}\right)^{0.75}\right)\right) & \text{when } r \geq r_c \\ \dfrac{\Gamma}{2\pi r}1.4\left(1 - \exp\left(-10\left(\dfrac{r_c}{b}\right)^{0.75}\right)\right)\left(1 - \exp\left(-1.2527\left(\dfrac{r}{r_c}\right)^2\right)\right) & \text{when } r \leq r_c \end{cases} \tag{3.31}$$

This model, whose swirl velocity distribution for various core radii is shown in Figure 3.11, was found to be a better representation of observed wake vortices velocity profiles than the models listed above, and it was used to initialise the wake vortex field for the 3D TASS simulations [Switzer, 1996; Shen et al., 1999; Proctor and Switzer, 2000]. The core radii used in the simulations were $r_c = 0.0395b$ for a B-757 and $r_c = 0.0496b$ for a DC-10, based on experimental estimates. In Gerz, Holzäpfel and Darracq [2002], the core radius was chosen to be: $r_c = 0.0412b$.

Smooth blending vortex model

The tangential velocity induced by an isolated smooth blending vortex filament is given by Gerz, Holzäpfel and Darracq [2002]:

$$V_\theta(r) = \frac{\Gamma}{2\pi r}\left(1 - \exp\left(\frac{-\beta_i (r/b)^2}{(1 + ((\beta_i/\beta_o)(r/b)^{4/5})^p)^{1/p}}\right)\right) \tag{3.32}$$

with $\beta_o = 10$, $\beta_i = 500$ and $p = 3$. These tuning parameters have no obvious physical meaning, but were adjusted to fit wind tunnel observations of a flapless rectangular wing.

Equation 3.32 suggests a core radius of 4.12% of the wing span, which is the value that Gerz, Holzäpfel and Darracq [2002] chose to use for all profiles in their review of wake vortex models.

Multiple scale vortex model

The multiple scale WVM – introduced by Jacquin et al. [2001] – results from a wind tunnel experimental study of the wake extended near field of a transport aircraft. The

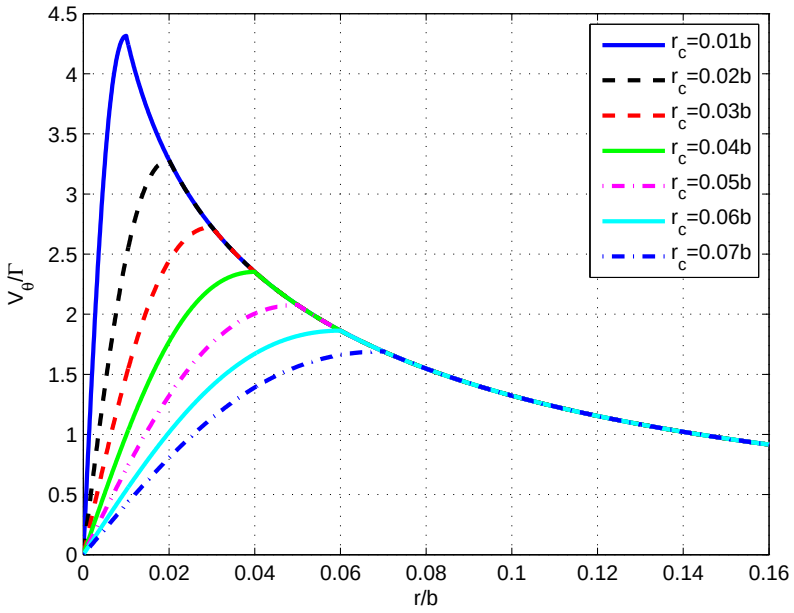

Figure 3.11: Proctor vortex model tangential velocity distribution for different core radii

swirl velocity induced by an isolated multiple scale vortex filament is given by Jacquin et al. [2001] and Gerz, Holzäpfel and Darracq [2002]:

$$V_\theta(r) = \begin{cases} \dfrac{\Gamma}{2\pi r_i}\dfrac{r}{\sqrt{r_i r_o}} & \text{when } r \geq r_i \\ \dfrac{\Gamma}{2\pi\sqrt{r_o r}} & \text{when } r_i \geq r \geq r_o \\ \dfrac{\Gamma}{2\pi r} & \text{when } r \leq r_o \end{cases} \tag{3.33}$$

with $r_o \approx 0.1b$ and $r_i \leq 0.01b$. The definitions of r_i and r_o are given in Subsection 3.4.1.

Figure 3.12 shows the multiple scale vortex model tangential velocity distribution for different values of r_i.

3.4.3 Choice of a Wake Vortex Model

The wake vortex models described above provide a simple and 'good enough' representation of the very complicated velocity fields induced by the wing-tip vortices behind an aircraft. CFD models should be used if a higher level of accuracy is required. In this subsection, an analysis of the models is made in order to facilitate the choice of a

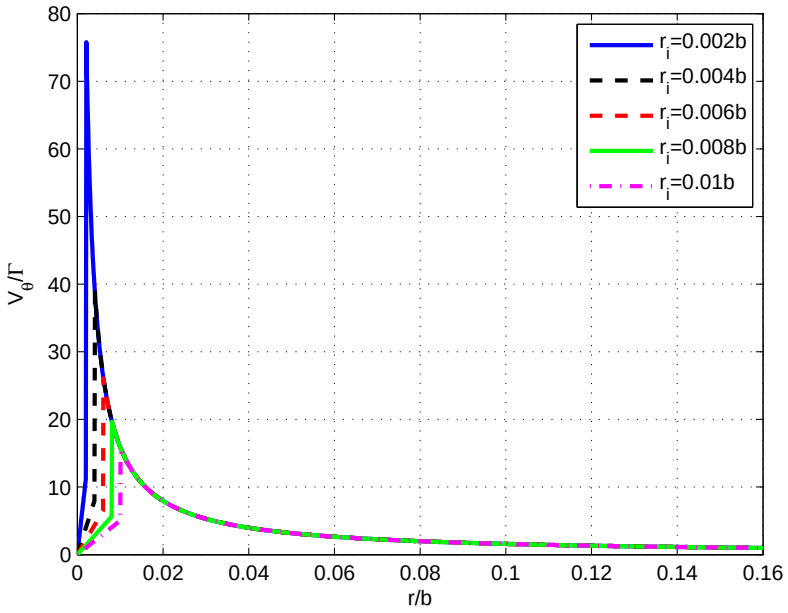

Figure 3.12: Multiple scale vortex model tangential velocity distribution for different internal core radii, $r_o = 0.1b$

velocity profile for the purposes of this work.

Figure 3.13 shows the swirl velocity distribution for the models listed in this subsection and Table 3.1 summarises the time-independent core radii used by various authors for these same models.

The difference between the tangential velocity distribution predictions obtained for $r/b \leq 0.1$ (see Figure 3.13) can be explained as follows:

- in most cases, the wake vortex models were tuned using experimental measurements for one specific air vehicle geometry and set of flight conditions. However, the wake characteristics can vary greatly from one set of conditions to another;

- the vortex core radius measurements were performed at a specific distance from the wake-generating vehicle, thereby influencing the peak value of tangential velocity.

However, for $r/b \geq 0.1$, the wake vortex models give similar predictions. Therefore, the choice of vortex model does not make much difference for the position range considered in formation flight or in air-to-air refueling.

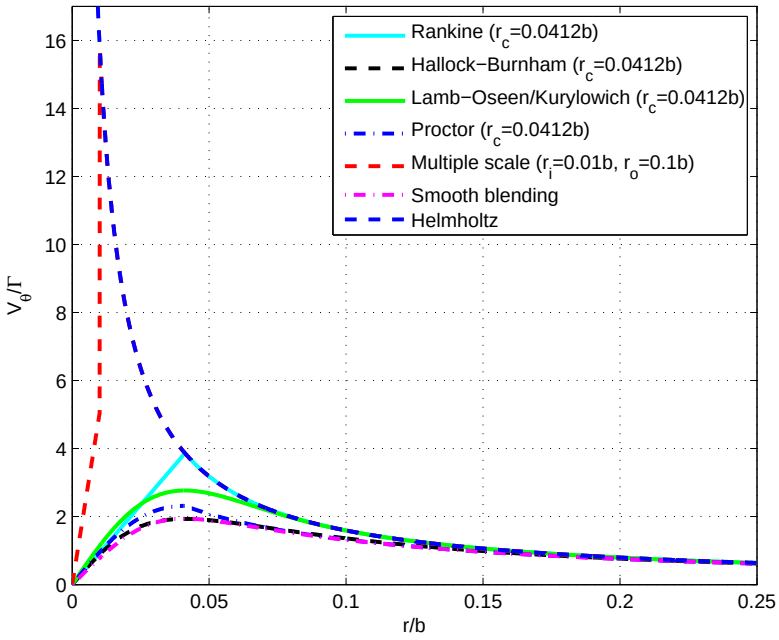

Figure 3.13: Comparison of wake vortex models

Table 3.1: Time-independent vortex core radii

Authors	Vortex Core Radius	Vortex Model
Blake and Multhopp [1998]	$r_c = 0.03b$	Hallock-Burnham
Hinton and Tatnall [1997]	$r_c = 0.05b$	Rankine, Hallock-Burnham, Lamb-Oseen
Gerz, Holzäpfel and Darracq [2002]	$r_c = 0.0412b$	Rankine, Hallock-Burnham, Lamb-Oseen, Proctor, Smooth blending
Zhang, Wang and Hardin [2003]	$r_c \approx 0.077b$	Hallock-Burnham, Lamb-Oseen
Shen et al. [1999]	$r_c \approx 0.045b$	Proctor
Denis [2004]	$0.5b \leq r_c \leq 10b$	Hallock-Burnham, Lamb-Oseen

For the purposes of this work, the vortex induced velocity profile was chosen on two criteria: its simplicity of implementation and the accuracy of its predictions. The Helmholtz model was eliminated because of its associated singularity at $r = 0$. The Rankine, Proctor and multiple scale models were discarded due to their multiple definition according to the value of r. The smooth blending model was eliminated due to the fact that it was not depending explicitly on a core radius but on three non-intuitive parameters, and was therefore more complex to tune than the other models. Finally, the Lamb-Oseen/Kurylowich model was preferred to the Hallock-Burnham model because of its documented use in association with a time-dependant core radius [Kurylowich, 1979; Sarpkaya, 1989; Dogan, Venkataramanan and Blake, 2005].

Furthermore, it is to be noted that apart from the Helmholtz model, which results from the Biot-Savart law (see Subsection 3.1.4), the vortex velocity profiles presented in Subsection 3.4.2 were originally developed to model the fully rolled-up trailing vortices behind an aircraft. Yet, the intention here is to apply such a velocity distribution to each downstream vortex branch of a vortex sheet representing a non fully rolled-up aircraft wake in the extended near field: it is expected that the counter-rotating vortex branches of two neighbouring horseshoe vortices will have a cancelling effect on each other, such that in the far field, the main vortex influence will still be coming from the wing-tip vortex lines. Therefore, the vortex model should be chosen accordingly.

The Lamb-Oseen and Kurylowich time-dependant core radii are represented in Figure 3.14. Although the Lamb-Oseen core radius definition $r_c = 2.24\sqrt{\nu\tau}$ gives a better match with the order of magnitude of the time-independent core radii listed in Table 3.1, the Kurylowich model ($r_c = 36.2\sqrt{\nu\tau/\cos(\varphi)^2}$) was preferred for its faster-growing core radius, which allows a quicker merging of the different vortices produced by a wing into a single pair of counter-rotating vortices, in accordance with Figure 3.15. Therefore, in the case of two air vehicles flying in formation, the following aircraft will more likely be subjected to the influence of the leader's wake vortex pair, rather than to the influence of their individual vortex branches.

3.5 Chapter Summary and Conclusions

In this chapter, overviews of potential flow theory, Prandtl's classical lifting line theory, and Weissinger's extended lifting line theory were given, leading to the choice of a wake vortex modelling technique. Weissinger's extended lifting line method was selected on the basis of its computational simplicity, its flexibility, its range of validity

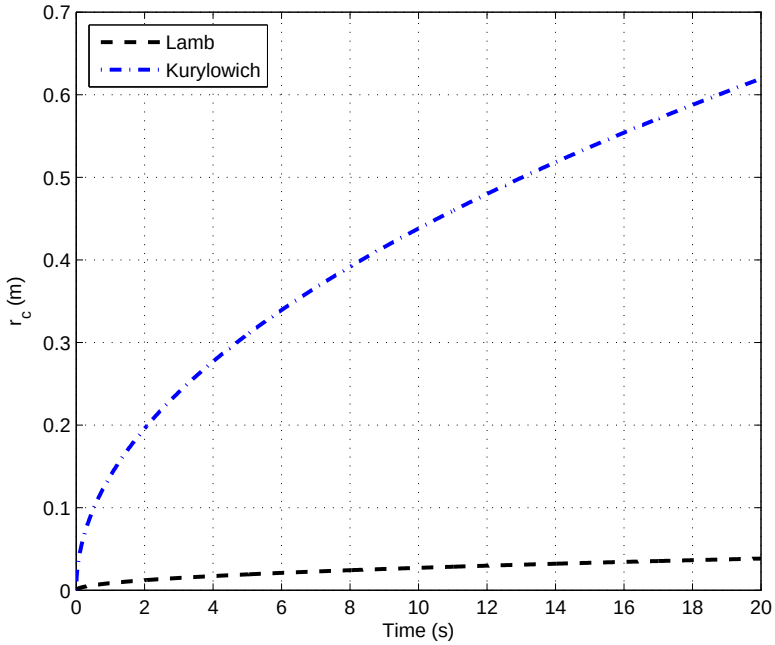

Figure 3.14: Vortex core radius

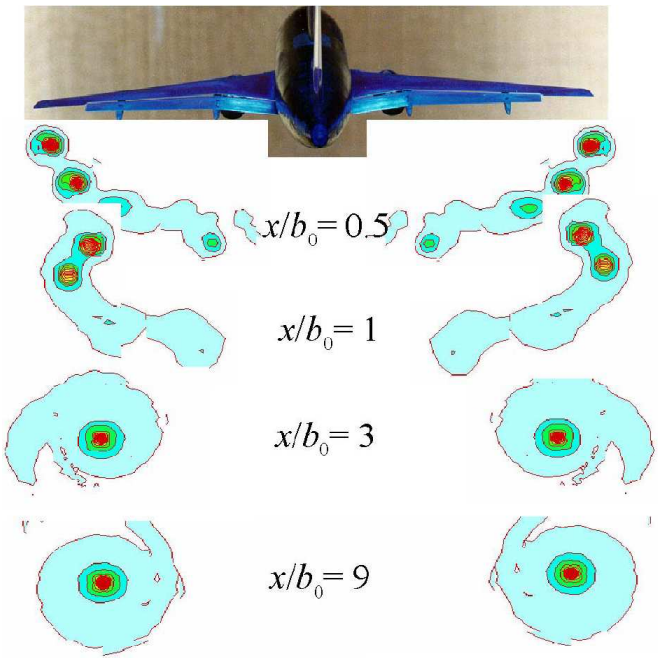

Figure 3.15: Formation of a vortex pair downstream of a flapped aircraft model, from Jacquin [2005]

and because it seems to provide the best compromise between accuracy and rapidity of execution for an average-performance computer.

The choice of a vortex velocity distribution profile and of a viscous core is also discussed. The definitions of viscous cores are reviewed, and nine vortex velocity profile models – namely Helmholtz, Rankine, Hallock-Burnham, Lamb-Oseen, Kurylovich, Proctor, smooth blending, multiple scales and Dogan's modified Helmholtz vortex model – are compared. The Kurylowich model, with a core radius $r_c = 36.2\sqrt{\nu\tau/\cos(\varphi)^2}$, was chosen for the simplicity of its implementation and the accuracy of its predictions.

Chapter 4

Wake Vortex Model Development

4.1 Introduction

This chapter presents the development of a MATLAB programme based on the extended lifting line theory (see Section 3.3). The code, called ELL, computes the steady-state velocity induced on one aircraft by the wake(s) of one or more other air vehicles. It supports 3D, subsonic multi-wing designs and takes account of the following geometric characteristics of each wing: span, aspect ratio, taper ratio, sweep, dihedral and twist. All vehicles are modeled using the same method to facilitate reconfiguration scenarios where the positions of the vehicles within the formation vary, thereby modifying the influence of one vehicle upon the other(s).

4.2 Principle

4.2.1 Modelling of the Air Vehicle

Each air vehicle is represented by its lifting surfaces. The surface is replaced by its 1/4-chord segment, and the associated vortex sheet by a flat rectangular surface composed of n_{seg} semi-infinite horseshoe vortices. These are attached to the 1/4 chord line, follow the chord up to the 3/4 chord line, and extend downstream to infinity parallel to the aircraft velocity vector $\mathbf{V}_\infty$, as illustrated in Figure 4.1.

Figure 4.2 shows the geometry of a basic air vehicle (main wing, fin and tailplane are represented), and Figure 4.3 shows its vortex layout for $\alpha = 5^\circ$ and $\beta = 0^\circ$ (in body axes). The red x-marks in Figure 4.2 represent the control points where the Weissinger boundary condition (airflow tangential to the wing surface) is met. These are located

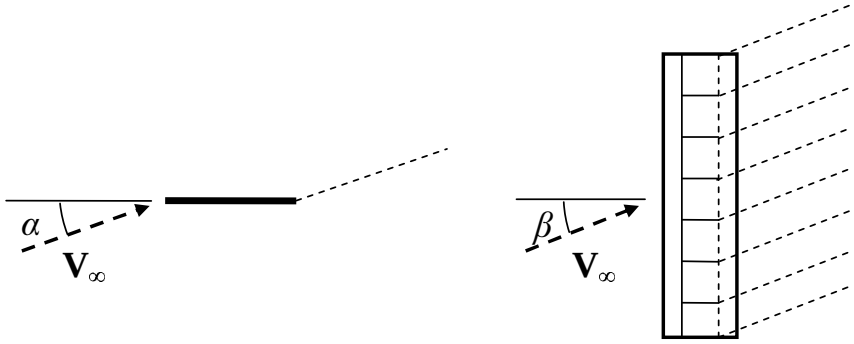

Figure 4.1: Vortex sheet positioning

along the 3/4 chord line, as seen in Subsection 3.3.1.

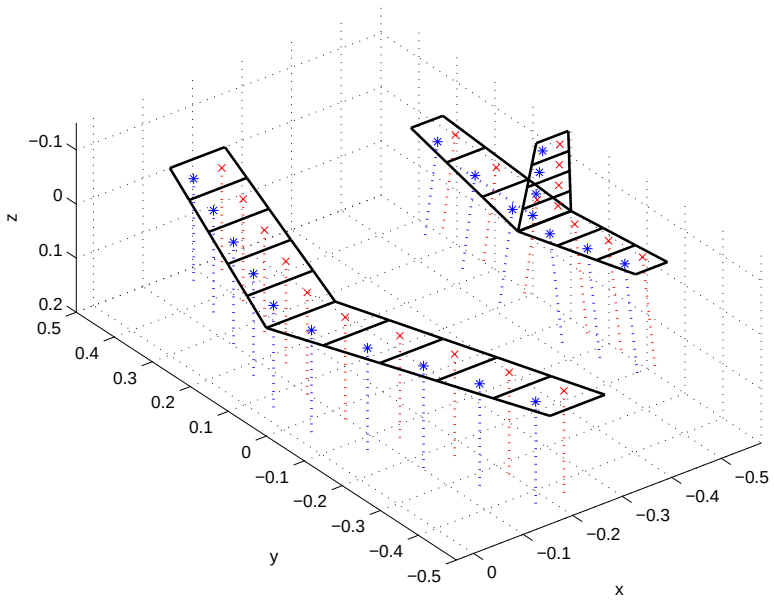

Figure 4.2: 3D wing control points and normals

Using the Weissinger extended lifting line theory rather than the Prandl's classical lifting line theory enables the modelling of wing planforms of different geometries, including swept, tapered wings with twist and/or dihedral. As an example, six wing planforms of various geometric characteristics are presented in Table 4.1 and illustrated in Figure 4.4.

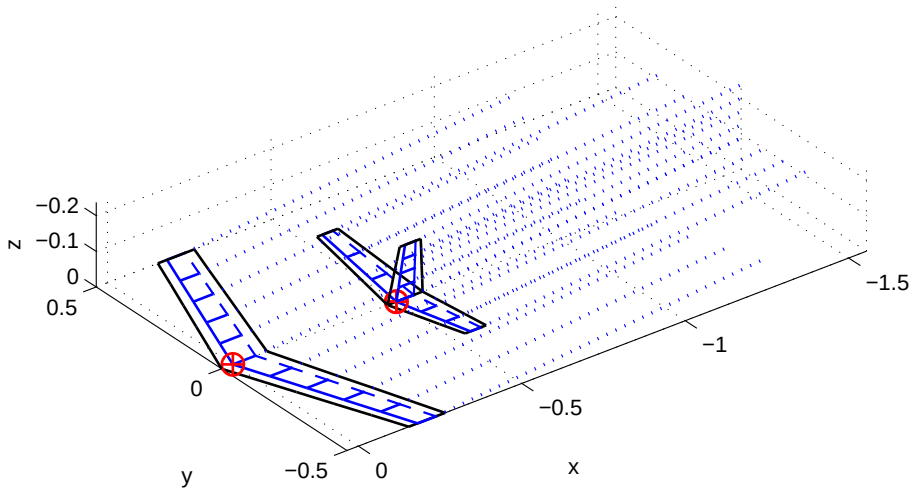

Figure 4.3: 3D wing configuration and vortex layout for $\alpha = 5$ deg, $\beta = 0$ deg

Table 4.1: Wing planforms

Characteristic	Wing A	Wing B	Wing C	Wing D	Wing E	Wing F
Wing span b (m)	2	2	2	2	2	2
Aspect ratio λ	8	12	8	8	8	8
Taper ratio ε	1	1	0.3	1	1	1
Sweep angle φ (deg)	0	0	0	20	0	0
Dihedral angle δ (deg)	0	0	0	0	10	0
Twist angle $+ve$ (deg)	0	0	0	0	0	-10

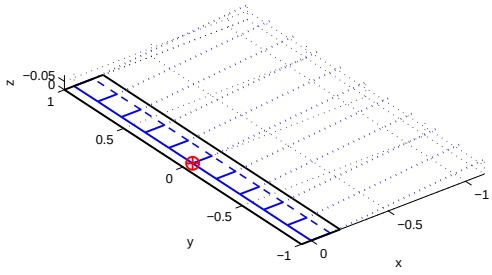

(a) Wing A

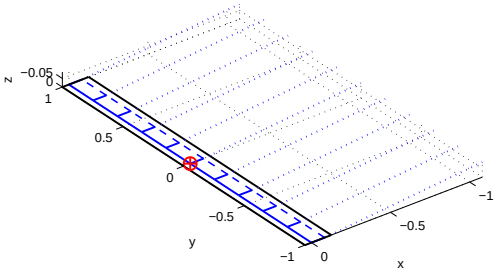

(b) Wing B

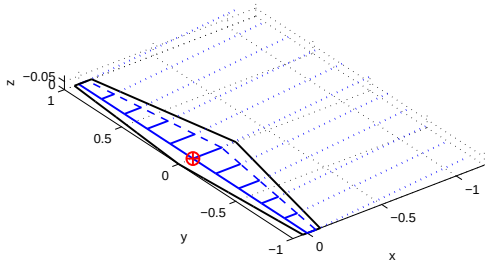

(c) Wing C

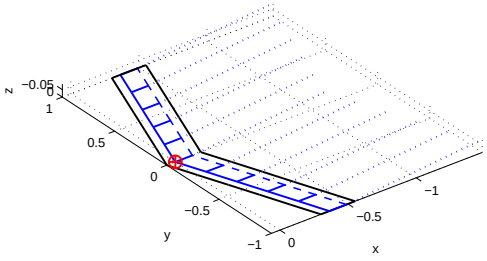

(d) Wing D

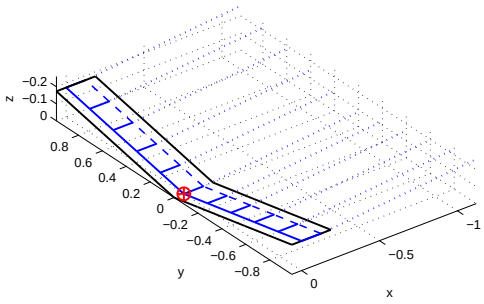

(e) Wing E

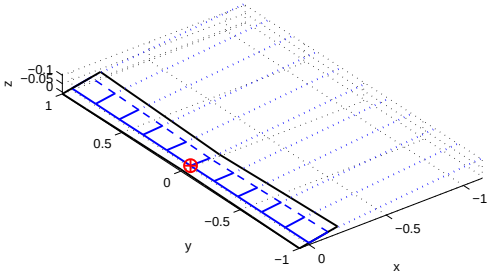

(f) Wing F

Figure 4.4: Modelling of different wing planforms & associated vortex wake layout for $\alpha = 5$ deg, $\beta = 0$ deg

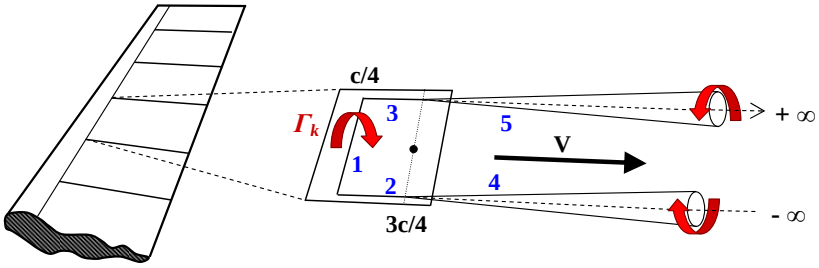

Figure 4.5: Schematic of an adapted horseshoe vortex

Each horseshoe vortex is composed of 5 straight branches, as shown in Figure 4.5. Branch 1 is bound to the 1/4-chord line of the wing; from there, Branches 2 and 3 follow the chord up to the 3/4-chord line; finally, Branches 4 and 5 extend downstream to infinity, in parallel with the upstream velocity vector **V**. The vortex shape was adapted in order to prevent any singularity due to an infinitely thin filament where all the vortex strength would be concentrated. A viscous core and time decay effect were added to the semi-infinite downstream branches (Branches 4 and 5) of each horseshoe vortex: a Kurylowich model (see Subsection 3.4.2) was used to represent the vorticity of these branches as a Gaussian distribution of standard deviation $r_c/\sqrt{2}$, where $r_c = 2.24\sqrt{\nu\tau}$ is the core radius, ν is the dynamic viscosity of the air, and τ is the vortex age.

4.2.2 Calculation of the Induced Velocity Field

The circulation along each horseshoe vortex is assumed to be constant. Its unknown distribution is determined by solving the fundamental equation of the extended lifting line theory (Equation 3.16) using Weissinger's boundary condition (Equation 3.13).

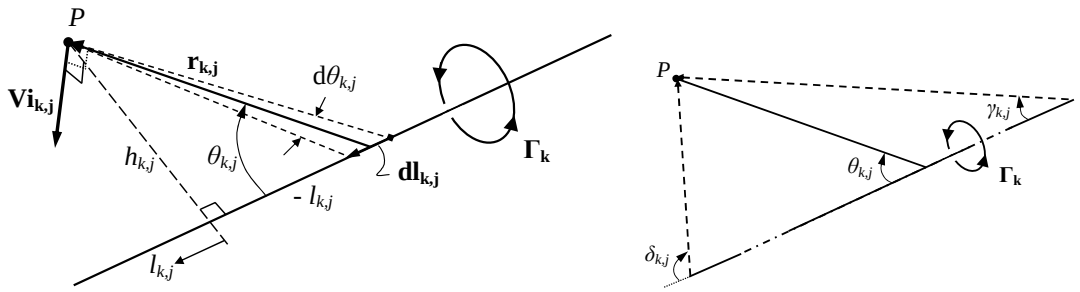

Figure 4.6: Branch j of the horseshoe vortex k

Once the circulation distribution is known, the velocity induced by the wake-generating

vehicle(s) can be calculated at any field point $P(x_P, y_P, z_P)$, using the Helmholtz profile (Equation 3.22) for Branches 1, 2 and 3 of each horseshoe vortex, and the Kurylowich velocity distribution (Equation 3.29) for Branches 4 and 5. The contribution of each branch $j \in \{1, \ldots, 5\}$ of the horseshoe vortex $k \in \{1, \ldots, \mathrm{n_{seg}}\}$, of strength Γ_k, to the induced velocity $\mathbf{V_{i_k}}$ at the field point $P(x_P, y_P, z_P)$ is given by:

$$\mathbf{V_{i_{k,j}}} = \begin{cases} \dfrac{\Gamma_k}{4\pi h_{k,j}} \Big(\cos(\gamma_{k,j}) - \cos(\delta_{k,j})\Big) \cdot \mathbf{n_{k,j}} & \text{for } j \in \{1,2,3\} \\ \dfrac{\Gamma_k}{4\pi h_{k,j}} \Big(\cos(\gamma_{k,j}) - \cos(\delta_{k,j})\Big) & \\ \qquad \left(1 - \exp\left(-1.26\left(\dfrac{h_{k,j}}{2.24\sqrt{\nu\tau_{k,j}}}\right)^2\right)\right) \cdot \mathbf{n_{k,j}} & \text{for } j \in \{4,5\} \end{cases} \tag{4.1}$$

where:

- $\mathbf{r_{k,j}}$ is the radius vector from the vortex filament element $\mathbf{dl_{k,j}}$ to the point P,
- $\mathbf{n_{k,j}}$ is the unit vector normal to $\mathbf{dl_{k,j}}$ and $\mathbf{r_{k,j}}$,
- $h_{k,j}$ is the perpendicular distance from the field point P to the branch line j,
- $\gamma_{k,j}$ and $\delta_{k,j}$ are the angles between $\mathbf{dl_{k,j}}$ and $\mathbf{r_{k,j}}$ at the vortex branch ends, and
- $\tau_{k,j}$ is the age of the vortex branch (defined as the distance of $P(x_P, y_P, z_P)$ from the origin of the wing (quarter-chord root point), divided by the airspeed V)

The parameters $\mathbf{r_{k,j}}$, $\mathbf{dl_{k,j}}$, $h_{k,j}$, $\gamma_{k,j}$ and $\delta_{k,j}$ are illustrated in Figure 4.6. In the case of the semi-infinite Branches 4 and 5, then $\gamma_{k,4} = 0$ and $\delta_{k,5} = \pi$.

The velocity induced at P by the horseshoe vortex k is equal to the sum of the contributions of its 5 branches:

$$\mathbf{V_{i_k}}(x_P, y_P, z_P) = \sum_{j=1}^{5} \mathbf{Vi_{k,j}}(x_P, y_P, z_P) \tag{4.2}$$

The total induced velocity at $P(x_P, y_P, z_P)$ is then obtained by adding the velocities induced by each of the $\mathrm{n_{seg}}$ horseshoe vortices used to model the lifting surfaces of the wake-generating vehicle(s):

$$\mathbf{V_i}(x_P, y_P, z_P) = \sum_{k=1}^{\mathrm{n_{seg}}} \mathbf{V_{i_k}}(x_P, y_P, z_P) \tag{4.3}$$

Figure 4.7 illustrates the vortex position behind a simple wing geometry (n_{seg} = 10, b = 1 m, λ = 6, ε = 0.8, ϕ = 20 deg, δ = 10 deg, and $+ve$ = 0 deg) for V = 20 m/s, α = 5 deg and β = 0 deg. The induced velocity field in the yz-plane at different values of x downstream of the wing is shown in Figure 4.8. The usual shape of wing-tip vortices can be clearly seen: downwash inboard of the wing-tip, and upwash outboard of it. Furthermore, the decay effect is easily observed, as the vortex core gets larger and its strength weaker when the Trefftz plane moves downstream. Finally, it should be noted that body axes were used to plot the induced velocity field, hence the seeming upward movement of the trailing vortices.

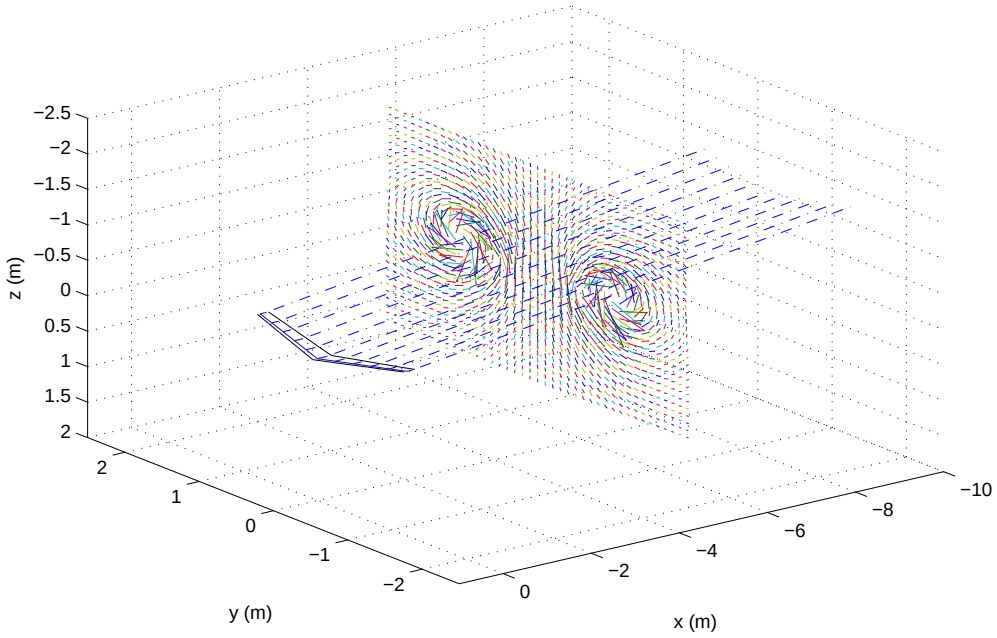

Figure 4.7: Vortex evolution and induced velocity field in the Trefftz plan

4.2.3 Induced Translational and Rotational Wind Components

Following a method developed by Dogan, Venkataramanan and Blake [2005], the velocity field induced by one or more air vehicles on a neighbouring aircraft is expressed as induced translational and rotational wind components. If N vehicles are flying in close proximity, the velocity induced on the vehicle Λ by the $N-1$ surrounding air vehicles is computed at each of the n_{seg_Λ} calculation points along the 1/4-chord line of the

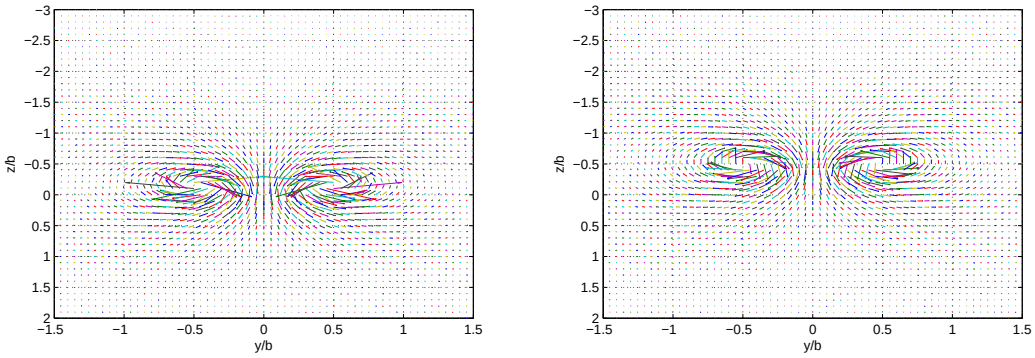

(a) $x = -b$ (b) $x = -5b$

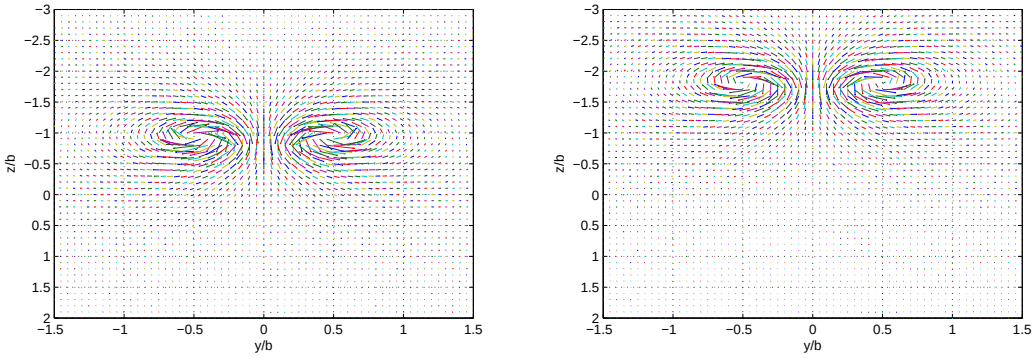

(c) $x = -10b$ (d) $x = -20b$

Figure 4.8: Slice views of the induced velocity field in the *yz*-plane behind a straight wing in its body axes – Kurylowich core radius $r_c = 36.2\sqrt{\nu\tau/\cos(\varphi)^2}$

vehicle Λ using equation 4.3. The induced velocity field thus obtained is highly non-uniform, and can be approximated around the CG of vehicle Λ as the sum of uniform wind components and uniform wind gradients [Dogan, Venkataramanan and Blake, 2005]:

$$\mathbf{V_i}(G_\Lambda) = \begin{pmatrix} \widetilde{V_{i_x}}(\Lambda) + \widetilde{\frac{\partial V_{i_x}}{\partial x}}(\Lambda) + \widetilde{\frac{\partial V_{i_x}}{\partial y}}(\Lambda) + \widetilde{\frac{\partial V_{i_x}}{\partial z}}(\Lambda) \\ \widetilde{V_{i_y}}(\Lambda) + \widetilde{\frac{\partial V_{i_y}}{\partial x}}(\Lambda) + \widetilde{\frac{\partial V_{i_y}}{\partial y}}(\Lambda) + \widetilde{\frac{\partial V_{i_y}}{\partial z}}(\Lambda) \\ \widetilde{V_{i_z}}(\Lambda) + \widetilde{\frac{\partial V_{i_z}}{\partial x}}(\Lambda) + \widetilde{\frac{\partial V_{i_z}}{\partial y}}(\Lambda) + \widetilde{\frac{\partial V_{i_z}}{\partial z}}(\Lambda) \end{pmatrix} \tag{4.4}$$

where:

$$\widetilde{\mathbf{V}}_\mathbf{i}(\Lambda) = \begin{cases} \widetilde{V_{i_x}}(\Lambda) &= \dfrac{1}{n_{seg_\Lambda}} \displaystyle\sum_{j=1}^{n_{seg_\Lambda}} V_{i_{x_j}} \\ \widetilde{V_{i_y}}(\Lambda) &= \dfrac{1}{n_{seg_\Lambda}} \displaystyle\sum_{j=1}^{n_{seg_\Lambda}} V_{i_{y_j}} \\ \widetilde{V_{i_z}}(\Lambda) &= \dfrac{1}{n_{seg_\Lambda}} \displaystyle\sum_{j=1}^{n_{seg_\Lambda}} V_{i_{z_j}} \end{cases} \tag{4.5}$$

and

$$\begin{cases} \widetilde{\frac{\partial V_{i_x}}{\partial x}}(\Lambda) = \dfrac{1}{n_{seg_\Lambda} - 1} \displaystyle\sum_{j=1}^{n_{seg_\Lambda}-1} \frac{V_{i_{x_{j+1}}} - V_{i_{x_j}}}{x_{j+1} - x_j} \\ \widetilde{\frac{\partial V_{i_y}}{\partial x}}(\Lambda) = \dfrac{1}{n_{seg_\Lambda} - 1} \displaystyle\sum_{j=1}^{n_{seg_\Lambda}-1} \frac{V_{i_{y_{j+1}}} - V_{i_{y_j}}}{x_{j+1} - x_j} \\ \widetilde{\frac{\partial V_{i_z}}{\partial x}}(\Lambda) = \dfrac{1}{n_{seg_\Lambda} - 1} \displaystyle\sum_{j=1}^{n_{seg_\Lambda}-1} \frac{V_{i_{z_{j+1}}} - V_{i_{z_j}}}{x_{j+1} - x_j} \end{cases} \tag{4.6}$$

The remaining partial derivatives $\partial/\partial y$ and $\partial/\partial z$ are similarly calculated. The components of the effective induced translational wind velocity vector $\widetilde{\mathbf{V}}_\mathbf{i}$ are then directly defined as $\widetilde{V_{i_x}}$, $\widetilde{V_{i_y}}$ and $\widetilde{V_{i_z}}$, and the components of the effective induced rotational wind velocity vector $\widetilde{\boldsymbol{\omega}}_\mathbf{i}$ are derived from the uniform wind gradients using:

$$\widetilde{\boldsymbol{\omega}_{\mathbf{i}}}(\Lambda) = \begin{cases} \widetilde{\omega_{i_x}}(\Lambda) &= \widetilde{\frac{\partial V_{i_z}}{\partial y}}(\Lambda) - \widetilde{\frac{\partial V_{i_y}}{\partial z}}(\Lambda) \\ \widetilde{\omega_{i_y}}(\Lambda) &= \widetilde{\frac{\partial V_{i_x}}{\partial z}}(\Lambda) - \widetilde{\frac{\partial V_{i_z}}{\partial x}}(\Lambda) \\ \widetilde{\omega_{i_z}}(\Lambda) &= \widetilde{\frac{\partial V_{i_y}}{\partial x}}(\Lambda) - \widetilde{\frac{\partial V_{i_x}}{\partial y}}(\Lambda) \end{cases} \tag{4.7}$$

NB: These partial derivatives are approximated using the averages along the spanwise axis of the wing, therefore the $\partial/\partial x$ and $\partial/\partial z$ terms are very small for most wing configurations (low swept and low dihedral angles). When it is the case, the corresponding derivatives can then be reasonably neglected. This is to be decided depending on the wing geometry.

4.2.4 Number of Horseshoe Vortices

The number of horseshoe vortices used to model a lifting surface also needs to be determined. This number depends on the level of accuracy needed: the larger the number of horseshoe vortices, the more accurate the results, but the slower the simulations.

In the following scenario, two identical wings – Λ_1 and Λ_2 – are considered. Their geometric parameters are given by: $b = 1$ m, $\lambda = 3$, $\varepsilon = 0.8$, $\phi = 20$ deg, $\delta = 10$ deg, and $+ve = 0$ deg; and they are composed of n_{seg} horseshoe vortices each: $n_{seg}(\Lambda_1) = n_{seg}(\Lambda_2) = n_{seg}$. They are flying in formation at $V = 20$ m/s, $\alpha = 8$ deg and $\beta = 0$ deg, with Λ_1 assuming the role of leader and Λ_2 being the follower.

The location of Λ_2's control points relative to Λ_1's wake – and therefore the velocity induced by Λ_1 on Λ_2 – depends not only on the relative position of Λ_1 and Λ_2, but also on their orientations. In order to estimate the minimum number of horseshoe vortices which should be used to model a lifting surface, two cases are considered:

- Case A: $(\phi, \theta, \psi) = (0, 0, 0)$ deg for both vehicles
- Case B: $(\phi, \theta, \psi) = (0, 8, 0)$ deg for both vehicles

These are illustrated in Figure 4.9 for $x_{rel} = -2b$, $y_{rel} = 0$ and $z_{rel} = 0$.

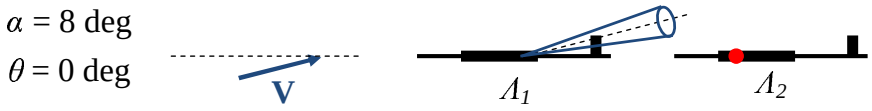

(a) Case A: $(\phi, \theta, \psi) = (0, 0, 0)$ deg

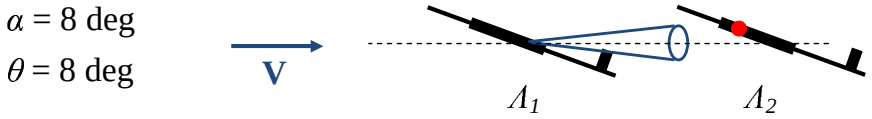

(b) Case B: $(\phi, \theta, \psi) = (0, 8, 0)$ deg

Figure 4.9: Location of Λ_2's control points (red) relative to Λ_1's wake (blue) – $x_{rel} = -2b$, $y_{rel} = 0$, $z_{rel} = 0$, $\alpha = 8$ deg, and $\beta = 0$ deg

In both cases, the variations with longitudinal spacing of the effective velocity components induced by Λ_1 on Λ_2 are shown in Figure 4.10 for different values of n_{seg}. Although the results are of similar magnitude, one difference is noticeable: in Case A, when the distance between the air vehicles $|x/b|$ increases, the components of the effective velocity induced by Λ_1 on Λ_2 quickly decrease to zero. In Case B, unless Λ_2 takes the lead of the formation ($x/b \geq 0$), the effect of Λ_1 on Λ_2 is approximately constant. This is because in Case B, Λ_1's vortices are aligned with the x-axis ($\alpha = \theta$), therefore when Λ_2 moves back from Λ_1 along the x-axis, its position relative to Λ_1's vortices remains the same. The slight decrease in the induced velocity strength when $-x/b$ increases is essentially due to the decay of Λ_1's vortices with time. In Case A, Λ_1's vortices are not aligned with Λ_2's x-axis, therefore when Λ_2 moves back from Λ_1 along the x-axis, the distance between its control points and Λ_1's vortices increases, thereby diminishing the influence of Λ_2 on Λ_1.

Figure 4.11 shows the variations with lateral spacing of the effective velocity induced by Λ_1 on Λ_2 in Cases A and B. The differences between Case A and Case B are more obvious than in Figures 4.10 and 4.13. First, in Case B, the y and z components of the induced velocity demonstrate a "saw-tooth" behaviour for $-1 \leq y/b \leq 1$ when $n_{seg} \leq 8$. This is because the fewer horseshoe vortices are used to model a wing, the further from each other they are located, and the longer it takes for the "middle" vortices to merge with the wing tip vortices into a single vortex pair downstream of the wing. In this intermediate stage, the following aircraft is subjected to the individual influence of each of the leader's vortices, hence the displayed saw-tooth outline. The reason why this saw-tooth outline is only visible in Case B and not in Case A is because of the location of Λ_2's control points relative to Λ_1's wake, as explained in the previous paragraph: in Case A, Λ_2's control points are in the periphery of Λ_1's wake, where they are subjected

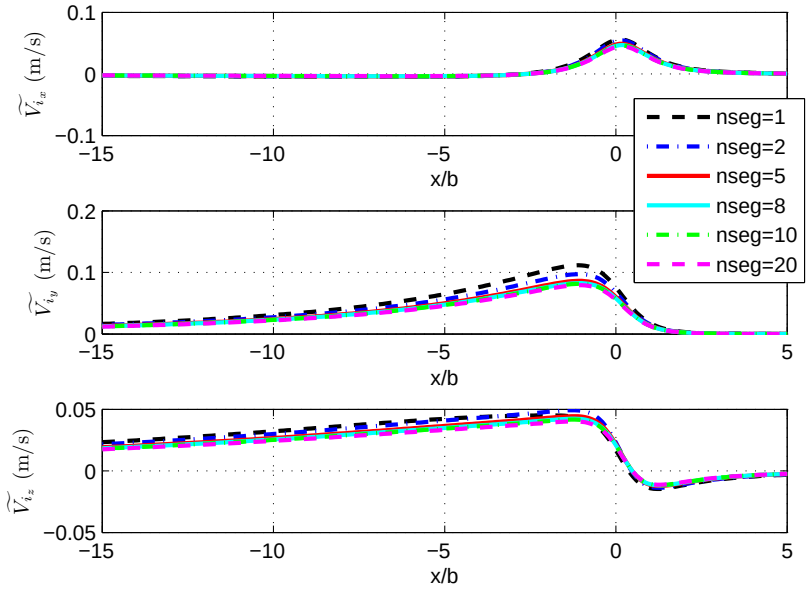

(a) Case A (θ = 0 deg)

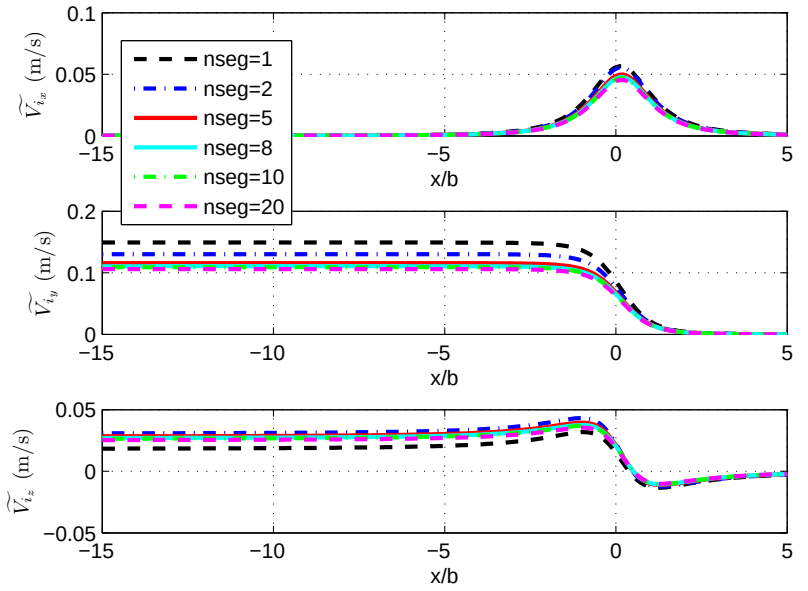

(b) Case B (θ = 8 deg)

Figure 4.10: Variations of the effective induced velocity components with longitudinal spacing, $y_{rel} = b$, $z_{rel} = b$

to an attenuated influence, whereas in case B, Λ_2's control points are much closer to the cores of Λ_1's vortices, which makes Λ_2 more sensitive to the strength variations of Λ_1's vortices.

In addition, different values of $\widetilde{V_{i_x}}$ and $\widetilde{V_{i_z}}$ are obtained in Case A and Case B, due to the position of Λ_1's wake relative to the reference frame: as mentioned earlier, in Case A, the wing bound vortex branches are aligned with the *x*-axis, and the trailing branches extend at an angle of 8 deg with the *x*-axis in the *xz*-plane. In Case B, it is the opposite. Consequently, $\widetilde{V_{i_z}}$ – which is mainly generated by Λ_1's trailing vortices – is much stronger in Case B than in Case A, and $\widetilde{V_{i_x}}$ – which is generated solely by Λ_1's bound vortices in Case B (and is therefore positive when $z_{rel} = 0$), and by Λ_1's both trailing and bound vortices in Case A (and is therefore negative when Λ_2 is in the upwash generated by Λ_1's wake, and positive when Λ_2 is in the downwash generated by Λ_1's wake) – is much stronger in Case A than in Case B.

Finally, when $n_{seg} = 1$, only two quarter chord meshing points are used, located at each wing tip. This does not permit the sweep angle, taper ratio and dihedral angle of a wing to be taken into account, as illustrated in Figure 4.12. The wing is then modelled as a flat rectangular surface, located slightly behind and below the original wing. Consequently, the values obtained for $\widetilde{V_{i_x}}$ and $\widetilde{V_{i_y}}$ when $n_{seg} = 1$ are incorrect.

Figure 4.13 shows the variations with vertical spacing of the effective velocity components induced by Λ_1 on Λ_2 in Cases A and B. Although, the plots are similar in shape and magnitude, two differences should be pointed out. First, compared to Case B, the components of $\widetilde{\mathbf{V}_\mathbf{i}}$ are slightly shifted towards $z \leq 0$ in Case A. Again, this is due to the fact that Λ_1's wake is not aligned with the *x*-axis, but is parallel to the incident airflow; therefore Λ_2 crosses Λ_1's wake when above Λ_1, i.e. for a negative value of *z*. The position and orientation of Λ_1's wake in Case A is also responsible for $\widetilde{V_{i_x}}$ reaching a maximum when Λ_2 crosses Λ_1's wake. This maximum does not exist in Case B since then $\widetilde{V_{i_x}}$ is only generated by Λ_1's bound vortices.

From Figures 4.10, 4.11 and 4.13, it can be seen that in both cases, the velocity induced by Λ_2 on Λ_1 converges rapidly as n_{seg} increases. In particular, $n_{seg} = 10$ gives as good results as $n_{seg} = 20$ for a much lower computational price. Consequently, using $n_{seg} = 10$ seems to be an excellent compromise between accuracy of results and computational costs.

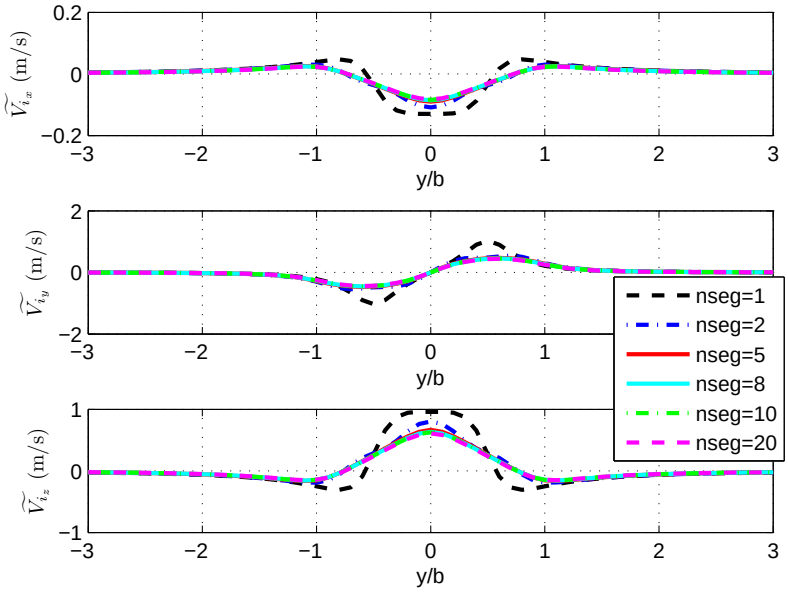

(a) Case A (θ = 0 deg)

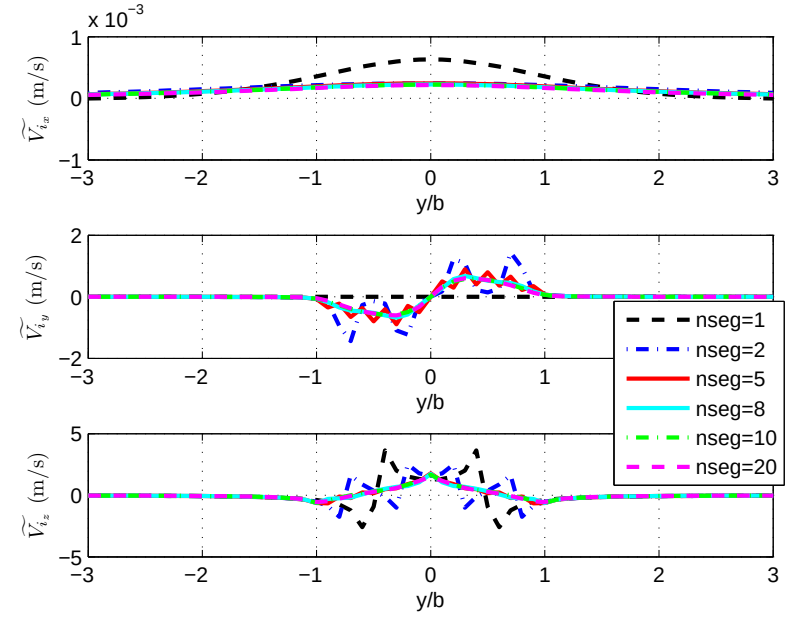

(b) Case B (θ = 8 deg)

Figure 4.11: Variations of the effective induced velocity components with lateral spacing, $x_{rel} = -2b$, $z_{rel} = 0$

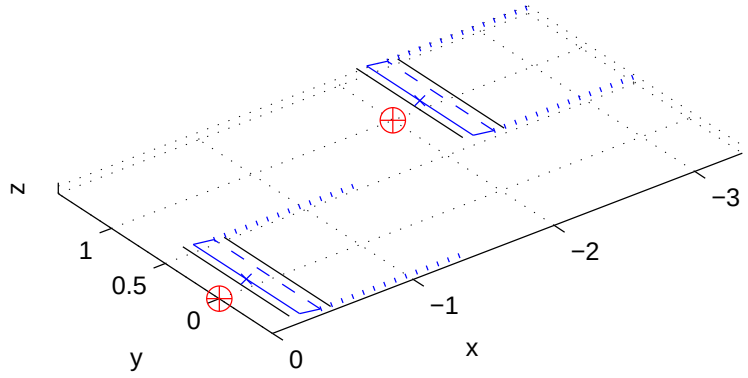

(a) $n_{seg} = 1$

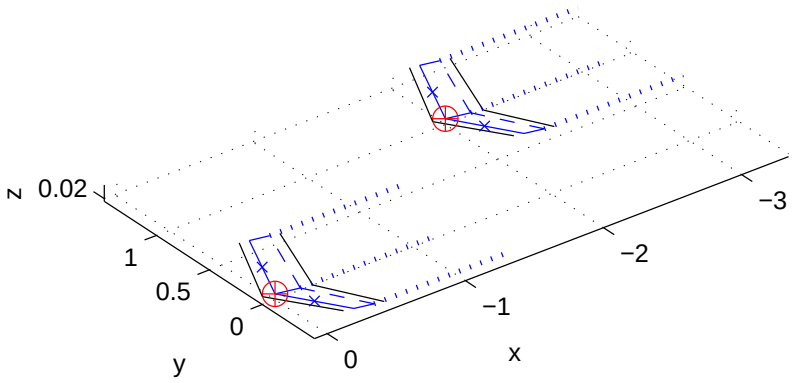

(b) $n_{seg} = 2$

Figure 4.12: $x_{rel} = -2b$, $y_{rel} = b$, $z_{rel} = 0$

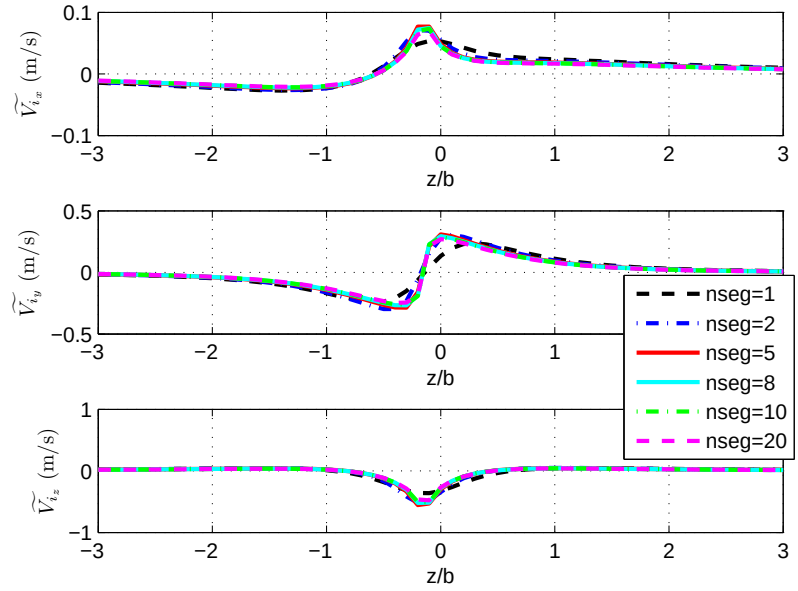

(a) Case A (θ = 0 deg)

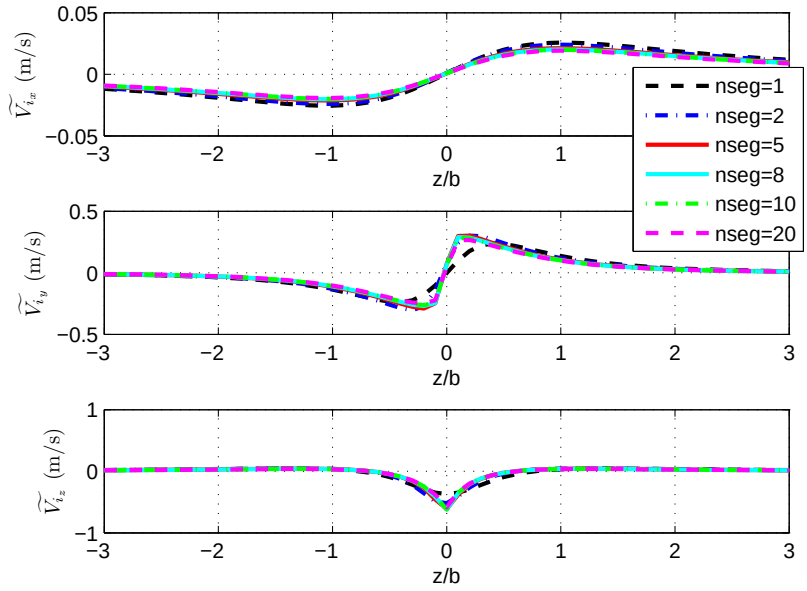

(b) Case B (θ = 8 deg)

Figure 4.13: Variations of the effective induced velocity components with vertical spacing, $x_{rel} = -b, y_{rel} = b$

4.2.5 Integration

This subsection briefly explains how the WVM has been integrated into Simulink simulations. In order to enable the air vehicles to exchange positions, the whole integration scheme needs to be symmetric. Consequently, the dynamics of all UAVs in the formation need to be modified to take account of the effects induced by the wakes of the others.

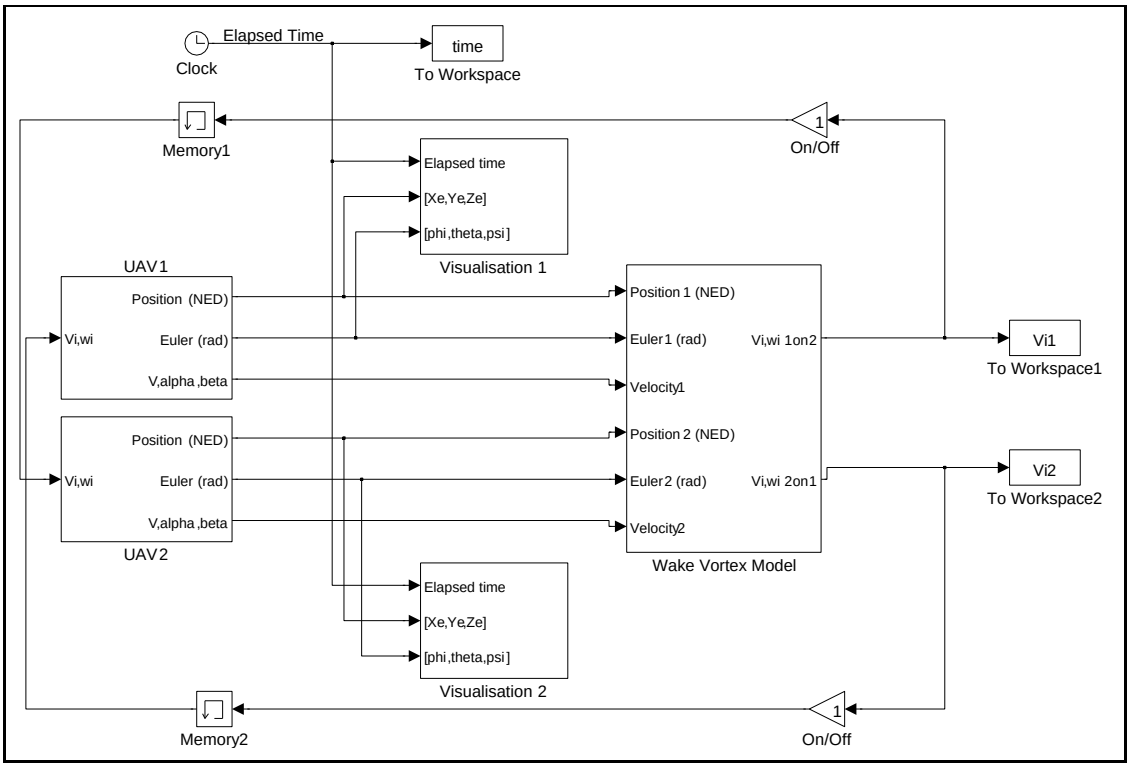

Figure 4.14: Simulink simulation model

Figure 4.14 shows how the WVM has been integrated in a two-vehicle formation flight simulation. The state parameters of each vehicle, such as their positions (x, y, z), their orientations (Euler angles: ϕ, θ, ψ) in a common North-East-Down inertial reference frame, and their respective airdata (V, α, β) are sent to the Wake Vortex Model s-function block, which calls the main MATLAB function of the airwake model, `ELLmain.m`. `ELLmain.m` calculates the effective translational and rotational wind velocities induced on each vehicle by its neighbour(s), and feeds them back into the wind terms of the vehicle dynamics, as shown in Figure 4.15.

The induced airspeed and angular rates can then be calculated for each vehicle Λ using

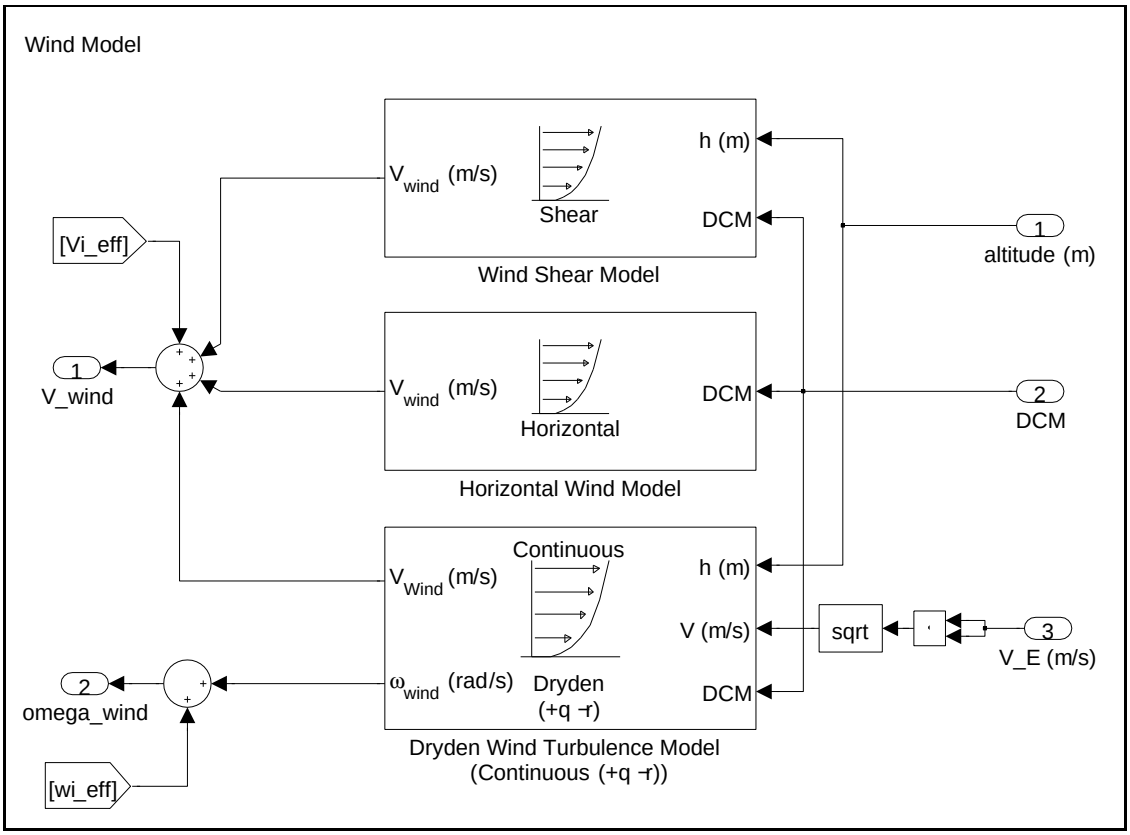

Figure 4.15: UAV wind model

the following equations:

$$\begin{cases} V_{x_\Delta}(\Lambda) = -\widetilde{V_{i_x}}(\Lambda) \\ V_{y_\Delta}(\Lambda) = -\widetilde{V_{iy}}(\Lambda) \\ V_{z_\Delta}(\Lambda) = -\widetilde{V_{i_z}}(\Lambda) \end{cases} \tag{4.8}$$

and:

$$\begin{cases} p_\Delta = -\widetilde{\omega_{i_x}} \\ q_\Delta = -\widetilde{\omega_{i_y}} \\ r_\Delta = -\widetilde{\omega_{i_z}} \end{cases} \tag{4.9}$$

As described in Dogan, Venkataramanan and Blake [2005], the main advantage of using this method is that it removes the need to explicitly compute the forces and moments induced by one vehicle in the equations of motion of the others. It is therefore more computationally efficient.

4.2.6 Limitations of the model

The limitations of the model are listed below:

- ELL is based on a small-perturbation potential flow theory, therefore reliable results can only be achieved for small angles of attack and subsonic conditions.
- The model does not allow the following effects to be taken into account: thickness, camber, fuselage, friction drag, and compressibility; the roll-up of the vortex sheet is also ignored.
- Finally, as the calculation points distribution of a wing is collapsed to a single line along its 1/4-chord line, the wake-induced pitching moment cannot be accurately calculated. A way to improve these results would be to use more calculation points for the estimation of the induced velocity field on the wings, and to locate these points at different values of x (ie chordwise). However, adding calculation points would lead to an increased computational complexity and slow down the simulations.

4.3 Wake Vortex Model Implementation

In this section, the vector from Point P_1 to Point P_2 is designated by $\mathbf{P_1P_2}$.

4.3.1 ELL Execution Chart and M-Files

The WVM execution chart is detailed in Table 4.2.

Table 4.2: Program execution chart

```
ELLmain.m
    geodata.m
    init.m
    vlm.m
        dis_wing.m
    solver.m
    velocity.m
```

A brief description of each module is given below. Further details and information are presented in the following subsections (Subsections 4.3.3- 4.3.7).

- `ELLmain.m`: main function. It calculates the velocity induced by the airwake(s) of one (or more) aircraft at the location of another air vehicle. Each vehicle can be composed of one or more lifting surfaces. `ELLmain.m` calls `geodata.m`, `init.m`, `vlm.m`, `solver.m` and `velocity.m` successively.
- `geodata.m`: initialises and stores the geometric parameters of the air vehicles in the structure *geo* (see Subsection 4.3.3).
- `init.m`: initialises and stores the state variables of the air vehicles in the structure *state* (see Subsection 4.3.4).
- `vlm.m`: meshes the lifting surface(s) and stores the relevant indices and coordinates in the structure *lattice*. The sub-routine `dis_wing.m` is called for the discretisation of the 1/4 chord line of each wing (see Subsection 4.3.3).
- `solver.m`: solver. Calculates the vorticity vector $\mathbf{G}$ by using the Biot-Savart law for each vortex line and the Weissinger boundary condition at the collocation points. The different steps of the resolution are explained in Subsection 4.3.6.
- `velocity.m`: calculates the effective velocity induced on one air vehicle by the wake(s) of the surrounding aircraft. Two different vortex velocity profiles are used to calculate the influence of the horseshoe vortices which constitute those wake(s): the Helmholtz vortex model is used for the bound vortices (Branches 1, 2 and 3), and the Lamb-Oseen vortex model for the trailing vortices (Branches 4 and 5).

4.3.2 Reference Frames

The systems of coordinates used in ELL are listed below:

North-East-Down (NED) Axes ($\mathcal{R}_{NED}$)

- $x > 0$ pointing North
- $y > 0$ pointing East
- $z > 0$ pointing Down

The NED reference frame is the one used in the Simulink simulations. Therefore, the input and output of `ELLmain.m` are expressed in NED.

South-East-Up (SEU) Axes ($\mathcal{R}_{SEU}$)

- $x > 0$ pointing South
- $y > 0$ pointing East
- $z > 0$ pointing Up

Because of its practical convenience, most calculations are carried out in this reference frame.

Body Axes of Aircraft Λ ($\mathcal{R}_b(\Lambda)$)

- $x > 0$ pointing frontwards
- $y > 0$ pointing starboard
- $z > 0$ pointing downwards

R_b is the conventional flight dynamics reference frame.

Modified Body Axes of Aircraft Λ ($\mathcal{R}'_b(\Lambda)$)

- $x > 0$ pointing backwards
- $y > 0$ pointing starboard
- $z > 0$ pointing upwards

$\mathcal{R}'_b$ is the conventional wind tunnel reference frame. It is the one used in `dis_wing.m` for the discretisation of the 1/4 chord line.

Direction Cosine Matrices (DCM) are introduced in order to transform coordinates and vectors between reference frames. In particular, for the wing Λ, the DCM from $\mathcal{R}_{NED}$ to $\mathcal{R}_b(\Lambda)$, or from $\mathcal{R}_{SEU}$ to $\mathcal{R}'_b(\Lambda)$ is given by:

$$\mathbf{DCM_{be}}(\Lambda) = \begin{pmatrix} DCM_{11} & DCM_{12} & DCM_{13} \\ DCM_{21} & DCM_{22} & DCM_{23} \\ DCM_{31} & DCM_{32} & DCM_{33} \end{pmatrix} \tag{4.10}$$

with:

$$\begin{aligned}
DCM_{11} &= \cos(\theta_\Lambda)\cos(\psi_\Lambda) \\
DCM_{12} &= \cos(\theta_\Lambda)\sin(\psi_\Lambda) \\
DCM_{13} &= -\sin(\theta_\Lambda) \\
DCM_{21} &= \sin(\phi_\Lambda)\sin(\theta_\Lambda)\cos(\psi_\Lambda) - \cos(\phi_\Lambda)\sin(\psi_\Lambda) \\
DCM_{22} &= \sin(\phi_\Lambda)\sin(\theta_\Lambda)\sin(\psi_\Lambda) + \cos(\phi_\Lambda)\cos(\psi_\Lambda) \\
DCM_{23} &= \sin(\phi_\Lambda)\cos(\theta_\Lambda) \\
DCM_{31} &= \cos(\phi_\Lambda)\sin(\theta_\Lambda)\cos(\psi_\Lambda) + \sin(\phi_\Lambda)\sin(\psi_\Lambda) \\
DCM_{32} &= \cos(\phi_\Lambda)\sin(\theta_\Lambda)\sin(\psi_\Lambda) - \sin(\phi_\Lambda)\cos(\psi_\Lambda) \\
DCM_{33} &= \cos(\phi_\Lambda)\cos(\theta_\Lambda)
\end{aligned}$$

where ϕ_Λ, θ_Λ and ψ_Λ are the Euler angles of wing Λ.

Unless otherwise stated, the reference frame considered in the remainder of this thesis is NED.

4.3.3 Initialisation of Geometric Parameters – `geodata.m`

The geometric parameters of the wings are initialised in `geodata.m`, and stored in the structure *geo*. A descriptive list of these parameters is presented here.

- **Number of wings,** n_{wing}: in ELL, every flat surface is considered a wing, i.e. there is no input or calculation difference between the main wing, the tailplane, or the fin of an aircraft.

Each wing is numbered, and each geometric parameter is orderly stored in a vector, i.e. for each geometric parameter, the value related to the Λ^{th} surface is stored as the Λ^{th} coefficient of the corresponding vector, whose size is equal to n_{wing}. For example,

$n_{wing} = 2$ and $n_{seg} = [10\ 5]$, means that two lifting surfaces are represented, the first one with 10 horseshoe vortices and the second one with 5 horseshoe vortices.

- **Number of horseshoe vortices, or discretisation segments,** n_{seg}: the higher n_{seg} is, the more accurate the results are, but the more computationally demanding and time consuming the calculations are.
- **Wing span,** b: the wing span is the distance from tip to tip of the wing.
- **Aspect ratio,** λ: the aspect ratio is defined as $\lambda = (2b)^2/S$, where S is the wing area.
- **Taper,** ε: the taper ratio is defined as $\varepsilon = c_{tip}/c_{root}$, where c_{tip} is the chord at the wing tip and c_{root} is the chord at the wing root.
- **Sweep,** φ: the sweep is defined as the angle between the quarter chord line and the y-axis.
- **Dihedral,** δ: the dihedral is the angle between the xy-plane and the quarter chord line.
- **Angle of incidence,** α_0: the 'angle of incidence' α_0 is the angle between the wing chord and the fuselage axis. It is different from the 'angle of attack' α, which is defined as the angle between the fuselage axis and the direction of the incoming airflow.
- **Twist,** *ve*: the wing twist (or washout) is defined as the angle between the tip chord and the root chord of the wing.
- **Symmetry,** *sym*: the symmetry option is a Boolean operator, which mirrors the wing in the xz-plane when set to 1. Usually, symmetry should be set for the main wing and the tailplane, but not for the fin.
- **Type,** *type*: the variable *type* defines the type of discretisation of the lifting line (linear if $type < 1$, sinusoidal if $type \geq 1$).

4.3.4 Initialisation of State Variables – `init.m`

The state variables are input into the main function `ELLmain.m`, and stored in the structure *state* when the m-file `init.m` is called. As for the structure *geo*, the position of each parameter in the vector represents the number of the corresponding wing.

For each air vehicle:

- **Wing Position, x_0, y_0 and z_0**: these three vectors represent the coordinates of the wing origin (defined as the 1/4 chord root point, which coincides with the aerodynamic centre of the wing in subsonic conditions) along the *x*, *y* and *z* axes respectively.
- **Orientation ϕ, θ and ψ**: these three vectors represent the Euler angles of the wing.
- **Direct Cosine Matrices $\mathbf{DCM_{be}}$**: from the NED reference frame to body axes, as defined in Equation 4.10.
- **Airspeed, V**: V represents the true airspeed, i.e. the speed of the aircraft relative to the air mass.
- **Angle of attack, α**: the angle of attack is defined as the angle between the fuselage axis and the direction of the incoming airstream in the *xz*-plane.
- **Angle of sideslip, β**: the angle of sideslip is defined as the angle between the fuselage axis and the direction of the incoming airstream in the *xy*-plane.

4.3.5 Wing Meshing – `vlm.m` and `dis_wing.m`

In this Subsection, for each wing Λ, $\Lambda \in \{1, \ldots, n_{wing}\}$, the corresponding body frame $\mathcal{R}'_b(\Lambda)$ is used.

Each lifting surface is meshed as illustrated in Figure 4.16.

In the sub-routine `dis_wing.m`, the wing geometric parameters initialised in `geodata.m` and stored in the structure *geo* are used to compute the coordinates $[x_1\ y_1\ z_1]$ of the panels' 1/4 chord knots X_1, the chord length $l(k)$ at the knot $X_1(k)$, and the unitary direction vector $\mathbf{d}(\mathbf{k})$ of the lifting line for panel k ($\mathbf{d}(\mathbf{k}) = [d_x(k)\ d_y(k)\ d_z(k)]$):

$$\forall k \in \{1, \ldots, n_{seg}+1\}, \quad X_1(k) = \begin{cases} x_1(k) &= \left|\frac{-b}{2} + (k-1)\cdot\frac{b}{n_{seg}}\right| \cdot \tan(\phi) \\ y_1(k) &= \left(\frac{-b}{2} + (k-1)\cdot\frac{b}{n_{seg}}\right) \cdot \cos(\delta) \\ z_1(k) &= \left|\frac{-b}{2} + (k-1)\cdot\frac{b}{n_{seg}}\right| \cdot \sin(\delta) \end{cases} \tag{4.11}$$

$$\forall k \in \{1, \ldots, n_{seg}+1\}, \quad l(k) = l_0 \cdot \left(1 + \left(\frac{-b}{2} + (k-1)\cdot\frac{b}{n_{seg}}\right)\cdot(\varepsilon - 1)\right) \tag{4.12}$$

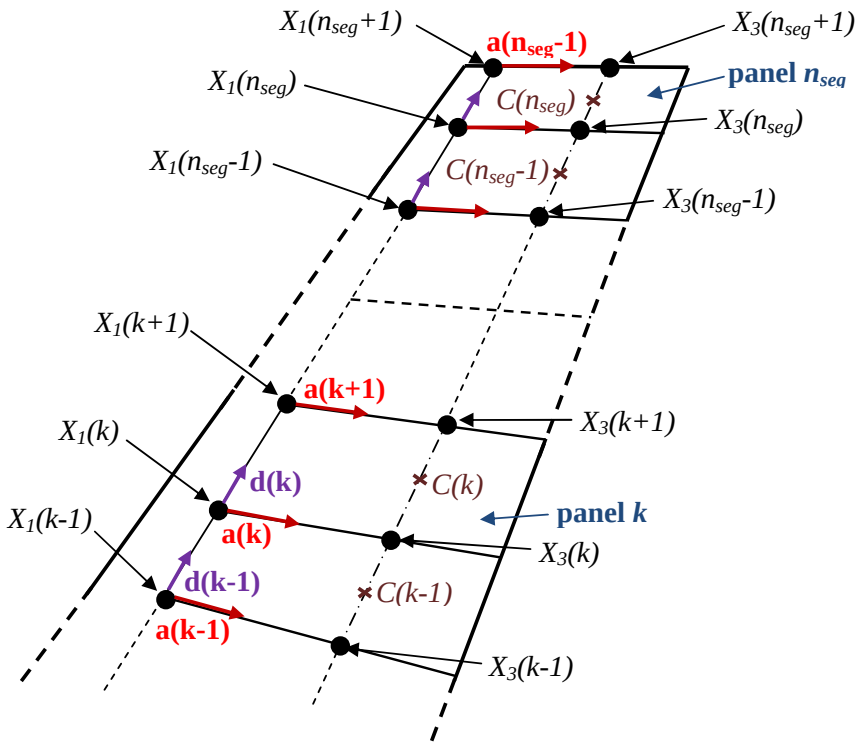

Figure 4.16: Wing planform meshing

$$\forall k \in \{1, \ldots, \mathrm{n_{seg}}\}, \quad \mathbf{d(k)} = \frac{\mathbf{X_1(k)X_1(k+1)}}{\|\mathbf{X_1(k)X_1(k+1)}\|} = \begin{cases} d_x(k) &= \dfrac{x_1(k+1) - x_1(k)}{|x_1(k+1) - x_1(k)|} \\ d_y(k) &= \dfrac{y_1(k+1) - y_1(k)}{|y_1(k+1) - y_1(k)|} \\ d_z(k) &= \dfrac{z_1(k+1) - z_1(k)}{|z_1(k+1) - z_1(k)|} \end{cases} \tag{4.13}$$

Then, in `vlm.m`, the coordinates $[x_m(k)\ y_m(k)\ z_m(k)]$ of the 1/4 chord middle point $X_m(k)$ of panel k are easily calculated:

$$\forall k \in \{1, \ldots, \mathrm{n_{seg}}\}, \quad X_m(k) = \begin{cases} x_m(k) &= \dfrac{x_1(k) + x_1(k+1)}{2} \\ y_m(k) &= \dfrac{y_1(k) + y_1(k+1)}{2} \\ z_m(k) &= \dfrac{z_1(k) + z_1(k+1)}{2} \end{cases} \tag{4.14}$$

If ve, δ and α_0 are respectively the twist angle, dihedral angle and angle of incidence of the wing, then the local values of twist angle, dihedral angle and angle of incidence at the 1/4 chord knots X_1 (ve_v, δ_v and $\alpha_{0,v}$) and middle points X_m ($ve_{m,v}$, $\delta_{m,v}$ and $\alpha_{0,m,v}$) are given by:

$$\forall k \in \{1, \ldots, \mathrm{n_{seg}} + 1\}, \quad \begin{cases} ve_v(k) &= ve \cdot \left| -1 + (k-1)\dfrac{2}{\mathrm{n_{seg}}} \right| \\ \delta_v(k) &= \delta \\ \alpha_{0,v}(k) &= ve_v + \alpha_0 \end{cases} \tag{4.15}$$

$$\forall k \in \{1, \ldots, \mathrm{n_{seg}}\}, \quad \begin{cases} ve_{m,v}(k) &= ve \cdot \left| -1 + \dfrac{2k-1}{\mathrm{n_{seg}}} \right| \\ \delta_{m,v}(k) &= \delta \\ \alpha_{0,m,v}(k) &= ve_{m,v} + \alpha_0 \end{cases} \tag{4.16}$$

The unitary direction vectors of the airfoil, at the 1/4 chord knots X_1 ($\mathbf{a} = [a_x \; a_y \; a_z]$) and middle points X_m ($\mathbf{a_m} = [a_{m,x} \; a_{m,y} \; a_{m,z}]$), are then given by:

$$\forall k \in \{1, \ldots, \mathrm{n_{seg}} + 1\}, \quad \mathbf{a(k)} = \begin{cases} a_x(k) &= \cos(\alpha_{0,v}(k)) \\ a_y(k) &= \dfrac{-y_1(k)}{\|y_1(k)\|} \cdot \sin(\delta_v(k)) \cdot \sin(\alpha_{0,v}(k)) \\ a_z(k) &= -\cos(\delta_v(k)) \cdot \sin(\alpha_{0,v}(k)) \end{cases} \tag{4.17}$$

$$\forall k \in \{1, \ldots, \mathrm{n_{seg}}\}, \quad \mathbf{a_m(k)} = \begin{cases} a_{m,x}(k) &= \cos(\alpha_{m,v}(k)) \\ a_{m,y}(k) &= \dfrac{-y_m(k)}{\|y_1(k)\|} \cdot \sin(\delta_{m,v}(k)) \cdot \sin(\alpha_{0,m,v}(k)) \\ a_{m,z}(k) &= -\cos(\delta_{m,v}(k)) \cdot \sin(\alpha_{0,m,v}(k)) \end{cases} \tag{4.18}$$

And the coordinates $[x_3 \; y_3 \; z_3]$ of the panels' 3/4 chord knots X_3 are determined as follows:

$$\forall k \in \{1, \ldots, \mathrm{n_{seg}}\}, \quad X_3(k) = \begin{cases} x_3(k) &= x_1(k) + \dfrac{l(k)}{2} \cdot a_x(k) \\ y_3(k) &= y_1(k) + \dfrac{l(k)}{2} \cdot a_y(k) \\ z_3(k) &= z_1(k) + \dfrac{l(k)}{2} \cdot a_z(k) \end{cases} \tag{4.19}$$

The coordinates $[x_c(k) \; y_c(k) \; z_c(k)]$ of the control points $X_c(k)$, located at the middle of the 3/4 chord segment of panel k, are:

$$\forall k \in \{1, \ldots, \mathrm{n_{seg}}\}, \quad X_c(k) = \begin{cases} x_c(k) &= \dfrac{x_3(k) + x_3(k+1)}{2} \\ y_c(k) &= \dfrac{y_3(k) + y_3(k+1)}{2} \\ z_c(k) &= \dfrac{z_3(k) + z_3(k+1)}{2} \end{cases} \tag{4.20}$$

The unitary aircraft velocity vector $\mathbf{e} = [e_x \; e_y \; e_z]$ is given by:

$$\mathbf{e} = \begin{cases} e_x &= -\cos(\alpha) \cdot \cos(\beta) \\ e_y &= \sin(\beta) \\ e_z &= -\cos(\beta) \cdot \sin(\alpha) \end{cases} \tag{4.21}$$

Finally, the unitary vector normal to the wing at panel k is:

$$\mathbf{n_k} = \mathbf{a_m(k)} \wedge \mathbf{d(k)} \tag{4.22}$$

After being calculated in the conventional wind tunnel body reference frame specific to each wing $\mathcal{R}'_b(\Lambda)$, $\Lambda \in \{1, \ldots, \mathrm{n_{wing}}\}$, these vectors and coordinates are converted into a common SEU system of coordinates $\mathcal{R}_{SEU}$, whose origin is taken as the origin of the VL. They are then concatenated:

$$\text{for each vector } W, \quad W = [\underbrace{\bullet \ldots \bullet}_{\text{Wing 1}} \underbrace{\bullet \ldots \bullet}_{\text{Wing 2}} \ldots \underbrace{\bullet \ldots \bullet}_{\text{Wing } \mathrm{n_{wing}}}]$$

and stored into the structure *lattice*.

4.3.6 Computation of the Vorticity Vector G – `solver.m`

This subsection describes the method to calculate the value of the vorticity vector:

$$\mathbf{G} = \left[\underbrace{\Gamma_1 \ldots \Gamma_{\mathrm{n_{seg}}(1)}}_{\text{Wing 1}} \underbrace{\Gamma_{\mathrm{n_{seg}}(1)+1} \ldots \Gamma_{\mathrm{n_{seg}}(1)+\mathrm{n_{seg}}(2)}}_{\text{Wing 2}} \ldots \underbrace{\Gamma_{\left(\sum_{k=1}^{\mathrm{n_{wing}}-1} \mathrm{n_{seg}}(k)\right)+1} \ldots \Gamma_{\sum_{k=1}^{\mathrm{n_{wing}}} \mathrm{n_{seg}}(k)}}_{\text{Wing } \mathrm{n_{wing}}} \right]' \tag{4.23}$$

In the following calculations, the mesh panels of all the wings are considered as a group, independently from the wing they represent. This allows the interactions between the different wings to be taken into account during the computation of **G**; therefore the vortices strengths of one vehicle are slightly modified by the presence of another vehicle in the vicinity.

The total number of panels is referred to as N, i.e.:

$$N = \sum_{k=1}^{\mathrm{n_{wing}}} \mathrm{n_{seg}}(k) \tag{4.24}$$

The influence of Panel k, $k \in \{1, \ldots, N\}$, on the control point $C(j) = X_c(j)$ of Panel j, $j \in \{1, \ldots, N\}$, is given by the Biot-Savart law (see Equation 3.5):

$$\mathbf{V_i^k(j)} = \Gamma_k \left(\frac{1}{4\pi} \int_k \frac{\mathbf{dl} \wedge \mathbf{MC(j)}}{\|\mathbf{MC(j)}\|^3} \right) \tag{4.25}$$

where $\int_k$ is the integral along the horseshoe vortex line k:

$$\int_k \dots \, \mathrm{d}l = \underbrace{\int_{-\infty}^{X_3(k)} \dots \, \mathrm{d}l}_{\text{Branch 4}} + \underbrace{\int_{X_3(k)}^{X_1(k)} \dots \, \mathrm{d}l}_{\text{Branch 2}} + \underbrace{\int_{X_1(k)}^{X_1(k+1)} \dots \, \mathrm{d}l}_{\text{Branch 1}} + \underbrace{\int_{X_1(k+1)}^{X_3(k+1)} \dots \, \mathrm{d}l}_{\text{Branch 3}} + \underbrace{\int_{X_3(k+1)}^{+\infty} \dots \, \mathrm{d}l}_{\text{Branch 5}} \tag{4.26}$$

The quantities C, X_1 and X_3 are illustrated in Figure 4.16.

The component of the velocity $\mathbf{V_i^k(j)}$ normal to Panel j is given by:

$$\left(\mathrm{V_i^k(j)}\right)_\mathrm{n} = \underbrace{\Gamma_k}_{\mathrm{G(k)}} \underbrace{\left(\frac{1}{4\pi} \int_k \frac{\mathbf{dl} \wedge \mathbf{MC(j)}}{\|\mathbf{MC(j)}\|^3} \right) \cdot \mathbf{n_j}}_{\mathrm{A(j,k)}} \tag{4.27}$$

where:

- $\mathbf{n_j}$ is the unitary vector normal to Panel j:

$$\mathbf{n_j} = \frac{\mathbf{X_1(j)C(j)} \wedge \mathbf{X_1(j+1)C(j)}}{\|\mathbf{X_1(j)C(j)}\| \, \|\mathbf{X_1(j+1)C(j)}\|} \tag{4.28}$$

- **G** is the unknown vorticity vector,
- **A** is the aerodynamic influence coefficient (AIC) matrix. It can be noted that the coefficients A(j, k) of the AIC matrix only depend on the vector distance between the horseshoe vortex k and the control point $C(j)$.

The magnitude of the total normal velocity induced by all the panels at $C(j)$ is then given by:

$$\left(\mathrm{V_i(j)}\right)_\mathrm{n} = \sum_{k=1}^{N} \left(\mathrm{V_i^k(j)}\right)_\mathrm{n} = \sum_{k=1}^{N} \mathrm{G(k)} \cdot \mathrm{A(j,k)} \tag{4.29}$$

or, in matrix form:

$$\mathbf{(V_i)_n} = \left[\left(\mathrm{V_i(1)}\right)_\mathrm{n} \; \dots \; \left(\mathrm{V_i(n_{seg})}\right)_\mathrm{n} \right]' = \mathbf{A} \cdot \mathbf{G} \tag{4.30}$$

Furthermore, in order to avoid the singularity which occurs when a vortex filament comes too close to a control point ($||\mathbf{MC(j)}|| \simeq 0$), a boundary parameter is introduced and defined as:

$$\epsilon = \max_{i\in\{1,\dots,N\}} 0.1\frac{b(i)}{\mathrm{n_{seg}}(i)} \tag{4.31}$$

According to Equation 4.26, the AIC matrix $\mathbf{A}$ can be expressed as the sum of 5 different AIC matrices, corresponding to the 5 branches of the horseshoe vortices:

$$\mathbf{A} = \underbrace{\mathbf{A_1}}_{\text{Branch 1}} + \underbrace{\mathbf{A_2}}_{\text{Branch 2}} + \underbrace{\mathbf{A_3}}_{\text{Branch 3}} + \underbrace{\mathbf{A_4}}_{\text{Branch 4}} + \underbrace{\mathbf{A_5}}_{\text{Branch 5}} \tag{4.32}$$

As each vortex branch is a straight line, the coefficients of their AIC matrices can be expressed as a sum of cosines. The coefficients of the AIC matrix $\mathbf{A_1}$, related to Branch 1, are given by:

$$\forall (j,k) \in \{1,\dots,N\}^2, \quad \mathrm{A_1(j,k)} = \frac{1}{4\pi}\int_{X_1(k)}^{X_1(k+1)} \frac{\mathbf{dl}\wedge\mathbf{MC(j)}}{||\mathbf{MC(j)}||^3}\cdot\mathbf{n_j} \tag{4.33}$$

with:

$$\mathbf{dl} = \frac{\mathbf{X_1(k)X_1(k+1)}}{||\mathbf{X_1(k)X_1(k+1)}||} \tag{4.34}$$

Consequently:

$$\begin{aligned}\mathrm{A_1(j,k)} &= \frac{1}{4\pi h_1(j,k)}\int_{\gamma_1(j,k)}^{\delta_1(j,k)} \sin(\theta)\,\mathrm{d}\theta\ (\mathbf{n_1(j,k)}\cdot\mathbf{n_j}) \\ &= \frac{1}{4\pi h_1(j,k)}\left(\cos(\gamma_1(j,k)) - \cos(\delta_1(j,k))\right)\ (\mathbf{n_1(j,k)}\cdot\mathbf{n_j})\end{aligned} \tag{4.35}$$

where:

$$\mathbf{n_1(j,k)} = \frac{\mathbf{X_1(k)X_1(k+1)}\wedge\mathbf{X_1(k)C(j)}}{||\mathbf{X_1(k)X_1(k+1)}||\,||\mathbf{X_1(k)C(j)}||} \tag{4.36}$$

$$\gamma_1(j,k) = \frac{\mathbf{X_1(k)X_1(k+1)}\cdot\mathbf{X_1(k)C(j)}}{||\mathbf{X_1(k)X_1(k+1)}||\,||\mathbf{X_1(k)C(j)}||} \tag{4.37}$$

$$\delta_1(j,k) = \frac{\mathbf{X_1(k)X_1(k+1)}\cdot\mathbf{X_1(k+1)C(j)}}{||\mathbf{X_1(k)X_1(k+1)}||\,||\mathbf{X_1(k+1)C(j)}||} \tag{4.38}$$

$$h_1(j,k) = \max\left(||\mathbf{X_1(k+1)C(j)}||\sin(\delta_1(j,k)),\epsilon\right) \tag{4.39}$$

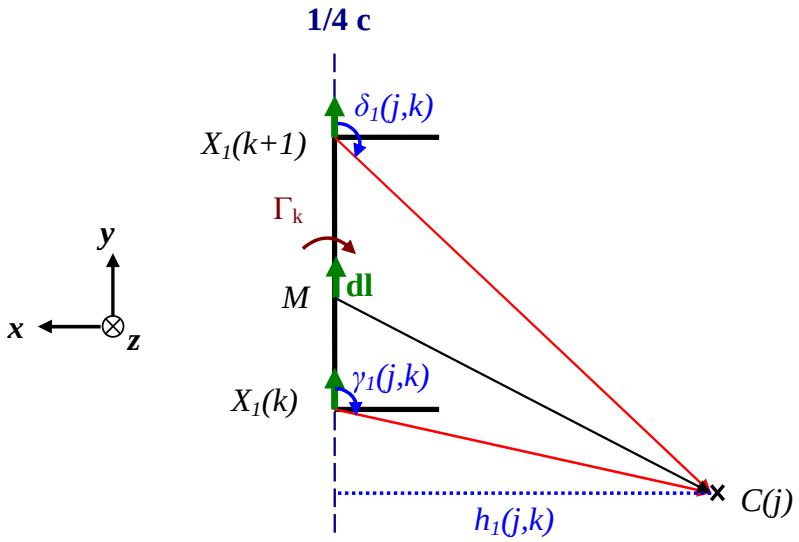

Figure 4.17: Calculation of the induced velocity field due to the 1st branch of the horseshoe vortex k

The quantities $h_1(j,k)$, $\gamma_1(j,k)$ and $\delta_1(j,k)$ are illustrated in Figure 4.17.

The coefficients of the AIC matrix $\mathbf{A_2}$, related to Branch 2, are calculated as follows:

$$\forall (j,k) \in \{1,\ldots,N\}^2, \quad \mathrm{A_2(j,k)} = \frac{1}{4\pi} \int_{X_3(k)}^{X_1(k)} \frac{\mathbf{dl} \wedge \mathbf{MC(j)}}{\|\mathbf{MC(j)}\|^3} \cdot \mathbf{n_j} \tag{4.40}$$

with:

$$\mathbf{dl} = \frac{\mathbf{X_3(k)X_1(k)}}{\|\mathbf{X_3(k)X_1(k)}\|} \tag{4.41}$$

Consequently:

$$\begin{aligned} \mathrm{A_2(j,k)} &= \frac{1}{4\pi h_2(j,k)} \int_{\gamma_2(j,k)}^{\delta_2(j,k)} \sin(\theta)\, \mathrm{d}\theta\, (\mathbf{n_2(j,k)} \cdot \mathbf{n_j}) \\ &= \frac{1}{4\pi h_2(j,k)} (\cos(\gamma_2(j,k)) - \cos(\delta_2(j,k)))\ (\mathbf{n_2(j,k)} \cdot \mathbf{n_j}) \end{aligned} \tag{4.42}$$

where:

$$\mathbf{n_2(j,k)} = \frac{\mathbf{X_3(k)X_1(k)} \wedge \mathbf{X_3(k)C(j)}}{\|\mathbf{X_3(k)X_1(k)}\| \, \|\mathbf{X_3(k)C(j)}\|} \tag{4.43}$$

$$\gamma_2(j,k) = \frac{\mathbf{X_3(k)X_1(k)} \cdot \mathbf{X_3(k)C(j)}}{\|\mathbf{X_3(k)X_1(k)}\| \, \|\mathbf{X_3(k)C(j)}\|} \tag{4.44}$$

$$\delta_2(j,k) = \frac{\mathbf{X_3(k)X_1(k)} \cdot \mathbf{X_3(k)C(j)}}{\|\mathbf{X_3(k)X_1(k)}\| \, \|\mathbf{X_1(k)C(j)}\|} \tag{4.45}$$

$$h_2(j,k) = \max\left(\|\mathbf{X_1(k)C(j)}\| \sin(\delta_2(j,k)), \epsilon\right) \tag{4.46}$$

The quantities $h_2(j,k)$, $\gamma_2(j,k)$ and $\delta_2(j,k)$ are illustrated in Figure 4.18.

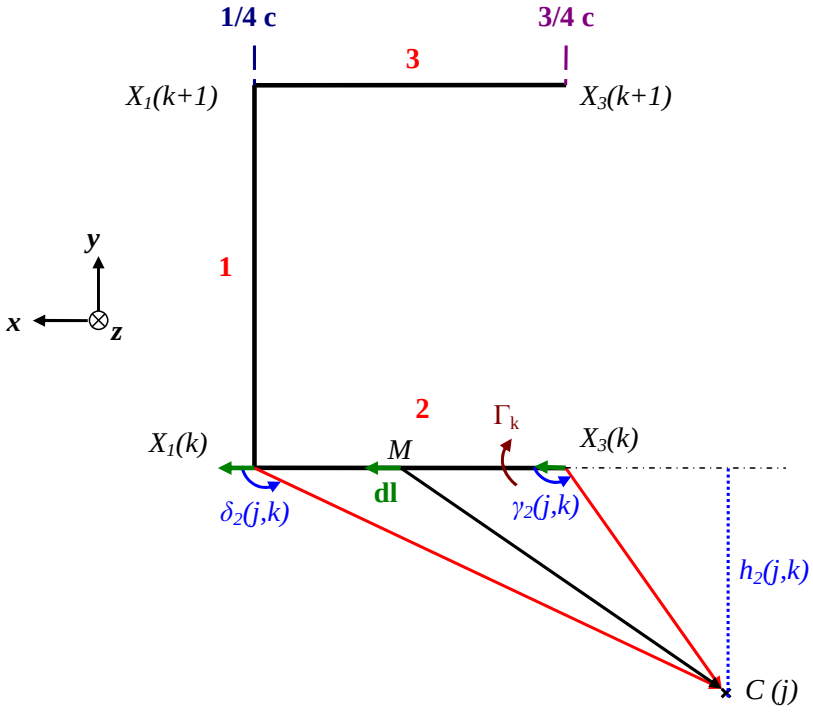

Figure 4.18: Calculation of the induced velocity field due to the 2^{nd} branch of the horseshoe vortex k

The coefficients of the AIC matrix $\mathbf{A_3}$, related to Branch 3, are calculated as follows:

$$\forall (j,k) \in \{1,\ldots,N\}^2, \quad \mathrm{A_3(j,k)} = \frac{1}{4\pi} \int_{X_1(k+1)}^{X_3(k+1)} \frac{\mathbf{dl} \wedge \mathbf{MC(j)}}{\|\mathbf{MC(j)}\|^3} \cdot \mathbf{n_j} \tag{4.47}$$

with:

$$\mathbf{dl} = \frac{\mathbf{X_1(k+1)X_3(k+1)}}{\|\mathbf{X_1(k+1)X_3(k+1)}\|} \tag{4.48}$$

Consequently:

$$\begin{aligned} \mathrm{A_3(j,k)} &= \frac{1}{4\pi h_3(j,k)} \int_{\gamma_3(j,k)}^{\delta_3(j,k)} \sin(\theta)\, \mathrm{d}\theta\, (\mathbf{n_3(j,k)} \cdot \mathbf{n_j}) \\ &= \frac{1}{4\pi h_3(j,k)} (\cos(\gamma_3(j,k)) - \cos(\delta_3(j,k)))\ (\mathbf{n_3(j,k)} \cdot \mathbf{n_j}) \end{aligned} \tag{4.49}$$

where:

$$\mathbf{n_3(j,k)} = \frac{\mathbf{X_1(k+1)X_3(k+1)} \wedge \mathbf{X_1(k+1)C(j)}}{\|\mathbf{X_1(k+1)X_3(k+1)}\|\,\|\mathbf{X_1(k+1)C(j)}\|} \tag{4.50}$$

$$\gamma_3(j,k) = \frac{\mathbf{X_1(k+1)X_3(k+1)} \cdot \mathbf{X_1(k+1)C(j)}}{\|\mathbf{X_1(k+1)X_3(k+1)}\|\,\|\mathbf{X_1(k+1)C(j)}\|} \tag{4.51}$$

$$\delta_3(j,k) = \frac{\mathbf{X_1(k+1)X_3(k+1)} \cdot \mathbf{X_3(k+1)C(j)}}{\|\mathbf{X_1(k+1)X_3(k+1)}\|\,\|\mathbf{X_3(k+1)C(j)}\|} \tag{4.52}$$

$$h_3(j,k) = \max\left(\|\mathbf{X_3(k+1)C(j)}\| \sin(\delta_3(j,k)), \epsilon\right) \tag{4.53}$$

The quantities $h_3(j,k)$, $\gamma_3(j,k)$ and $\delta_3(j,k)$ are illustrated in Figure 4.19.

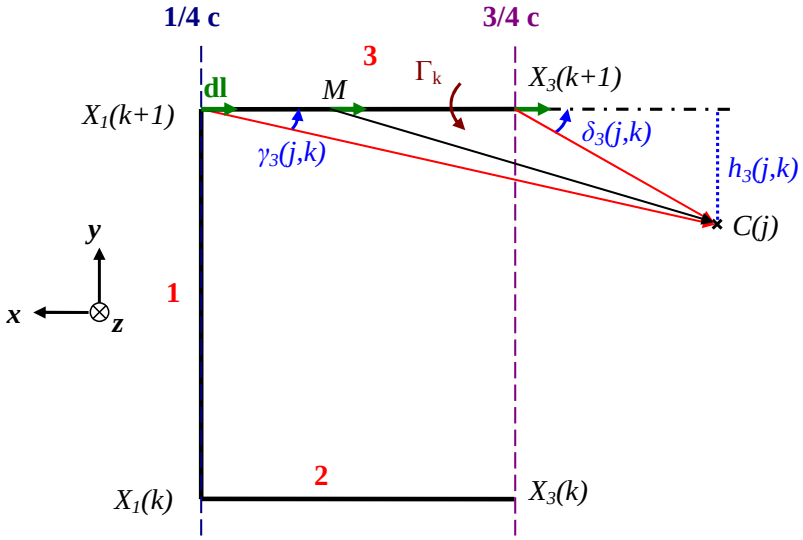

Figure 4.19: Calculation of the induced velocity field due to the 3^{rd} branch of the horseshoe vortex k

The coefficients of the AIC matrix $\mathbf{A_4}$, related to Branch 4, are calculated as follows:

$$\forall (j,k) \in \{1,\ldots,N\}^2, \quad \mathrm{A_4(j,k)} = \frac{1}{4\pi} \int_{-\infty}^{X_3(k)} \frac{\mathbf{dl} \wedge \mathbf{MC(j)}}{\|\mathbf{MC(j)}\|^3} \cdot \mathbf{n_j} \tag{4.54}$$

with:

$$\mathbf{dl} = \frac{\mathbf{V}}{\|\mathbf{V}\|} \tag{4.55}$$

Consequently:

$$\begin{aligned} A_4(j,k) &= \frac{1}{4\pi h_4(j,k)} \int_0^{\delta_4(j,k)} \sin(\theta)\, d\theta\, (\mathbf{n_4(j,k)} \cdot \mathbf{n_j}) \\ &= \frac{1}{4\pi h_4(j,k)} (1 - \cos(\delta_4(j,k)))\ (\mathbf{n_4(j,k)} \cdot \mathbf{n_j}) \end{aligned} \tag{4.56}$$

where:

$$\mathbf{n_4(j,k)} = \frac{\mathbf{V} \wedge \mathbf{X_3(k)C(j)}}{\|\mathbf{V}\|\,\|\mathbf{X_3(k)C(j)}\|} \tag{4.57}$$

$$\delta_4(j,k) = \frac{\mathbf{V} \cdot \mathbf{X_3(k)C(j)}}{\|\mathbf{V}\|\,\|\mathbf{X_3(k)C(j)}\|} \tag{4.58}$$

$$h_4(j,k) = \max\left(\|\mathbf{X_3(k)C(j)}\| \sin(\delta_4(j,k)), \epsilon\right) \tag{4.59}$$

The quantities $h_4(j,k)$ and $\delta_4(j,k)$ are illustrated in Figure 4.20.

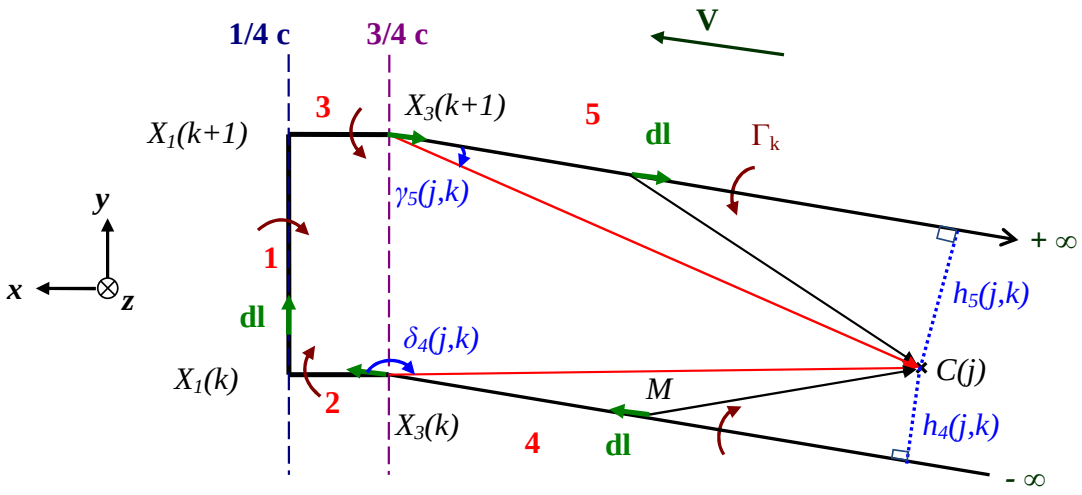

Figure 4.20: Calculation of the induced velocity field due to the 4^{th} and 5^{th} branches of the horseshoe vortex k

The coefficients of the AIC matrix $\mathbf{A_5}$, related to Branch 5, are calculated as follows:

$$\forall (j,k) \in \{1,\ldots,N\}^2, \quad A_5(j,k) = \frac{1}{4\pi} \int_{X_3(k+1)}^{+\infty} \frac{\mathbf{dl} \wedge \mathbf{MC(j)}}{\|\mathbf{MC(j)}\|^3} \cdot \mathbf{n_j} \tag{4.60}$$

with:

$$\mathbf{dl} = \frac{-\mathbf{V}}{||\mathbf{V}||} \tag{4.61}$$

Consequently:

$$\begin{aligned} \mathrm{A_5(j,k)} &= \frac{1}{4\pi h_5(j,k)} \int_{\gamma_5(j,k)}^{\pi} \sin(\theta)\, \mathrm{d}\theta\, (\mathbf{n_5(j,k)} \cdot \mathbf{n_j}) \\ &= \frac{1}{4\pi h_5(j,k)} (\cos(\gamma_5(j,k)) + 1)\ (\mathbf{n_5(j,k)} \cdot \mathbf{n_j}) \end{aligned} \tag{4.62}$$

where:

$$\mathbf{n_5(j,k)} = \frac{-\mathbf{V} \wedge \mathbf{X_3(k+1)C(j)}}{||\mathbf{V}||\, ||\mathbf{X_3(k+1)C(j)}||} \tag{4.63}$$

$$\gamma_5(j,k) = \frac{-\mathbf{V} \cdot \mathbf{X_3(k+1)C(j)}}{||\mathbf{V}||\, ||\mathbf{X_3(k+1)C(j)}||} \tag{4.64}$$

$$h_5(j,k) = \max\left(||\mathbf{X_3(k+1)C(j)}|| \sin(\gamma_5(j,k)), \epsilon\right) \tag{4.65}$$

The quantities $h_5(j,k)$ and $\gamma_5(j,k)$ are illustrated in Figure 4.20.

Once the AIC matrix **A** has been determined, the boundary condition of Weissinger, which states that the airflow must be tangential to each wing surface at its control points, is applied:

$$\forall j \in \{1, \ldots, N\}, \quad (\mathrm{V_i(j)})_\mathrm{n} + \mathbf{V}_\infty\mathbf{(j)} \cdot \mathbf{n_j} = 0 \tag{4.66}$$

where $\mathbf{V}_\infty\mathbf{(j)}$ is the unperturbed incoming flow, equal to the opposite of the airspeed of the vehicle to which Panel j belongs: $\mathbf{V}_\infty = -\mathbf{V}$.

In matrix form, Equation 4.66 becomes:

$$\underbrace{(\mathbf{V_i})_\mathbf{n}}_{\mathbf{A} \cdot \mathbf{G}} = \mathbf{V_n} \tag{4.67}$$

with:

$$\mathbf{V_n} = -\left[\mathbf{V}_\infty\mathbf{(1)} \cdot \mathbf{n_1}\ \ldots\ \mathbf{V}_\infty\mathbf{(N)} \cdot \mathbf{n_N}\right]' \tag{4.68}$$

Hence:

$$\mathbf{G} = \mathbf{A}^{-1} \cdot \mathbf{V_n} \tag{4.69}$$

4.3.7 Computation of the Induced Velocity – `velocity.m`

Once the vorticity vector **G** is known, the velocity $\mathbf{V_i}(\mathbf{\Lambda})$ induced on the aircraft Λ by the surrounding air vehicles is calculated at the 1/4 chord middle points $X_m(j_\Lambda)$ of the panels j_Λ of Λ, as the sum of the contributions of each branch of the horseshoe vortices belonging to the surrounding aircraft:

$$\mathbf{V_i}(\mathbf{j_\Lambda}) = \underbrace{\mathbf{V_{i,1}}(\mathbf{j_\Lambda})}_{\text{Branch 1}} + \underbrace{\mathbf{V_{i,2}}(\mathbf{j_\Lambda})}_{\text{Branch 2}} + \underbrace{\mathbf{V_{i,3}}(\mathbf{j_\Lambda})}_{\text{Branch 3}} + \underbrace{\mathbf{V_{i,4}}(\mathbf{j_\Lambda})}_{\text{Branch 4}} + \underbrace{\mathbf{V_{i,5}}(\mathbf{j_\Lambda})}_{\text{Branch 5}} \tag{4.70}$$

The computation of these contributions is similar to the computation of the AIC $A_p(j, k)$, $p \in \{1, \ldots, 5\}$ carried out in `solver.m` (see Subsection 4.3.6), with the following differences:

- $C = X_m$ instead of $C = X_j$, i.e. for each panel, the induced velocity is computed on its 1/4 chord line middle point rather than on its 3/4 chord line middle point.
- Only the horseshoe vortices of the surrounding vehicles are considered. This is achieved through modifying the vorticity vector **G** such that $\Gamma_{j_\Lambda} = 0$ for the panels j_Λ of aircraft Λ.
- The Lamb-Oseen velocity profile is used in lieu of the Helmholtz model for Branches 4 and 5 of each horseshoe vortex, as shown in Figure 4.21. This removes the need to use the boundary parameter ϵ in the calculation of $h_p(j, k)$, $p \in \{1, \ldots, 5\}$.

Therefore:

$$\mathbf{V_{i,1}}(\mathbf{j_\Lambda}) = \sum_{k=1}^{N} \frac{\Gamma_k}{4\pi h_1(j_\Lambda, k)} \left(\cos(\gamma_1(j_\Lambda, k)) - \cos(\delta_1(j_\Lambda, k))\right) \cdot \mathbf{n_1}(\mathbf{j_\Lambda}, \mathbf{k}) \tag{4.71}$$

$$\mathbf{V_{i,2}}(\mathbf{j_\Lambda}) = \sum_{k=1}^{N} \frac{\Gamma_k}{4\pi h_2(j_\Lambda, k)} \left(\cos(\gamma_2(j_\Lambda, k)) - \cos(\delta_2(j_\Lambda, k))\right) \cdot \mathbf{n_2}(\mathbf{j_\Lambda}, \mathbf{k}) \tag{4.72}$$

$$\mathbf{V_{i,3}}(\mathbf{j_\Lambda}) = \sum_{k=1}^{N} \frac{\Gamma_k}{4\pi h_3(j_\Lambda, k)} \left(\cos(\gamma_3(j_\Lambda, k)) - \cos(\delta_3(j_\Lambda, k))\right) \cdot \mathbf{n_3}(\mathbf{j_\Lambda}, \mathbf{k}) \tag{4.73}$$

$$\mathbf{V_{i,4}}(\mathbf{j_\Lambda}) = \sum_{k=1}^{N} \frac{\Gamma_k}{4\pi h_4(j_\Lambda, k)} \left(1 - \cos(\delta_4(j_\Lambda, k))\right) \cdot \mathbf{n_4}(\mathbf{j_\Lambda}, \mathbf{k}) \tag{4.74}$$

$$\mathbf{V_{i,5}}(\mathbf{j_\Lambda}) = \sum_{k=1}^{N} \frac{\Gamma_k}{4\pi h_5(j_\Lambda, k)} \left(\cos(\gamma_5(j_\Lambda, k)) + 1\right) \cdot \mathbf{n_5}(\mathbf{j_\Lambda}, \mathbf{k}) \tag{4.75}$$

where:

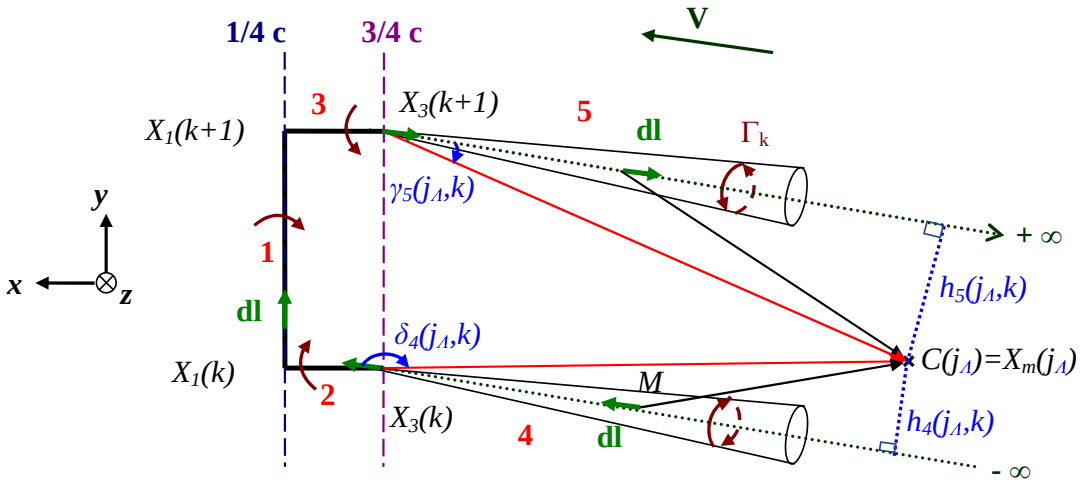

Figure 4.21: Calculation of the induced velocity field due to the 4^{th} and 5^{th} branches of the horseshoe vortex k using the Lamb-Oseen vortex model

- $\Gamma_k = 0$ when the panel k belongs to Λ,
- $\gamma_1(j_\Lambda, k)$, $\gamma_2(j_\Lambda, k)$, $\gamma_3(j_\Lambda, k)$, $\gamma_5(j_\Lambda, k)$, $\delta_1(j_\Lambda, k)$, $\delta_2(j_\Lambda, k)$, $\delta_3(j_\Lambda, k)$, $\delta_4(j_\Lambda, k)$, $\mathbf{n_1}(\mathbf{j_\Lambda}, \mathbf{k})$, $\mathbf{n_2}(\mathbf{j_\Lambda}, \mathbf{k})$, $\mathbf{n_3}(\mathbf{j_\Lambda}, \mathbf{k})$, $\mathbf{n_4}(\mathbf{j_\Lambda}, \mathbf{k})$ and $\mathbf{n_5}(\mathbf{j_\Lambda}, \mathbf{k})$ are defined in Subsection 4.3.6,
- $h_1(j_\Lambda, k)$, $h_2(j_\Lambda, k)$, $h_3(j_\Lambda, k)$, $h_4(j_\Lambda, k)$ and $h_5(j_\Lambda, k)$ are given by:

$$h_1(j_\Lambda, k) = \|\mathbf{X_1(k+1)C(j)}\| \sin(\delta_1(j,k)) \quad (4.76)$$

$$h_2(j_\Lambda, k) = \|\mathbf{X_1(k)C(j)}\| \sin(\delta_2(j,k)) \quad (4.77)$$

$$h_3(j_\Lambda, k) = \|\mathbf{X_3(k+1)C(j)}\| \sin(\delta_3(j,k)) \quad (4.78)$$

$$h_4(j_\Lambda, k) = \|\mathbf{X_3(k)C(j)}\| \sin(\delta_4(j,k)) \quad (4.79)$$

$$h_5(j_\Lambda, k) = \|\mathbf{X_3(k+1)C(j)}\| \sin(\gamma_5(j,k)) \quad (4.80)$$

From these, the induced translational and rotational wind velocities can be easily calculated using Equations 4.5, 4.6 and 4.7:

$$\widetilde{\mathbf{V}}_\mathbf{i}(\Lambda) = \frac{1}{n_{seg_\Lambda}} \sum_{j_\Lambda=1}^{n_{seg_\Lambda}} \mathbf{V_i(j_\Lambda)} \quad (4.81)$$

and

$$\widetilde{\boldsymbol{\omega}}_{\mathbf{i}}(\Lambda) = \begin{cases} \widetilde{\omega_{i_x}}(\Lambda) = \dfrac{1}{n_{seg_\Lambda} - 1} \displaystyle\sum_{j_\Lambda=1}^{n_{seg_\Lambda}-1} \left(\dfrac{V_{i_z}(j_\Lambda + 1) - V_{i_z}(j_\Lambda)}{y_m(j_\Lambda + 1) - y_m(j_\Lambda)} - \dfrac{V_{i_y}(j_\Lambda + 1) - V_{i_y}(j_\Lambda)}{z_m(j_\Lambda + 1) - z_m(j_\Lambda)} \right) \\ \widetilde{\omega_{i_y}}(\Lambda) = \dfrac{1}{n_{seg_\Lambda} - 1} \displaystyle\sum_{j_\Lambda=1}^{n_{seg_\Lambda}-1} \left(\dfrac{V_{i_x}(j_\Lambda + 1) - V_{i_x}(j_\Lambda)}{z_m(j_\Lambda + 1) - z_m(j_\Lambda)} - \dfrac{V_{i_z}(j_\Lambda + 1) - V_{i_z}(j_\Lambda)}{x_m(j_\Lambda + 1) - x_m(j_\Lambda)} \right) \\ \widetilde{\omega_{i_z}}(\Lambda) = \dfrac{1}{n_{seg_\Lambda} - 1} \displaystyle\sum_{j_\Lambda=1}^{n_{seg_\Lambda}-1} \left(\dfrac{V_{i_y}(j_\Lambda + 1) - V_{i_y}(j_\Lambda)}{x_m(j_\Lambda + 1) - x_m(j_\Lambda)} - \dfrac{V_{i_x}(j_\Lambda + 1) - V_{i_x}(j_\Lambda)}{y_m(j_\Lambda + 1) - y_m(j_\Lambda)} \right) \end{cases} \tag{4.82}$$

$\widetilde{\mathbf{V}}_{\mathbf{i}}(\Lambda)$ and $\widetilde{\boldsymbol{\omega}}_{\mathbf{i}}(\Lambda)$ can then be directly used with the wind terms of Λ's Simulink model, as explained in Subsection 4.2.5.

4.4 Chapter Summary and Conclusions

In this chapter, the development and implementation of a one-lifting-line VLM to model the aerodynamic interactive effects between two or more air vehicles flying in formation is discussed. The code (ELL) computes the steady-state velocities induced on one air vehicle by the wake(s) of the others. Each aircraft is represented by its lifting surfaces. Each surface is replaced by its 1/4 chord segment, and the vortex sheet by a flat rectangular surface composed of n_{seg} semi-infinite horseshoe vortices. Their strength is determined through the application of the Weissinger boundary condition, which states that at the collocation points of the wing (one per horseshoe vortex), the airflow is tangential to the wing surface.

Once the vortices strengths are known, the velocities induced on one air vehicle by other aircraft in the formation can be calculated at different points along its 1/4 chord line. For that, a Helmholtz velocity distribution is used to calculate the influence of the branches of the vortices bound to the wings of the neighbouring vehicles, and a Lamb-Oseen vortex model is used for the trailing branches of those vortices.

The induced velocity field thus obtained is highly non-uniform, and can be approximated around the CG of the vehicle as the sum of uniform wind components and uniform wind gradients, following a method developed by Dogan, Venkataramanan and Blake [2005]. The components of the effective induced translational and rotational wind velocities can then be derived, and directly integrated in the aircraft Simulink

model with its wind terms.

Chapter 5

Wake Vortex Model Verification and Validation

Unless otherwise specified, all angles considered in this chapter are in degrees.

5.1 Preliminary Comment

From a computational point of view, there is no difference between single- and multi-wing vehicles: the velocity induced by the main wing of one air vehicle on its tailplane is calculated in the same way as the velocity induced by the wing of one aircraft on the wing of another aircraft. The only difference between a configuration where the wings belong to distinct airplanes and a configuration where the wings are part of the same vehicle is that in the first case, the wings can potentially move independently from one another, while in the second case, the wings will keep the exact same relative position and orientation throughout the manoeuvres. Therefore, for the verification and validation tests discussed in this section, the air vehicles are represented by their main wing only.

5.2 Definitions

The *Department of Defense Dictionary of Military and Associated Terms* [2001] proposes the following definitions of the terms 'verification' and 'validation' in computer modeling and simulation:

- **Verification** is the process of determining that a model or simulation implementation accurately represents the developers conceptual description and specifications.

- **Validation** is the process of determining the degree to which a model or simulation is an accurate representation of the real world from the perspective of the intended uses of the model or simulation.

In other words, validation ensures that an appropriate model or simulation implementation was built, whereas verification ensures that the model or simulation implementation was built in a correct way.

5.3 Verification of the Wake Vortex Model

A number of tests were carried out in order to verify ELL. These are discussed in this section.

5.3.1 'Test Vehicle' Geometric Parameters

The geometric parameters of the test vehicle(s) used for the verification of ELL are presented in Table 5.1. The parameters listed in Table 5.1 are defined in Subsection 4.3.3. The number of horseshoe vortices per wing (n_{seg}) was chosen equal to 5. Although this is less than the number recommended in Subsection 4.2.4, this is enough for verification purposes, as the aim of the verification is not to check the accuracy of the results but to check that there is no computational error in the code.

Table 5.1: Test vehicle's geometric parameters – Verification

n_{seg}	b	λ	ε	φ	δ	α_0	ve	sym	$type$
5	1 m	6	1	0 deg	0 deg	0 deg	0 deg	1	0

5.3.2 Influence of the Reference Frame on the Induced Velocity

In this subsection, the airspeed, angle of attack, and angle of sideslip of all vehicles, whatever their Euler angles, are supposed to be $V = 25$ m/s, $\alpha = 5$ deg and $\beta = 0$ deg respectively.

Test for one vehicle only

For a single vehicle, there is no velocity induced by a neighbouring aircraft. Therefore, measuring the influence of the reference frame amounts to calculating the vorticity

vector **G** of the air vehicle for several sets of position and orientation. A few cases are presented in Table 5.2.

As expected, these quantities are independent of the position and orientation of the vehicle.

Test for two air vehicles

The purpose of this test is to verify that the induced velocity vector $\mathbf{V_i}$ obtained for two aircraft in a given configuration is independent of the reference frame.

Two air vehicles are considered, Λ_1 and Λ_2. Their respective positions and orientations are given by the coordinates $[x_1, y_1, z_1]$ and $[x_2, y_2, z_2]$, and the Euler angles $(\phi_1, \theta_1, \psi_1)$ and $(\phi_2, \theta_2, \psi_2)$ in the Earth frame (NED) $\mathcal{R}_E$. The body frames of Λ_1 and Λ_2 are referred to as $\mathcal{R}_{B_1}$ and $\mathcal{R}_{B_2}$ respectively.

It is now considered that the Earth frame $\mathcal{R}_E$ is rotated around its centre O by the Euler angles $(\phi_R, \theta_R, \psi_R)$. The new reference frame thus obtained is referred to as $\mathcal{R}_0$.

The DCM of interest are listed below:

- DCM_{B_1E} from $\mathcal{R}_E$ to $\mathcal{R}_{B_1}$,
- DCM_{B_2E} from $\mathcal{R}_E$ to $\mathcal{R}_{B_2}$, and
- DCM_{E0} from $\mathcal{R}_0$ to $\mathcal{R}_E$.

The total rotations matrices for Λ_1 and Λ_2 are introduced as, respectively:

- $R_1 = DCM_{B_1E} \cdot DCM_{E0}$ from $\mathcal{R}_0$ to $\mathcal{R}_{B_1}$
- $R_2 = DCM_{B_2E} \cdot DCM_{E0}$ from $\mathcal{R}_0$ to $\mathcal{R}_{B_2}$

As each matrix R_k, $k \in \{1, 2\}$ is the product of two rotation matrices, it is also a rotation matrix and can be expressed as the DCM of three Euler angles, named $(\Phi_1, \Theta_1, \Psi_1)$ and $(\Phi_2, \Theta_2, \Psi_2)$ respectively:

$$\forall k \in \{1, 2\}, \quad R_k = \begin{pmatrix} R_k(1,1) & R_k(1,2) & R_k(1,3) \\ R_k(2,1) & R_k(2,2) & R_k(2,3) \\ R_k(3,1) & R_k(3,2) & R_k(3,3) \end{pmatrix} \tag{5.1}$$

Table 5.2: Influence of the position and orientation of one air vehicle on its vorticity and induced velocity vectors

Coordinates $[x, y, z]$	Euler angles (ϕ, θ, ψ)	**G**	$\mathbf{V_i}$
$[0, 0, 0]$	$(0, 0, 0)$	$[-0.7524, -0.8946, -0.9257, -0.8946, -0.7524]$	$[0, 0, 0]$
$[0, 0, 0]$	$(33, 14, 68)$	$[-0.7524, -0.8946, -0.9257, -0.8946, -0.7524]$	$[0, 0, 0]$
$[13, 2, 34]$	$(33, 14, 68)$	$[-0.7524, -0.8946, -0.9257, -0.8946, -0.7524]$	$[0, 0, 0]$
$[0, -5, 5]$	$(90, 90, 90)$	$[-0.7524, -0.8946, -0.9257, -0.8946, -0.7524]$	$[0, 0, 0]$
$[-7, 6, 2]$	$(180, 180, 180)$	$[-0.7524, -0.8946, -0.9257, -0.8946, -0.7524]$	$[0, 0, 0]$

with:

$$
\begin{aligned}
R_k(1,1) &= \cos(\Theta_k)\cos(\Psi_k) \\
R_k(1,2) &= \cos(\Theta_k)\sin(\Psi_k) \\
R_k(1,3) &= -\sin(\Theta_k) \\
R_k(2,1) &= \sin(\Phi_k)\sin(\Theta_k)\cos(\Psi_k) - \cos(\Phi_k)\sin(\Psi_k) \\
R_k(2,2) &= \sin(\Phi_k)\sin(\Theta_k)\sin(\Psi_k) + \cos(\Phi_k)\cos(\Psi_k) \\
R_k(2,3) &= \sin(\Phi_k)\cos(\Theta_k) \\
R_k(3,1) &= \cos(\Phi_k)\sin(\Theta_k)\cos(\Psi_k) + \sin(\Phi_k)\sin(\Psi_k) \\
R_k(3,2) &= \cos(\Phi_k)\sin(\Theta_k)\sin(\Psi_k) - \sin(\Phi_k)\cos(\Psi_k) \\
R_k(3,3) &= \cos(\Phi_k)\cos(\Theta_k)
\end{aligned}
$$

If $\cos(\Theta_k) \neq 0$, i.e. if $\Theta_k \neq \pm\pi/2$, the new Euler Angles $(\Phi_k, \Theta_k, \Psi_k)$, $k \in \{1,2\}$, can be extracted from R_k as follows:

$$\Phi_k = \frac{180}{\pi} \cdot \text{atan2}(\sin(\Phi_k), \cos(\Phi_k)) = \frac{180}{\pi} \cdot \text{atan2}(R_k(2,3), R_k(3,3)) \quad (5.2)$$

$$\Theta_k = \frac{180}{\pi} \cdot \arcsin(\sin(\Theta_k)) = -\frac{180}{\pi} \cdot \arcsin(R_k(1,3)) \quad (5.3)$$

$$\Psi_k = \frac{180}{\pi} \cdot \text{atan2}(\sin(\Psi_k), \cos(\Psi_k)) = \frac{180}{\pi} \cdot \text{atan2}(R_k(1,2), R_k(1,1)) \quad (5.4)$$

where $\text{atan2}(y,x)$, $(x,y) \in \mathbb{R}^2$, is the four quadrant arctangent of x and y.

The reason why the function atan2 is used rather than arctan is because, unlike $\arctan(y/x)$ whose results are limited to the interval $[-\pi/2, \pi/2]$, $\text{atan2}(y,x)$ takes account of the signs of both components x and y to return an angle in the correct quadrant of the interval $[-\pi, \pi]$.

The coordinates of Λ_1 ($[X_1, Y_1, Z_1]'$) and Λ_2 ($[X_2, Y_2, Z_2]'$) in $\mathcal{R}_0$ are given by:

$$[X_1, Y_1, Z_1]' = DCM_{0E} \cdot [x_1, y_1, z_1]' \quad (5.5)$$

$$[X_2, Y_2, Z_2]' = DCM_{0E} \cdot [x_2, y_2, z_2]' \quad (5.6)$$

where DCM_{0E} is the DCM from $\mathcal{R}_E$ to $\mathcal{R}_0$: $DCM_{0E} = (DCM_{E0})^{-1}$.

The induced velocity vector $\mathbf{V_i}$ is then computed for both vehicles with the following input variables:

- $(\mathbf{V_i})_{\mathcal{R}_E}$ in $\mathcal{R}_E$: Λ_1 (position: $[x_1, y_1, z_1]$, Euler angles: $(\phi_1, \theta_1, \psi_1)$, airdata: (V, α, β)) and Λ_2 (position: $[x_2, y_2, z_2]$, Euler angles: $(\phi_2, \theta_2, \psi_2)$, airdata: (V, α, β));
- $(\mathbf{V_i})_{\mathcal{R}_0}$ in $\mathcal{R}_0$: Λ_1 (position: $[X_1, Y_1, Z_1]$, Euler angles: $(\Phi_1, \Theta_1, \Psi_1)$, airdata: (V, α, β)) and Λ_2 (position: $[X_2, Y_2, Z_2]$, Euler angles: $(\Phi_2, \Theta_2, \Psi_2)$, airdata: (V, α, β));

The induced velocity vector $\mathbf{V_i}$ components depend on the reference frame where they are calculated. Therefore, for the comparison to be valid, they should be expressed in the same reference frame. $\mathcal{R}_E$ was chosen and the induced velocity vector $(\mathbf{V_i})_{\mathcal{R}_0}$ calculated in $\mathcal{R}_0$ was expressed in $\mathcal{R}_E$ using:

$$(\mathbf{V_i})_{\mathcal{R}_E} = DCM_{E0} \cdot (\mathbf{V_i})_{\mathcal{R}_0} \tag{5.7}$$

The results for a few of the configurations of Λ_1, Λ_2 and $\mathcal{R}_0$ tested are presented in Table 5.3. From this table, it can be verified that, as expected, the determination of the induced velocity vector $\mathbf{V_i}$ is independent of the reference frame.

5.3.3 Influence of the Distance Between the Air Vehicles of a Formation

In this subsection, the influence on the induced velocity of the separation between air vehicles is verified. For that, the vorticity vector $\mathbf{G}$ and the induced velocity vector $\mathbf{V_i}$ are computed for two vehicles (Λ_1 and Λ_2) in formation, and compared to the vorticity vector $\mathbf{G}$ and the induced velocity vector $\mathbf{V_i}$ obtained in the case of a single air vehicle (Table 5.2). The distance between Λ_1 and Λ_2 is increased, and it is expected to recover the same result as in the case of one aircraft only when Λ_1 and Λ_2 are sufficiently far from each other for their interactive coupling to become insignificant.

The results of some of the configurations tested are reported in Table 5.4. Each aircraft's body frame is supposed to be aligned with the NED Earth frame ($(\phi, \theta, \psi) = (0, 0, 0)$), i.e. the vehicles are flying a straight level trajectory heading North. Their airspeed, angle of attack, and angle of sideslip are given by: $V = 25$ m/s, $\alpha = 5$ deg and $\beta = 0$ deg respectively.

As seen in Subsection 4.3.6, the vorticity vector $\mathbf{G}$ is the concatenation of the circulation along all the horseshoe vortices. In the case of one vehicle only:

Table 5.3: Influence of the reference frame on the vorticity and induced velocity vectors of two vehicles in formation

(ϕ,θ,ψ)	Wings coordinates and Euler angles				$(\mathbf{V_i})_{\mathcal{R}_E}(\Lambda_1)$	$(\mathbf{V_i})_{\mathcal{R}_E}(\Lambda_2)$
(17,32,86)	$[x_1, y_1, z_1]$	$(\phi_1, \theta_1, \psi_1)$	$[x_2, y_2, z_2]$	$(\phi_2, \theta_2, \psi_2)$	[-0.0029,0.0007,-0.0014]	[0.0013,0.0142,0.0162]
	[1,1,-1]	(0,0,0)	[-2,2,1]	(0,0,0)		
	$[X_1, Y_1, Z_1]$	$(\Phi_1, \Theta_1, \Psi_1)$	$[X_2, Y_2, Z_2]$	$(\Phi_2, \Theta_2, \Psi_2)$	[-0.0029,0.0007,-0.0014]	[0.0013,0.0142,0.0162]
	[-1.21,0.58,-1.09]	(17,32,86)	[-1.68,-0.76,2.37]	(17,32,86)		
(0,90,0)	$[x_1, y_1, z_1]$	$(\phi_1, \theta_1, \psi_1)$	$[x_2, y_2, z_2]$	$(\phi_2, \theta_2, \psi_2)$	[0.0023,-0.0013,-0.0036]	[0.0019,-0.0025,-0.0036]
	[0,0,0]	(0,0,90)	[-2,2,-1]	(0,0,0)		
	$[X_1, Y_1, Z_1]$	$(\Phi_1, \Theta_1, \Psi_1)$	$[X_2, Y_2, Z_2]$	$(\Phi_2, \Theta_2, \Psi_2)$	[0.0023,-0.0013,-0.0036]	[0.0019,-0.0025,-0.0036]
	[0,0,0]	(90,0,90)	[-1,2,2]	(0,90,0)		
(0,0,90)	$[x_1, y_1, z_1]$	$(\phi_1, \theta_1, \psi_1)$	$[x_2, y_2, z_2]$	$(\phi_2, \theta_2, \psi_2)$	[0.0048,0.0014,0.0014]	[-0.0004,-0.0190,-0.0169]
	[0,0,0]	(0,0,0)	[-2,2,-1]	(90,0,0)		
	$[X_1, Y_1, Z_1]$	$(\Phi_1, \Theta_1, \Psi_1)$	$[X_2, Y_2, Z_2]$	$(\Phi_2, \Theta_2, \Psi_2)$	[0.0048,0.0014,0.0014]	[-0.0004,-0.0190,-0.0169]
	[0,0,0]	(0,0,90)	[-2,-2,-1]	(90,0,90)		
(33,-45,18)	$[x_1, y_1, z_1]$	$(\phi_1, \theta_1, \psi_1)$	$[x_2, y_2, z_2]$	$(\phi_2, \theta_2, \psi_2)$	[0.0078,-0.0015,-0.0256]	[-0.0020,-0.0870,-0.0995]
	[0,0,0]	(10,10,10)	[-1,1,0]	(10,10,10)		
	$[X_1, Y_1, Z_1]$	$(\Phi_1, \Theta_1, \Psi_1)$	$[X_2, Y_2, Z_2]$	$(\Phi_2, \Theta_2, \Psi_2)$	[0.0078,-0.0015,-0.0256]	[-0.0020,-0.0870,-0.0995]
	[0,0,0]	(29.69,-40.44,36.22)	[-1.30,0.46,-0.32]	(29.69,-40.44,36.22)		

$$\forall k \in \{1, \ldots, n_{seg}\}, \quad \mathbf{G}(k) = \mathbf{G}(n_{seg} - k) \tag{5.8}$$

This is to be expected as the wing and its meshing are symmetric across the *xz*-plane. Furthermore, as Λ_1 is in the velocity field of no other vehicle, $\mathbf{V_i} = 0$.

For two air vehicles in formation, the symmetry accross the *xz*-plane is broken by the presence of Λ_2 on the side of Λ_1. Therefore, Equation 5.8 is not valid anymore.

In the cases reported in Table 5.4, Λ_2 is situated in the outer, and due to $\alpha \geq 0$, lower section of Λ_1's port trailing vortex, where it is subjected to forward-wash, port sidewash and upwash, as testified by the sign of $\mathbf{V_i}$ components. Likewise, as Λ_1 is influenced by the outer, higher section of Λ_2's starboard wake vortex, it is subjected to some backwash, port sidewash and upwash induced by Λ_2. Obviously, Λ_2 being behind Λ_1, the effects of Λ_2 on Λ_1 are much weaker than the effects of Λ_1 on Λ_2.

The components of **G** confirm this beneficial interaction: the absolute values of the components of **G** in Table 5.4 are higher than those of **G** in the case of one vehicle alone (see Table 5.2). As **G** is directly related to the production of lift, this means that the lift coefficients of Λ_1 and Λ_2 when in such a beneficial formation configuration are higher than the lift coefficient of Λ_1 alone.

As expected, this beneficial aerodynamic coupling decreases as the distance between Λ_1 and Λ_2 increases. For a large enough separation, the results of one wing only are recovered.

5.3.4 Influence of the Incoming Airflow

This subsection discusses the influence of the airdata (airspeed V, angle of attack α and angle of sideslip β) on the vorticity vector **G** of one air vehicle Λ. In order to simplify the analysis of the results, $n_{seg}(\Lambda)$ is taken equal to 1. Therefore, **G** is a scalar equal to the strength Γ of Λ's single horseshoe vortex.

The evolution of $\mathbf{G} = \Gamma$ with α, β and V is shown in Figures 5.1, 5.2 and 5.3 respectively.

According to the Kutta-Joukowski theorem (see Equation 3.8), the lift L generated on Λ is proportional to its airspeed V ($V = -V_\infty$) and to its vortex strength Γ. In addition,

Table 5.4: Vorticity and induced velocity vectors for two vehicles in formation

Coordinates		**G**		**V_i**	
Λ_1	Λ_2	Λ_1	Λ_2	Λ_1	Λ_2
		-0.7635	-0.7826		
0	-1	-0.9064	-0.9440	-0.0007	0.0231
0	-1	-0.9364	-1.0017	-0.0014	-0.1568
0	0	-0.9037	-1.0141	-0.0255	-0.2389
		-0.7591	-0.9264		
		-0.7545	-0.7600		
0	-2	-0.8970	-0.9052	-0.0001	0.0033
0	-2	-0.9279	-0.9387	-0.0003	-0.0072
0	0	-0.8967	-0.9099	-0.0053	-0.0323
		-0.7540	-0.7681		
		-0.7527	-0.7538		
0	-5	-0.8950	-0.8964	-0.0000	0.0005
0	-5	-0.9260	-0.9276	-0.0001	-0.0009
0	0	-0.8950	-0.8966	-0.0008	-0.0046
		-0.7527	-0.7542		
		-0.7524	-0.7525		
0	-20	-0.8947	-0.8948	$-0.0009 \cdot 10^{-3}$	$0.0295 \cdot 10^{-3}$
0	-20	-0.9257	-0.9258	$-0.0034 \cdot 10^{-3}$	$-0.0544 \cdot 10^{-3}$
0	0	-0.8947	-0.8948	$-0.0495 \cdot 10^{-3}$	$-0.2784 \cdot 10^{-3}$
		-0.7524	-0.7525		
		-0.7524	-0.7524		
0	-100	-0.8946	-0.8946	$-0.0004 \cdot 10^{-4}$	$0.0118 \cdot 10^{-4}$
0	-100	-0.9257	-0.9257	$-0.0014 \cdot 10^{-4}$	$-0.0217 \cdot 10^{-4}$
0	0	-0.8946	-0.8946	$-0.0197 \cdot 10^{-4}$	$-0.1111 \cdot 10^{-4}$
		-0.7524	-0.7524		

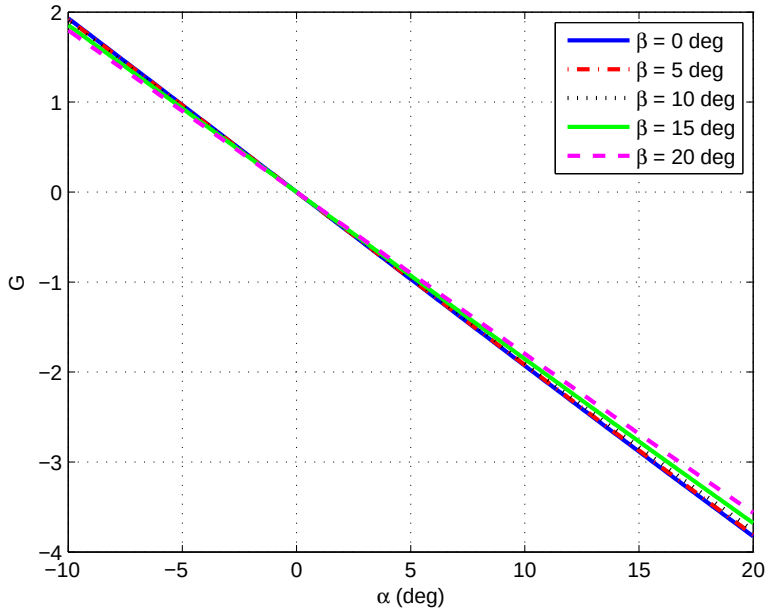

Figure 5.1: Evolution of the vorticity with the angle of attack – $V = 25$ m/s

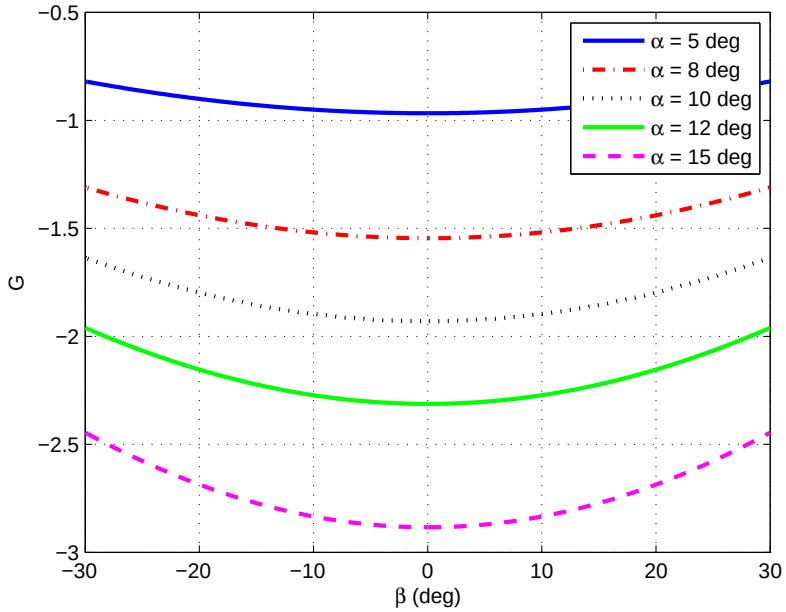

Figure 5.2: Evolution of the vorticity with the angle of sideslip – $V = 25$ m/s

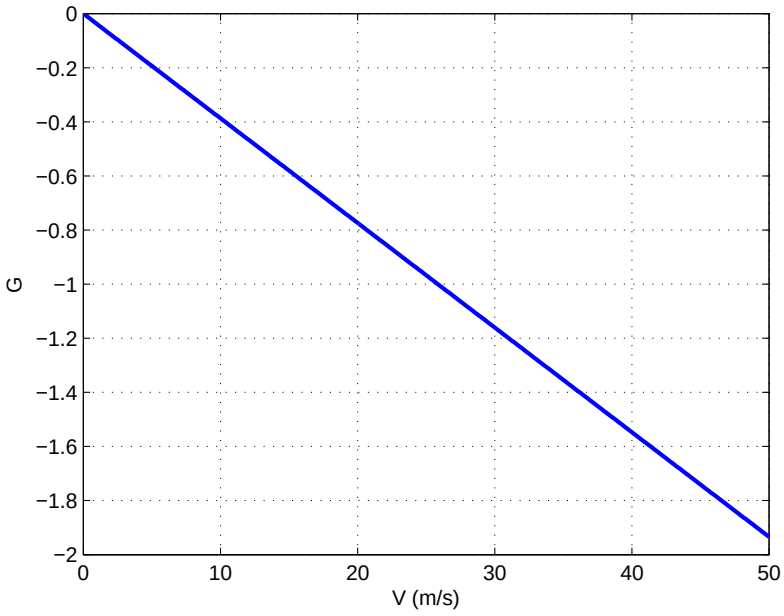

Figure 5.3: Evolution of the vorticity with the airspeed – $\alpha = 5$ deg, $\beta = 0$ deg

according to the definition of the lift coeffitient C_L, L can also be written as:

$$L = \frac{1}{2}\rho_\infty S V^2 C_L \tag{5.9}$$

where S is the reference area of Λ, and C_L is proportional to the angle of attack α. Therefore, **G** should be proportional to α and to V. This was verified in Figures 5.1 and 5.3 respectively.

In Figure 5.2, the symmetry of Λ across the xz-plane is recovered in the symmetry of **G** with β. Furthermore, $||\mathbf{G}||$ reaches its maximum when $\beta = 0$, i.e. more lift is produced when there is no sideslip. This result can also be observed in Figure 5.1 as the slope increases when $|\beta|$ decreases.

5.4 Validation of the Wake Vortex Model

This section presents the computational results obtained with ELL for two air vehicles flying in close formation at $V_0 = 19.8171$ m/s, $\alpha_0 = 8$ deg, and $\beta_0 = 0$ deg. The results, presented in the body axes of the following aircraft, are compared to wind-tunnel measurements [Blake and Gingras, 2004], to predictions from the planar vortex lattice

method HASC95 (with 540 panels used to model each aircraft: 36 in the spanwise direction and 15 in the chordwise direction) [Blake and Gingras, 2004], and to computational results obtained by Dogan, Venkataramanan and Blake [2005] using a modified Horseshoe Vortex Model (HVM). The effects of the wake generated by the upstream vehicle (referred to as the leader or Λ_1) upon the downstream vehicle (referred to as the follower or Λ_2) are analysed.

5.4.1 Test Configuration and Preliminary Observations

The test vehicles are two 1/13-scale Lockheed tailless aircraft models consisting of a 65 deg delta wing with a sawtooth trailing edge with sweep angles of 25 deg. For the wind-tunnel test, the inlets were blocked and both models were mounted in close proximity at an angle of attack of 8 deg relative to the freestream. The test configuration is illustrated in Figure 5.4.

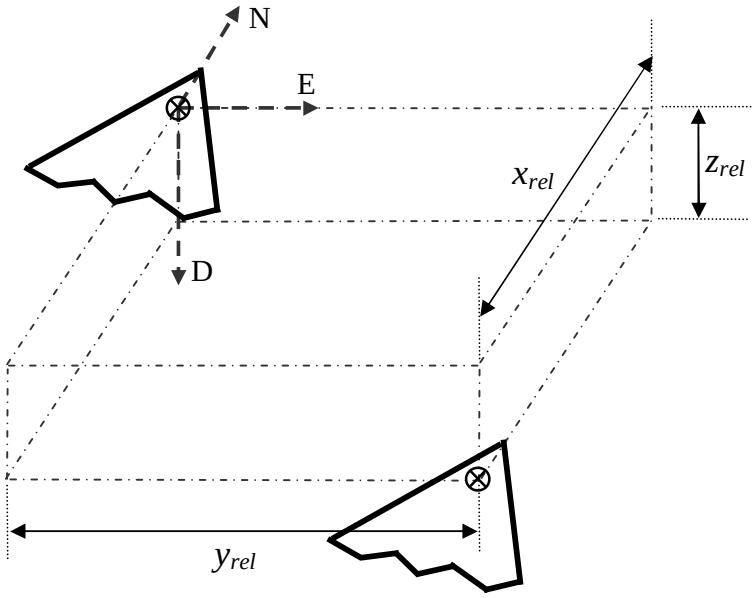

Figure 5.4: Test configuration

Such a configuration is similar to Case B in Figure 4.9, with $\alpha = \theta = 8$ deg.

The geometric parameters for both wings, as used in ELL, are described in Table 5.5. The parameters listed in Table 5.5 are defined in Subsection 4.3.3. The number of horseshoe vortices per wing (n_{seg}) was chosen equal to 10 following the discussion in Subsection 4.2.4.

Table 5.5: Test vehicle's geometric parameters – Validation

n_{seg}	b	λ	ε	φ	δ	α_0	ve	sym	$type$
10	0.8796 m	1.7394	0	58 deg	0 deg	0 deg	0 deg	1	0

As can be seen from Figure 5.5, the UAVs saw-tooth trailing edges cannot be properly modelled with ELL (due to the use of only one chordwise panel), and are therefore represented with a straight line.

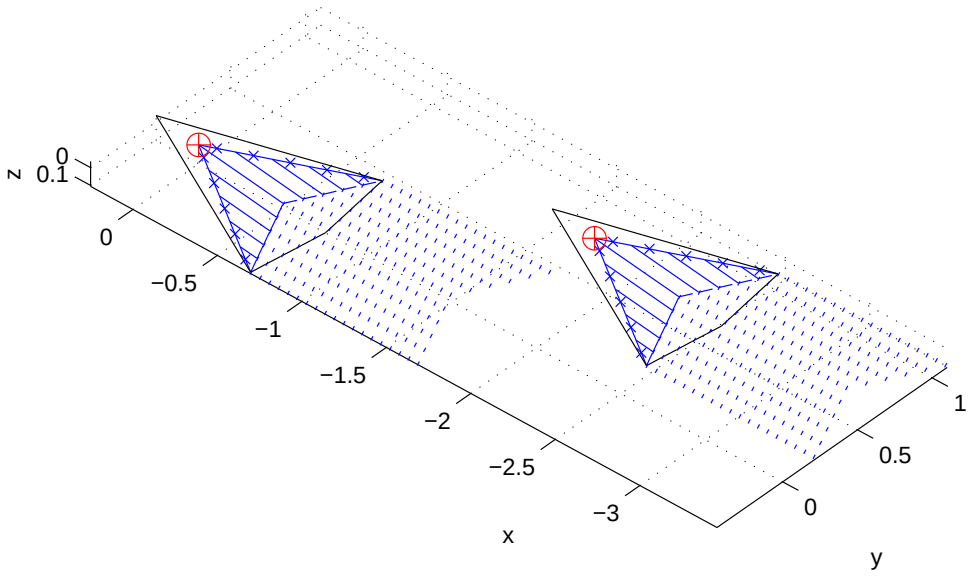

Figure 5.5: ELL: air vehicle geometry and vortex layout

HASC95 uses a flat wake approximation, i.e. the trailing legs of the horseshoe vortices extend downstream to infinity, parallel to the *xy* body plane, and do not vary with the angle of attack. In comparison, both Dogan's model and ELL represent the trailing legs of the horseshoe vortices as extending downstream to infinity, parallel to the freestream direction. The difference between Dogan's model and ELL mainly comes from the number of horseshoe vortices used to model the wing: Dogan uses only one horseshoe vortex, which only allows basic wing planforms to be represented, whereas ELL uses a variable number of horseshoe vortices, which allows a more accurate representation of the wing geometry. Typically, Dogan's model is only valid for untapered wings and the 65 deg delta wings used for wind tunnel testing were approximated as untapered

30-deg wings.

Besides, Dogan's horseshoe vortex is a 3-leg horseshoe vortex, whose trailing legs separate from the wing surface at the 1/4-chord line (i.e. where the bound vortex is attached to the wing), whereas ELL's horseshoe vortices follow the wing surface chordwise up to the 3/4-chord line before separating to extend downstream to infinity.

Another difference worth noting between Dogan's method and ELL concerns the modelling of the following UAV. Dogan uses a stick diagram composed of 4 sticks to represent the aircraft body: one along the x body axis representing the fuselage length, one along the z body axis representing the fuselage height, and finally two sticks representing each wing (with dihedral and sweep angles). In comparison, ELL uses the same wing discretisation model for all UAVs. As already mentioned, the motivation behind this choice is to facilitate the simulation of reconfiguration scenarios where each vehicle may have to fulfill both wake-generating and wake-encountering functions, depending on its position in the formation.

Finally, in order to take account of the fact that the moment generated about the CG of an air vehicle is all the greater as the application point of the generating force is further away (lever arm), Dogan, Venkataramanan and Blake [2005] uses a weighted averaging function for the calculation of the effective induced wind gradients. Such a function is not used in ELL, although it could easily be added if needed.

5.4.2 Effective Induced Wind Velocities

Due to the test vehicle geometry (high sweep and no dihedral), the $\partial/\partial z$ terms in the computation of the effective induced rotational wind velocity vector $\widetilde{\boldsymbol{\omega}}_{\mathbf{i}}$ were neglected and Equation 4.7 was rewritten as:

$$\widetilde{\boldsymbol{\omega}}_{\mathbf{i}}(\Lambda) = \begin{cases} \widetilde{\omega_{i_x}}(\Lambda) &= \dfrac{\widetilde{\partial V_{i_z}}}{\partial y}(\Lambda) \\ \widetilde{\omega_{i_y}}(\Lambda) &= -\dfrac{\widetilde{\partial V_{i_z}}}{\partial x}(\Lambda) \\ \widetilde{\omega_{i_z}}(\Lambda) &= \dfrac{\widetilde{\partial V_{i_y}}}{\partial x}(\Lambda) - \dfrac{\widetilde{\partial V_{i_x}}}{\partial y}(\Lambda) \end{cases} \tag{5.10}$$

The variations with lateral spacing of the incremental translational and rotational wind

velocities induced by Λ_1 on Λ_2 are shown in Figure 5.6. They are compared to Dogan's modified HVM results [Dogan, Venkataramanan and Blake, 2005]. As $\beta = 0$ deg, all plots are perfectly symmetric against y. The peak value of $\widetilde{V_{i_z}}$ is obtained when Λ_2 is lined up behind Λ_1: that is when the downwash originated from each wing-tip vortex combines with the same maximum intensity. At this point, it can be noticed that the effects of the wing-tip vortices on $\widetilde{V_{i_y}}$ are cancelling each other, as are the effects of the wing-tip vortices on the effective induced rotational wind velocities $\widetilde{\omega_{i_x}}$ and $\widetilde{\omega_{i_z}}$. Furthermore, the angle between Λ_1's trailing vortices and Λ_2's x body axis causes a slight backwash when Λ_2 is located in the downwash generated by Λ_1, and a slight forward-wash when Λ_2 is located in the upwash generated by Λ_1.

The differences between Dogan's modified HVM and ELL's estimates for the translational components come from the fact that Dogan's horseshoe vortices separate from the wing surface at its 1/4-chord line, whereas with ELL, the separation occurs at the wing 3/4-chord line. As a consequence, the vortices are positioned higher relatively to Λ_2 in Dogan's case than in our case. Λ_2 moves along the $z = 0$ line, which, in Dogan's case, corresponds to the centre-line of the vortex, whence the higher upwash and downwash experienced. In our case, the $z = 0$ line crosses the vortex in its upper part, where the sidewash is stronger. Also, a difference is to be noted in the forward-wash. This is due to the fact that in Dogan's case, the effects of Λ_1 upon Λ_2 are integrated over Λ_2's whole body length, whereas in our case they are only integrated along the 1/4-chord line of its wings. As a consequence, the overall offset between Λ_2 and Λ_1's 1/4-chord line bound vortex (responsible for the back/forward-wash) is higher in Dogan's case than in our case, thereby inducing a stronger forward-wash effect.

Likewise, the difference between Dogan's modified HVM and ELL's estimates for the rotational components stem from the differences in the estimation of the translational components, and from Dogan's use of a weighted averaging function for the calculation of the wind gradients induced by Λ_1 on Λ_2.

The variations with longitudinal spacing of the incremental translational and rotational wind velocities induced by Λ_1 on Λ_2 are shown in Figure 5.7. Λ_2 being situated starboard ($y_{rel} \geq 0$) and below ($z_{rel} \geq 0$) Λ_1, it is – as expected – subjected to starboard sidewash ($\widetilde{V_{i_y}} \geq 0$) and upwash ($\widetilde{V_{i_z}} \leq 0$). The presence of the vortex decay can be seen from the fact that all the induced velocities slowly tend to zero when the longitudinal distance between Λ_1 and Λ_2 increases. The "bumps" in $\widetilde{V_{i_x}}$ and $\widetilde{V_{i_z}}$ around $x/b = 0$ are due to the effects of Λ_1's 1/4-chord line bound vortex as Λ_2 passes just above it. Finally, $x \geq 0$ corresponds to Λ_2 being in front of Λ_1, where it is subjected to almost

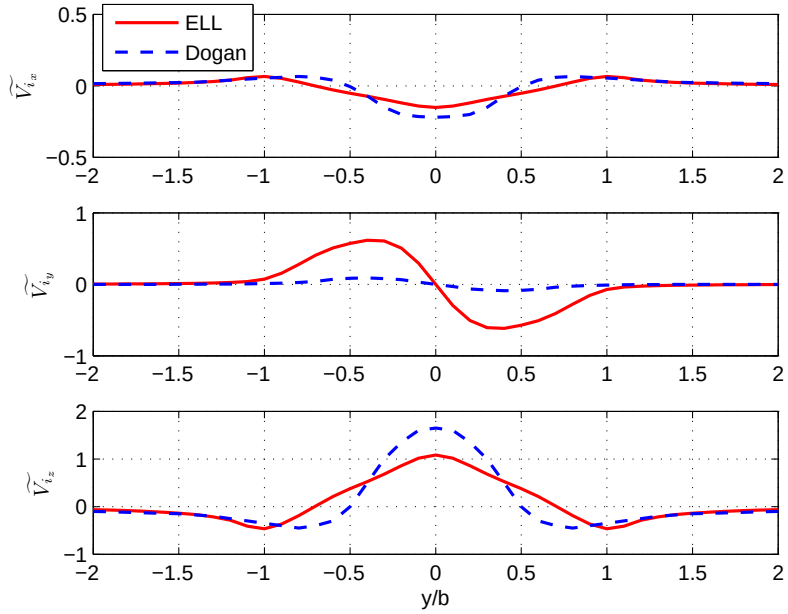

(a) Translational components (m/s)

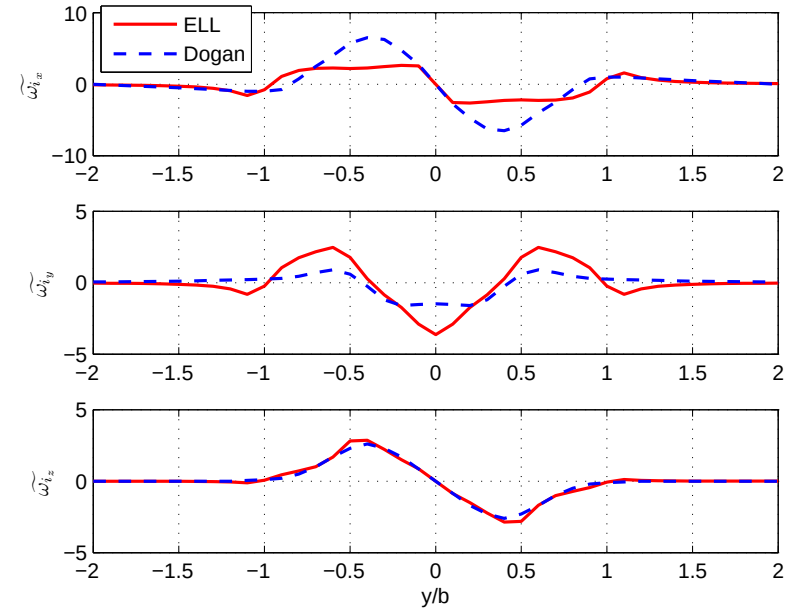

(b) Rotational components (deg/s)

Figure 5.6: Variations of the effective induced wind velocity with lateral spacing – $x_{rel} = -2b$, $z_{rel} = 0$

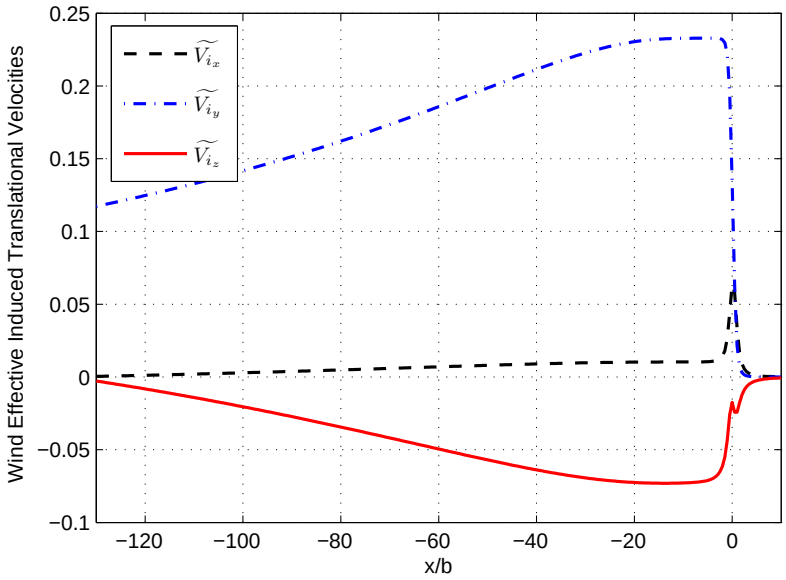

(a) Translational components (m/s)

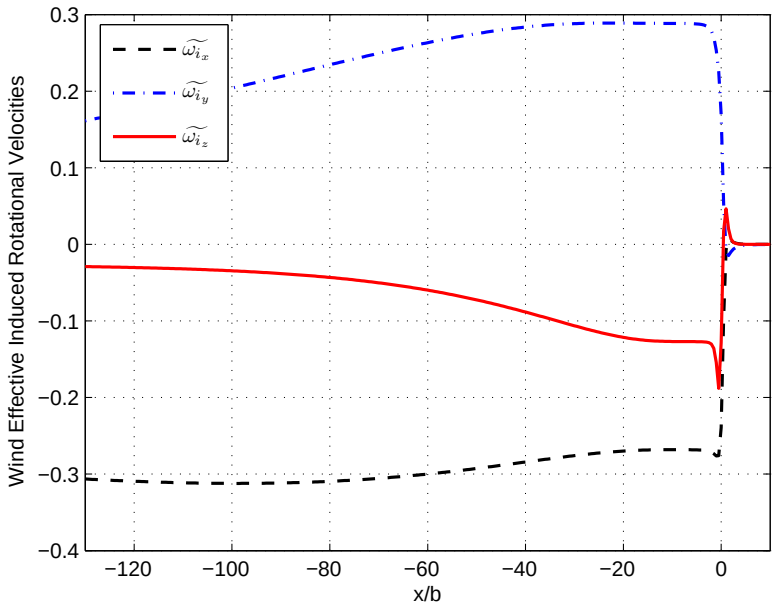

(b) Rotational components (deg/s)

Figure 5.7: Variations of the effective induced wind velocity with longitudinal spacing $-\ y_{rel} = b, z_{rel} = b/2$

no influence from Λ_1.

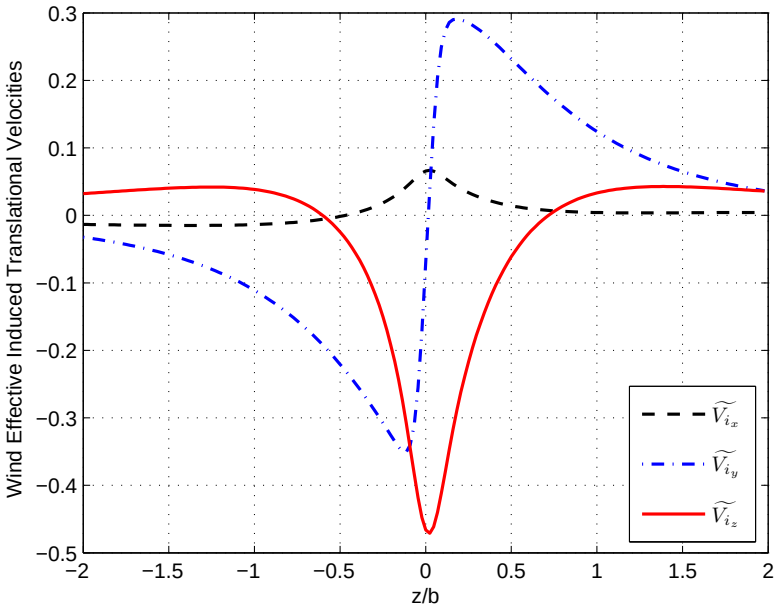

(a) Translational components (m/s)

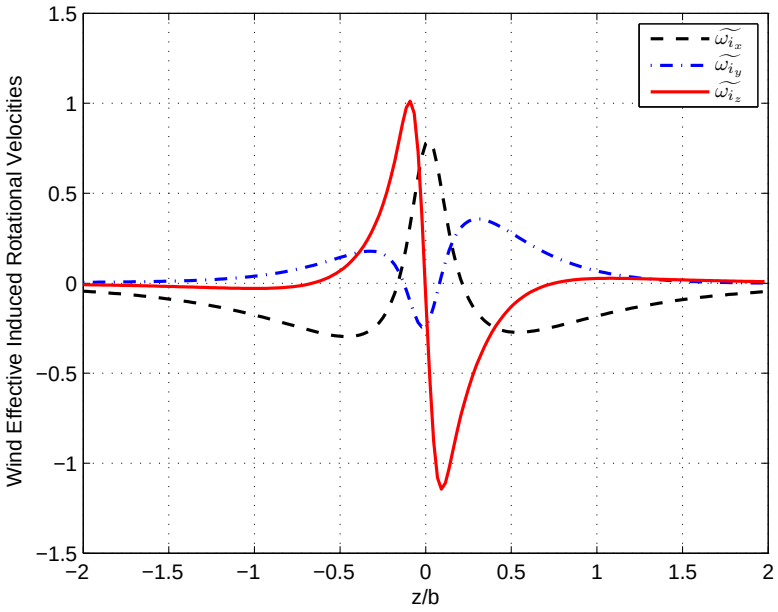

(b) Rotational components (deg/s)

Figure 5.8: Variations of the effective induced wind velocity with vertical spacing – $x_{rel} = -2b, y_{rel} = b$

The variations with vertical spacing of the incremental translational and rotational wind velocities induced by Λ_1 on Λ_2 are shown in Figure 5.8. The follower is situated starboard ($y_{rel} \geq 0$) and behind ($x_{rel} \leq 0$) the leader. Consequently, it is subjected to port sidewash ($\widetilde{V_{i_y}} \leq 0$) when above the wake, to starboard sidewash ($\widetilde{V_{i_y}} \geq 0$) when below the wake, and to upwash ($\widetilde{V_{i_z}} \leq 0$) and forward-wash ($\widetilde{V_{i_x}} \geq 0$) when near the wake ($z \simeq 0$). The slight asymmetry between $z/b \leq 0$ and $z/b \geq 0$ and the reason why the plots look slightly shifted towards $z/b \leq 0$ is because the wake vortex sheet is not symmetric against z. This is due to the fact that it separates from Λ_1 at its 3/4-chord, which, for $\alpha = 8$ deg, is situated below the line $z = 0$, i.e. at $z \geq 0$. The peak value of $\widetilde{V_{i_z}}$ is obtained when Λ_2 is at the same level as Λ_1's wake vortex sheet. That is also when the peak value of $\widetilde{V_{i_x}}$ is reached and when $V_{i_y}(z)$ suddenly changes direction, leading to a steep change of sign in $\widetilde{V_{i_y}}$ and an abrupt in $\widetilde{\omega_{i_y}}$.

5.4.3 Incremental Aerodynamic Forces and Moments Coefficients

As literature data sets are usually provided in terms of induced forces and moments coefficients, these were computed from the induced velocity field obtained with ELL, and compared to wind tunnel tests measurements [Blake and Gingras, 2004], HASC95 computational results [Blake and Gingras, 2004], and Dogan's results [Dogan, Venkataramanan and Blake, 2005].

Computation from the Induced Wind Velocity and Induced Body Rates

The build-up equations used for direct computation of the aerodynamic force and moment coefficients from the induced wind velocity and induced body rates are those used by Dogan, Venkataramanan and Blake [2005]:

$$C_D = C_{D_0} + \frac{\partial^2 C_D}{\partial \alpha^2}\alpha^2 \tag{5.11}$$

$$C_L = C_{L_0} + C_{L_\alpha}\alpha + C_{L_q}\left(\frac{qc}{2V}\right) \tag{5.12}$$

$$C_{LL} = C_{LL_0} + \left(C_{LL_{\beta_0}} + \frac{\partial C_{LL_\beta}}{\partial \alpha}\alpha\right)\beta + C_{LL_p}\left(\frac{pb}{2V}\right) + \left(C_{LL_{r_0}} + \frac{\partial C_{LL_r}}{\partial \alpha}\alpha\right)\left(\frac{rb}{2V}\right) \tag{5.13}$$

$$C_M = C_{M_0} + C_{M_\alpha}\alpha + C_{M_q}\left(\frac{qc}{2V}\right) \tag{5.14}$$

where V is the vehicle's airspeed, (p, q, r) its angular rates, α its angle of attack, and β its angle of sideslip.

In the case of one vehicle only, the vehicle's airspeed V_1, angular rates (p_1, q_1, r_1), angle of attack α_1 and angle of sideslip β_1 are defined as follows (in $\mathcal{R}_b$):

$$V_1 = \|\mathbf{V_1}\| = V_0 \cdot \left\| \begin{pmatrix} -\cos(\alpha_0)\cos(\beta_0) \\ -\sin(\beta_0) \\ -\sin(\alpha_0)\cos(\beta_0) \end{pmatrix} \right\| = V_0 \tag{5.15}$$

$$\begin{bmatrix} p_1 \\ q_1 \\ r_1 \end{bmatrix} = \begin{bmatrix} 0 \\ 0 \\ 0 \end{bmatrix} \tag{5.16}$$

$$\alpha_1 = \operatorname{atan}\left(\frac{V_{1_z}}{V_{1_x}}\right) = 0 \tag{5.17}$$

$$\beta_1 = \operatorname{asin}\left(\frac{V_{1_y}}{\|\mathbf{V_1}\|}\right) = 0 \tag{5.18}$$

In the case of both vehicles in formation, the airspeed V_2, angular rates (p_2, q_2, r_2), angle of attack α_2 and angle of sideslip β_2 of the follower are defined as follows (in $\mathcal{R}_b$):

$$V_2 = \|\mathbf{V_2}\| = \|\mathbf{V_1} - \mathbf{DCM_{be}} \cdot \widetilde{\mathbf{V_{i,2}}}\| \tag{5.19}$$

$$\begin{bmatrix} p_2 \\ q_2 \\ r_2 \end{bmatrix} = -\mathbf{DCM_{be}} \cdot \widetilde{\boldsymbol{\omega}_{\mathbf{i,2}}} \tag{5.20}$$

$$\alpha_2 = \operatorname{atan}\left(\frac{V_{2_z}}{V_{2_x}}\right) \tag{5.21}$$

$$\beta_2 = \operatorname{asin}\left(\frac{V_{2_y}}{\|V_2\|}\right) \tag{5.22}$$

where $\widetilde{\mathbf{V_{i,2}}}$ and $\widetilde{\boldsymbol{\omega}_{\mathbf{i,2}}}$ are the effective translational and rotational velocities induced by Λ_1 on Λ_2.

Whence the build-up equations for the incremental aerodynamic coefficients:

$$\Delta C_D = \frac{\partial^2 C_D}{\partial \alpha^2}\left({\alpha_2}^2 - {\alpha_1}^2\right) \tag{5.23}$$

$$\Delta C_L = C_{L_\alpha}(\alpha_2 - \alpha_1) + C_{L_q}\left(\frac{q_2 c}{2V_2}\right) \tag{5.24}$$

$$\Delta C_{LL} = C_{LL_{\beta_0}}(\beta_2 - \beta_1) + \frac{\partial C_{LL_\beta}}{\partial \alpha}\alpha_2\beta_2 - \frac{\partial C_{LL_\beta}}{\partial \alpha}\alpha_1\beta_1 + C_{LL_p}\left(\frac{p_2 b}{2V_2}\right) + \left(C_{LL_{r_0}} + \frac{\partial C_{LL_r}}{\partial \alpha}(\alpha_2 - \alpha_1)\right)\left(\frac{r_2 b}{2V_2}\right) \quad (5.25)$$

$$\Delta C_M = C_{M_\alpha}(\alpha_2 - \alpha_1) + C_{M_q}\left(\frac{q_2 c}{2V_2}\right) \quad (5.26)$$

Incremental Lift Coefficient, ΔC_L

The variations of the incremental lift coefficient with lateral and vertical spacing are shown in Figures 5.9 and 5.10 respectively. On both plots, ELL results are very close to HASC95 results, with HASC95 using 540 calculation panels on each vehicle and ELL using only 10.

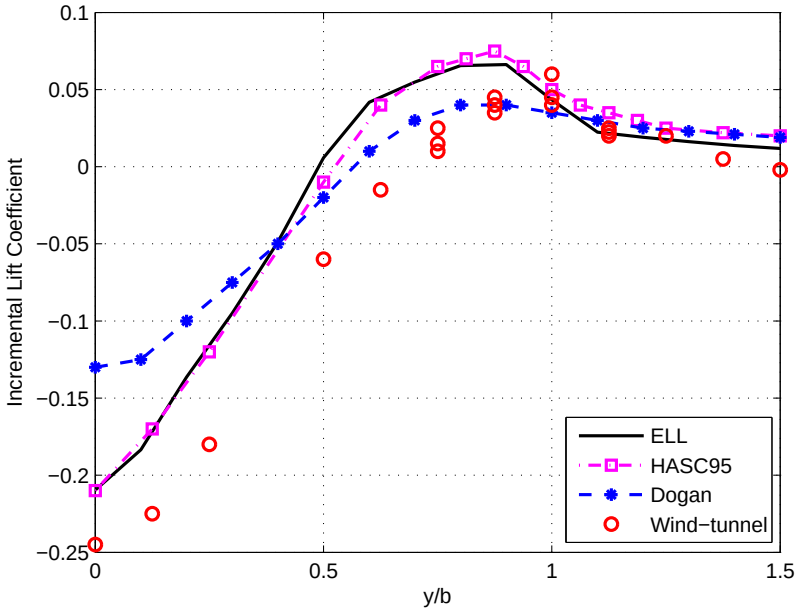

Figure 5.9: Variations of the incremental lift coefficient with lateral spacing – $x_{rel} = -2b$, $z_{rel} = 0$

From Figure 5.9, it can be seen that the maximum lift loss is encountered when Λ_2 is positioned directly behind Λ_1, i.e. when the induced downwash is maximum. As Λ_2 moves sideways, the downwash intensity decreases (i.e. the incremental lift coefficient

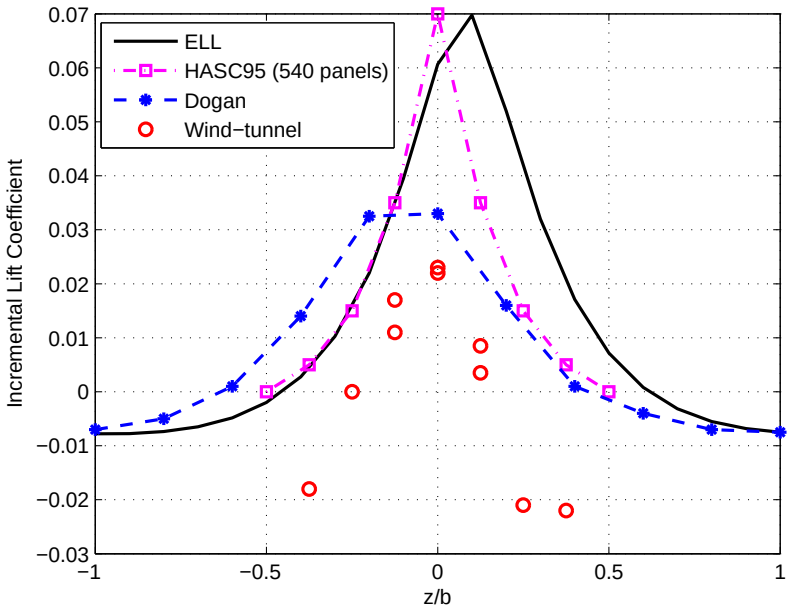

Figure 5.10: Variations of the incremental lift coefficient with vertical spacing – $x_{rel} = -2b$, $y_{rel} = 0.75b$

increases), and upwash is encountered as Λ_2 passes Λ_1's wing tip. The maximum upwash is encountered at $y \simeq 0.8b$, which is consistent with the optimum lateral spacing for formation flight [Blake, 2000]. As Λ_2 keeps on moving outboard of Λ_1, the effect fades away and the incremental lift coefficient tends to zero.

Figure 5.10 shows the vertical variations of the wake-induced lift coefficient for $y = 0.75b$, i.e for a lateral spacing close to the optimal one. It shows a maximum upwash for $z \approx 0.1b$, i.e. when Λ_2 is aligned behind Λ_1's wake – which happens when Λ_2's quarter-chord line is aligned with Λ_1's three-charter-chord line. This result is also consistent with the "sweet spot" position determined by Blake [2000]. The maximum wake-induced lift increment is over-estimated, but the trend is well predicted.

Incremental Drag Coefficient, ΔC_D

The variations of the incremental drag coefficient with lateral and vertical spacing are shown in Figures 5.11 and 5.12 respectively. In both cases, a good match is found between ELL's predictions and the wind-tunnel measurements.

Both ELL's predictions and the wind tunnel measurements show that the maximum

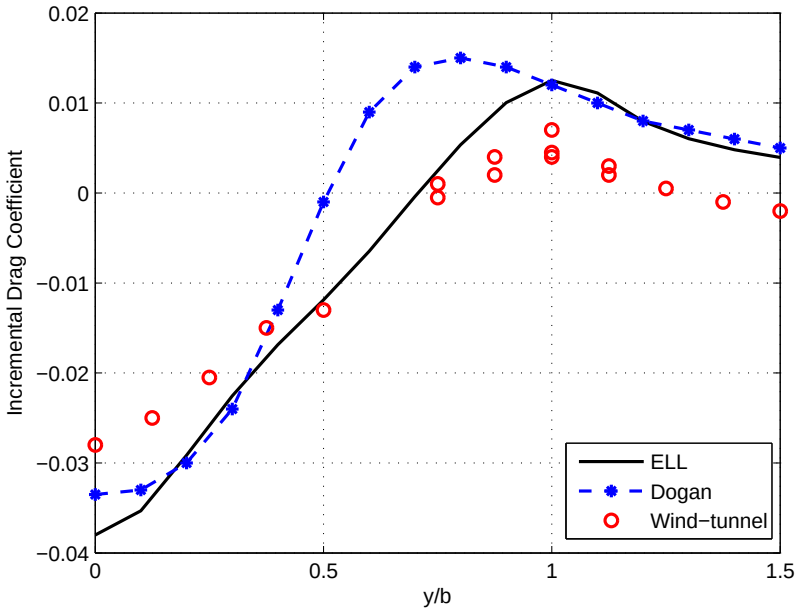

Figure 5.11: Variations of the incremental drag coefficient with lateral spacing – $x_{rel} = -2b$, $z_{rel} = 0$

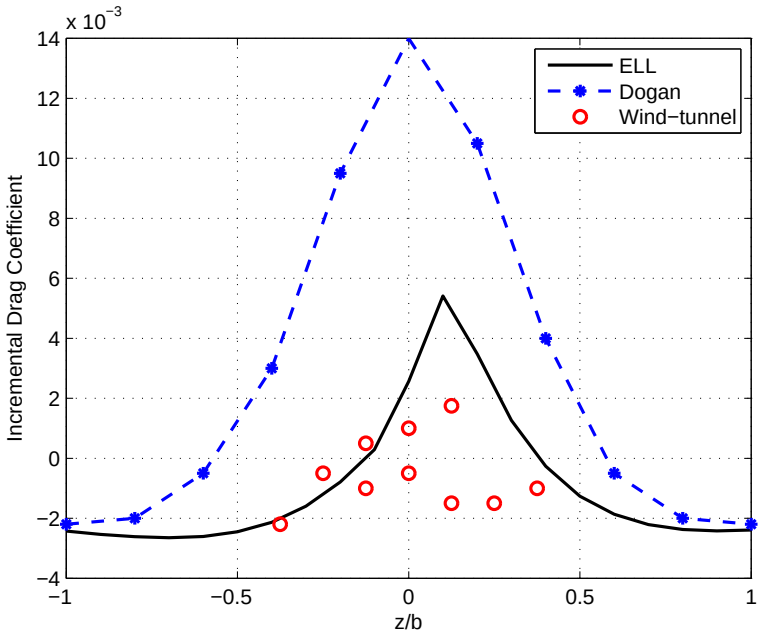

Figure 5.12: Variations of the incremental drag coefficient with vertical spacing – $x_{rel} = -2b$, $y_{rel} = 0.75b$

wake-induced drag increment is obtained for $|y/b| = 1$ and $z/b \approx 0.1$, i.e. when Λ_2 is aligned with Λ_1's wing tip vortices. This peak in incremental lift-induced drag is caused by the peak in incremental lift shown in Figures 5.11 and 5.12. Furthermore, similarly to Dogan's estimates, the peak values given by ELL are slightly over-predicted.

Incremental Rolling Moment Coefficient, ΔC_{LL}

The variations of the incremental rolling moment coefficient with lateral and vertical spacing are shown in Figures 5.13 and 5.14 respectively. The induced rolling moment is the largest vortex-induced effect and the most critical for flight safety, therefore it should be accurately predicted; according to Blake and Gingras [2004], a maximum (30 deg) elevon deflection gives a rolling moment increment of -0.022, so the effect of Λ_1 upon Λ_2 is similar to a full control deflection. This result confirms the importance of wake-induced effects in close formation flight and the necessity to include them within simulation models.

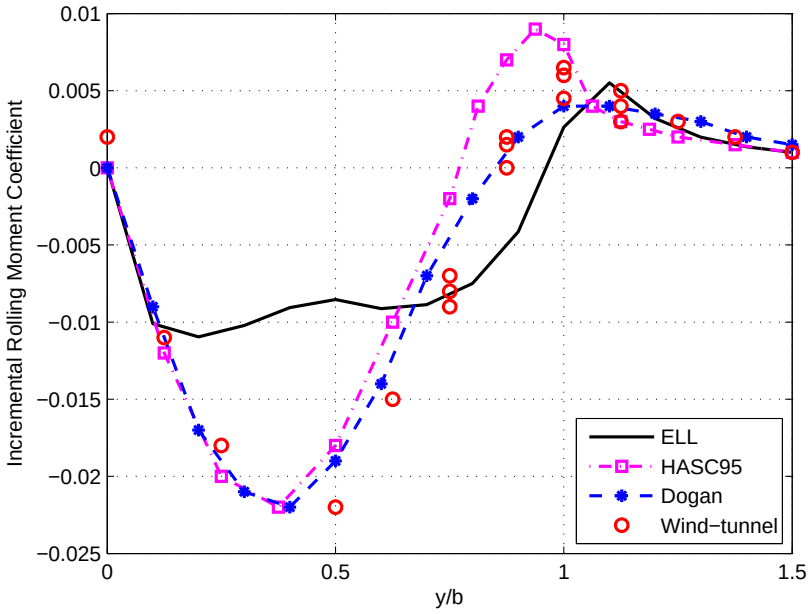

Figure 5.13: Variations of the incremental rolling moment coefficient with lateral spacing – $x_{rel} = -2b$, $z_{rel} = 0$

As can be seen from Figure 5.13, the variations of the incremental rolling moment coefficient with lateral spacing are reasonably well predicted for $|y/b| \leq 0.1$ and $|y/b| \geq 1$. For $0.1 < |y/b| < 1$, the match with wind tunnel data is acceptable, although not as ac-

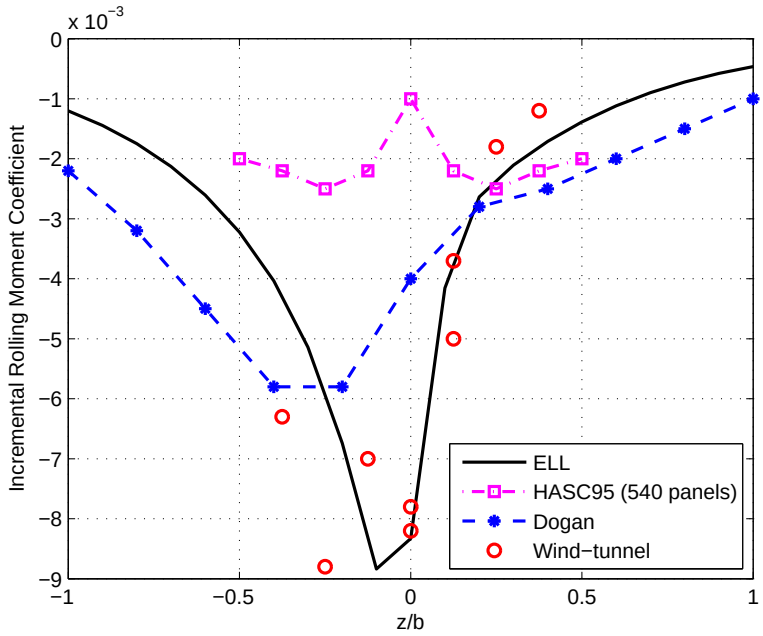

Figure 5.14: Variations of the incremental rolling moment coefficient with vertical spacing – $x_{rel} = -2b$, $y_{rel} = 0.75b$

curate as the estimates obtained by Dogan or with HASC95: the peak is larger, flatter, and its magnitude is under-estimated; furthermore, the incremental rolling moment coefficient slightly increases around $|y/b| \approx 0.5$, causing a small upward "bump". These differences can be explained by taking the following elements into account:

(i) ELL uses a larger viscous core than the other codes, where the vortex swirl is distributed over a wider radius, hence the width and flatness of the peak;

(ii) unlike HASC95, ELL meshes the wings using only 1 chordwise panel, hence a lack of precision;

(iii) unlike Dogan's method, ELL uses no weighted averaging function in the computation of the effective rotational induced wind components;

(iv) finally, the space between Dogan's trailing vortices is taken as $b \cdot \pi/4$ (i.e smaller), whereas ELL considers it to be equal to b (i.e. larger).

Because of points (iii) and (iv), there exists a zone where the differential downwash between both wing-tips is lessened, causing a weaker rolling moment to be generated. This zone is situated between the strong downwash area caused by the proximity of the wing-tip vortex core ($|y/b| \approx 1$) and the strong downwash area due to the combination of downwashes caused by both starboard and port wing-tip vortices ($|y/b| \approx 0$), i.e. at

$|y/b| \approx 0.5$.

A good match is found between the variations of the incremental rolling moment coefficient with vertical spacing as predicted by ELL (see Figure 5.14) and the wind-tunnel measurements.

Pitching Moment Coefficient, ΔC_M

The variations of the incremental pitching moment coefficient with lateral and vertical spacing are shown in Figures 5.15 and 5.16 respectively. In the specific case of highly swept wings, the control points are distributed along the x-axis as well as the y-axis, which enables the pitching moment coefficient to be estimated by ELL.

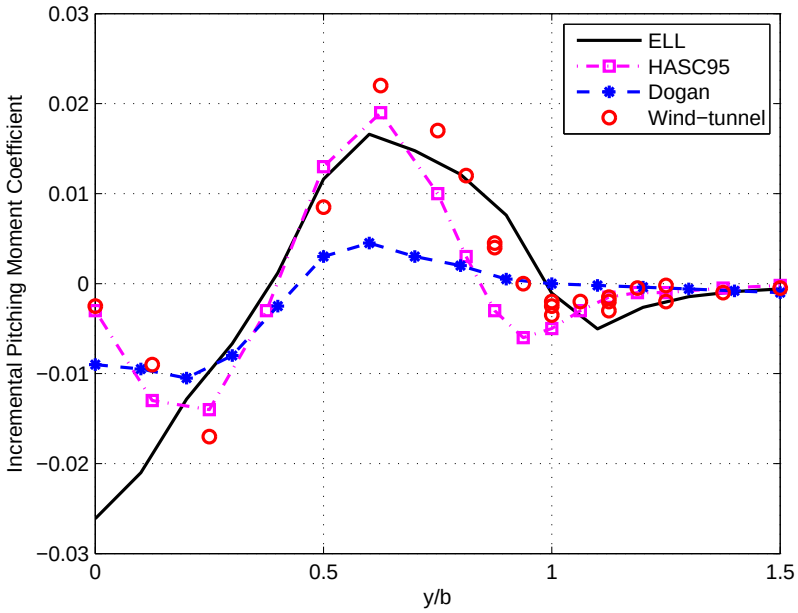

Figure 5.15: Variations of the incremental pitching moment coefficient with lateral spacing – $x_{rel} = -2b$, $z_{rel} = 0$

Again, ELL's predictions are in good agreement with the wind-tunnel measurements. However, a slight difference can be observed in the variations of the incremental pitching moment coefficient with lateral spacing (see Figure 5.15) for $|y/b| \leq 0.3$. This can be explained by the fact that ELL meshes the wing in the spanwise direction only, unlike HASC95 which also includes chordwise panels, and Dogan's method which uses a stick diagram representation of the air vehicle. Therefore, ELL's estimates of the pitch-

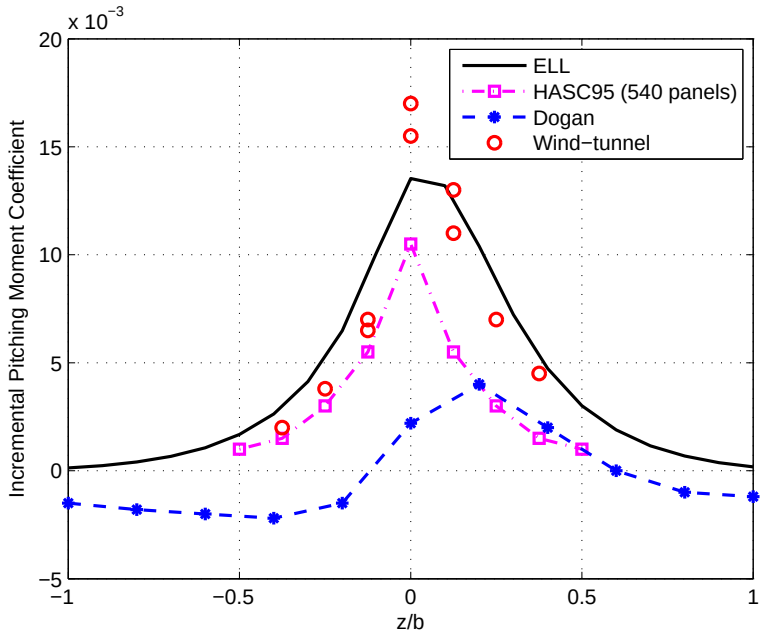

Figure 5.16: Variations of the incremental pitching moment coefficient with vertical spacing – $x_{rel} = -2b$, $y_{rel} = 0.75b$

ing moment coefficient are not as accurate as they would be if more control points were used along the x-axis.

Finally, as in Figures 5.10 and 5.12, the maximum pitching moment coefficient increment is reached for $z \approx 0.1b$ due to the fact that the wake separates from the wing at its three-quarter-chord line rather than its quarter-chord line.

5.4.4 Computational Time

For 2 UAVs, the total time taken by an Intel(R) Xeon(R) CPU E5410 @ 2.33GHz, 2.00GB of RAM to model the wings and to compute the induced velocity field generated by one air vehicle upon the other is: $\simeq$ 0.015 s for 4 discretisation segments per wing; $\simeq$ 0.029 s for 6 discretisation segments per wing; $\simeq$ 0.072 s for 10 discretisation segments per wing. Consequently the rapidity of execution is sufficient for the model to be used in near real-time simulations.

5.5 Chapter Summary and Conclusions

ELL was satisfactorily verified and its results compared satisfactorily with the published data. It is to be noted that the aim of ELL is not to get a perfect match, but to obtain a match which is good enough to predict the qualitative, and to some extent, the quantitative effects of aerodynamic interactions between air vehicles flying in close proximity, using a fast and efficient method. In that sense, the ELL method presents numerous advantages, including its simplicity, modularity, transparency (which makes it a more flexible method), and real-time benefits.

Chapter 6

Simulation of Wake Vortex Effects for UAVs in Close Formation Flight

6.1 Introduction

A Simulink Aerosonde model was derived based on that provided in the Unmanned Dynamics AeroSim Blockset *Unmanned Dynamics Aerosim Blockset Official Website: http://www.u-dynamics.com/aerosim/* [N.d.], and adapted for use with the Mathworks Aerospace Blockset. The airframe model was trimmed, linearised, augmented, and a control scheme (attitude hold, velocity hold, altitude hold, and heading hold) was developed for trajectory tracking using PID control (see Appendix A). The Aerosonde UAV is presented in Section 6.2. A comparative analysis is performed in Section 6.3 in order to determine whether the tailplane should be taken into account in the computation of the wake-induced effects. Section 6.4 demonstrates the FCS capabilities through the analysis of the Aerosonde response to a transient wind gust. A simulation of two Aerosonde models flying in close formation along a pre-determined path was then performed to test the WVM. The leader is referred to as Λ_1, and the follower as Λ_2. Sections 6.5 and 6.6 present the simulation results obtained for, respectively, a formation keeping and a formation reconfiguration scenario.

6.2 Aerosonde UAV

The Aerosonde (see Figure 6.1) is a small UAV, which is mainly used for long-range weather data acquisition missions over oceanic and remote areas in harsh conditions. It rose to fame in August 1998, when it became the first UAV to cross the North Atlantic, after a 26 hr 45 min long autonomous flight [Niculescu, 2001].

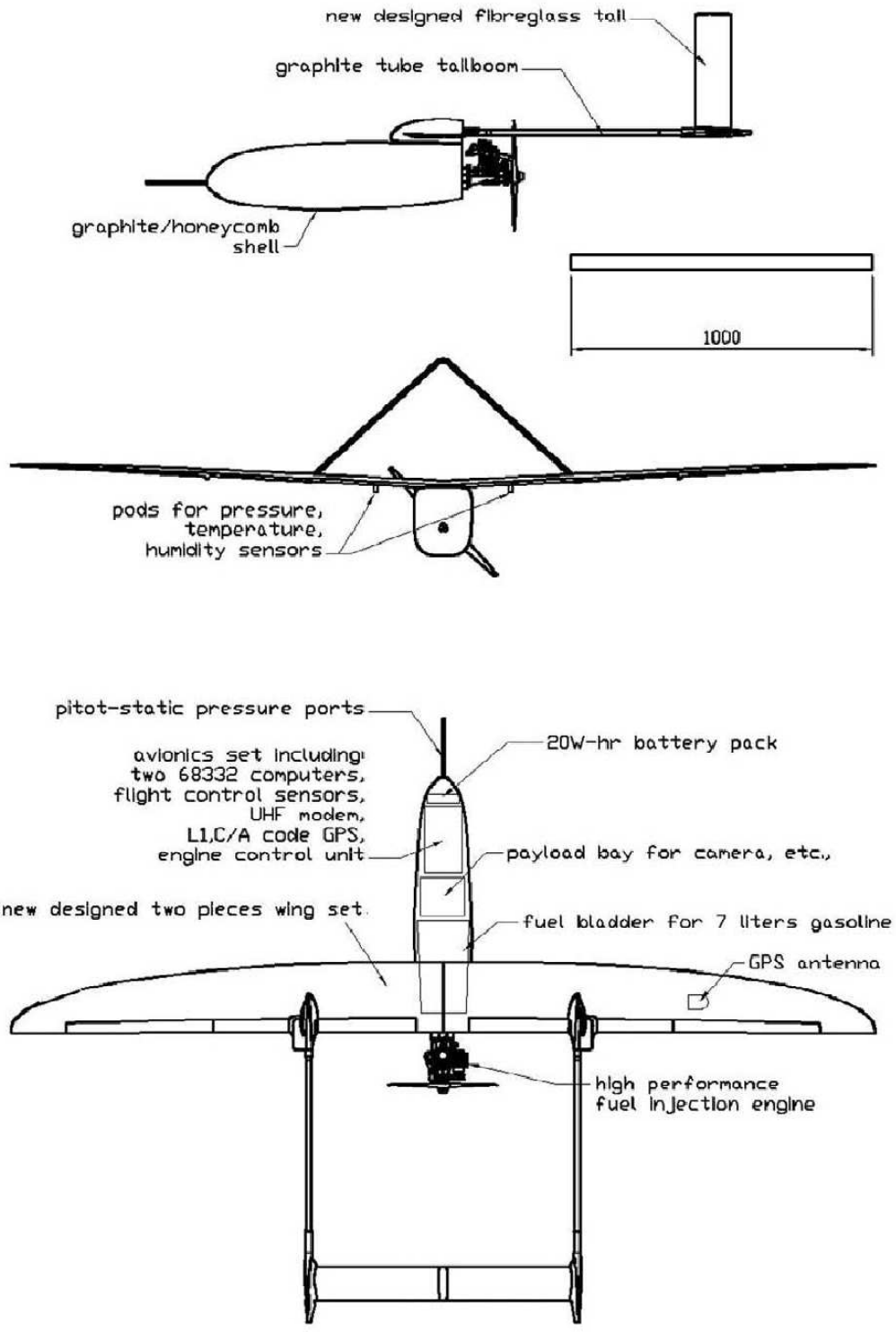

Figure 6.1: Aerosonde UAV (from Callus [2008])

The Aerosonde geometric parameters as used by ELL to calculate the wake vortex induced effects are listed in Table 6.1 and illustrated in Figure 6.2.

Table 6.1: Aerosonde's geometric parameters as used by ELL

	n_{seg}	b	λ	ε	φ	δ	α_0	ve	sym	$type$
Wing	10	2.9 m	15	0.4	4 deg	3 deg	0 deg	0 deg	1	0
Tailplane	10	1.1 m	7.8	1	0 deg	-43 deg	0 deg	0 deg	1	0

6.3 Should the Tailplane be Taken Into Account in the Computation of the Wake-Induced Effects?

In order to determine whether the tailplane should be taken into account in the computation of the wake-induced effects, the effective translational and rotational velocities induced by one Aerosonde UAV (the leader, referred to as Λ_1) on another Aerosonde UAV (the follower, referred to as Λ_2) when flying in formation were calculated: (i) considering their wings only; (ii) considering both their wings and their tailplanes. The velocity parameters and Euler angles of both vehicles are taken equal to: $V = 25$ m/s, $\alpha = 3$ deg, $\beta = 0$ deg, $\phi = 0$ deg, $\theta = 3$ deg and $\psi = 0$ deg.

The results are presented and compared in Figures 6.3, 6.5 and 6.6. It is to be noted that due to the Aerosonde geometry (no sweep and very little dihedral), the $\partial/\partial x$ and $\partial/\partial z$ terms in the computation of the effective induced rotational wind velocity vector $\widetilde{\boldsymbol{\omega}}_{\mathbf{i}}$ were neglected and Equation 4.7 was rewritten as:

$$\widetilde{\boldsymbol{\omega}}_{\boldsymbol{i}}(\Lambda) = \begin{cases} \widetilde{\omega_{i_x}}(\Lambda) &= \dfrac{\partial \widetilde{V_{i_z}}}{\partial y}(\Lambda) \\ \widetilde{\omega_{i_y}}(\Lambda) &= 0 \\ \widetilde{\omega_{i_z}}(\Lambda) &= -\dfrac{\partial \widetilde{V_{i_x}}}{\partial y}(\Lambda) \end{cases} \tag{6.1}$$

Figure 6.3 shows the variations of $\widetilde{\mathbf{V}}_{\mathbf{i}}$ and $\widetilde{\boldsymbol{\omega}}_{\mathbf{i}}$ components with longitudinal spacing for $y_{rel} = b$ and $z_{rel} = b/2$, i.e. for Λ_2 below and starboard of Λ_1. The rotational wind velocity induced by Λ_1 on Λ_2 is very similar for both configurations (wing only and wing + tailplane). However, there are some differences in the components of the effective induced translational wind velocity: although the general trend for each of these

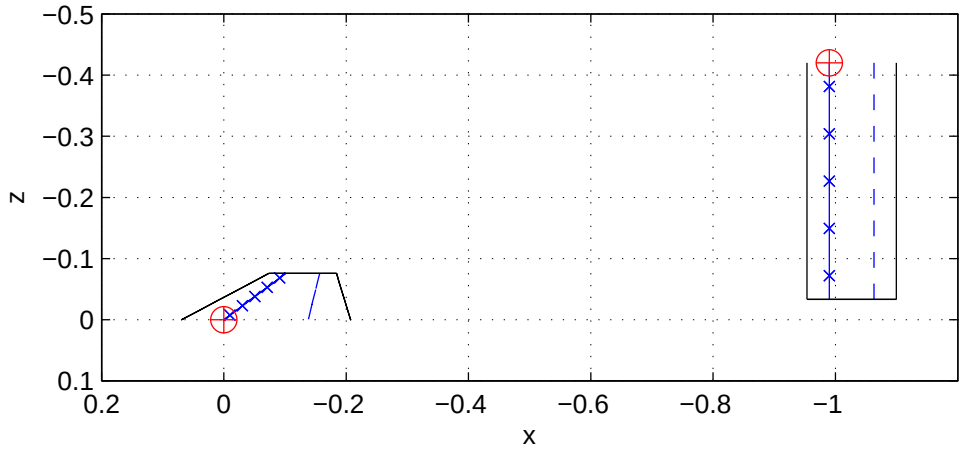

(a) Side View

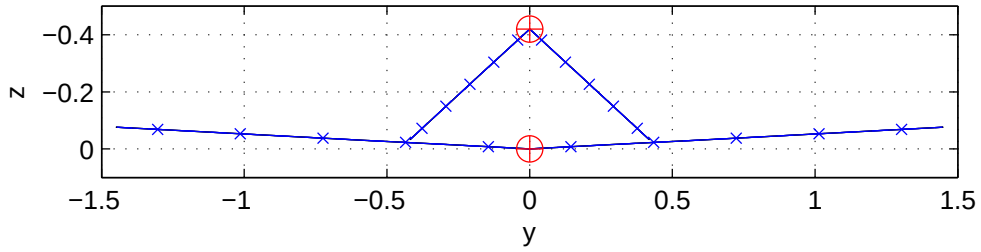

(b) Rear View

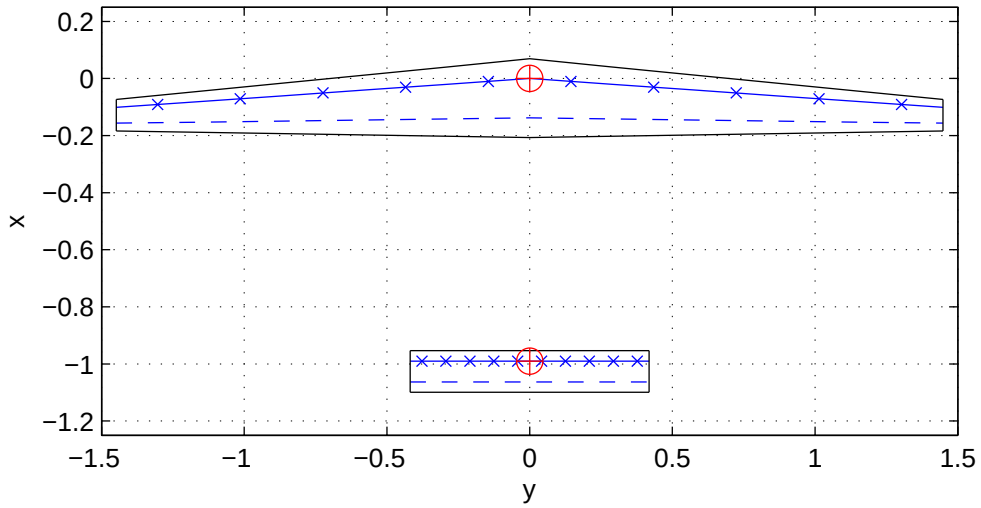

(c) Top View

Figure 6.2: ELL Aerosonde model

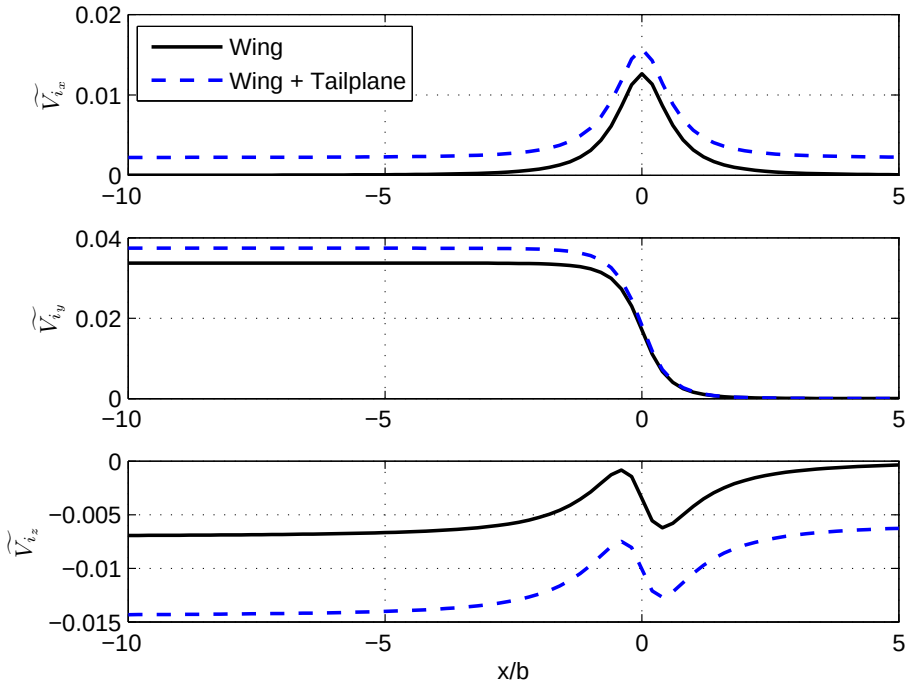

(a) Translational components (m/s)

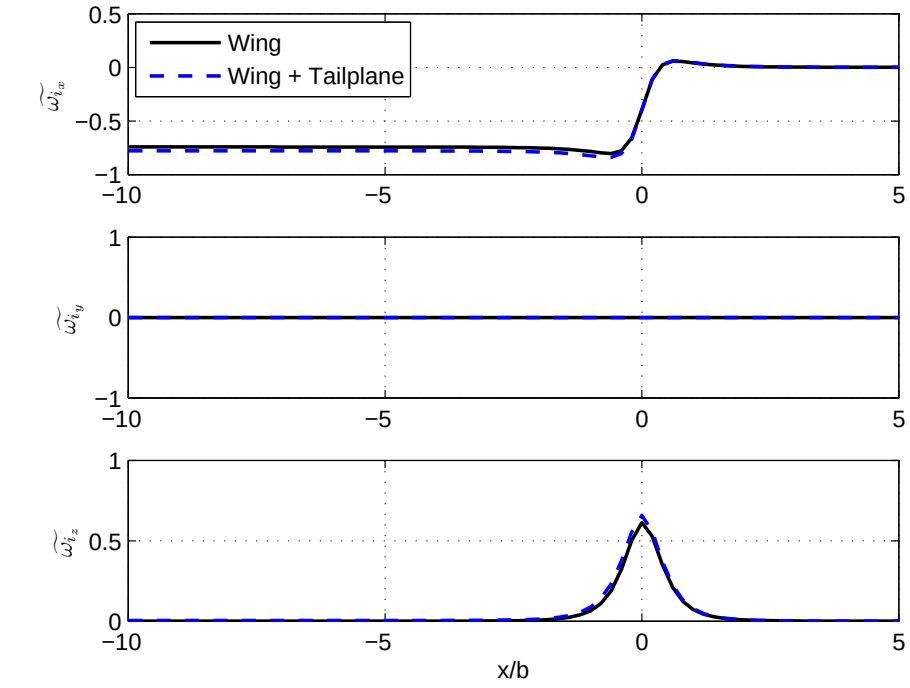

(b) Rotational components (deg/s)

Figure 6.3: Variations of $\widetilde{\mathbf{V}}_\mathbf{i}$ and $\widetilde{\boldsymbol{\omega}}_\mathbf{i}$ components with longitudinal spacing – $y_{rel} = b$ and $z_{rel} = b/2$

components remain unchanged, taking the tailplane into account adds a positive contribution to $\widetilde{V_{i_x}}$ and $\widetilde{V_{i_y}}$, and a negative contribution to $\widetilde{V_{i_z}}$. This result might appear as surprising as the tailplane generally produces negative lift in order to balance the pitching moment generated by the wing and possibly the fuselage, and stabilise the airplane. Consequently, the vortices produced by the tailplane should be in the opposite direction to those generated by the main wing, thereby diminishing the magnitude of the components of $\widetilde{\mathbf{V_i}}$. This would be valid, however for a classic configuration where tailplane and fin are two separate surfaces. Furthermore, it is to be noted that to achieve such an effect, the tailplane is usually mounted with a negative angle of incidence, which is not the case of our model of the Aerosonde UAV. Also, at this stage of the development, ELL does not accommodate the use of control surfaces, such as an elevator, that would enable the tailplane's effect to be more realistic.

Such a justification was verified by recalculating the variations of $\widetilde{\mathbf{V_i}}$ and $\widetilde{\boldsymbol{\omega}_\mathbf{i}}$ with longitudinal spacing for $y_{rel} = b$ and $z_{rel} = b/2$ after setting a negative angle of incidence for the tailplane (taken equal to -5 deg). The results then obtained are shown in Figure 6.4. As expected, taking the tailplane into account now adds a negative contribution to $\widetilde{V_{i_x}}$, and a positive contribution to $\widetilde{V_{i_z}}$. The reason why Λ_1's tailplane's contribution to Λ_2's $\widetilde{V_{i_y}}$ is still positive is because in such a configuration, $\widetilde{V_{i_y}}$ is mainly caused by the tailplane's bound vortex, which has a dihedral angle $\delta = -43$ deg. The fact that the bound vortices, rather than the trailing vortices, are the main cause for the generation of $\widetilde{V_{i_y}}$ is confirmed by the fact that when the tailplane is taken into account, the increment of $\widetilde{V_{i_y}}$ on Λ_2 is roughly the same whether Λ_2 is in front or behind Λ_1, unlike Figure 6.3.

The variations of $\widetilde{\mathbf{V_i}}$ and $\widetilde{\boldsymbol{\omega}_\mathbf{i}}$ components with lateral spacing for $x_{rel} = -2b$ and $z_{rel} = -0.1b$ are shown in Figure 6.5. In the case when only the wings are considered, $\widetilde{V_{i_x}} \leq 0$, whereas $\widetilde{V_{i_x}} \geq 0$ when both the wings and tailplanes are taken account of. This is due to the fact that in the first case, Λ_2 is located above Λ_1's wake, hence the presence of a backwash, whereas in the second case, Λ_2 is located above the wake generated by Λ_1's wings, but below the wake generated by Λ_1's; as Λ_2 is closer to Λ_1's tailplane than to its wings, the forward-wash generated by the tailplane over-compensate the backwash generated by the wings, hence the positive value of $\widetilde{V_{i_x}}$. In addition, in the case when both wings and tailplanes are considered, two "bumps" are visible in the variations of $\widetilde{V_{i_y}}$, $\widetilde{\omega_{i_x}}$ and $\widetilde{\omega_{i_z}}$. These "bumps" – located at $y/b \approx 0.5$, i.e. behind the tips of the tailplane – are caused by the "tailplane-tip" vortices.

Finally, the variations of $\widetilde{\mathbf{V_i}}$ and $\widetilde{\boldsymbol{\omega}_\mathbf{i}}$ components with vertical spacing for $x_{rel} = -2b$ and $y_{rel} = b$, i.e. for Λ_2 behind and starboard of Λ_1, are shown in Figure 6.6. As with the

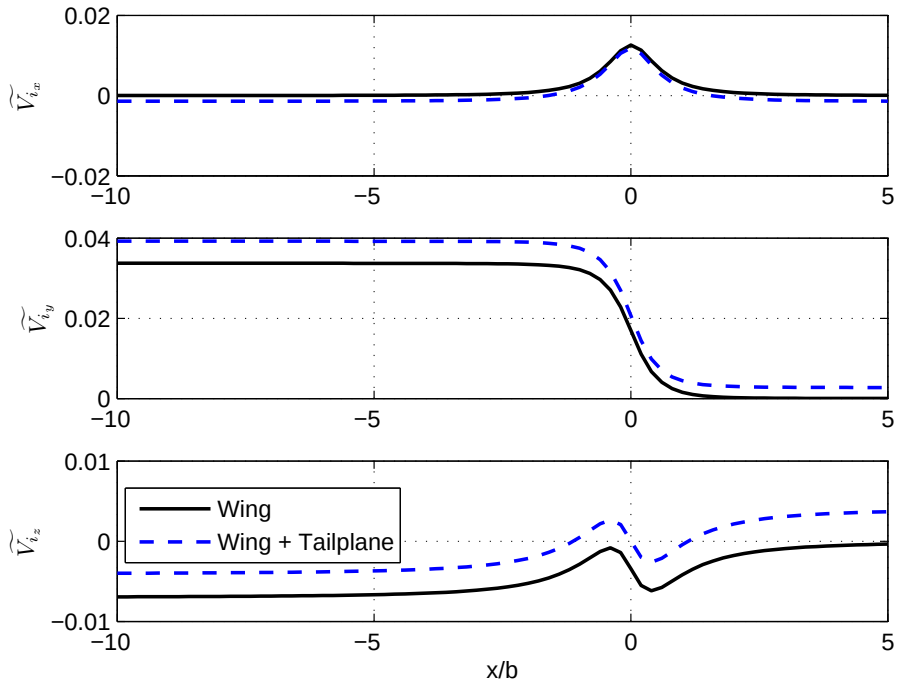

(a) Translational components (m/s)

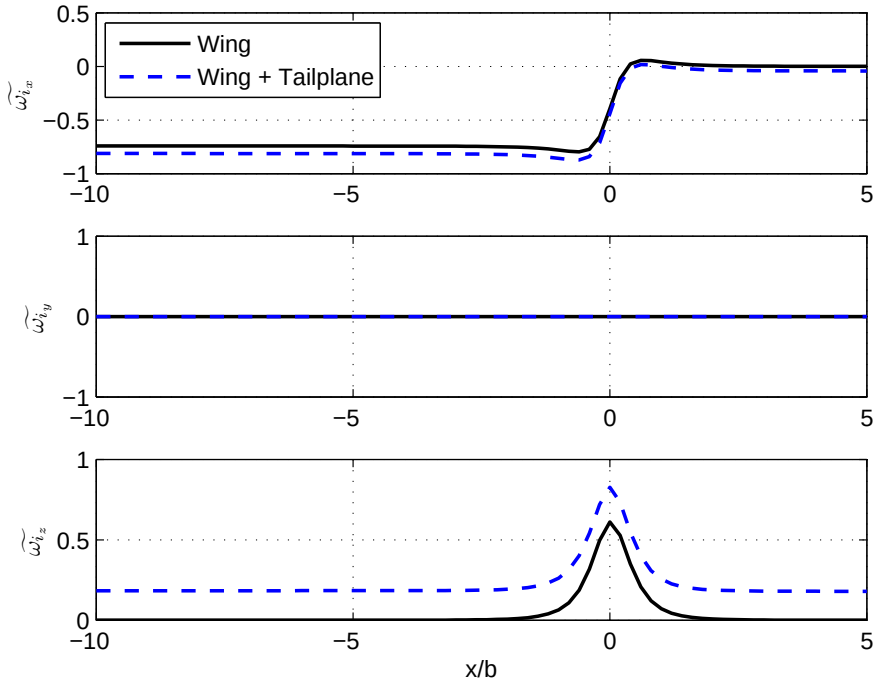

(b) Rotational components (deg/s)

Figure 6.4: Variations of $\widetilde{\mathbf{V}}_\mathbf{i}$ and $\widetilde{\boldsymbol{\omega}}_\mathbf{i}$ components with longitudinal spacing in the case where the tailplane has a negative angle of incidence (-5 deg) – $y_{rel} = b$ and $z_{rel} = b/2$

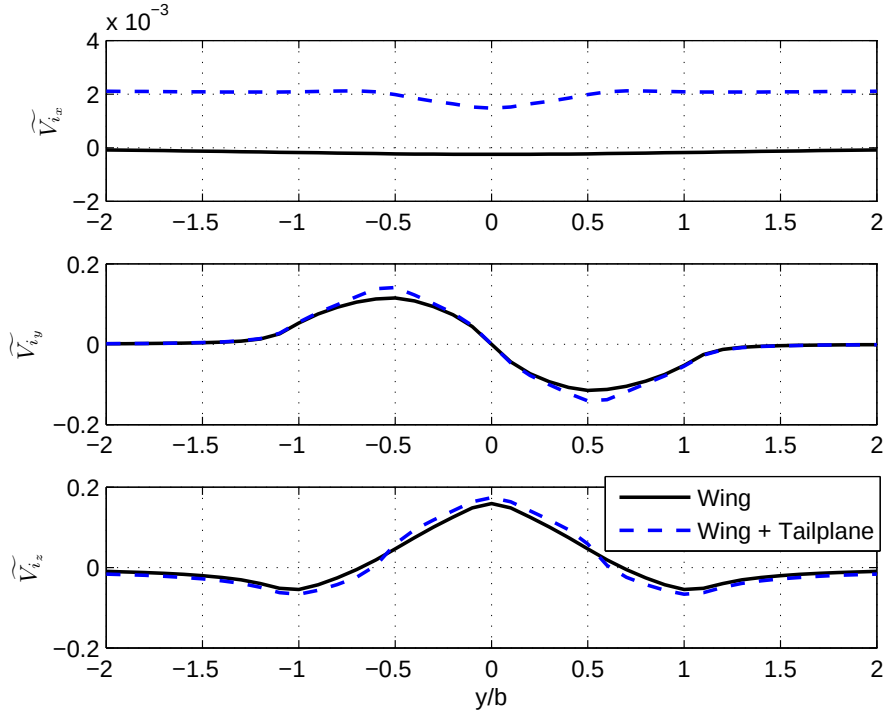

(a) Translational components (m/s)

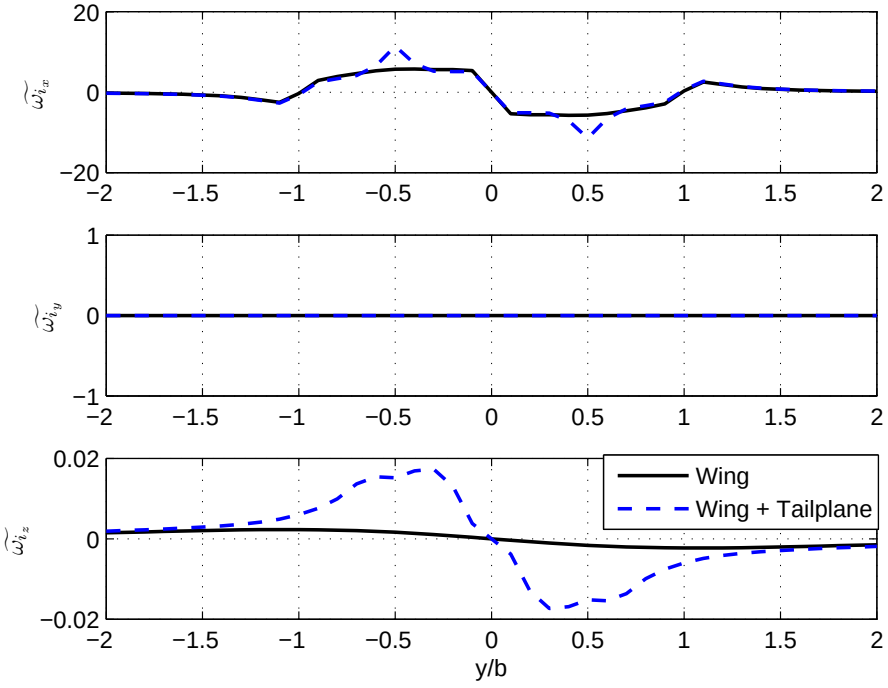

(b) Rotational components (deg/s)

Figure 6.5: Variations of $\widetilde{\mathbf{V}}_\mathbf{i}$ and $\widetilde{\boldsymbol{\omega}}_\mathbf{i}$ components with lateral spacing – $x_{rel} = -2b$ and $z_{rel} = -0.1b$

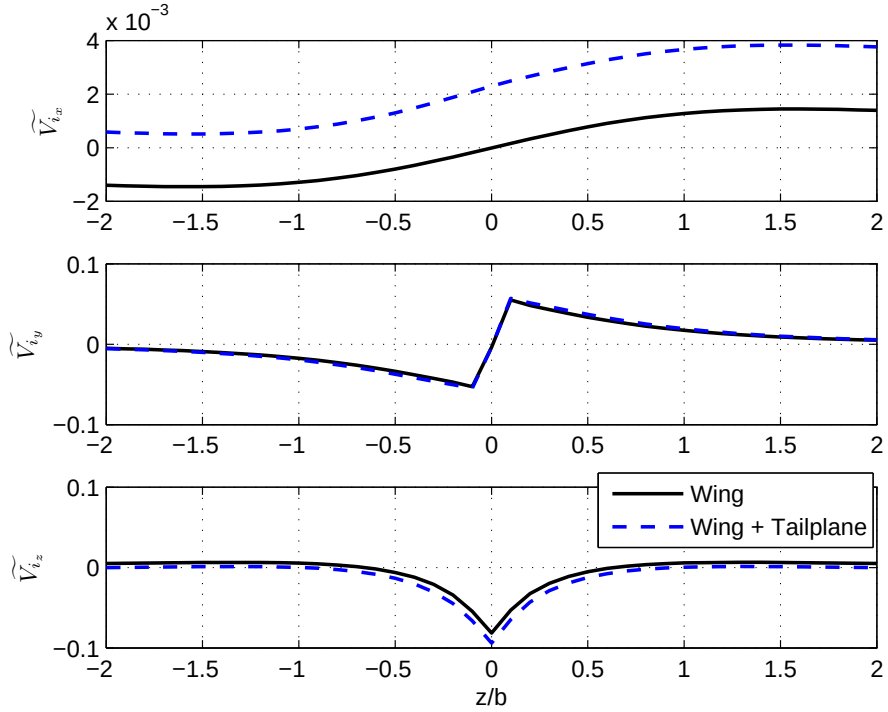

(a) Translational components (m/s)

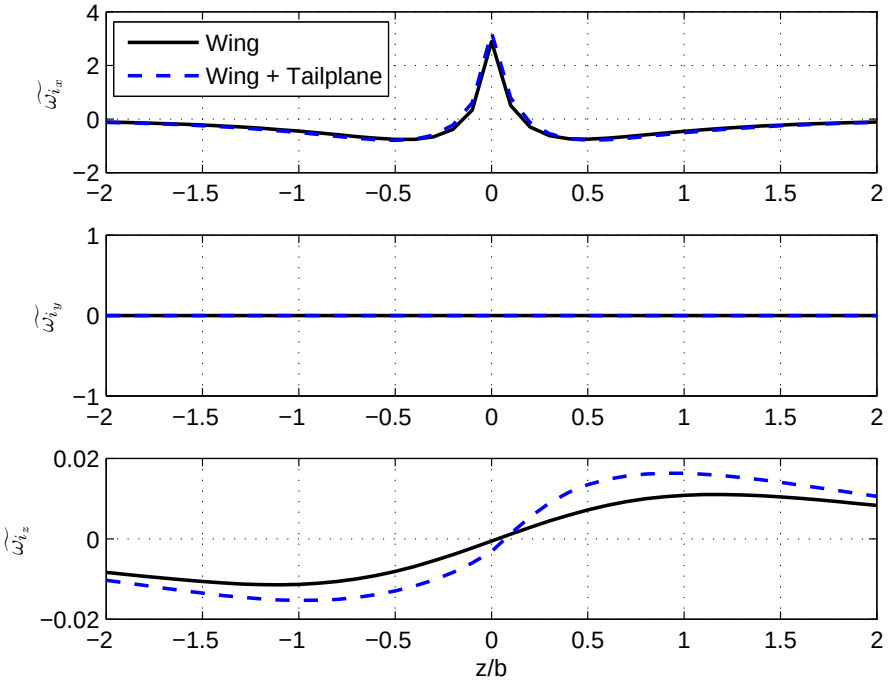

(b) Rotational components (deg/s)

Figure 6.6: Variations of $\widetilde{\mathbf{V}}_\mathbf{i}$ and $\widetilde{\boldsymbol{\omega}}_\mathbf{i}$ components with vertical spacing – $x_{rel} = -2b$ and $y_{rel} = b$

variations with lateral spacing (see Figure 6.5), the differences between the two cases are the most visible in the plots of $\widetilde{V_{i_x}}$ and $\widetilde{\omega_{i_z}}$. However, these are also the plots where the order of magnitude is the smallest. The same is true for the plots of $\widetilde{V_{i_x}}$ and $\widetilde{V_{i_z}}$ in Figure 6.3. Therefore, it does not seem necessary to include the tailplane in the calculation of the wake-induced effects, as doing so would add considerable computation complexity and bring only minor improvements to the results' accuracy.

6.4 Response to a Transient Wind Gust

In order to demonstrate the FCS capabilities, the Aerosonde response to a transient wind gust is analysed. It is reminded that details concerning the FCS design can be found in Appendix A. The gust model is shown in Figure 6.7. Two wind gusts of different lengths are applied: the first wind gust (40 s long) shows how the FCS reacts to a change in the atmospheric environment; the second gust (20 s long) shows how the Aerosonde model recovers from an external perturbation.

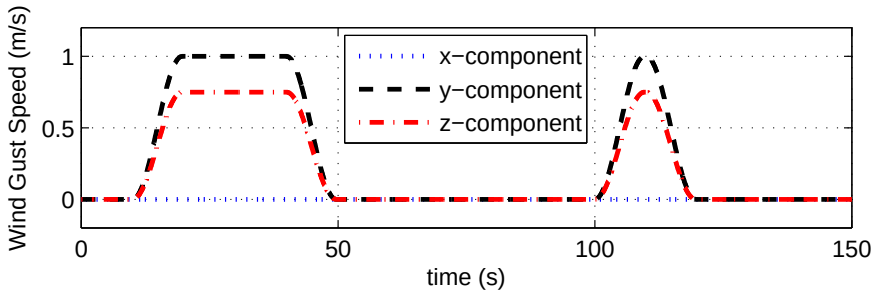

Figure 6.7: Transient wind gust model

The vehicle's position and velocity parameters are shown in Figures 6.8 and 6.9 respectively, its Euler angles in Figure 6.10 and its control settings in Figure 6.11. The simulation is started at trim conditions and a track angle slightly different from the trim track angle is commanded. As a consequence, an initial transient in d_y, χ, β, ϕ, ξ and ζ can be observed, as the aircraft uses the ailerons and rudder to correct its track angle and cancel its off-track error.

The vertical component of the gust causes an altitude drop of about 1 m between $t = 10$ s and $t = 20$ s (time for the gust to reach its maximum intensity), while the lateral component causes a perturbation in track angle χ. These are immediately countered by the controls, namely the throttle setting τ and the elevator η to counteract the loss of

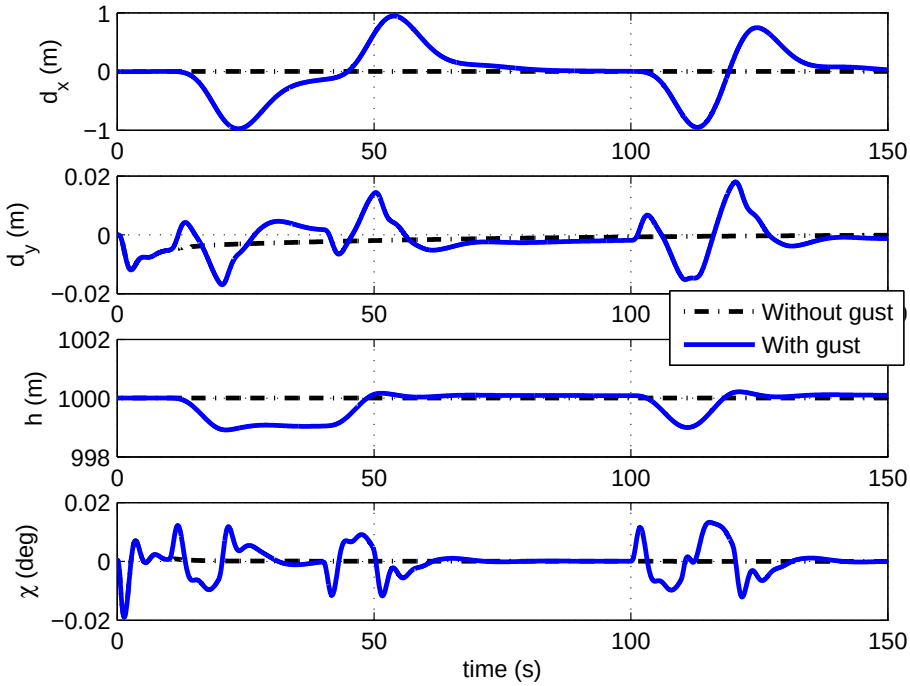

Figure 6.8: Response to a transient wind gust – Position parameters

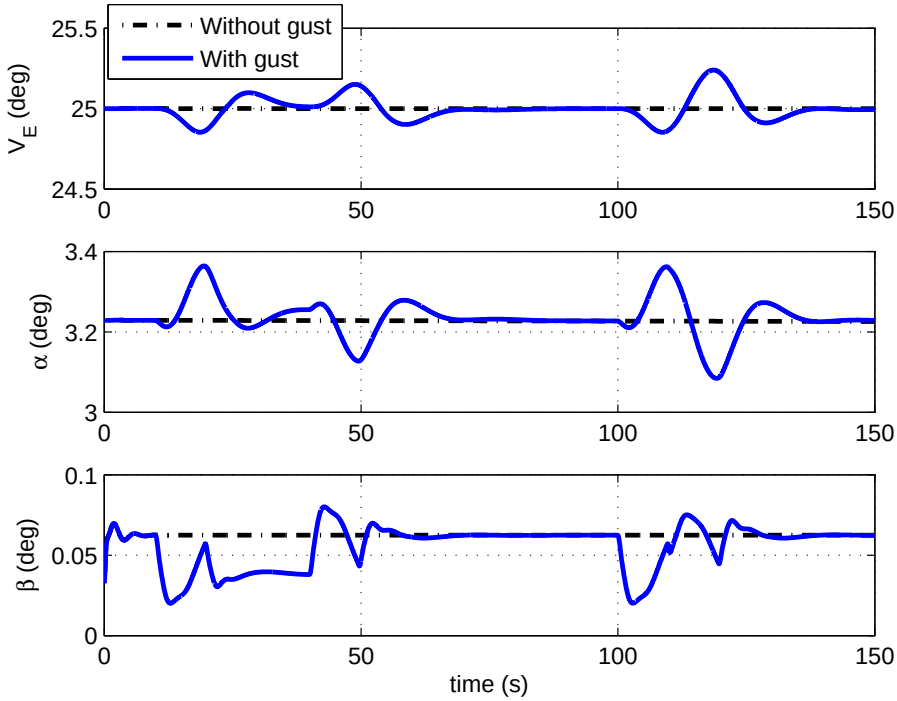

Figure 6.9: Response to a transient wind gust – Velocity parameters

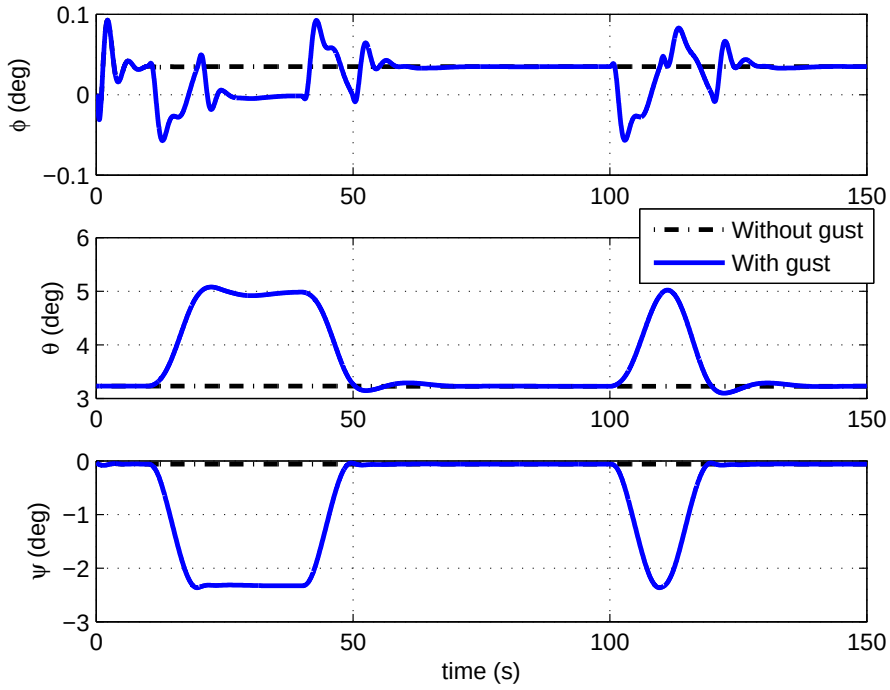

Figure 6.10: Response to a transient wind gust – Euler angles

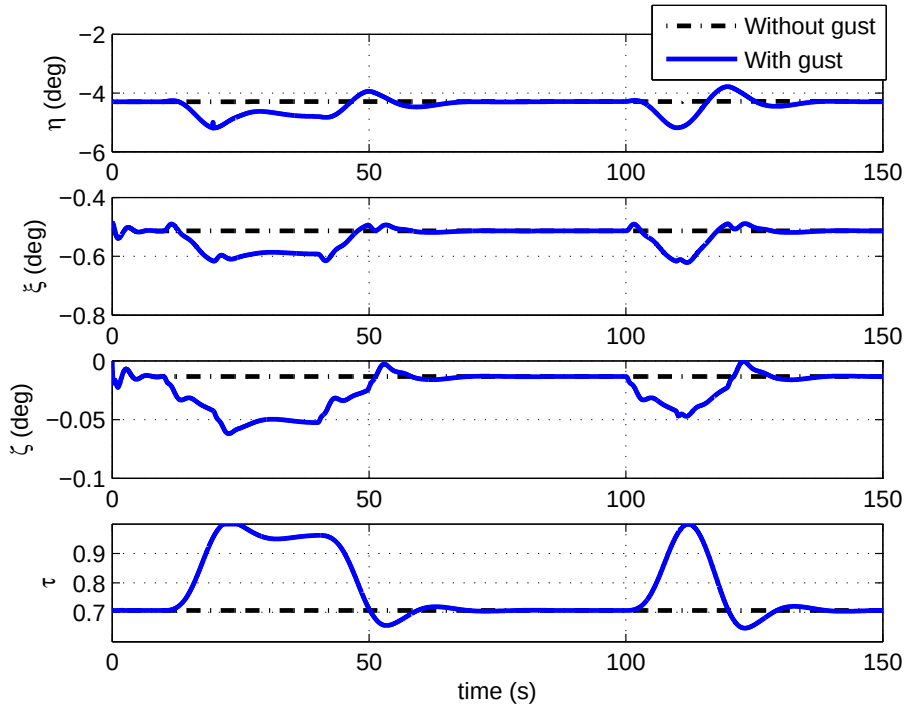

Figure 6.11: Response to a transient wind gust – Control surfaces deflections & throttle setting

altitude, and the ailerons ξ and the rudder ζ to correct the track angle and cancel the off-track error. However the Aerosonde, being a very light aircraft (about 13 kg when loaded), is very sensitive to perturbations, especially when they are in the vertical direction where a wider wing surface is exposed. The thrust keeps on augmenting to fight the loss of altitude until it saturates, which causes the UAV to slow down, and to start building up an along-track distance error (d_x). The Aerosonde then slowly stabilises, but still struggles to get back to its initial altitude as all its other parameters get closer to their nominal values ($V_E = 25$ m/s, $\chi = 0$ deg, and $d_x = d_y = 0$ m). When the wind gust fades, between $t = 40$ s and $t = 50$ s, the high level of thrust causes the Aerosonde to overtake its reference point ($d_x \geq 0$). Likewise, the high ailerons and rudder deflections, previously necessary to counteract the lateral component of the gust and keep the UAV on track, now lead the Aerosonde to deviate in the opposite direction ($d_y \geq 0$). The altitude error is quickly canceled, and the Aerosonde gets back to its initial situation within 30 s.

In the case of the short wind gust (between $t = 100$ s and $t = 120$ s), the same trends are observed as the Aerosonde swings to port and starboard, and back and forth of its reference point, before fully recovering within 20 s after the end of the gust.

These results show that the Aerosonde's behavior in case of a transient wind gust is satisfactory, and therefore validate the suitability of the FCS for most flying conditions.

6.5 Formation Keeping

This section presents the results obtained for a two-vehicle formation keeping scenario. Two Aerosonde UAVs are flying in formation such that Λ_2 is 2 wingspans behind, 1 wingspan starboard, and 0.3 wingspan below Λ_1. The effects of Λ_1's wake on Λ_2 are studied. Λ_1's trajectory is a straight and level line heading North ($\chi = 0$), and Λ_2 is to follow Λ_1 while keeping the same longitudinal and lateral relative distances, namely $d_x = -2\equiv - 5.8$ m and $d_y = b = 2.9$ m, and the same altitude $h = 999.13$ m.

Figure 6.12 shows the average velocity field induced by Λ_1 on Λ_2. As Λ_2 is positioned in the lower and outer part of Λ_1's starboard wing-tip vortex, it is subjected to induced upwash ($\widetilde{Vi_z} \leq 0$), starboard sidewash ($\widetilde{Vi_y} \geq 0$) and a slight forward-wash ($\widetilde{Vi_x} \geq 0$).

Figures 6.13, 6.14, 6.15 and 6.16 show Λ_2's position and velocity parameters, Euler angles, and control settings respectively, both in the absence and in the presence of Λ_1's

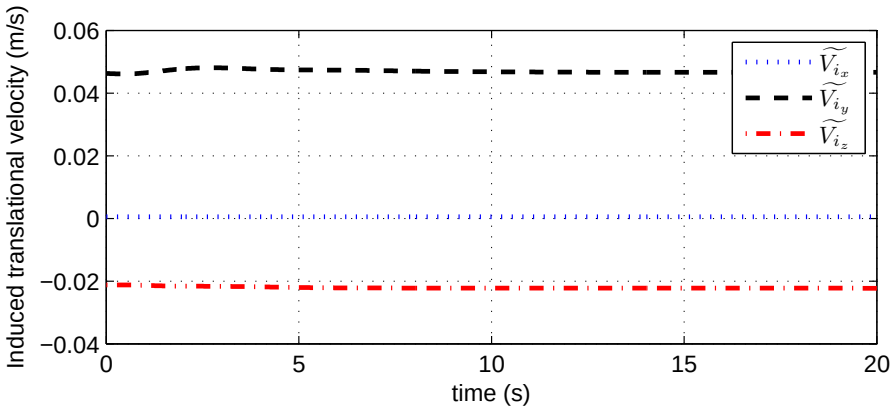

Figure 6.12: Formation keeping – Effective translational velocity induced by Λ_1 on Λ_2

wake-induced effects.

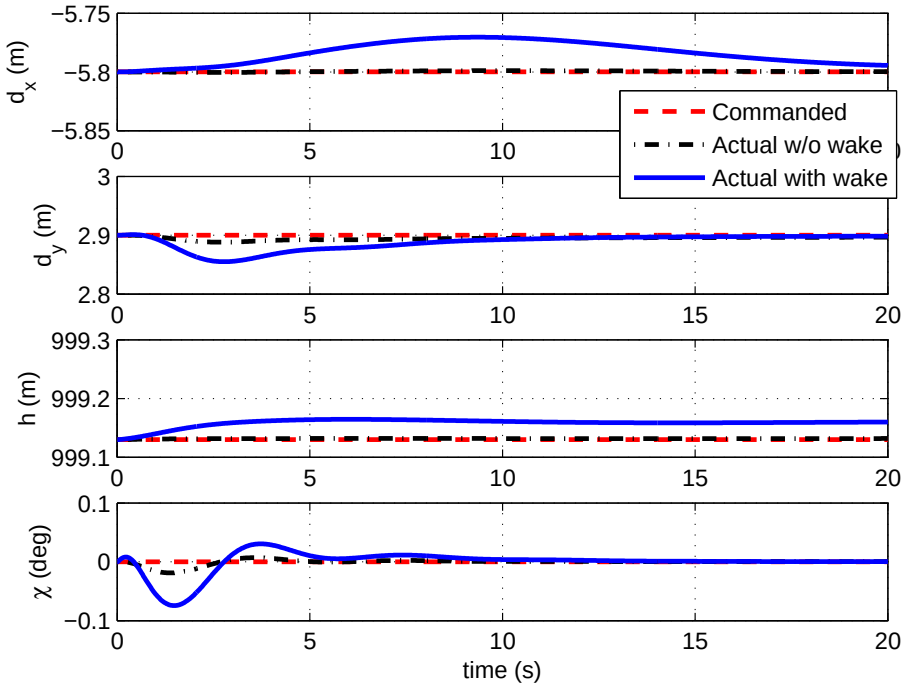

Figure 6.13: Formation keeping – Λ_2's position parameters with and without Λ_1's wake-induced effects

In the case where the wake-induced effects are not taken into account, there is very little variation in the above mentioned quantities, which – when applicable – are very close to the commanded ones. However, when the wake-induced effects are added to the simulation model, Λ_2 deviates from its commanded position (c.f. Figure 6.13) and

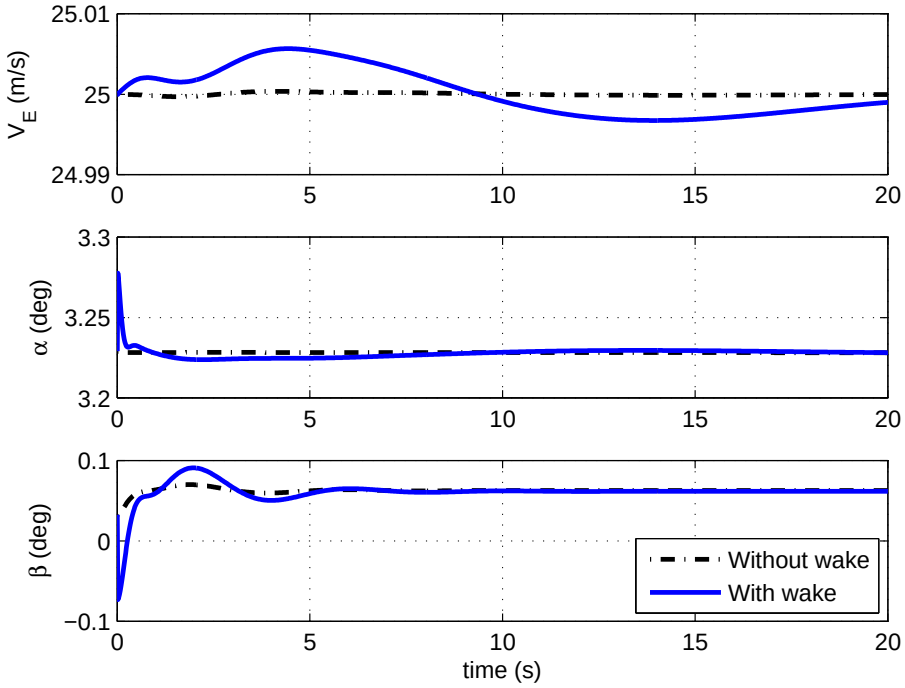

Figure 6.14: Formation keeping – Λ_2's velocity parameters with and without Λ_1's wake-induced effects

needs to be re-trimmed (c.f. Figure 6.16) in order to maintain the formation.

Longitudinally, the small forward-wash that Λ_2 is subjected to causes it to slightly overtake its commanded position (see V_E in Figure 6.14 and d_x in Figure 6.13), while the upwash – whose effect can also be observed in the variations of the angle of attack α (see Figure 6.14) – causes a small positive altitude error (see h in Figure 6.13) that the FCS tries to reduce by decreasing the elevator deflection η (see Figure 6.16). Finally, the strong sidewash creates a strong angle of sideslip β (see Figure 6.14) and causes Λ_2 to yaw to the left ($\psi \leq 0$ in Figure 6.15), thereby deviating it from the commanded track angle ($\chi \geq 0$ in Figure 6.13). This movement is counteracted by a negative impulse rudder input, which excites the dutch roll mode, and causes slight lateral-directional oscillations.

These plots illustrate the difficulty to control an aircraft when it is subjected to the wake-vortex effects induced by another vehicle: the FCS, which was giving satisfactory results in the case of a transient wind gust, copes with airwake-induced effects with more difficulty. In particular, it struggles to cancel the along-track and altitude errors.

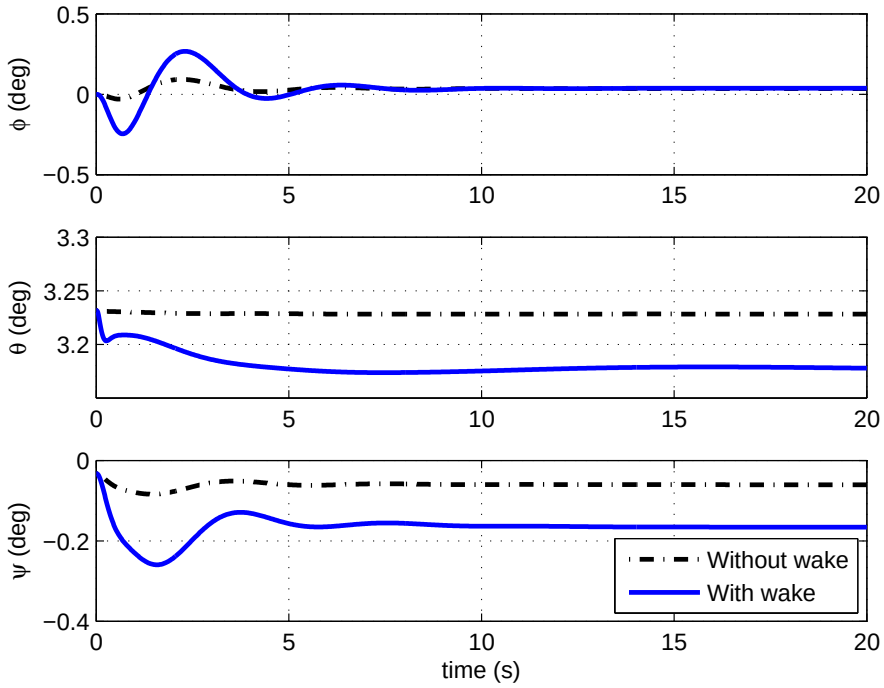

Figure 6.15: Formation keeping – Λ_2's Euler angles with and without Λ_1's wake-induced effects

6.6 Formation Reconfiguration

This section presents the results obtained for a formation reconfiguration scenario. Two Aerosonde UAVs are flying in formation such that Λ_2 is 3 wingspans behind, 1 wingspan starboard, and 0.2 wingspan below Λ_1. As in section 6.5, Λ_1's trajectory is a straight and level line heading North ($\chi = 0$). In this scenario, Λ_2 is first to follow Λ_1, and then to overtake it and to re-position itself so as to become the new leader of the formation, 3 wingspans in front, 1 wingspan starboard, and 0.2 wingspan above Λ_1. The reconfiguration scenario is illustrated in Figure 6.17. The effects of the wake of one vehicle upon the dynamics of the other vehicle are studied.

Figures 6.18 and 6.19 show the position parameters for Λ_1 and Λ_2 respectively. The reconfiguration scenario can be decomposed as follows:

- $0 \leq t \leq 10$ s: Λ_2 is flying in formation behind Λ_1;
- $10 \leq t \leq 15$ s: Λ_2 descends about 1 wing span below Λ_1;
- $20 \leq t \leq 35$ s: Λ_2 overtakes Λ_1 (they become level in the North direction at $t \simeq 34$ s);

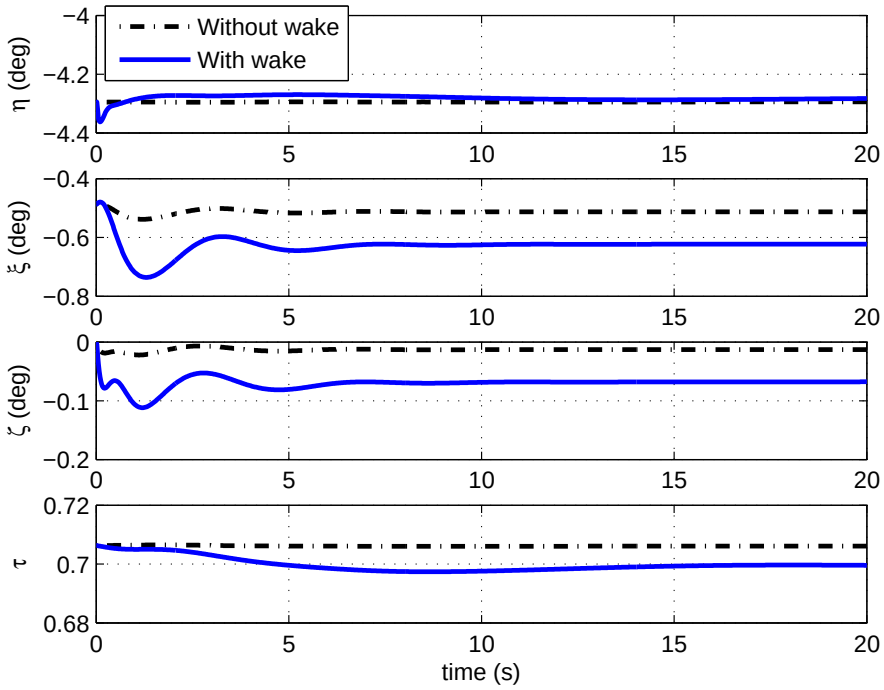

Figure 6.16: Formation keeping – Λ_2's control surfaces deflections & throttle setting with and without Λ_1's wake-induced effects

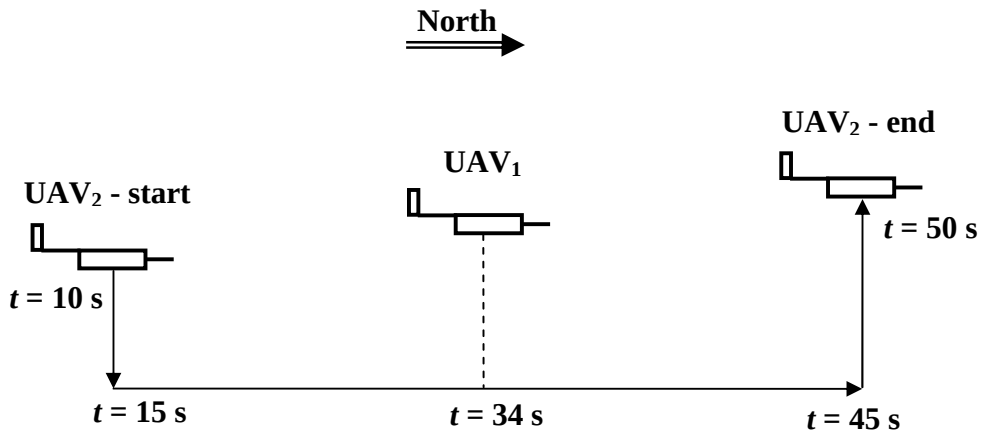

Figure 6.17: Formation reconfiguration scenario – View from East

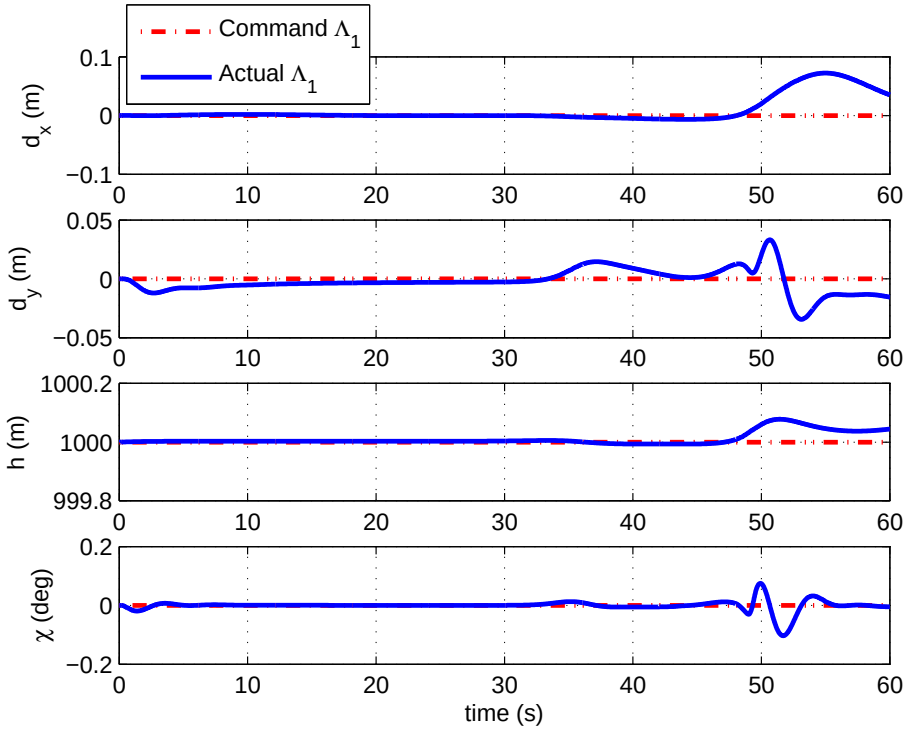

Figure 6.18: Formation reconfiguration – Λ_1's position parameters

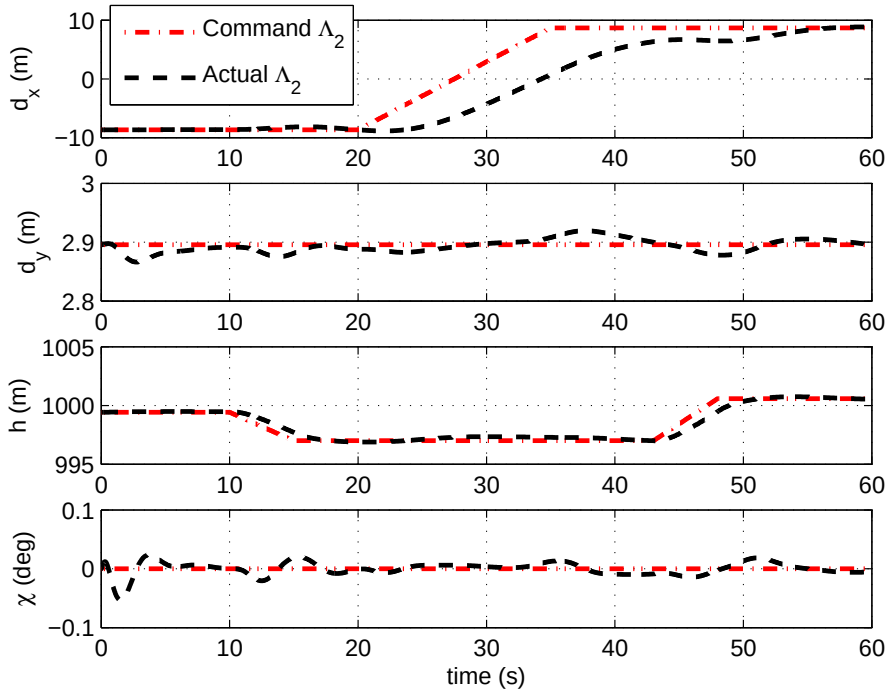

Figure 6.19: Formation reconfiguration – Λ_2's position parameters

- $45 \leq t \leq 50$ s: Λ_2 climbs back 0.2 wingspan higher than Λ_1;
- $50 \leq t \leq 60$ s: Λ_1 is flying in formation behind Λ_2;

The average velocity fields induced by Λ_1 on Λ_2, and Λ_2 on Λ_1 are shown in Figure 6.20, and the airdata parameters, Euler angles, and control settings for both UAVs in Figures 6.21, 6.22, and 6.23 respectively.

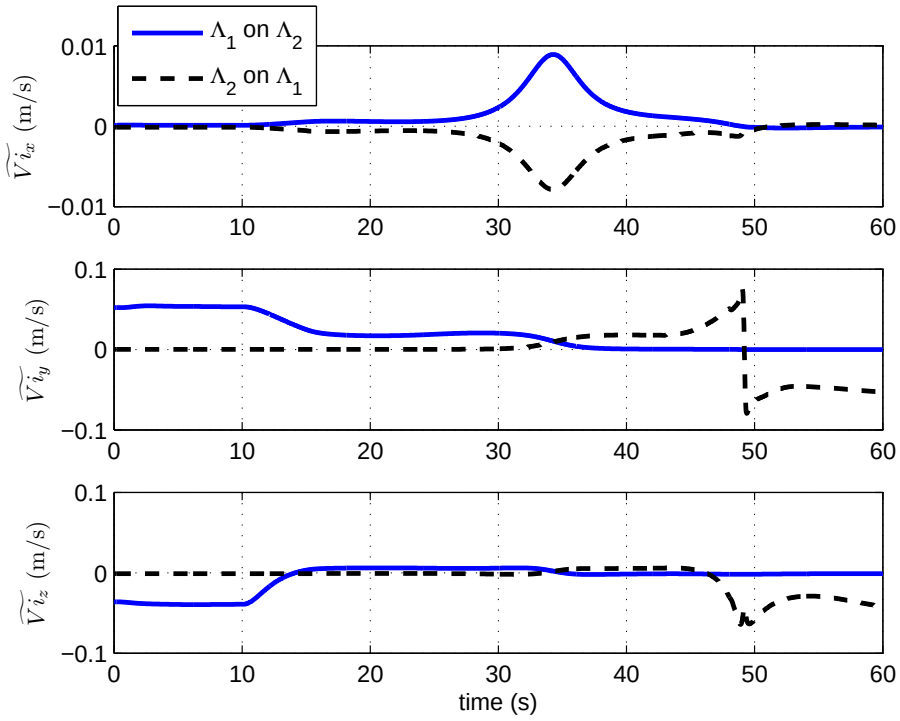

Figure 6.20: Formation reconfiguration – Λ_1 and Λ_2's average induced velocities

As expected, each vehicle is only subjected to the wake effects induced by the other when it is in the following position of the formation, i.e. $t \leq 34$ s for Λ_2, and $t \geq 34$ s for Λ_1. These effects are described below.

- $0 \leq t \leq 10$ s: Λ_2 is positioned in the lower and outer part of Λ_1's starboard wingtip vortex, where it is subjected to some upwash ($\widetilde{Vi_z} \leq 0$), starboard sidewash ($\widetilde{Vi_y} \geq 0$) and a barely visible forward-wash ($\widetilde{Vi_x} \geq 0$) (c.f. Figure 6.20). Also, as for the formation keeping scenario described in section 6.5, the presence of this induced velocity field triggers Λ_2's dutch roll mode (c.f. the time histories of d_y and χ in Figure 6.19, β in Figure 6.21, ϕ and ψ in Figure 6.22, and ξ and ζ in Figure 6.23).

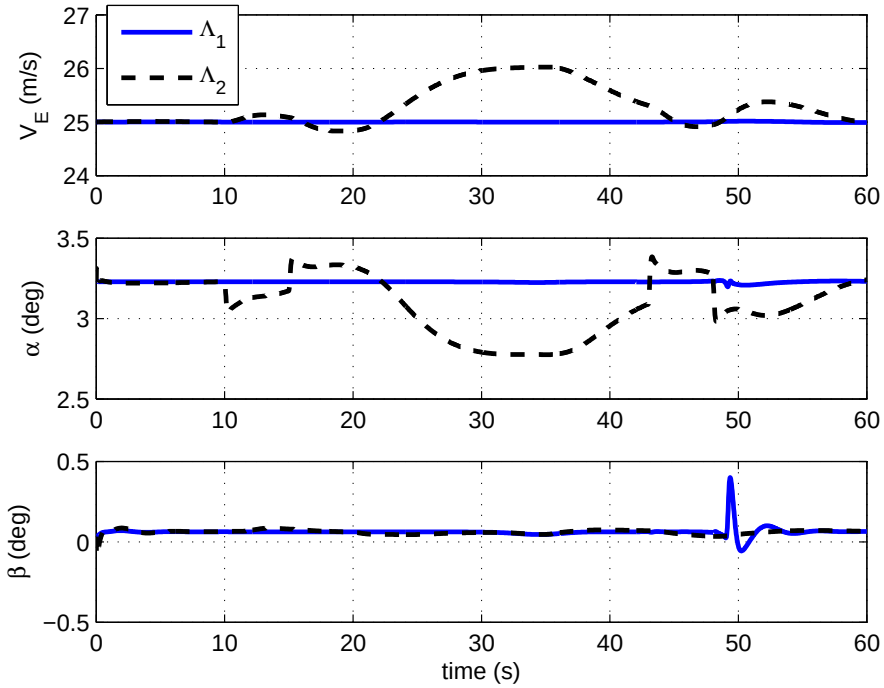

Figure 6.21: Formation reconfiguration – Λ_1 and Λ_2's airdata parameters

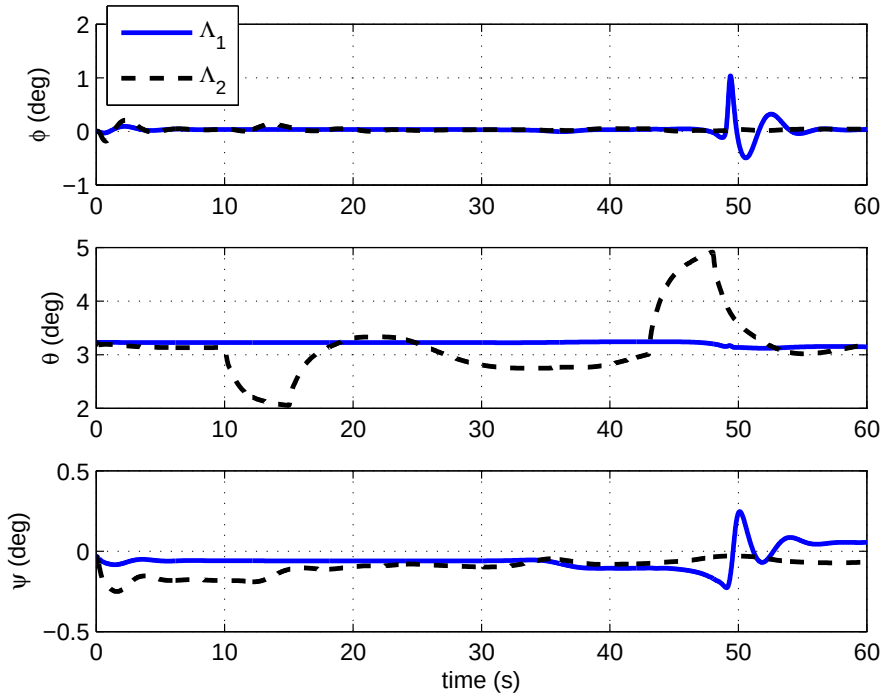

Figure 6.22: Formation reconfiguration – Λ_1 and Λ_2's Euler angles

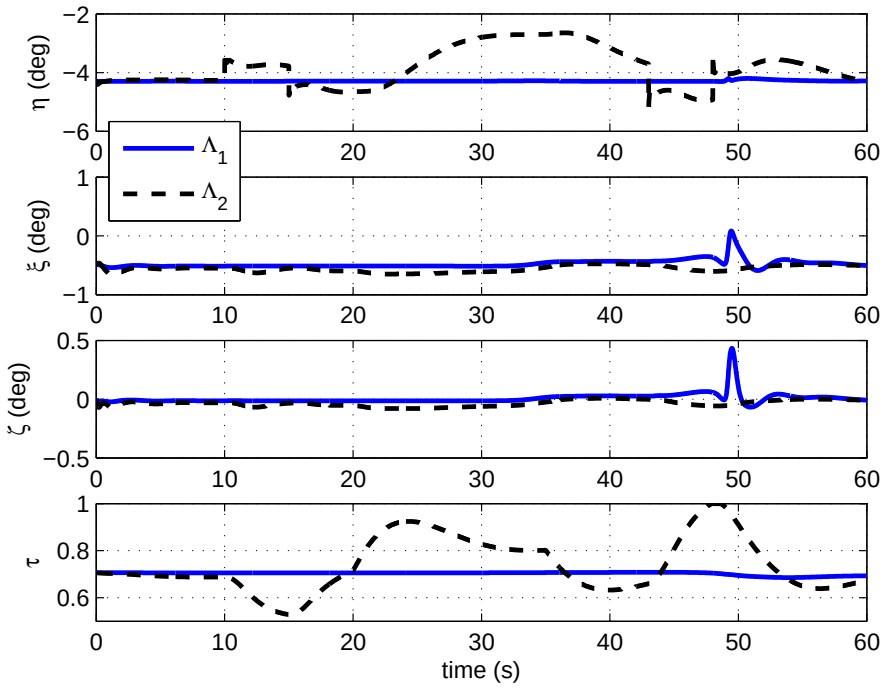

Figure 6.23: Formation reconfiguration – Λ_1 and Λ_2's control surfaces deflections & throttle settings

- $10 \leq t \leq 15$ s, Λ_2's descent, as shown by the decrease of h, α, θ, the elevator deflection η and the throttle setting τ, while V_E slightly increases (c.f. Figures 6.19, 6.21, 6.22, and 6.23). The wake effects induced by Λ_1 on Λ_2 get weaker, as shown in Figure 6.18, 6.20, 6.21, 6.22 and 6.23.

- $20 \leq t \leq 34$ s: Λ_2 is about 1 wingspan below Λ_1, where it experiences a slight downwash ($Vi_z \geq 0$ in Figure 6.20), and is commanded to overtake Λ_1 (c.f. d_x in Figure 6.19). As a consequence, the thrust is augmented (c.f. τ in Figure 6.23), leading to an increase in the velocity V_E and a decrease in the angle of attack α (c.f. Figure 6.21).

- $t = 34$ s: Λ_2 is exactly below Λ_1. At that point, each UAV is sensitive to the influence of the other's bound vortex, which induces some back-wash for Λ_1, and forward-wash for Λ_2.

- $34 \leq t \leq 43$ s: Λ_1 is above, port, and behind Λ_2, where it is subjected to starboard sidewash, slight back-wash and slight downwash.

- $43 \leq t \leq 48$ s, Λ_2's climb: h, α, θ and the elevator deflection η increase accordingly (c.f. Figures 6.19, 6.21, 6.22, and 6.23). The wake effects induced by Λ_2

on Λ_1 get stronger, as shown in Figures 6.18, 6.20, 6.21, 6.22 and 6.23, and reach a maximum at $t \simeq 49$ s, i.e. when Λ_2 crosses Λ_1's horizontal plan.

- $50 \leq t \leq 60$ s: the configuration is similar to the initial formation except that the follower (now Λ_1) is positioned port of the leader (now Λ_2), i.e. in the lower and outer part of Λ_2's port wing-tip vortex, where it is subjected to some upwash ($\widetilde{Vi_z} \leq 0$), port sidewash ($\widetilde{Vi_y} \geq 0$) and a small forward-wash ($\widetilde{Vi_x} \geq 0$) (c.f. Figure 6.20).

6.7 Chapter Summary and Conclusions

This chapter presents the simulation results obtained for two Aerosonde UAVs flying in formation. Two test scenarios – formation keeping and formation reconfiguration – are described in order to illustrate the challenges inherent to close proximity flying, and demonstrate how ELL can be used within the simulations to assess and analyse mutual aerodynamic coupling effects, thereby supporting the design of suitable automatic control systems and the development of close formation flying procedures.

In particular, it is shown that the follower's FCS has difficulties coping with the interactions induced by the leader's wake and struggles to cancel the resulting along-track and altitude errors. This is because the longitudinal dynamics has two inputs, namely engine thrust and elevator; however the engine thrust actuation has a low bandwidth, and hence cannot cancel the higher frequency disturbances resulting from the wake. This is a critical issue for formation flight safety, as a collision between the following and the leading air vehicles could result. Hence, other higher bandwidth actuation mechanisms, such as air brakes and spoilers, should be considered for a better control of the follower in such situations.

In addition, the simulation of a formation reconfiguration manoeuvre is of particular interest, as it demonstrates that – unlike previous work carried out in this field [Venkataramanan and Dogan, 2004*a*; Dogan and Venkataramanan, 2005] – ELL enables the lead and trail air vehicles to exchange positions during the simulations, thereby removing the necessity to pre-allocate a role to each UAV: this is automatically done by ELL depending on the relative positions of the UAVs in the formation.

Chapter 7

Conclusion

The aim of this research was to develop a realistic airwake model to be used in simulations of aircraft flying in close proximity in order to permit the assessment of the risks and issues associated with wake vortex evolution and encounter. This chapter recapitulates how this aim was achieved, highlights the contributions to knowledge and suggests areas for further development.

7.1 Research Summary

In Chapter 2, a review of the work published in the field of characterisation, modelling and simulation of wake vortex effects, as well as autonomous formation flight (including autonomous air-to-air refuelling) was undertaken. Two main approaches to the real-time or near real-time modelling of wake vortices were identified, namely: (i) look-up databases and (ii) online computational methods. Compared to the look-up databases, the online computational methods have the advantages of being more flexible, less costly to generate, less computationally demanding to operate and more generic as, unlike the databases, they are not restricted to a specified air vehicle and range of flight conditions. However, when using an online computational method, a compromise needs to be found between accuracy of the results on the one hand, and cost and rapidity of execution on the other.

Four categories of online computational techniques were reviewed, including (from the simplest to the most involved): (i) the methods based on Prandtl's lifting line theory; (ii) VLMs (Vortex Lattice Methods); (iii) the improved methods which take account of the roll-up of the wake; and (iv) online CFD computations. Amongst these categories, the methods based on Prandtl's lifting line theory and the VLMs were found to be of particular interest as their computational efficiency enables them to be used in real-time

on average-performance computers.

It was also found that in all the previous studies where a WVM is included in a real-time or near real-time simulation of air vehicles flying in formation, the wake-generating and the wake-encountering vehicles were modelled in different ways. This "unidirectionality" of the WVM has a number of consequences:

1. the WVM implicitly requires the preliminary knowledge of the aircraft positions in relation to one another,

2. the WVM does not permit the computation of the effects induced by the follower on the leader; however, these effects – although smaller in magnitude than those induced by the leader on the follower – do exist;

3. the leading and following air vehicles cannot easily exchange position during a simulation; therefore, reconfiguration scenarios are limited.

This last point is problematic as the reconfiguration of the air vehicles in a formation is at the least beneficial (all vehicles can successively take advantage of the up-current induced by the others), and at the most a critical necessity (for example in the case of the failure or the loss of one entity in the formation). This consideration provided an additional requirement for the WVM developed as part of this research: it should be "multi-directional" in order to take account of the effects induced by the follower on the leader and to permit reconfiguration manoeuvres.

The theoretical background on which the WVM development was based is explained in Chapter 3: overviews of potential flow theory, Prandtl's classical lifting line theory, and Weissinger's extended lifting line theory are given, leading to the choice of a wake vortex modelling technique. Weissinger's extended lifting line method, as an intermediate between the basic Prandtl's lifting line theory and the more involved VLMs, seemed to provide the best compromise between accuracy and rapidity of execution for an average-performance computer, and therefore appeared to be the most suitable technique. Its additional advantages include its computational simplicity, its flexibility (a variable number of horseshoe vortices can be chosen depending on the level of accuracy needed) and the fact that, unlike Prandtl's lifting line theory, it is valid for wings of any planform – including swept wings – and aspect ratio.

The choices of a vortex velocity distribution profile and of a viscous core are also discussed in Chapter 3. For this purpose, the definitions of viscous cores were reviewed, and nine vortex velocity profile models – namely Helmholtz, Rankine, Hallock-Burnham,

Lamb-Oseen, Kurylovich, Proctor, smooth blending, multiple scales and Dogan's modified Helmholtz vortex model – were compared. The Kurylowich model, with a core radius $r_c = 36.2\sqrt{\nu\tau/\cos(\varphi)^2}$, was selected for the simplicity of its implementation and the accuracy of its predictions.

In Chapter 4, the development and implementation of a WVM are presented. The WVM, which – as stated above – is based on Weissinger's extended lifting line theory, meets the initial requirements that it:

- be generic and easily adapted to fit any wing planform and air vehicle configuration,
- be computationally rapid enough to be used in real-time or near real-time simulations, and
- be sufficiently representative to support studies of aerodynamic interaction between multiple air vehicles during formation reconfiguration and air-to-air refuelling simulations.

The code, named ELL, computes the steady-state velocities induced on one air vehicle by the wake(s) of the others. Each aircraft is represented by its lifting surfaces. Each surface is replaced by its 1/4 chord segment, and the vortex sheet by a flat rectangular surface composed of n_{seg} semi-infinite horseshoe vortices. Their strength is determined through the application of the Weissinger boundary condition, which states that at the collocation points of the wing (one per horseshoe vortex), the airflow is tangential to the wing surface. Once the vortices strengths are known, the velocities induced on the vehicle by other aircraft in the formation can be calculated at different points along its 1/4 chord line. For that, a Helmholtz velocity distribution is used to calculate the influence of the branches of the vortices bound to the wings of the neighbouring vehicles, and a Lamb-Oseen vortex model is used for the trailing branches of those vortices.

The induced velocity field thus obtained is highly non-uniform, and can be approximated around the CG of the vehicle as the sum of uniform wind components and uniform wind gradients, following a method developed by Dogan, Venkataramanan and Blake [2005]. The components of the effective induced translational and rotational wind velocities can then be derived, and directly integrated in the aircraft Simulink model with its wind terms.

The limitations of the WVM are listed below.

- As ELL is based on a small-perturbation potential flow theory, reliable results can only be achieved for small angles of attack and subsonic conditions. However these conditions are met in cruise where reconfiguration and air-to-air refuelling manoeuvres usually take place.

- ELL does not allow the following effects to be taken into account: thickness, camber, fuselage, friction drag, and compressibility; the roll-up of the vortex sheet is also ignored. Again, this is not a problem as in close formation flight, the air vehicles are located in the near wake region of one another, where the wakes are not fully rolled-up and where the rigid wake approximation is adequate.

- As part of the rigid wake approximation, ELL considers the shape of the wake to remain unchanged, even when the wake-generating vehicle is manoeuvering: at each time step, the wake is represented as a flat rectangular surface which extends downstream to infinity parallel to the velocity vector. Obviously, this is not the case in reality, where the wake tends to follow the trajectory of its generating aircraft. However – and as for the previous point regarding the roll-up of the vortex sheet – this is not be an issue for close formation flight scenarios where the distance between the vehicles is small.

- Finally, the distribution of a wing's calculation points is collapsed to its 1/4-chord line. Such a configuration – although justified by the fact that the generation of wing-tip vortices is essentially a spanwise phenomenon (due to the wing spanwise load distribution) – causes inaccuracy in the calculation of the wake-induced pitching moments for low-sweep-angle wings. A way to improve the accuracy of these results would be to add a chordwise discretisation of the wing; however, this would increase the computational complexity of the code and slow down the simulations. Also, apart from the estimation of the incremental pitching moment – which is neither the most significant, nor the more critical wake-induced effect in formation flight – the resulting gain in accuracy for the computation of the other aerodynamic forces and moments would be insignificant (as confirmed by the validation results in Chapter 5).

The verification and validation processes of ELL are described in Chapter 5. The verification process included the analysis of the influence on the induced velocity field of the choice of a reference frame, of the distance between two vehicles of a formation, and of the airspeed, angle of attack and angle of sideslip of the incoming airflow. The validation process consisted of comparing the effective induced wind velocities and the incremental aerodynamic forces and moments coefficients obtained with ELL with

experimental and computational results published by Blake and Gingras [2004] and Dogan, Venkataramanan and Blake [2005]. The results of the verification tests proved to be consistent, and ELL's estimates compared satisfactorily with the published data, thereby verifying and validating the code. It should be noted that the aim of ELL is not to get a perfect match, but to obtain a match which is good enough to predict the qualitative, and to some extent, the quantitative effects of aerodynamic interactions between air vehicles flying in close proximity, using a fast and efficient method. In that sense, the ELL method shows numerous advantages, including its simplicity, modularity, transparency (which makes it a more flexible method), and real-time benefits.

Chapter 6 presents simulation results obtained for two Aerosonde UAVs flying in formation. After demonstrating the Aerosonde's FCS capabilities through the analysis of the UAV's response to a transient wind gust, two test scenarios – formation keeping and formation reconfiguration – were analysed. The "multi-directionality" of ELL was verified and the challenges inherent to close proximity flying were illustrated. Furthermore, these test scenarios demonstrated how ELL can be used within the simulations to assess and analyse mutual aerodynamic coupling effects, thereby supporting the design of suitable automatic control systems and the development of close formation flying procedures. In particular, it was shown that the follower's FCS has difficulties coping with the interactions induced by the leader's wake and struggles to cancel the resulting along-track and altitude errors. This is a critical issue for formation flight safety, as such errors could potentially cause a collision between the following and the leading air vehicles. Finally, through the simulation of a formation reconfiguration manoeuvre, it was demonstrated that – unlike previous work carried out in this field [Venkataramanan and Dogan, 2004*a*; Dogan and Venkataramanan, 2005] – ELL enables the lead and trail air vehicles to exchange positions during the simulations, thereby removing the necessity to pre-allocate a role to each UAV: this is automatically done by ELL depending on the relative positions of the UAVs in the formation.

7.2 Contributions to Knowledge

The contributions to knowledge which have been made as part of this work are summarised below:

- Development, implementation, verification, and validation of a novel WVM (ELL) based on the Weissinger extended lifting line method in association with a Kurylowich velocity profile and viscous core.

- Demonstration of how ELL can be used within near real-time simulations to assess and analyse mutual aerodynamic coupling effects and support the design of suitable automatic control systems.

- Demonstration of ELL's "multi-directionality": in a formation, ELL calculates the influence of all the vehicles on one another and not only the effects induced by the leader(s) on the follower(s). Also, ELL takes account of the fact that the wake of one air vehicle is affected by the presence and position of another air vehicle nearby and modify the characteristics of the wake accordingly.

- Demonstration that ELL can be used in simulations of reconfiguration scenarios where leading and following air vehicles exchange positions.

Furthermore, ELL was successfully implemented within the Cobham SE as part of the ASTRAEA programme.

7.3 Suggestions for Future Work

A number of interesting possibilities exist to extend, deepen or complete the research presented in this thesis. These are briefly discussed in this section. Firstly, although the WVM has been tested for three and more air vehicles, no simulation of more than two aircraft has been performed. Scenarios involving more than three vehicles could be carried out to help understand how the airwakes interact during close formation flights and to analyse the consequences on the development of safe, autonomous multiple air vehicle operation procedures.

The second suggestion would be to test the WVM and the FCS in more complicated situations, such as a full air-to-air refuelling scenario (receiver to enter the refuelling domain, to join the racetrack of the tanker at the rendez-vous point, to follow the tanker and to position itself for refuelling, before exiting the racetrack and the refuelling box). The aerodynamic effect of the refuelling equipment (either boom and receptacle or probe and drogue) could also be modelled and taken into account.

Another possibility would be to explore different ways to improve the FCS for close formation flight. For example, other formation structures, such as the leader-wingman or the behavioural approaches, could be used, assessed and compared to the VL structure. Also, in order to cope better with the longitudinal and vertical positioning errors

resulting from the wake-induced high frequency disturbances and lower the risk of collisions, high bandwidth actuation mechanisms such as slats, flaps, spoilers and/or air brakes should be considered for inclusion in the FCS design.

Future work could also be carried out to improve the SE. A proper geometric model of the Aerosonde could be designed, and an interactive planform could be developed to enable the simultaneous simulation and visualisation of multi-vehicle deployments.

Finally, the use of ELL – which is currently limited to close formation flight scenarios – could be extended to more general formation flight scenarios. This would invalidate the rigid wake approximation and require that the code be amended so as to include the roll-up of the wake vortex sheet and record its position as a function of time.

References

Allen, A. and C. Breitsamter. 2009. "Experimental Investigation of Counter-Rotating Four Vortex Aircraft Wake." *Aerospace Science and Technology* 13(2-3):114–129.

Anderson, J.D. 2007. *Fundamentals of Aerodynamics*. Fourth ed. Boston: McGraw-Hill.

ASTRAEA Website: http://www.projectastraea.co.uk/. N.d. Accessed on 19.08.2009. **URL:** *http://www.projectastraea.co.uk/*

AVDS Official Website: http://www.rassimtech.com/. N.d. Accessed on 06.03.2009. **URL:** *http://www.rassimtech.com/*

Bertin, J.J and M.L. Smith. 1998. *Aerodynamics for Engineers*. Third ed. Prentice-Hall International.

Beukenberg, M. and D. Hummel. 1990. Aerodynamics, Performance and Control of Airplanes in Formation Flight. In *Proceedings of the 17th Congress of ICAS*. Vol. 2 Stockholm, Sweden: pp. 1777–1794.

Blake, W. and D. Multhopp. 1998. Design, Performance and Modeling Considerations for Close Formation Flight. In *AIAA Atmospheric Flight Mechanics Conference and Exhibit*. AAIA 98-4343 Boston, MA: pp. 476–486.

Blake, W.B. 2000. An Aerodynamic Model for Simulation of Close Formation Flight. In *AIAA Modeling and Simulation Technologies Conference and Exhibit*. AAIA 2000-4304 Denver, CO: pp. 421–431.

Blake, W.B. and D.R. Gingras. 2004. "Comparison of Predicted and Measured Formation Flight Interference Effects." *Journal of Aircraft* 41(2):201–207.

Blake, W.B., E.G. Dickes and D.R. Gingras. 2004. UAV Aerial Refueling - Wind Tunnel Results and Comparison with Analytical Predictions. In *AIAA Atmospheric Flight Mechanics Conference and Exhibit*. AAIA 2004-4820 Providence, RI.

Bloy, A.W. and K.A. Lea. 1995. "Directional Stability of a Large Receiver Aircraft in Air-to-Air Refueling." *Journal of Aircraft* 32(2):453–455.

Bloy, A.W., K.A.M. Ali and V. Trochalidis. 1987. "The Longitudinal Dynamic Stability and Control of a Large Receiver Aircraft During Air-to-Air Refueling." *Aeronautical Journal* 91(902):64–71.

Bloy, A.W. and M. Joumaa. 1995*a*. "Lateral and Directional Stability and Control in Air-to-Air Refuelling." *Proceedings of the Institution of Mechanical Engineers Part G-Journal of Aerospace Engineering* 209(G4):299–305.

Bloy, A.W. and M. Joumaa. 1995*b*. "Trailing Vortex Effects on Large Receiver Aircraft." *Journal of Aircraft* 32(6):1198–1204.

Bloy, A.W. and M.G. West. 1994. "Interference Between Tanker Wing Wake with Roll-Up and Receiver Aircraft." *Journal of Aircraft* 31(5):1214–1216.

Bloy, A.W., M.G. West, K.A. Lea and M. Joumaa. 1993. "Lateral Aerodynamic Interference Between Tanker and Receiver in Air-to-Air Refueling." *Journal of Aircraft* 30(5):705–710.

Bloy, A.W. and M.M. Khan. 2001. "Modeling of the Receiver Aircraft in Air-To-Air Refueling." *Journal of Aircraft* 38(2):393–396.

Bloy, A.W. and M.M. Khan. 2002. "Modelling of the Hose and Drogue in Air-to-Air Refuelling." *Aeronautical Journal* 106(1055):17–26.

Bloy, A.W., P.J. Lamont, H.A. Abu-Assaf and K.A.M. Ali. 1986. "The Lateral Dynamic Stability and Control of a Large Receiver Aircraft During Air-to-Air Refueling." *Aeronautical Journal* 90(896):237–243.

Bloy, A.W. and V. Trochalidis. 1989. "The Performance and Longitudinal Stability and Control of Large Receiver Aircraft During Air to Air Refuelling." *Aeronautical Journal* 93(930):367–378.

Bloy, A.W. and V. Trochalidis. 1990. "The Aerodynamic Interference Between Tanker and Receiver Aircraft During Air-to-Air Refueling." *Aeronautical Journal* 94(935):165–171.

Bloy, A.W., V. Trochalidis and M.G. West. 1991. "The Aerodynamic Interference Between a Flapped Tanker Aircraft and a Receiver Aircraft During Air-to-Air Refueling." *Aeronautical Journal* 95(948):274–282.

Bramesfeld, G. and M.D. Maughmer. 2008. "Effects of Wake Rollup on Formation-Flight Aerodynamics." *Journal of Aircraft* 45(4):1167–1173.

Callus, P.J. 2008. Novel Concepts for Conformal Load-bearing Antenna Structure. Technical Report DSTO-TR-2096 Australian Government, Department of Defence, Defence Science and Technology Organisation, Air Vehicles Division (AVD).

Capetta, R., F. Giulietti and M. Innocenti. 2001. WakeCAD: Aerodynamics Interference Caculation Toolbox for Aircraft Design, Simulation and Control. In *AIAA Guidance, Navigation, and Control Conference and Exhibit*. AIAA 2001-4180 Montreal, Canada.

Cheng, Z., D.S. Necsulescu, B. Kim and J.Z. Sasiadek. 2008. Nonlinear Control for UAV Formation Flying. In *Proceedings of the 17th IFAC World Congress*. Seoul, Korea: pp. 791–796.

Cobleigh, B. 2002. Capabilities and Future Applications of the NASA Autonomous Formation Flight (AFF) Aircraft. In *AIAA's 1st Technical Conference and Workshop on Unmanned Aerospace Vehicles*. Portsmouth, VA.

Dalamagkidis, K., K.P. Valavanis and L.A. Piegl. 2008. "On Unmanned Aircraft Systems Issues, Challenges and Operational Restrictions Preventing Integration into the National Airspace System." *Progress in Aerospace Sciences* 44:503–519.

De Bruin, A. 2000*a*. "WAke Vortex Evolution and ENCounter (WAVENC)." *Air & Space Europe* 2(5):84–87.

De Bruin, A.C. 2000*b*. WAVENC, Wake Vortex Evolution and Wake Vortex Encounter. Publishable Synthesis Report NLR-TR-2000-079 NLR.

Denis, A. 2004. A Simplified Vortex Sheet Roll-up Method for Formation Flight. Master's thesis, Massachusetts Institute of Technology.

Department of Defense Dictionary of Military and Associated Terms. 2001. Technical Report Joint Publication 1-02 Joint Chiefs of Staff, The Pentagon, Washington, DC. (As Ammended Through 31 August 2005).

DeYoung, J. and C.W. Harper. 1948. Theoretical Symmetric Span Loading at Subsonic Speeds for Wings Having Arbitrary Plan Form. Technical Report 921 NACA.

Dibley, R.P, M.J. Allen and N. Nabaa. 2007. Autonomous Airborne Refueling Demonstration Phase I Flight-Test Results. In *AIAA Atmospheric Flight Mechanics Conference and Exhibit*. AIAA 2007-6639 Hilton Head, SC.

Doebbler, J., T. Spaeth, J. Valasek, M.J. Monda and H. Schaub. 2007. "Boom and Receptacle Autonomous Air Refueling Using Visual Snake Optical Sensor." *Journal of Guidance, Control, and Dynamics* 30(6):1753–1769.

Dogan, A., E. Kim and W. Blake. 2007. "Control and Simulation of Relative Motion for Aerial Refueling in Racetrack Maneuvers." *Journal of Guidance, Control, and Dynamics* 30(5):1551–1557.

Dogan, A., S. Sato and W. Blake. 2005. Flight Control and Simulation for Aerial Refueling. In *AIAA Guidance, Navigation, and Control Conference and Exhibit*. AIAA 2005-6264 San Francisco, CA.

Dogan, A. and S. Venkataramanan. 2005. "Nonlinear Control for Reconfiguration of Unmanned-Aerial-vehicle Formation." *Journal of Guidance, Control, and Dynamics* 28(4):667–678.

Dogan, A., S. Venkataramanan and W. Blake. 2005. "Modeling of Aerodynamic Coupling Between Aircraft in Close Proximity." *Journal of Aircraft* 42(4):941–955.

Dogan, A., T.A. Lewis and W. Blake. 2008*a*. "Flight Data Analysis and Simulation of Wind Effects During Aerial Refueling." *Journal of Aircraft* 45(6):2036–2048.

Dogan, A., T.A. Lewis and W. Blake. 2008*b*. Wake-Vortex Induced Wind with Turbulence in Aerial Refueling - Part A: Flight Data Analysis. In *AIAA Atmospheric Flight Mechanics Conference and Exhibit*. AIAA 2008-6696 Honolulu, HI.

Dogan, A., T.A. Lewis and W. Blake. 2008*c*. Wake-Vortex Induced Wind with Turbulence in Aerial Refueling - Part B: Model and Simulation Validation. In *AIAA Atmospheric Flight Mechanics Conference and Exhibit*. AIAA 2008-6697 Honolulu, HI.

Durston, A.D. 1993. LinAir: A Multi-Element Discrete Vortex Weissinger Aerodynamics Prediction Method. Technical Memorandum 108786 NASA.

FlightGear Official Website: http://www.flightgear.org/. N.d. Accessed on 06.03.2009. **URL:** *http://www.flightgear.org/*

Gerz, T., F. Holzäpfel and D. Darracq. 2002. "Commercial Aircraft Wake Vortices." *Progress in Aerospace Sciences* 38:181–208.

Gimenes, R., D. Castro Silva, L. Paulo Reis and E. Oliveira. 2008. Flight Simulation Environments Applied to Agent-Based Autonomous UAVs. In *Proceedings of ICEIS 2008 – 10th International Conference on Enterprise Information Systems*. pp. 243–246.

Giulietti, F. and G. Mengali. 2004. "Dynamics and Control of Different Aircraft Formation Structures." *Aeronautical Journal* 108(1081):117–124.

Giulietti, F., L. Pollini and M. Innocenti. 2000. "Autonomous Formation Flight." *IEEE Control Systems Magazine* 20(6):34–44.

Giulietti, F., M. Innocenti, M. Napolitano and L. Pollinia. 2005. "Dynamic and Control Issues of Formation Flight." *Aerospace Science and Technology* 9(1):65–71.

Greene, G.C. 1986. "An Approximate Model of Vortex Decay in the Atmosphere." *Journal of Aircraft* 23:566–573.

Hansen, J., B. Cobleigh, R. Ray, J. Vachon and K. Ennix. 2002. Vortex-Induced Aerodynamic Effects on a Trailing F-18 Aircraft Flying in Close Formation. In *AIAA's 1st Technical Conference and Workshop on Unmanned Aerospace Vehicles*. AIAA 2002-3432 Portsmouth, VA.

Hansen, J.L. and B.R. Cobleigh. 2002. Induced Moment Effects of Formation Flight Using two F/A-18 Aircraft. In *AIAA Atmospheric Flight Mechanics Conference and Exhibit*. AIAA 2002-4489 Monterey, CA.

Hansen, J.L., J.E. Murray and N.V. Campos. 2004. The NASA Dryden AAR Project: A Flight Test Approach to an Aerial Refueling System. In *AIAA Atmospheric Flight Mechanics Conference and Exhibit*. AIAA 2004-4939 Providence, RI.

Hanson, C.E., M.J. Allen, J. Ryan and S.R. Jacobson. 2002. Flight Test Results for an Autonomous Formation Flight Control System. In *AIAA Atmospheric Flight Mechanics Conference and Exhibit*. AAIA 2002-3431 Portsmouth, VA.

Hinton, D.A. 1996. An Aircraft Vortex Spacing System (AVOSS) For Dynamical Wake Vortex Spacing Criteria. In *Proceedings of the AGARD FDP Symposium on "The Characterisation & Modification of Wakes from Lifting Vehicles in Fluid"*. Vol. AGARD-CP-584 Trondheim, Norway.

Hinton, D.A. and C.R. Tatnall. 1997. A Candidate Wake Vortex Strength Definition for Application to the NASA Aircraft Vortex Spacing System (AVOSS). NASA Technical Memorandum 110343 NASA Langley Research Center.

Hoeijmakers, H.W.M. 1996. Vortex Wakes in Aerodynamics. In *Proceedings of the AGARD FDP Symposium on "The Characterisation & Modification of Wakes from Lifting Vehicles in Fluid"*. Vol. AGARD-CP-584 Trondheim, Norway.

Holzäpfel, F., M. Frech, T. Gerz, A. Tafferner, K.-U. Hahn, C. Schwarz, H.-D. Joos, B. Korn, H. Lenz, R. Luckner and G. Hohne. 2009. "Aircraft Wake Vortex Scenarios Simulation Package – WakeScene." *Aerospace Science and Technology* 13:1–11.

Houghton, E.L. and P.W. Carpenter. 1993. *Aerodynamics for Engineering Students*. Fourth ed. Edward Arnold.

Hummel, D. 1996. The Use of Aircraft Wakes to Achieve Power Reductions in Formation Flight. In *Proceedings of the AGARD FDP Symposium on "The Characterisation & Modification of Wakes from Lifting Vehicles in Fluid"*. Vol. AGARD-CP-584 Trondheim, Norway.

Jacquin, L. 2005. "Aircraft Trailing Vortices: an Introduction." *Comptes Rendus Physique* 6(4-5):395–398.

Jacquin, L., D. Fabre, P. Geffroy and E. Coustols. 2001. The Properties of a Transport Aircraft Wake in the Extended Near Field: an Experimental Study. In *39th AIAA Aerospace Sciences Meeting and Exhibit*. AIAA 2001-1038 Reno, NV.

Jenkinson, L.R., R.E. Caves and D.P. Rhodes. 1995. Automatic Formation Flight "A preliminary investigation into the application to civil operations". In *1st AIAA Aircraft Engineering, Technology, and Operations Congress*. AIAA 95-3898 Los Angeles, CA.

Karakus, C., H. Akilli and B. Sahin. 2008. "Formation, structure, and development of near-field wing tip vortices." *Proceedings of the Institution of Mechanical Engineers Part G: Journal of Aerospace Engineering* 222:13–22.

Karkehabadi, R. 2004. "Wind-Tunnel Measurements of Hazard Posed by Lift-Generated Wakes." *Journal of Aircraft* 41(6):1424–1429.

Katz, J. and A. Plotkin. 2001. *Low-Speed Aerodynamics*. Second ed. Cambridge University Press.

Kenny, J., K. Takeda and G. Thomas. 2008. Real-Time Computational Fluid Dynamics for Flight Simulation. In *The Interservice/Industry Training, Simulation & Education Conference (I/ITSEC)*. Orlando, FL.

Kurylowich, G. 1979. A Method for Assessing the Impact of Wake Vortices on USAF Operations. Technical Report AFFDL-TR-79-3060 Air Force Flight Dynamics Laboratory Wright-Patterson Air Force Base, OH 45433.

Lavretsky, E. and K. Misovec. 2002. Phase I: Formation Flight Control Design. In *AIAA's 1st Technical Conference and Workshop on Unmanned Aerospace Vehicles*. AAIA 2002-3429 Portsmouth, VA.

Le Moigne, A. and N. Qin. 2006. LES with Numerical Dissipation for Aircraft Wake Vortices. In *44th AIAA Aerospace Sciences Meeting and Exhibit*. AIAA 2006-1258 Reno, NV.

Lewis, T.A. 2008. Flight Data Analysis and Simulation of Wind Effects during Aerial Refueling. Master's thesis, The University of Texas at Arlington.

Loh, R., Y. Bian and T. Roe. 2009. "UAVs in Civil Airspace: Safety Requirements." *IEEE A&E Systems Magazine* 24:5–17.

Margason, R.J., S.O. Kjelgaard, W.L. III Sellers, C.E.K. Jr. Morris, K.B. Walkey and E.W. Shields. 1985. Subsonic Panel methods – A Comparison of Several Production Codes. In *AIAA 23rd Aerospace Sciences Meeting*. AIAA 85-0280 Reno, NV.

McFarlane, C., T.S. Richardson and C.D.C. Jones. 2007. Cooperative Control During Boom Air-to-Air Refueling. In *AIAA Guidance, Navigation and Control Conference and Exhibit*. AIAA 2007-6586 Hilton Head, SC.

Melin, T. 2000. A Vortex Lattice MATLAB Implementation for Linear Aerodynamic Wing Applications. Master's thesis, Royal Institute of Technology (KTH), Sweden.

Modi, A., L.N. Long and P.E. Plassmann. 2002. Real-Time Visualization of Wake-Vortex Simulations using Computational Steering and Beowulf Clusters. In *5th International Conference on Vector and Parallel Processing Systems and Applications (VECPAR)*. Portugal.

Myatt, J.H. and W.B. Blake. 1999. Aerodynamic Database Issues for Modeling Close Formation Flight. In *AIAA Modeling and Simulation Technologies Conference*. AAIA 99-4194 Portland, OR: pp. 317–327.

Nalepka, J.P. and J.L. Hinchman. 2005. Automated Aerial Refueling: Extending the Effectiveness of Unmanned Air Vehicles. In *AIAA Modeling and Simulation Technologies Conference and Exhibit*. AIAA 2005-6005 San Francisco, CA.

Nelson, R.C. 1974. The Dynamic Response of Aircraft Encountering Aircraft Wake Turbulence. Technical Report AFFDL-TR-74-29 Wrigh-Patterson AFB Flight Dynamics Laboratory.

Niculescu, M. 2001. Lateral Track Control Law for Aerosonde UAV. In *39th AIAA Aerospace Sciences Meeting and Exhibit*. AIAA 20010016 Reno, NV.

Owens, D.B. 1998. Weissinger's Model of the Nonlinear Lifting-Line Method for Aircraft Design. In *Proceedings of the 36th Aerospace Sciences Meeting and Exhibit*. Reno, NV.

Pachter, M., J.J. D'Azzo and A.W. Proud. 2001. "Tight Formation Flight Control." *Journal of Guidance, Control, and Dynamics* 24(2):246–254.

Proceedings of the AGARD Fluid Dynamics Panel Symposium on "The Characterisation & Modification of Wakes from Lifting Vehicles in Fluid". 1996. Number AGARD-CP-584 Tronheim, Norway: AGARD.

Proctor, F.H. and G.F. Switzer. 2000. Numerical Simulation of Aircraft Trailing Vortices. In *9th Conference on Aviation, Range and Aerospace Meteorology*. Number 7.12 American Meteorology Society pp. 511–516.

Qureshi, S. 2008. The Design of a Trajectory Following Controller for Unmanned Aerial Vehicles. Master's thesis, School of Engineering, Cranfield University.

Rasmussen, S.J. and G.B. Breslin. 1997. AVDS: a Flight Systems Design Tool for Visualization and Engineer-in-the-Loop Simulation. In *AIAA Guidance, Navigation, and Control Conference and Exhibit*. AIAA 1997-3467 New-Orleans, LA.

Rasmussen, S.J. and P.R. Chandler. 2002. MultiUAV: a Multiple UAV Simulation for Investigation of Cooperative Control. In *Proceedings of the 2002 Winter Simulation Conference*. San Diego, CA: pp. 869–877.

Rossow, V.J. and K.D. James. 2000. "Overview of Wake-Vortex Hazards During Cruise." *Journal of Aircraft* 37(6):960–975.

Rutishauser, David K. and Cornelius J. O'Connor. 2001. The NASA Aircraft VOrtex Spacing System (AVOSS): Concept Demonstration Results and Future Direction. Technical Report NASA-2001-46atca-dkr NASA Langley.

Saban, D. and J. Whidborne. 2009*a*. Integration of Wake Vortex Effects in Simulations of UAVs in Close Formation Flight. In *24th International UAV Systems Conference*. Bristol, UK: pp. 23.1–23.14.

Saban, D. and J.F. Whidborne. 2009*b*. Modeling of Wake Vortex Effects for Unmanned Air Vehicle Simulations. In *AIAA Modeling and Simulation Technologies Conference*. AIAA 2009-5686 Chicago, OH.

Saban, D., J.F. Whidborne and A.K. Cooke. 2009. "Simulation of Wake Vortex Effects for UAVs in Close Formation Flight." *Aeronautical Journal* 113(1149):727–738.

Sarpkaya, T. 1989. "Computational Methods With Vortices – The 1988 Freeman Scholar Lecture." *Journal of Fluids Engineering* 111:5–52. Transactions of the ASME.

Schlichting, H. 1979. *Aerodynamics of the Airplane*. McGraw-Hill.

Seanor, B., G. Campa, Y. Gu, M. Napolitano, L. Rowe and M. Perhinschi. 2004. Formation Flight Test Results for UAV Research Aircraft Models. In *AIAA 1st Intelligent Systems Technical Conference*. AAIA 2004-6251 Chicago, IL: pp. 230–243.

Shen, S., F. Ding, J. Han, Y.-L. Lin and S. P. Arya. 1999. Numerical Modeling Studies of Wake Vortices: Real Case Simulations. In *AIAA 37th Aerospace Sciences Meeting and Exhibit*. AIAA 1999-0755 Reno, NV.

Shim, H.D., J.-S. Han and H.-T. Yeo. 2009. "A Development of Unmanned Helicopters for Industrial Applications." *Journal of Intelligent and Robotic Systems* 54:407–421.

Sorton, E.F. and S. Hammaker. 2005. Simulated Flight Testing of an Autonomous Unmanned Aerial Vehicle Using FlightGear. In *AIAA Infotech@Aerospace 2005 Conference and Exhibit*. AIAA 2005-7083 Arlington, VA.

Spence, G.T., A. Le Moigne, D.J. Allerton and N. Qin. 2007. "Wake Vortex Model for Real-Time Flight Simulation Based on Large Eddy Simulation." *Journal of Aircraft* 44(2):467–475.

Spence, G.T., D.J. Allerton, A. Le Moigne and N. Qin. 2005. Real-Time Model of Wake Vortices Based on Large Eddy Simulation Datasets. In *AIAA Modeling and Simulation Technologies Conference and Exhibit*. AIAA 2005-6205 San Fracisco, CA.

Switzer, G.F. 1996. Validation Tests of TASS for Application to 3-D Vortex Simulations. NASA Contractor Report 4756 NASA.

Tandale, M.D., R. Bowers and J. Valasek. 2006. "Trajectory Tracking Controller for Vision-Based Probe and Drogue Autonomous Aerial Refueling." *Journal of Guidance, Control, and Dynamics* 29(4):846–857.

The Mathworks Official Website: http://www.mathworks.com/. N.d. Accessed on 21.10.2009.
URL: *http://www.mathworks.com/*

Tornado Website: http://www.redhammer.se/tornado/index.html. N.d. Accessed on 12.05.2008.
URL: *http://www.redhammer.se/tornado/index.html*

Unmanned Dynamics Aerosim Blockset Official Website: http://www.u-dynamics.com/aerosim/. N.d. Accessed on 27.01.2009.
URL: *http://www.u-dynamics.com/aerosim/*

Vachon, M.J., R.J. Ray, K.R. Walsh and K. Ennix. 2002. F/A–18 Aircraft Performance Benefits Measured During the Autonomous Formation Flight Project. In *AIAA Flight Mechanics Conference and Exhibit*. AIAA 2002-4491 Monterey, CA.

Valasek, J., K. Gunnam, J. Kimmett, M.D. Tandale, Junkins J.L. and D. Hughes. 2005. "Vision-Based Sensor and Navigation System for Autonomous Air Refueling." *Journal of Guidance, Control, and Dynamics* 28(5):979–989.

Venkataramanan, S. and A. Dogan. 2004*a*. Dynamic Effects of Trailing Vortex with Turbulence & Time-varying Inertia in Aerial Refueling. In *AIAA Atmospheric Flight Mechanics Conference and Exhibit*. AIAA 2004-4945 Providence, RI.

Venkataramanan, S. and A. Dogan. 2004*b*. Modeling of Aerodynamic Coupling Between Aircraft in Close Proximities. In *AIAA Atmospheric Flight Mechanics Conference and Exhibit*. AIAA 2004-5172 Providence, RI.

Venkataramanan, S. and A. Dogan. 2004*c*. A Multi-UAV Simulation for Formation reconfiguration. In *AIAA Modeling and Simulation Technologies Conference and Exhibit*. AIAA 2004-4800 Providence, RI.

Venkataramanan, S., A. Dogan and W. Blake. 2003. Vortex Effect Modelling In Aircraft Formation Flight. In *AIAA Atmospheric Flight Mechanics Conference and Exhibit*. AIAA 2003-5385 Austin, TX.

Vlachos, P. and D. Telionis. 2003. Wing-tip-to-wing-tip Aerodynamic Interference. In *AIAA 41st Aerospace Sciences Meeting and Exhibit*. AIAA 2003-0609 Reno, NV.

Wagner, G., D. Jacques, W. Blake and M. Pachter. 2001. An Analytical Study of Drag Reduction in Tight Formation Flight. In *AIAA Atmospheric Flight Mechanics Conference and Exhibit*. AIAA 2001-4075 Montreal, Canada.

Wagner, G., D. Jacques, W. Blake and M. Pachter. 2002. Flight Test Results of Close Formation Flight for Fuel Savings. In *AIAA Atmospheric Flight Mechanics Conference and Exhibit*. AIAA 2002-4490 Monterey, CA.

Waishek, J., A. Dogan and W. Blake. 2009. "Derivation of the Dynamics Equations of Receiver Aircraft in Aerial Refueling." *Journal of Guidance, Control, and Guidance* 32(2):585–597.

Wang, Z. and D.T. Mook. 2003. Numerical Aerodynamic Analysis of Formation Flight. In *41st Aerospace Sciences Meeting and Exhibit*. AAIA 2003-610 Reno, NV.

Weissinger, J. 1947. The Lift Distribution of Swept-Back Wings. Technical Memorandum 1120 NACA.

Zhang, Y., F.Y. Wang and J.C. Hardin. 2003. Spectral Characteristics of Wake Vortex Sound During Roll-Up. Contractor Report NASA/CR-2003-212673 NASA Langley Research Center.

Appendix A

Aerosonde's Flight Control System Design

The Aerosonde UAV model used in association with ELL in Chapter 6 was derived from the one provided in the Unmanned Dynamics AeroSim Blockset [*Unmanned Dynamics Aerosim Blockset Official Website: http://www.u-dynamics.com/aerosim/*, N.d.] and adapted for use with the Mathworks Aerospace Blockset by Dr J.F. Whidborne. For the purposes of this research, it was trimmed, linearised, augmented, and a control scheme (attitude hold, velocity hold, altitude hold, and heading hold) was developed for trajectory tracking using PID control. The aim of this appendix is to give an overview of the Aerosonde model FCS: the trimming and linearisation processes are explained in Section A.1, and the Stability Augmentation System (SAS), attitude control system, autopilot and trajectory tracker are briefly described in Sections A.2, A.3, A.4 and A.5 respectively. The work presented in this appendix has been adapted from Qureshi [2008].

A.1 Trimming and Linearisation

A.1.1 Trimming

The Aerosonde model was trimmed for straight and level flight. The state vector **x**, input vector **u** and output vector **y** were chosen as:

$$\mathbf{x} = \begin{bmatrix} u & v & w & \phi & \theta & \psi & X_e & Y_e & Z_e & p & q & r & f & \Omega \end{bmatrix}^T \tag{A.1}$$

$$\mathbf{u} = \begin{bmatrix} \eta & \xi & \zeta & \tau \end{bmatrix}^T \tag{A.2}$$

$$\mathbf{y} = \begin{bmatrix} V & \alpha & \beta & \phi & \theta & \psi & X_e & Y_e & Z_e \end{bmatrix}^T \tag{A.3}$$

The initial conditions used for trimming the Aerosonde open loop model are listed in Tables A.1 (initial state vector), A.2 (initial state derivative vector), A.3 (initial input vector) and A.4 (initial output vector).

Table A.1: Initial state vector, $\mathbf{x_0}$

Variable	Trim Value	Status	Definition
u	25 m/s		Straight and level flight condition
v	0 m/s		
w	0 m/s		
ϕ	0 rad		Straight and level flight condition
θ	0 rad		
ψ	0 rad		
X_e	0 m		Aircraft initial position
Y_e	0 m	Fixed	
Z_e	-1000 m	Fixed	
p	0 rad/s	Fixed	Straight and level flight condition
q	0 rad/s	Fixed	
r	0 rad/s	Fixed	
f	2 kg	Fixed	Aircraft mass and CG position change during flight due to fuel consumption
Ω	5236 rpm		Initial engine speed

The data obtained for trimmed flight are summarised in Table A.5.

A.1.2 Linearisation

The Aerosonde model was then linearised around its trim conditions (determined by $\mathbf{x_{trim}}$, $\mathbf{u_{trim}}$ and $\mathbf{y_{trim}}$) using the Matlab command `linmodv5.m`, and the four matrices of the state-space representation (Equation A.4) were obtained:

$$\dot{\mathbf{x}} = \mathbf{A} \cdot \mathbf{x} + \mathbf{B} \cdot \mathbf{u} \tag{A.4}$$

$$\mathbf{y} = \mathbf{C} \cdot \mathbf{x} + \mathbf{D} \cdot \mathbf{u} \tag{A.5}$$

Table A.2: Initial state derivative vector, $\dot{\mathbf{x}}_\mathbf{0}$

Variable	Trim Value	Status	Definition
$\dot{u}$	0 m/s^2	Fixed	
$\dot{v}$	0 m/s^2	Fixed	Straight and level flight condition
$\dot{w}$	0 m/s^2	Fixed	
$\dot{\phi}$	0 rad/s	Fixed	
$\dot{\theta}$	0 rad/s	Fixed	Straight and level flight condition
$\dot{\psi}$	0 rad/s	Fixed	
$\dot{X}_e$	25 m/s	Fixed	
$\dot{Y}_e$	0 m/s	Fixed	Straight and level flight condition
$\dot{Z}_e$	0 m/s	Fixed	
$\dot{p}$	0 rad/s^2	Fixed	
$\dot{q}$	0 rad/s^2	Fixed	Straight and level flight condition
$\dot{r}$	0 rad/s^2	Fixed	
$\dot{f}$	0 kg/s		
$\dot{\Omega}$	0 rpm/s	Fixed	

Table A.3: Initial input vector, $\mathbf{u}_\mathbf{0}$

Variable	Trim Value	Status	Definition
η	-0.1 rad		
ξ	0 rad		Straight and level flight condition
ζ	0 rad		
τ	0.5		Half-throttle

where **A**, **B**, **C** and **D** are the state, input, output and transmission matrices respectively. The longitudinal and lateral-directional dynamics were then decoupled by separating their respective states, and used for basic stability augmentation:

- Longitudinally:

$$\dot{\mathbf{x}_{\mathbf{longi}}} = \mathbf{A_{longi}} \cdot \mathbf{x_{longi}} + \mathbf{B_{longi}} \cdot u_{longi} \tag{A.6}$$

$$\mathbf{y_{longi}} = \mathbf{C_{longi}} \cdot x_{longi} + \mathbf{D_{longi}} \cdot \mathbf{u_{longi}} \tag{A.7}$$

Table A.4: Initial output vector, $\mathbf{y_0}$

Variable	Trim Value	Status	Definition
V	25 m/s	Fixed	Straight and level flight condition
α	0 rad		
β	0 rad		
ϕ	0 rad	Fixed	Straight and level flight condition
θ	0 rad		
ψ	0 rad		
X_e	0 m		
Y_e	0 m	Fixed	Straight and level flight condition
Z_e	-1000 m	Fixed	Straight and level flight condition

Table A.5: Data for trimmed flight

State trim $\mathbf{x_{trim}}$		Derivative trim $\dot{\mathbf{x}}_{\mathbf{trim}}$	Input trim $\mathbf{u_{trim}}$		Output trim $\mathbf{y_{trim}}$	
u	24.960 m/s	0.0000 m/s^2	η	-0.0750	V	25.000
v	0.0142 m/s	0.0000 m/s^2	ξ	-0.0085	α	0.0564
w	1.4082 m/s	0.0000 m/s^2	ζ	-0.0007	β	0.0006
ϕ	0.0000 rad	0.0000 rad/s	τ	0.07063	ϕ	0.0000
θ	0.0564 rad	0.0000 rad/s			θ	0.0564
ψ	-0.0006 rad	0.0000 rad/s			ψ	0.0006
X_e	0.0000 m	25.000 m/s			X_e	0.0000
Y_e	0.0000 m	0.0000 m/s			Y_e	0.0000
Z_e	-1000.0 m	0.0000 m/s			Z_e	-1000.0
p	0.0000 rad/s	0.0000 rad/s^2				
q	0.0000 rad/s	0.0000 rad/s^2				
r	0.0000 rad/s	0.0000 rad/s^2				
f	2.0000 kg	0.0000 kg/s				
Ω	545.40 rpm	0.0000 rpm/s				

with:

$$\mathbf{x_{longi}} = \begin{bmatrix} u & w & q & \theta & Z_e & X_e & \Omega \end{bmatrix}^T \tag{A.8}$$

$$\mathbf{u_{longi}} = \begin{bmatrix} \eta & \tau \end{bmatrix}^T \tag{A.9}$$

$$\mathbf{y_{longi}} = x_{longi} = \begin{bmatrix} u & w & q & \theta & Z_e & X_e & \Omega \end{bmatrix}^T \tag{A.10}$$

- Laterally-directionally:

$$\dot{\mathbf{x}}_{\mathbf{lat}} = \mathbf{A}_{\mathbf{lat}} \cdot \mathbf{x}_{\mathbf{lat}} + \mathbf{B}_{\mathbf{lat}} \cdot \mathbf{u}_{\mathbf{lat}} \tag{A.11}$$

$$\mathbf{y}_{\mathbf{lat}} = \mathbf{C}_{\mathbf{lat}} \cdot x_{lat} + \mathbf{D}_{\mathbf{lat}} \cdot \mathbf{u}_{\mathbf{lat}} \tag{A.12}$$

with:

$$\mathbf{x}_{\mathbf{lat}} = \begin{bmatrix} v & \phi & \psi & p & r & Y_e \end{bmatrix}^T \tag{A.13}$$

$$\mathbf{u}_{\mathbf{lat}} = \begin{bmatrix} \xi & \zeta \end{bmatrix}^T \tag{A.14}$$

$$\mathbf{y}_{\mathbf{lat}} = \mathbf{x}_{\mathbf{lat}} = \begin{bmatrix} v & \phi & \psi & p & r & Y_e \end{bmatrix}^T \tag{A.15}$$

The characteristics of the open loop longitudinal and lateral-directional stability modes are presented in Tables A.6 and A.7 respectively. Table A.6 shows that both the SPPO and the phugoid modes are stable and under-damped.

Table A.6: Longitudinal open loop dynamics - Eigenvalues

Eigenvalues	Damping	Freq. (rad/s)	Mode
0.00	–	–	Surge
$-4.45 \pm 10.5i$	0.390	11.4	SPPO
-3.22	–	–	Engine dynamics
$-6.00 \cdot 10^{-2} \pm 0.531i$	–	–	Phugoid
$-6.60 \cdot 10^{-4}$	1.00	$6.60 \cdot 10^{-4}$	Heave

As for the lateral-directional dynamics, Table A.7 shows that both the Dutch roll and the roll subsidence modes are stable. The spiral mode, however, has a real positive eigenvalue and is therefore unstable. This is probably due to the unidirectional rotation of the propeller as well as to the unconventional shape of the tailplane. The other poles listed in Tables A.6 and A.7 are due to the engine dynamics and to the inclusion of the navigation equations; they do not contribute to the airframe stability.

Table A.7: Lateral-directional open loop dynamics - Eigenvalues

Eigenvalues	Damping	Freq. (rad/s)	Mode
0.00	–	–	Sway
0.00	–	–	Heading
-19.9	–	–	Roll subsidence mode
$-1.28 \pm 5.83i$	0.214	5.96	Dutch roll mode
$5.33 \cdot 10^{-2}$	–	–	Spiral mode

A.2 Stability Augmentation System

A.2.1 Architecture

The architecture of the Aerosonde's SAS is shown in Figure A.1. It is comprised of:

- **a pitch axis stabiliser** which consists of a pitch rate and a pitch attitude to elevator feedbacks (gains: K_{q_η} and K_{θ_η}),
- **a yaw damper** which consists of a yaw rate to rudder feedback (gain: K_{r_ζ}) with a washout filter (time constant T_r), and
- **a spiral mode stabiliser** (to compensate the destabilising effect of the washout filter on the spiral mode) which consists of a bank angle to aileron feedback (gain: K_{ϕ_ξ}).

Furthermore, an aileron to rudder interlink (gain: K_{ari}) has been added in order to prevent sideslip during the execution of a turn.

A.2.2 Gains

The SAS' gains, as well as the washout filter time constant, are listed in Table A.8.

Table A.8: Gains and time constant - SAS

K_{q_η}	K_{θ_η}	K_{r_ζ}	T_r	K_{ϕ_ξ}	K_{ari}
-0.28	-1	-0.25	0.75	-0.2	0.5

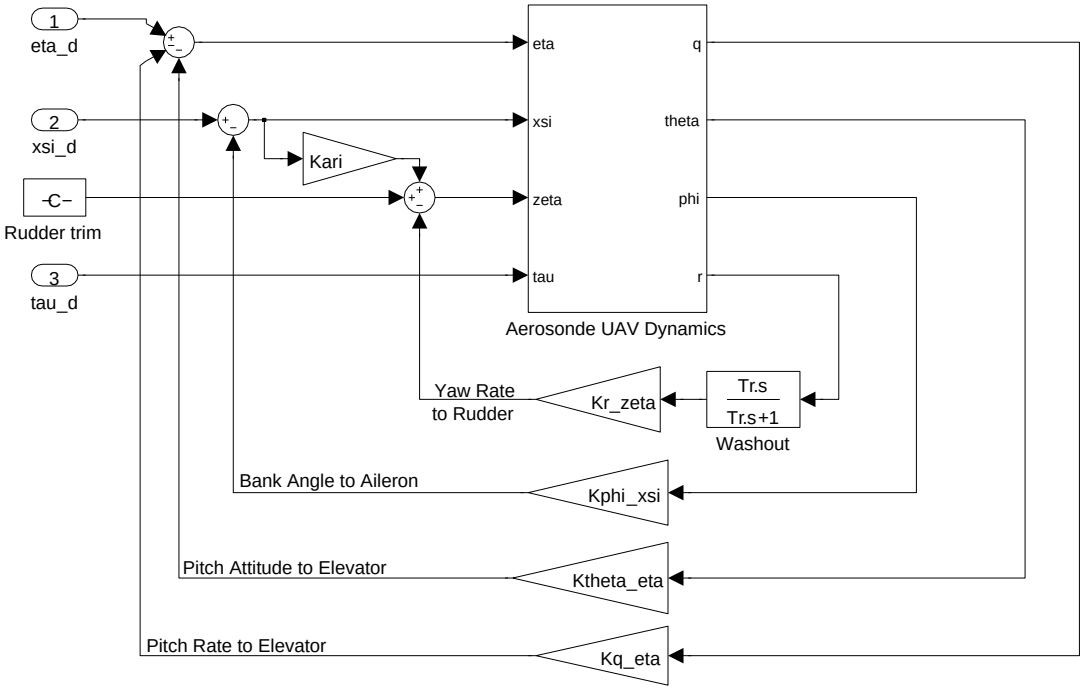

Figure A.1: Architecture of the Aerosonde's SAS

A.2.3 Time Responses

The dynamic modes of the unaugmented and augmented Aerosonde UAV are illustrated in the following time responses: the SPPO is shown through the Aerosonde's response to an elevator step input (Figure A.2), the phugoid is shown through the Aerosonde's response to an elevator impulse input (Figure A.3), the Dutch roll is shown through the Aerosonde's response to a rudder impulse input (Figure A.4), the roll subsidence mode is shown through the Aerosonde's response to an aileron step input (Figure A.5), and spiral mode is shown through the Aerosonde's response to an aileron impulse input (Figure A.6).

A.3 Attitude Control System

A.3.1 Architecture

The attitude control system is wrapped around the SAS. Its architecture is shown in Figure A.7. It is comprised of:

- **a pitch attitude controller** which consists of a pitch angle to elevator demand feedback with P+I compensation (gains: K_{p_θ} and K_{i_θ}), and

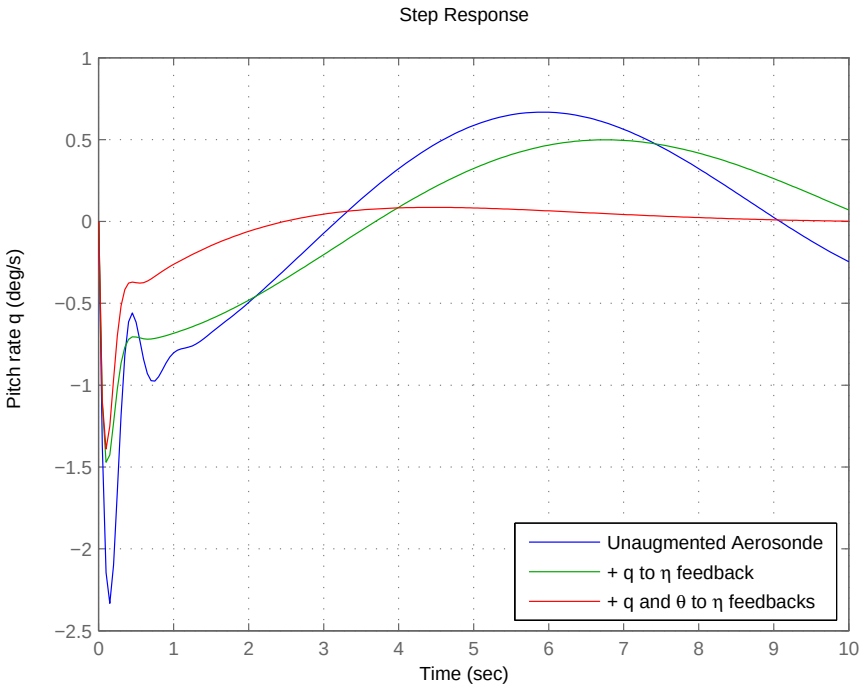

Figure A.2: SAS – Aerosonde's response to unit (deg) elevator step input – SPPO

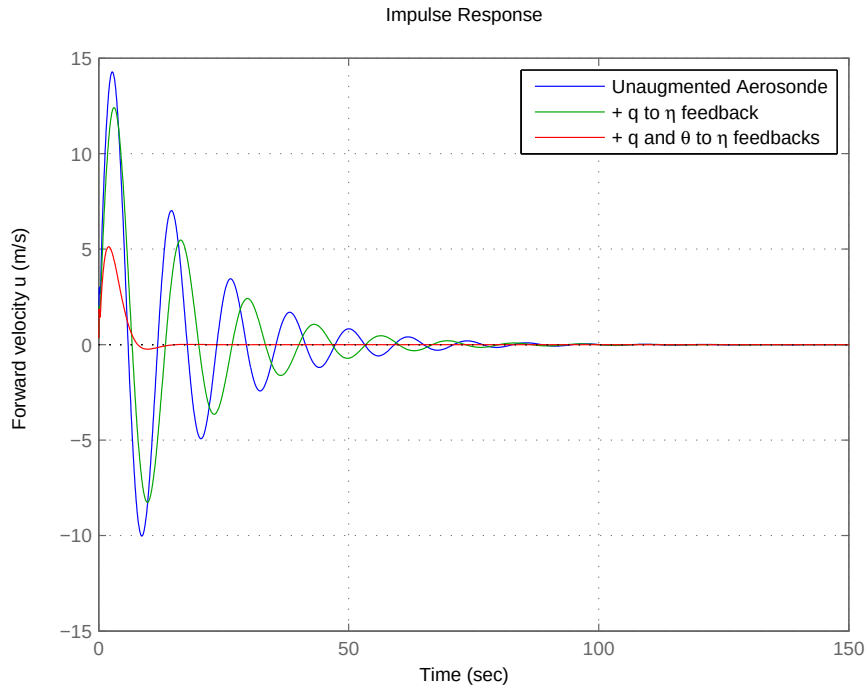

Figure A.3: SAS – Aerosonde's response to unit (deg) elevator impulse input – Phugoid

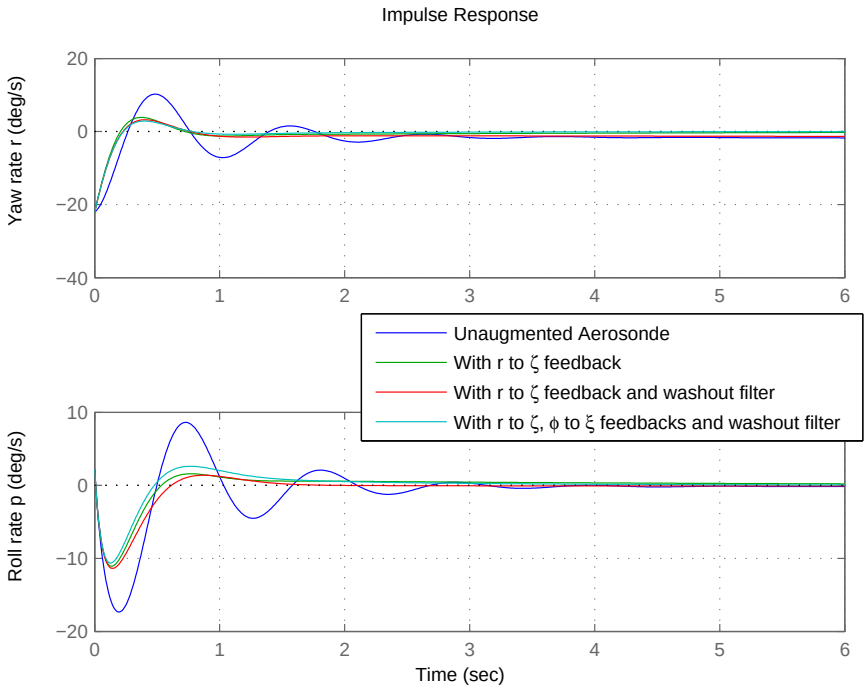

Figure A.4: SAS – Aerosonde's response to unit (deg) rudder impulse input – Dutch Roll

- **a roll attitude controller** which consists of a bank angle to aileron demand feedback with P+I compensation (gains: K_{p_ϕ} and K_{i_ϕ}).

Furthermore, a saturation limit – corresponding to the elevator full deflection angles – has been applied to the elevator demand. In order to prevent integration errors once the system attains its saturation limit (causing it to behave as an open loop system), an anti-wind up scheme has also been added.

A.3.2 Gains

The attitude control system's gains are listed in Table A.9.

Table A.9: Gains - Attitude control system

K_{p_θ}	K_{i_θ}	K_{p_ϕ}	K_{i_ϕ}
-0.8	-0.8	-0.2	-0.1

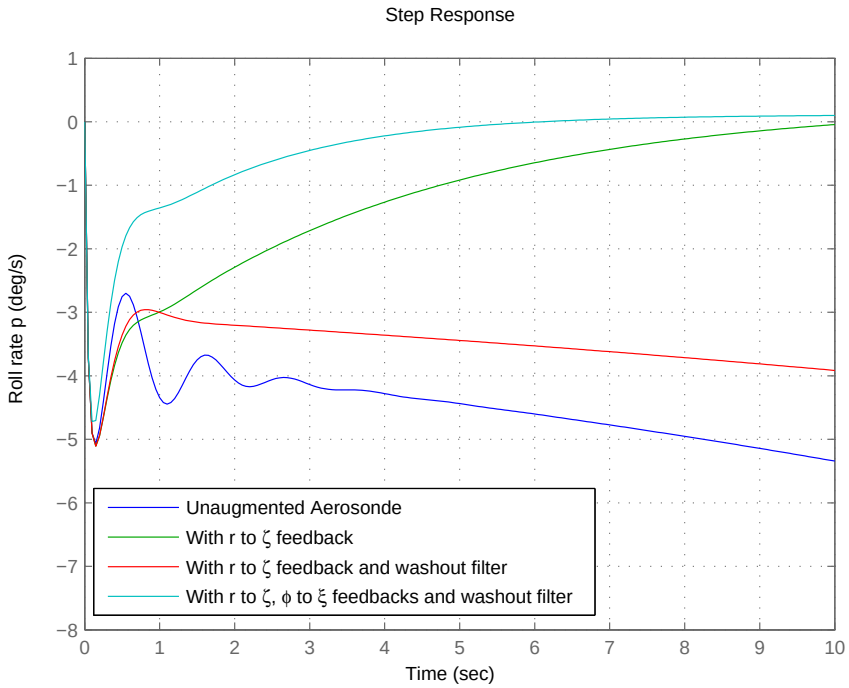

Figure A.5: SAS – Aerosonde's response to unit (deg) aileron step input – Roll Subsidence Mode

A.3.3 Time Responses

The Aerosonde's response to an elevator step input is shown in Figure A.8, and the Aerosonde's response to an aileron step input is shown in Figure A.9. These demonstrate the characteristics of the attitude control system (pitch attitude and roll attitude controllers respectively).

A.4 Autopilot

A.4.1 Architecture

The autopilot is wrapped around the attitude control system. Its architecture is shown in Figure A.10. It is comprised of:

- **a speed controller** which consists of a velocity to throttle demand feedback with P+I compensation (gains: $K_{p\_V_e}$ and $K_{i\_V_e}$),
- **an altitude controller** which consists of an altitude to elevator demand feedback with PID compensation (gains: $K_{p\_Z_e}$, $K_{i\_Z_e}$ and $K_{d\_Z_e}$), and

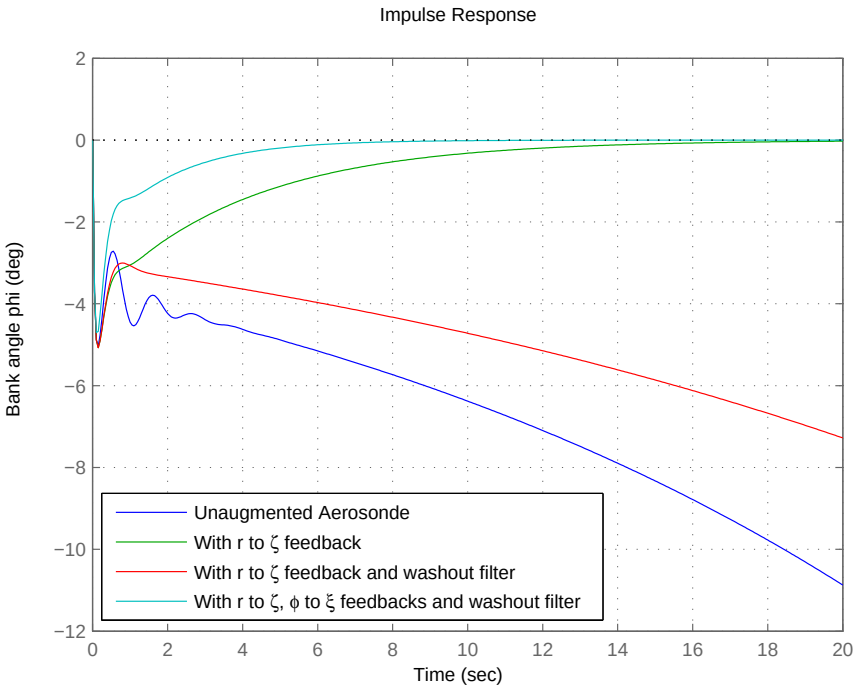

Figure A.6: SAS – Aerosonde's response to unit (deg) aileron impulse input – Spiral Mode

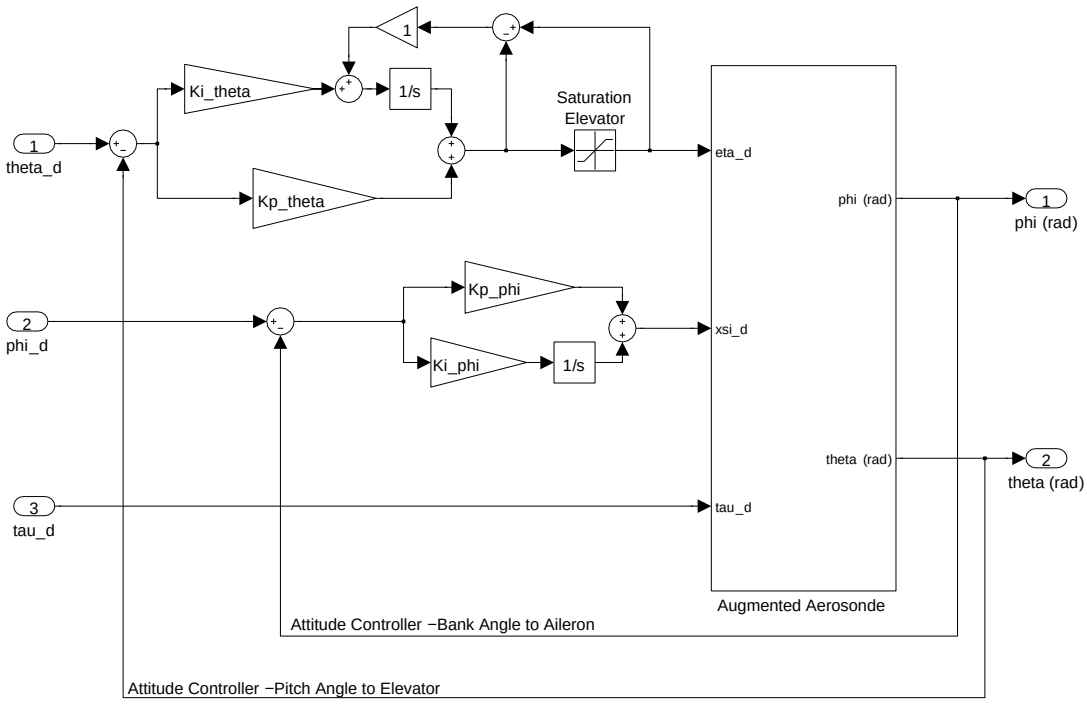

Figure A.7: Architecture of the Aerosonde's attitude control system

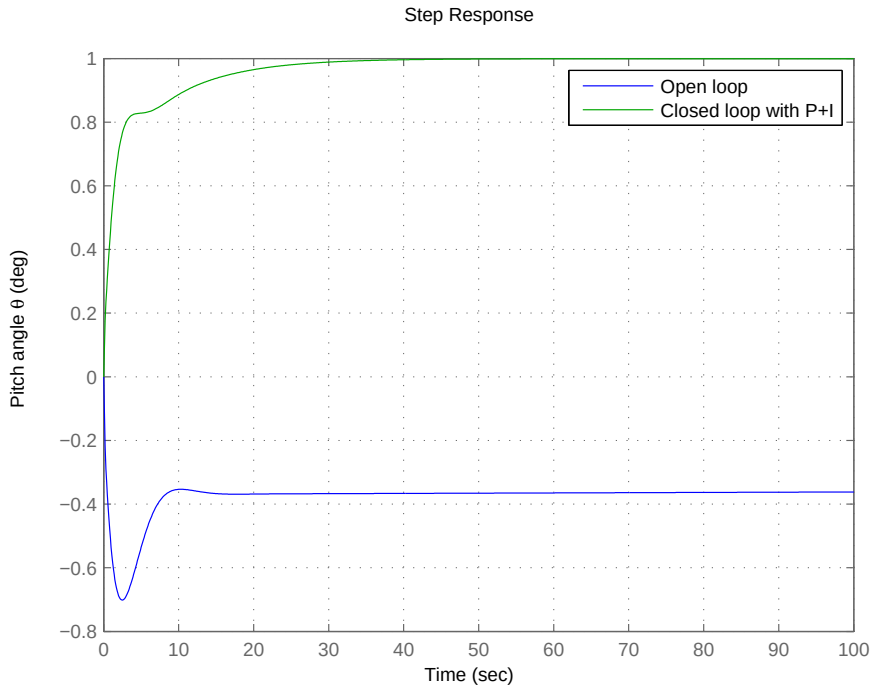

Figure A.8: Attitude control system – Aerosonde's response to unit (deg) elevator step input – Pitch attitude hold

- **a heading controller** which consists of heading to bank angle demand feedback with P+I compensation (gains: K_{p_χ} and K_{i_χ})

Furthermore, a saturation limit – corresponding to the throttle being fully closed and fully open respectively – has been applied to the throttle demand. As for the pitch attitude controller, an anti-wind up scheme has then been added in order to prevent integration errors once the system attains its saturation limit.

A.4.2 Gains

The autopilot's gains are listed in Table A.10.

Table A.10: Gains - Autopilot

$K_{p\_Z_e}$	$K_{i\_Z_e}$	$K_{d\_Z_e}$	K_{p_χ}	K_{i_χ}	$K_{p\_V_e}$	$K_{i\_V_e}$
-0.03	-0.0001	-0.05	0.7	0.001	0.5	0.15

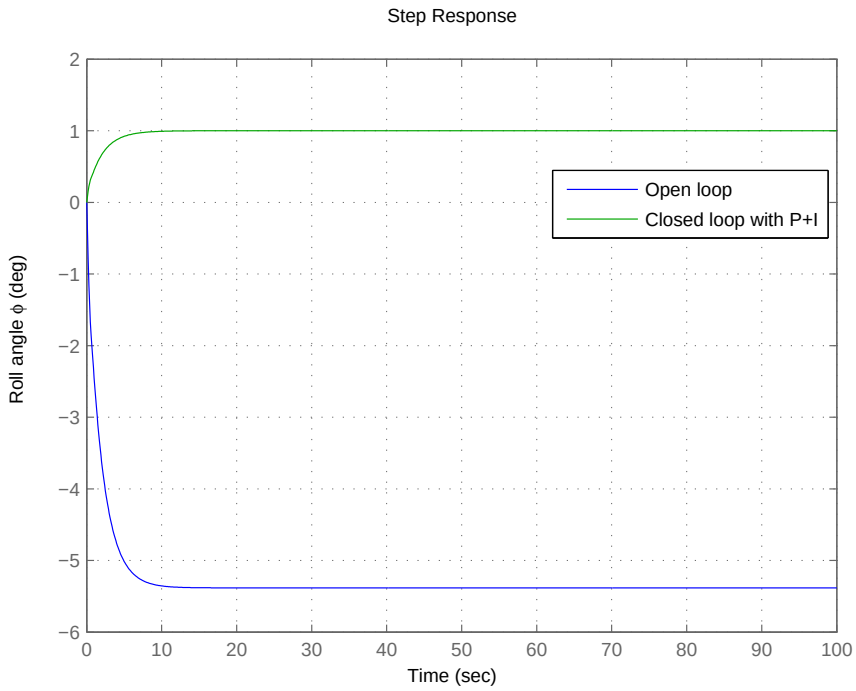

Figure A.9: Attitude control system – Aerosonde's response to unit (deg) aileron step input – Roll angle hold

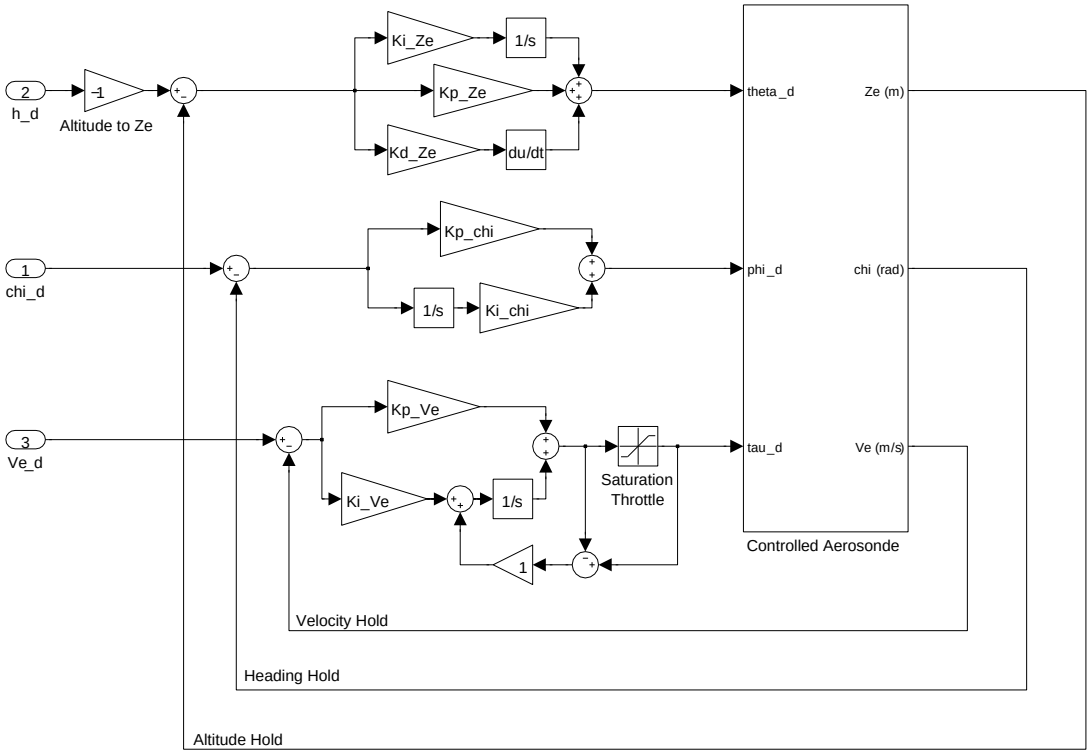

Figure A.10: Architecture of the Aerosonde's autopilot

A.4.3 Characteristics of the Closed Loop Stability Modes

The characteristics of the closed loop longitudinal stability modes are presented in Table A.11. All the poles are stable (negative real part), and the dampings of the SPPO and of the phugoid modes have been significantly improved (from $\zeta_{SPPO} = 0.390$ to $\zeta_{SPPO} = 0.579$ and from $\zeta_{Phugoid} = 0.112$ to $\zeta_{Phugaid} = 0.588$ respectively).

Table A.11: Longitudinal closed loop dynamics - Eigenvalues

Eigenvalues	Damping	Freq. (rad/s)	Mode
$-3.37 \cdot 10^{-3}$	–	–	
-0.301	–	–	
$-0.211 \pm 0.289i$	0.588	0.358	Phugoid
$-0.824 \pm 1.02i$	0.627	1.31	
-2.78	–	–	
$-8.04 \pm 11.3i$	0.579	13.9	SPPO

Similarly, the characteristics of the closed loop lateral-directional stability modes are presented in Table A.12. All the poles are now stable (negative real part), including the pole corresponding to the spiral mode. Also, the damping of the Dutch roll mode has improved (from $\zeta_{DR} = 0.214$ to $\zeta_{DR} = 0.800$), and the time constant of the roll subsidence mode has slightly increased (from $T_R = 0.0503$ s to $T_R = 0.0617$ s).

Table A.12: Lateral-directional closed loop dynamics - Eigenvalues

Eigenvalues	Damping	Freq. (rad/s)	Mode
$-1.44 \cdot 10^{-3}$	–	–	
$-0.264 \pm 0.253i$	0.722	0.365	
-0.542	–	–	Spiral mode
-2.10	–	–	
$-4.90 \pm 3.67i$	0.800	6.12	Dutch roll mode
-16.2	–	–	Roll subsidence mode

A.4.4 Time Responses

The characteristics of the speed controller are illustrated in Figure A.11 through the Aerosonde time response to a unit thrust step input. Likewise, the characteristics of

the altitude controller and the heading controller are illustrated in Figures A.13, **??** and A.14 through the Aerosonde time responses to a unit altitude step input and to a unit heading step input respectively.

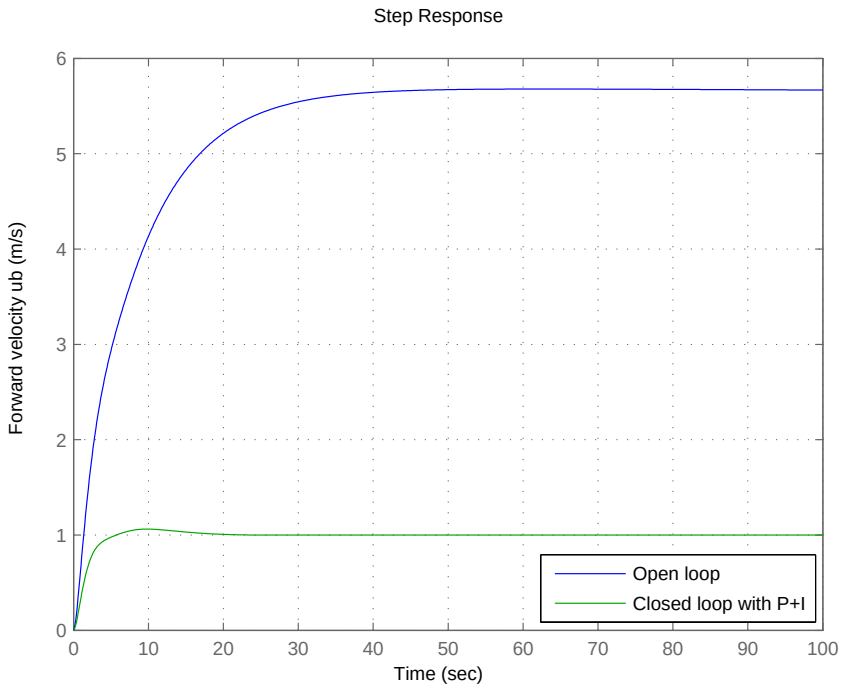

Figure A.11: Autopilot – Aerosonde's response to unit thrust step input – Velocity hold

A.5 Trajectory Tracker

A.5.1 Architecture

The trajectory tracker is wrapped around the autopilot. Its architecture is shown in Figure A.10. It is comprised of:

- an off-track controller which consists of an off-track distance to track angle demand feedback with PID compensation (gains: $K_{p\_Y_e}$, $K_{i\_Y_e}$ and $K_{d\_Y_e}$),
- an along-track controller which consists of an along-track error to velocity demand feedback with P compensation (gain: $K_{p\_X_e}$).

Also, two saturation limits have been added: the first one, of ±7.5 m/s, has been applied to the velocity demand to prevent the Aerosonde UAV from exceeding its speed

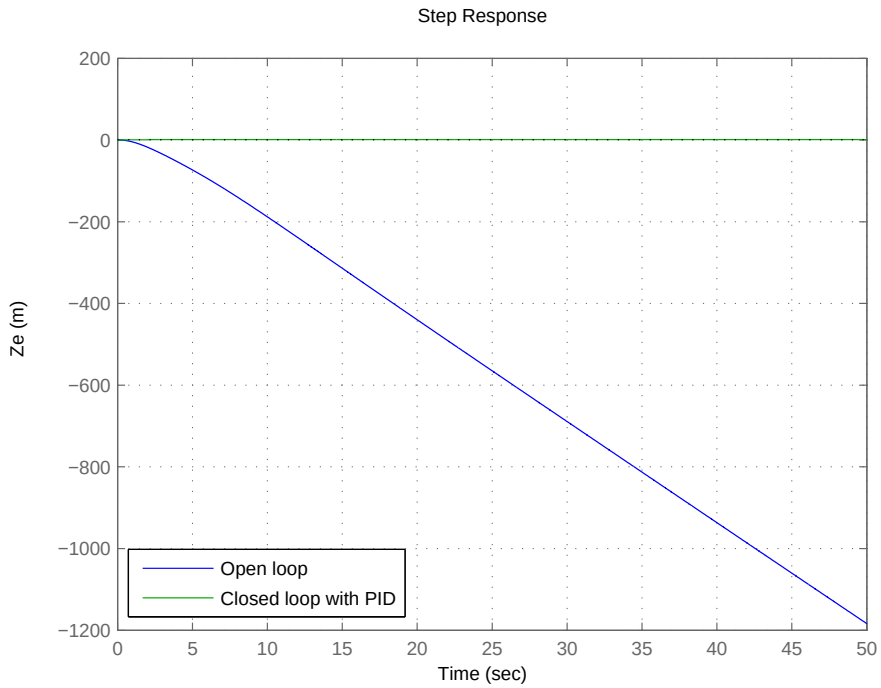

Figure A.12: Autopilot – Aerosonde's response to unit altitude step input – Altitude hold

limitations, and the second one, of ±40 deg, has been applied to the track angle demand (in association with an anti-wind up scheme) to prevent too steep a turn.

A number of quantities are introduced in order to calculate the off-track and along-track distances. These are:

- X_d, Y_d and Z_d are the coordinates of the UAV's demanded position in $\mathcal{R}_{NED}$,
- $\mathbf{V_d} = [V_{d_x}; V_{d_y}; V_{d_z}]^T$ is the UAV's demanded velocity vector in $\mathcal{R}_{NED}$,
- X_e, Y_e and Z_e are the coordinates of the UAV's current position in $\mathcal{R}_{NED}$,
- $\mathbf{V_e} = [V_{e_x}; V_{e_y}; V_{e_z}]^T$ is the UAV's current velocity vector in $\mathcal{R}_{NED}$,
- $\chi_e = \text{atan2}(V_{e_y}/V_{e_x})$ is the UAV's demanded heading,
- $\mathbf{d} = [X_e - X_d; Y_e - Y_d; Z_e - Z_d]^T$ is the distance vector between the UAV's demanded and current positions in $\mathcal{R}_{NED}$, and
- $\mathbf{dV} = \mathbf{V_e} - \mathbf{V_d}$ is the relative velocity vector in $\mathcal{R}_{NED}$.

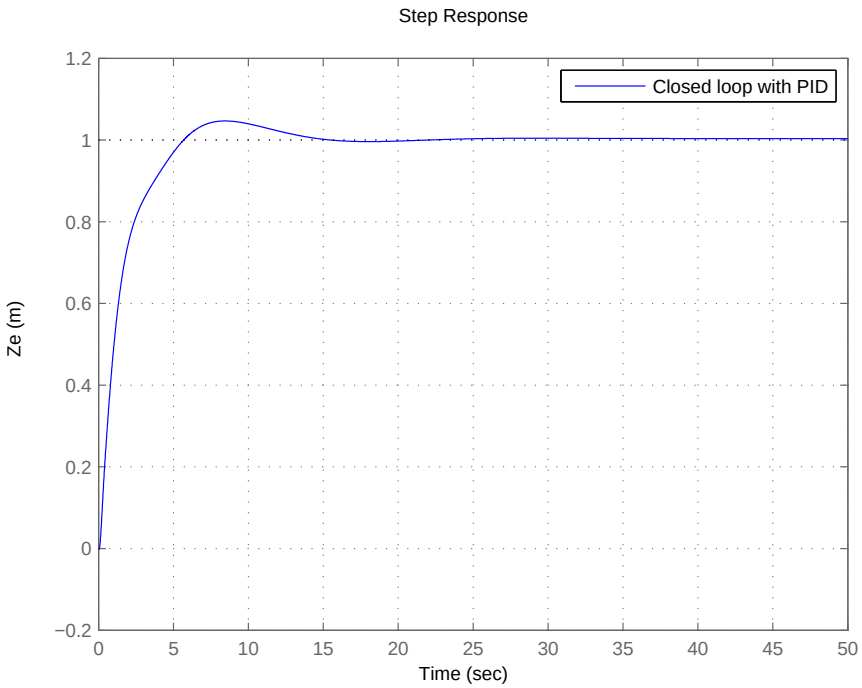

Figure A.13: Autopilot – Aerosonde's closed loop altitude response to unit altitude step input – Altitude hold

If $\mathcal{R}_d$ is the reference frame defined by (**u**,**v**,**n**) where **u** is the unit vector parallel to $\mathbf{V_d}$ and **n** is the unit vector pointing in the downwards direction, the rotation matrix **R** from $\mathcal{R}_{NED}$ to $\mathcal{R}_d$ is given by:

$$\mathbf{R} = \begin{pmatrix} \cos(\chi_d) & -\sin(\chi_d) & 0 \\ \sin(\chi_d) & \cos(\chi_d) & 0 \\ 0 & 0 & 1 \end{pmatrix} \tag{A.16}$$

The distance vector between the UAV's demanded and current positions and the relative velocity vector can then be expressed in $\mathcal{R}_d$ as, respectively:

$$\mathbf{d_d} = \mathbf{R}^{-1} \cdot \mathbf{d} = [d_{d_x}; d_{d_y}; d_{d_z}]^T \tag{A.17}$$

$$\mathbf{dV_d} = \mathbf{R}^{-1} \cdot \mathbf{dV} = [dV_{d_x}; dV_{d_y}; dV_{d_z}]^T \tag{A.18}$$

From there, the along-track distance (ATD), off-track distance (OTD) and off-track distance derivative (dOTD) are easily deduced:

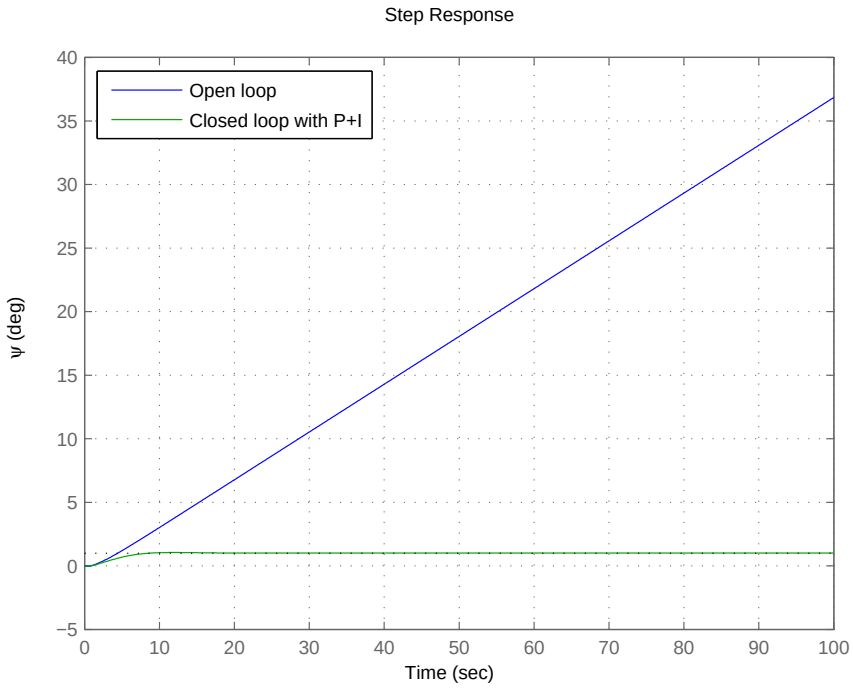

Figure A.14: Autopilot – Aerosonde's closed loop heading response to unit heading step input – Heading hold

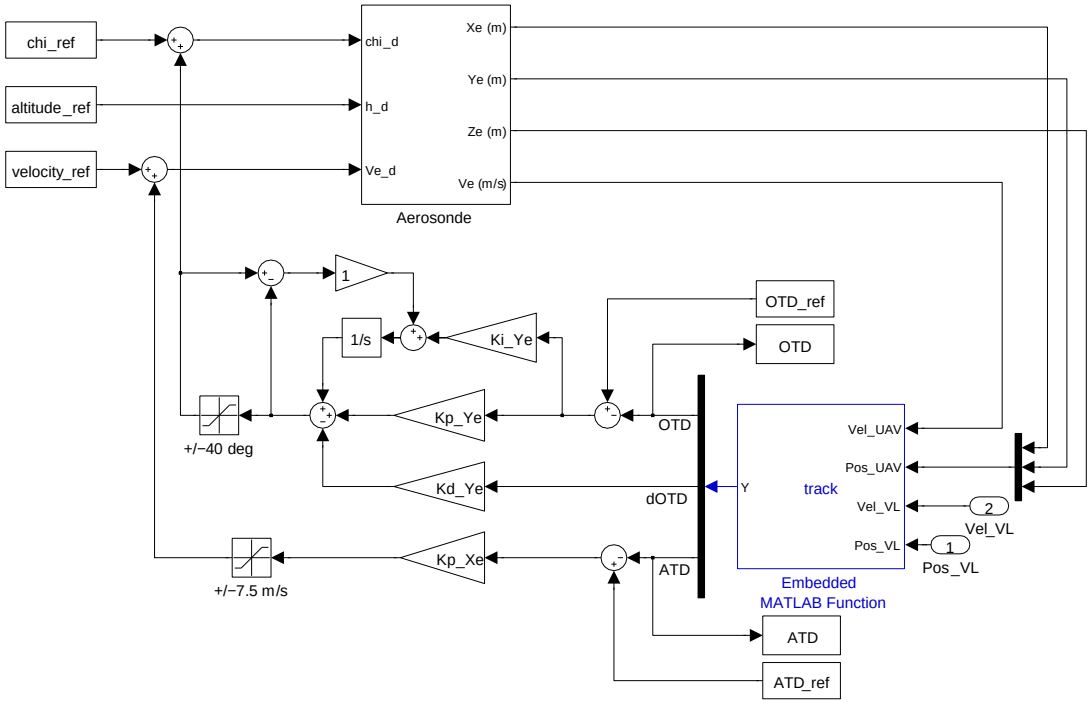

Figure A.15: Architecture of the Aerosonde's trajectory tracker

$$\text{ATD} = d_{d_x} \tag{A.19}$$

$$\text{OTD} = d_{d_y} \tag{A.20}$$

$$\text{dOTD} = dV_{d_y} \tag{A.21}$$

This calculation process is illustrated in Figure A.16.

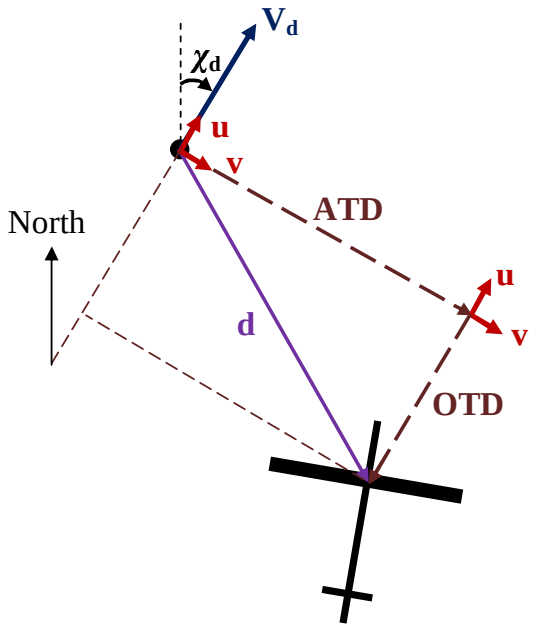

Figure A.16: Calculation of the off-track and along-track distances

A.5.2 Gains

The trajectory tracker's gains are listed in Table A.13.

Table A.13: Gains - Trajectory tracker

Kp_{Y_e}	Ki_{Y_e}	Kd_{Y_e}	Kp_{X_e}
0.18	0.0025	0.6	0.125

A.5.3 Time Responses

Figures A.17 and A.18 demonstrates the Aerosonde's trajectory tracker capabilities, in a scenario where the Aerosonde UAV is commanded to move to a position 100m to the North, 10m to the East and 10m lower than its initial position.

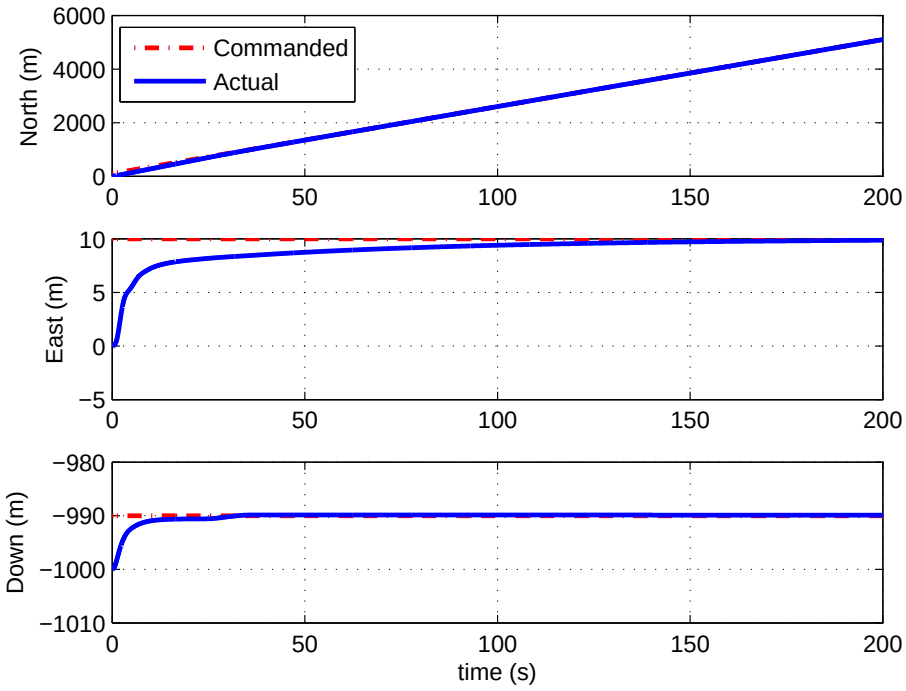

Figure A.17: Demonstration of the Aerosonde UAV's tracking capability

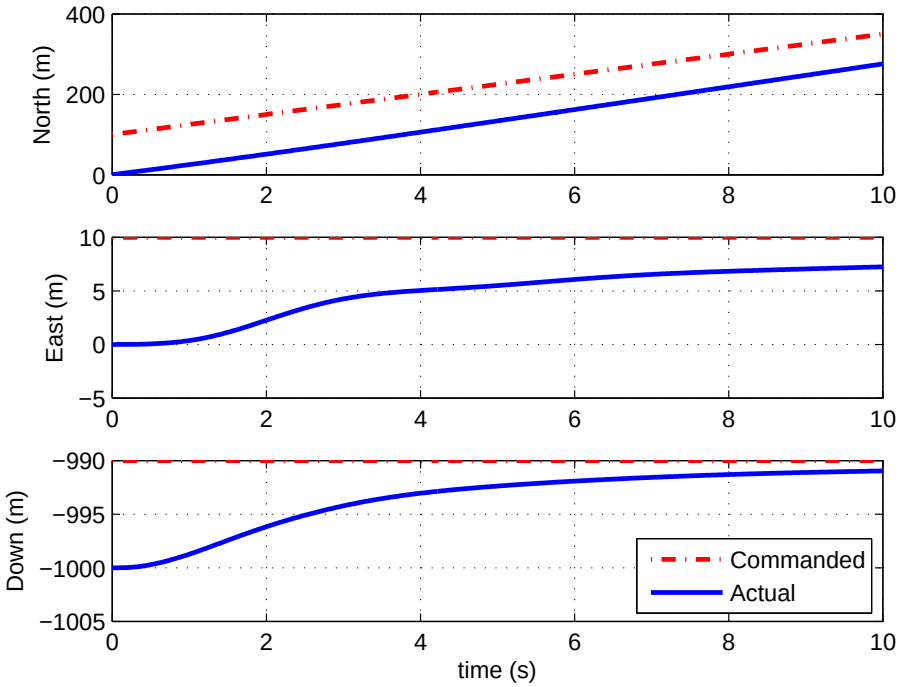

Figure A.18: Demonstration of the Aerosonde UAV's tracking capability – Initial behaviour

Appendix B

Development of a Synthetic Environment

The aim of the SE is to to facilitate the evaluation of multiple air vehicle dynamic interactions by using an animated display of the aircraft's trajectories in addition to the strip charts of interest (Euler angles, angular rates, angle of attack, angle of sideslip, airspeed, coordinates, etc.). As mentioned in Section 1.5, this is achieved by interfacing the simulation environment Simulink with a visualisation software package, such as:

- FlightGear [*FlightGear Official Website: http://www.flightgear.org/*, N.d.; Sorton and Hammaker, 2005], which is readily and freely available and has a direct interface capability with Simulink, or
- AVDS [*AVDS Official Website: http://www.rassimtech.com/*, N.d.; Rasmussen and Breslin, 1997], which also has a direct interface capability with MATLAB and Simulink.

It is to be noted that FlightGear's primary use is as a flight simulator, whereas AVDS has been developed as a real-time interactive visual tool for FCS engineering. Furthermore, when used as a visualisation tool (rather than as an online flight simulator), FlightGear is limited to the display of one air vehicle only, whereas AVDS can be coupled with simulations of multiple vehicle deployments.

B.1 Objective Requirements

The principal objective requirements for the SE development include:

- The SE must be capable of real-time or near real-time operation.

- The SE must support the use of standard flight dynamics software tools for air vehicle system evaluation, such as MATLAB/Simulink.
- The SE tools must have a visualisation capability sufficient to show close proximity multiple air vehicle engagements in a realistic scenario.

B.2 System Architecture and Operation

B.2.1 FlightGear

The interface between Simulink and FlightGear has been adapted from the pre-existing AV-SAVE (Air Vehicle Simulation and Visualisation Environment), developed at Cranfield University by Tony Steer. The AV-SAVE comprises of a number of high specification PCs, complete with accelerated 3D graphics cards, connected using 100 Mbits/s Ethernet over a Local Area Network (LAN). It uses MATLAB/Simulink to model and simulate the air vehicle's dynamics and FlightGear to provide the 3D models and 'real-world' visualisation environment. The individual PCs communicate using the User Datagram Protocol (UDP) over Internet Protocol (IP). The simplicity of UDP reduces the overhead from using the protocol and the services it provides are adequate for this specific application. AV-SAVE currently consists of the following 3 sub-systems:

- A Simulation Control Station (SCS), which runs Matlab/Simulink
- An air vehicle external 3D visualisation station (FlightGear Server)
- 'Out-of-Cockpit' visual displays

The setup of the PC system is illustrated in Figure B.1: one PC acts as the FlightGear server and drives the 'Out-of-Cockpit Visuals' PC over the LAN. 'Out-of-Cockpit Visuals' is a computer system that has the ability to display the left, centre and right view offset on three adjacent monitors respectively. The SCS PC runs the MATLAB/Simulink models and simulation environment by sending air vehicle state information via Ethernet to the FlightGear server.

B.2.2 AVDS

Theoretically, AV-SAVE can be used in association with AVDS, through the "Network Connection" block available in the AVDS toolbox for MATLAB. However, this has

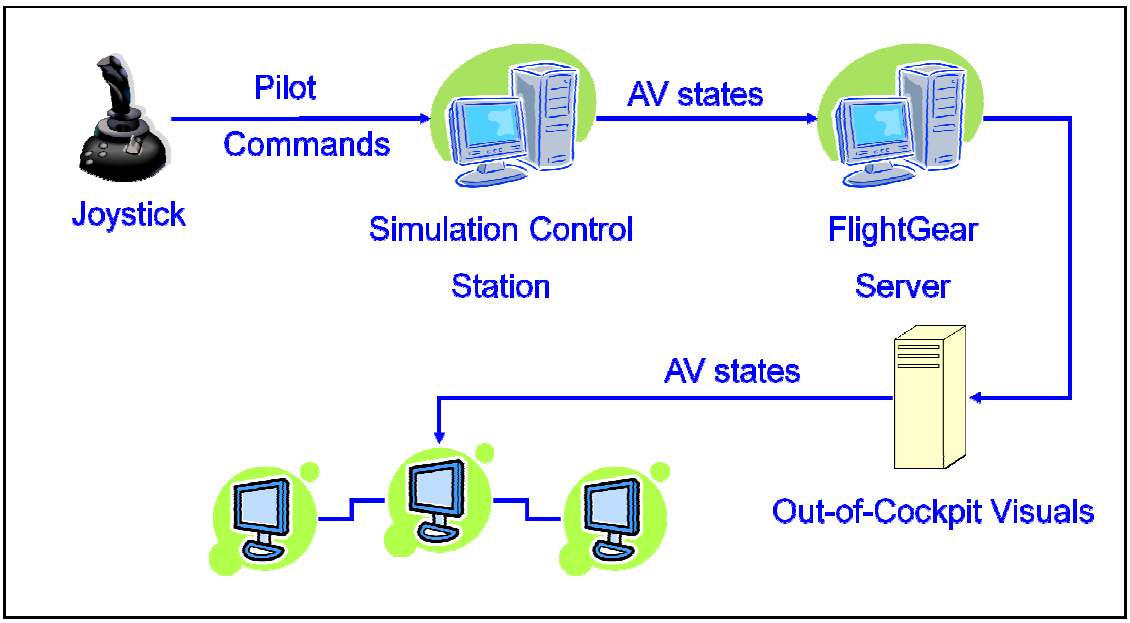

Figure B.1: AV-SAVE system architecture

not been set up yet, and could be the object of some further work. For the research presented in this thesis, AVDS and MATLAB/Simulink have been used on the same computer via the "Data Playback" option, also available in the AVDS blockset. The way the AVDS "Data Playback" block is connected to the Simulink vehicle model is shown in Figure B.2.

For each vehicle in the simulation, the elapsed time, the coordinates (in NED and in feet) and the Euler angles (in degrees) are sent to a "Playback Save" block where they are saved. In the case of the Aerosonde simulations performed in Chapter 6, two additional – and optional – parameters are used:

- the craft mask (2147353727), i.e. the appearance of the aircraft (here set to a fully visible vehicle with the gear up),

- the craft type (11), i.e. the craft image to be used during the visualisation (here set to the resized image of the Lambda Unmanned Research vehicle, as there is no image of the Aerosonde UAV available in the AVDS Aircraft Image library).

AVDS can then graphically animate the vehicle(s).

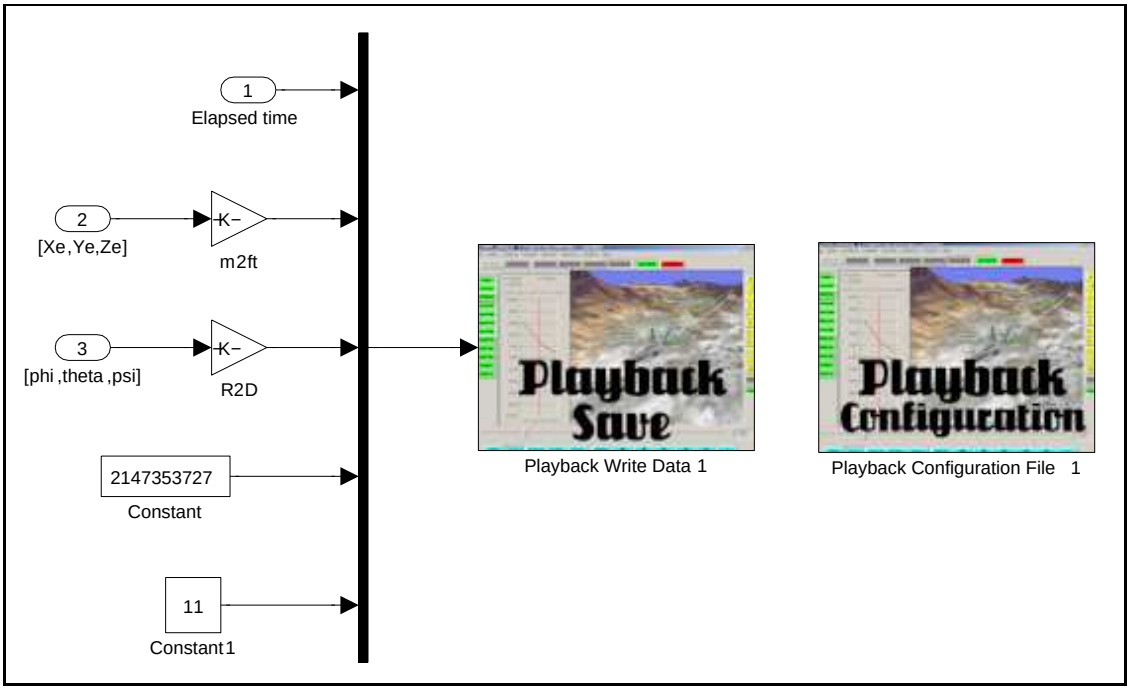

Figure B.2: Interface between the AVDS "Playback Save" block and the Simulink vehicle model

B.3 Screenshots

Some screenshots are presented in this section. Figure B.3 shows the Demon UAV (flight demonstrator of the FLAVIIR programme) flying above London and above Essex. The simulations have been run using MATLAB/Simulink and visualised using FlightGear. Figure B.4 shows the AVDS visualisation of two Lambda Unmanned Research vehicles (in lieu of two Aerosonde UAVs) flying in formation.

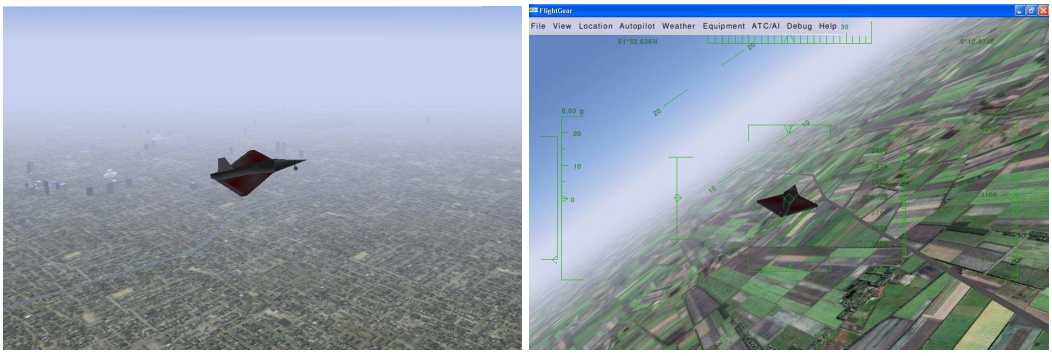

(a) Demon UAV flying above London (b) Demon UAV flying above Essex

Figure B.3: Visualisation of the Demon UAV using FlightGear

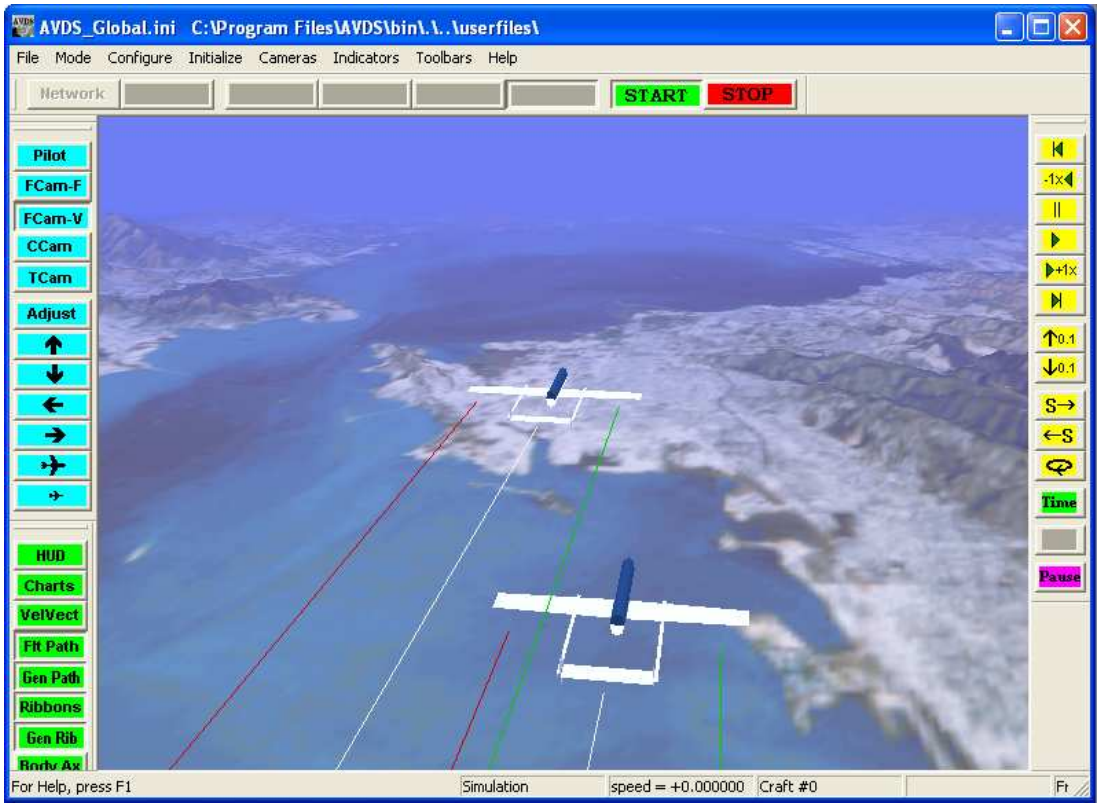

Figure B.4: Visualisation of multiple vehicle deployment using AVDS

Appendix C

List of Publications

Journal Papers

- Deborah Saban, James F. Whidborne and Alastair Cooke. 2009. "Simulation of Wake Vortex Effects for UAVs in Close Formation Flight". *Aeronautical Journal* 113(1149):727-738.

Conference Papers

- Deborah Saban and James F. Whidborne. Modeling of Wake Vortex Effects for Unmanned Air Vehicle Simulations. In *AIAA Modeling and Simulation Technologies Conference*. AIAA 2009-5686 Chicago, Illinois, August 10-13 2009.

- Deborah Saban and James F. Whidborne. Integration of Wake Vortex Effects in Simulations of UAVs in Close Formation Flight. In *24th Bristol International Unmanned Air Vehicle Systems Conference*, pp. 23.1–23.14. Bristol, UK, March 30-April 1 2009.

Prize Reports

- Research statement for the Eric Beverley Bursary 2007, awarded by the Worshipful Company of Coachmakers and Coach Harness Makers of London.

- Research statement for the IAWA (International Aviation Womens Association) International Scholarship 2008.